Volcanic plumes from explosive basaltic eruptions: the case of Mount Etna (Italy)

Eveanjelene Snee

School of Earth and Environmental Sciences

Cardiff University

Submitted in partial fulfilment of the requirements for the degree of

Doctor of Philosophy

August 2021

ABSTRACT

Explosive basaltic eruptions at Mount Etna, Italy, distinguished by a lava fountain surrounded by a tephra plume, have occurred frequently in recent decades. The associated injection of tephra into the atmosphere creates a hazard to local and regional communities. Despite this, the plume dynamics are poorly-understood. To improve the understanding of this phenomena, I investigate coupled tephra plumes – lava fountains through three approaches. First, I develop a new integral model that explicitly considers the denser, coarse inner lava fountain and its effect on the surrounding tephra plume. Depending on the grain-size distribution and partitioning of initial mass flow rate (MFR) into the lava fountain, a coupled tephra plume can go higher or lower than a standard tephra plume for a given initial MFR. Secondly, I examine the relationship between plume dynamics and eruption deposits. While neither the initial MFR from a standard or the newly-developed integral model correlate to the deposit-derived MFR, the modelled MFR at the point above the lava fountain in the newly-developed model does, suggesting that these plumes have significant fallout that is not captured in typical deposit measurements. Specifically, the cone-deposit itself must be considered to account for the discrepancy between the deposit-derived and modelled initial MFRs. Finally, these results are supported by visible-wavelength video analysis of these eruptions. Qualitative analysis shows that lava fountains and tephra plumes are not fully-coupled, that lava fountains occur in the centre of tephra plumes and that surrounding material (volcanic gas and loose particles) are entrained into the plumes. Rotation of the plumes in some eruptions is also examined, although I show that its effect on plume dynamics is insignificant. Determined wind and radial entrainment coefficients are also comparable to those of standard tephra plumes. Together, these findings highlight that lava fountains significantly affect the rise of coupled tephra plumes.

DECLARATION

This work has not been submitted in substance for any other degree or award at this or any other university or place of learning, nor is being submitted concurrently in candidature for any degree or other award.

STATEMENT 1

This thesis is being submitted in partial fulfilment of the requirements for the degree of PhD.

STATEMENT 2

This thesis is the result of my own independent work/investigation, except where otherwise stated, and the thesis has not been edited by a third party beyond what is permitted by Cardiff University's Policy on the Use of Third Party Editors by Research Degree Students. Other sources are acknowledged by explicit references. The views expressed are my own.

STATEMENT 3

I hereby give consent for my thesis, if accepted, to be available online in the University's Open Access repository and for inter-library loan, and for the title and summary to be made available to outside organisations.

Signed ______________________________ (candidate)   Date ______________

STATEMENT REGARDING PUBLISHED WORK

In this thesis, substantial parts of Chapter 2 and smaller segments of Chapter 3 have already been published in Snee et al., (2021).

While the wording and the figures are essentially the same between Snee et al., (2021) and this thesis, they have been reformatted to suit the required style of a thesis. This includes significant changes to the Introduction. The wording of the remaining text has not been changed as it is the most concise and effective way to deliver the scientific points to the reader.

While Snee et al., (2021) does have multiple other co-authors, I did the model development, modelling investigation and the writing of this paper. The other co-supervisors offered guidance on the manuscript itself and on tackling any numerical issues. However, this equated to no more than the assistance given from supervisors.

E. Snee et al. (2021). A model for buoyant tephra plumes coupled to lava fountains with an application to the 29th of August 2011 paroxysmal eruption at Mount Etna, Italy. *Journal of Geophysical Research: Solid Earth*

ACKNOWLEDGEMENTS

First, thank you to all my academic supervisors (Dr Wim Degruyter, Dr Simona Scollo, Professor Costanza Bonadonna and Professor Huw Davies), who gave me this opportunity to contribute to volcanology and guided my work over the past 4 years. A special mention goes to my former and main supervisor Dr Wim Degruyter. Thank you for committing to this project even after leaving Cardiff. Your support and guidance have been vital to this PhD. I have learnt so much from you, without which I wouldn’t be the scientist I am today. On a similar note, I would also like to say a big thank you to my ’honorary’ supervisors: Dr Eduardo Rossi, Dr Valentin Freret-Lorgeril and Dr Paul Jarvis. While helping me was never your job description, your guidance and help over these past few years has been invaluable. Secondly, thank you to all my office mates in Cardiff, and a big thank you to Huw, who took over as my main supervisors for the 2nd half of my PhD. I would also like to thank all in the Geneva physical volcanology group, who adopted me into their group. This inclusion gave me the opportunity to discuss all things volcanology and feel part of a research family. Similarly, I would like to thank all my friends and family, who supported me becoming a volcanologist since our first holiday to Tenerife. I would also like to thank my PhD funders, NERC G4+ DTP, for financially supporting this PhD project, as well as my CASE partner, INGV-OE. And finally thank you once again to Paul. You have been my support through this PhD adventure and I can’t wait for the next one.

TABLE OF CONTENTS

LIST OF FIGURES

LIST OF TABLES

CHAPTER 1

INTRODUCTION

Basaltic volcanism is one of the most common types of volcanic activity on the planet. Most commonly, basaltic volcanic activity is characterised by effusive lava flows, such as in Hawaii (Cashman et al. 2014; Dietterich et al. 2021) and Iceland (e.g., Pedersen et al. (2017)), or low-intensity short-lived explosions, such as at Stromboli, Italy, (Ripepe et al. 2008) and Yasur, Vanuatu (Bani et al. 2013; Woitischek et al. 2020). However, larger explosive basaltic volcanism can also occur. These large explosive events can differ in size. For example, the 122 BC Mount Etna Plinian eruption, Italy, generated a plume which reached heights of 24-26 km above sea level (a.s.l), and had an estimated initial mass flow rate (MFR), defined as the rate of mass through a point, of 5-8.5 $\times 10^7$ kg s^{-1} (Coltelli et al. 1998). Similarly, the large basaltic explosive Plinian eruption of Tarawera, New Zealand, in 1886 also produced a tephra plume, from a 7 km long fissure, that went higher than 28 km a.s.l (Walker et al. 1984). However, basaltic volcanism can also generate eruptions that lie in between the low intensity explosions and the large scale Plinian eruptions. An example of these are eruptions that produce both a tephra plume and a lava fountain.

Eruptions that produce both a tephra plume and a lava fountain are referred to as paroxysmal eruptions (Alparone et al. 2003; Calvari et al. 2018). While other eruption styles, e.g., large explosions at Stromboli (Rosi et al. 2006; Bertagnini et al. 2011; Métrich et al. 2021), are sometime also referred to as paroxysmal eruption, in this thesis paroxysmal eruptions will refer only to those eruptions that are characterised by a co-existing tephra plume and lava fountain. Typically, these eruptions begin with Strombolian activity, known

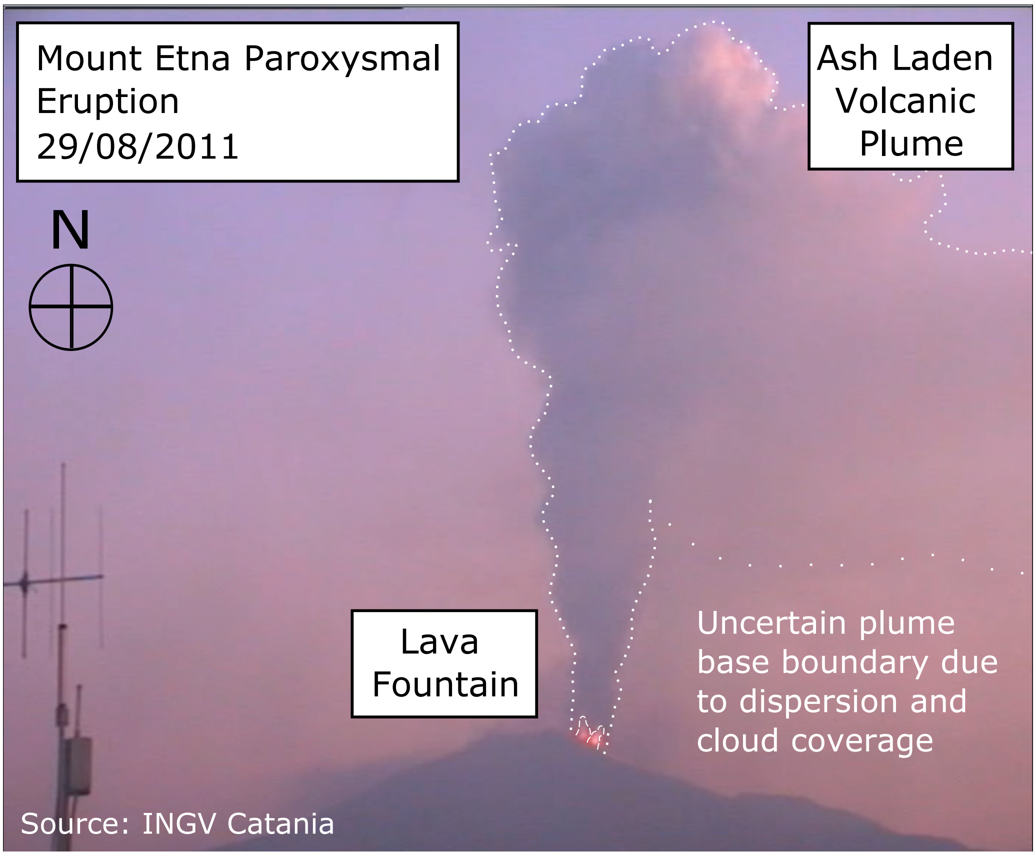

Fig. 1.1 An example of a tephra plume that is coupled to a lava fountain. Example is of the 29th of August 2011 paroxysmal eruption of Mount Etna, Italy. Source: INGV-OE.

as the resumption phase, that transitions into a sustained paroxysmal phase (Alparone et al. 2003). This phase is characterised by a lava fountain that is surrounded by a sustained tephra plume and is often referred to as the climax of the eruption (Figure 1.1). Examples of volcanoes that have had paroxysmal eruptions include Mount Etna (Italy), Izu Oshima (Japan) and Villarrica (Chile) (Mannen 2006; Calvari et al. 2018; Romero et al. 2018). Lava flows also often occur during the eruptions (Vicari et al. 2011; Ganci et al. 2013). Additionally, the volcanic plumes from these eruptions have reached altitudes of above 10 km a.s.l into the atmosphere (Mannen 2006; Calvari et al. 2018; Romero et al. 2018).

One of the most serious hazards from paroxysmal eruptions is due to the dispersion of tephra. Tephra is defined as any fragmented magma erupted by a volcano (Fisher 1961). Tephra can pose a significant hazard to the local and regional communities. Ballistic fallout and proximal tephra fall can damage local infrastructure and power supplies (Andronico et al. 2015; Osman et al. 2019), while volcanic tephra can affect regional airspace (Guffanti et al. 2009; Dingwell and Rutgersson 2014; Prata and Rose 2015). Tephra also poses a direct risk to human health as it can cause, if inhaled, chronic pulmonary disease and other respiratory issues (Gudmundsson 2011; Damby et al. 2017). It can also cause irritation to the eyes (Heggie 2009; Gudmundsson 2011; Carlsen et al. 2012b; Carlsen et al. 2012a). The mechanism for which the tephra is transported to the atmosphere, where it can pose a hazard to a much larger spatial scale, is by volcanic plumes. As a result, the dynamics of volcanic plumes of paroxysmal eruptions are vital processes that need to be understood to assess the hazard posed by the associated tephra.

In this thesis, I will focus on understanding tephra plumes that co-exist with lava fountains from paroxysmal eruptions. In this introductory Chapter I will start by giving a brief background to Mount Etna, one of the most active volcanoes in the world that frequently has paroxysmal eruptions, and the main focus of this thesis. I will briefly describe the tectonic setting of Mount Etna before focusing on its pre-historic and recent volcanic activity. I will then provide a background on volcanic plumes. This includes descriptions of their structure, fundamental dynamics and how they can be modelled. Finally, I will conclude by stating the aims and objectives of this thesis.

1.1 Mount Etna Volcano

Mount Etna is the tallest ($\sim$ 3300 m a.s.l) (Neri et al. 2008) and most active volcano in mainland Europe. Located on the Italian island of Sicily (Figure 1.2a and b), it dominates the skyline above the city of Catania. Roughly around 1.2 million people (Bonaccorso et al. 2011) live in the region around the volcano. The volcano poses a number of hazards to the local population. This includes tephra fallout, which can affect infrastructure, crops, sewage system and repository health (Barnard 2004; Andronico et al. 2015). It can also be an issue for the local airport and flights in the region (Barnard 2004; Scollo et al. 2013). Lava flows, which can originate on the flank of the volcano in the event of a fissure eruption, can also pose a danger (Duncan et al. 1996; Corsaro et al. 1996; Del Negro et al. 2020). As a result, it is important to study the volcanic activity of Mount Etna.

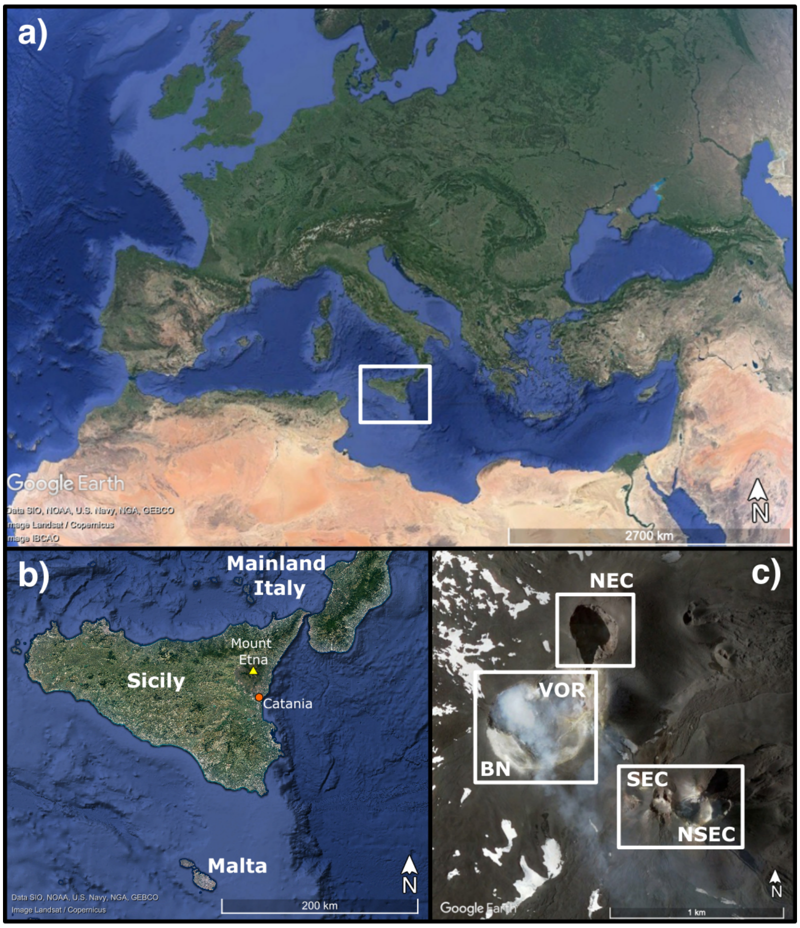

Fig. 1.2 a) A map showing the location of Sicily (white box) in Europe. b) A map showing the location of Mount Etna on the Italian island of Sicily. c) A map showing the locations of the main active craters at the summit region of Mount Etna.

The morphology of Mount Etna is complex. As Mount Etna is a stratovolcano, the slopes of the volcano are steep. Here, multiple cinder cones exist (Mulas et al. 2016). The top of Mount Etna is referred to as the summit region and is characterised by multiple active open-conduit volcanic vents. Notably, these include the North East crater (NEC), Bocca Nuova (BN), Voragine (VOR), the South East crater (SEC) and the New South East crater (NSEC). The NSEC is the newest of these craters. It started to form on the side of the SEC in 2011 from paroxysmal eruptions (see Section 1.1.2 for further details on the paroxysmal eruptions at Mount Etna) and reached a height of over 200 m in just three years (Behncke et al. 2014; De Beni et al. 2015). Figure 1.2c shows the location of each of these craters at the summit of Mount Etna. Although paroxysmal eruptions typically occur in the summit region, other eruption styles can also occur on the slopes (e.g., the 2018 Christmas eruption, Calvari et al. (2020)).

The monitoring of the volcanic activity of Mount Etna is the responsibility of the Istituto Nazionale di Geofisica e Vulcanologia, Osservatorio Etneo (INGV-OE). They do so through a range of approaches that includes monitoring of the volcanic gas (Aiuppa et al. 2007), ground deformation (Neri et al. 2009), seismicity (Alparone et al. 2003; Alparone et al. 2007), field surveys (Andronico et al. 2013; Andronico et al. 2014a; Andronico et al. 2014b), videos (visible and thermal) (Scollo et al. 2009; Scollo et al. 2014; Scollo et al. 2019; Corradino et al. 2020), and other remote sensing approaches (Scollo et al. 2009; Donnadieu et al. 2016; Corradini et al. 2018). Often, these observations are used in conjunction to allow INGV-OE to form an integrated understanding of the complex volcanic processes occurring under the surface (e.g., Andronico et al. (2005) and Bonaccorso et al. (2011)). Together, the methodologies allow the volcanic unrest and geological changes of the area to be characterised and constantly monitored.

During an eruption, monitoring and forecasting of the tephra plumes take place to be able to assess the volcanic hazard in real time. This is achieved through a multidisciplinary approach (cameras, satellite, and numerical modelling) (Scollo et al. 2019). INGV-OE use observations of the plume height from the visible videos or from satellites to then constrain an integral model for volcanic plumes (Degruyter and Bonadonna 2012). This allows for parameters such as the initial MFR to be determined, which can then be used as an input into dispersion models to make a hazard assessment of the tephra dispersal (Scollo et al. 2013; Scollo et al. 2019). A sedimentation model is also used to model the fallout of large clasts from the tephra plume (Rossi et al. 2019; Osman et al. 2019). This approach allows for the hazard for specific eruptions to be characterised quickly and for the relevant information to be provided to the National Department of Civil Protection (DPC) (Scollo et al. 2019).

1.1.1 Tectonics and pre-historic volcanic activity

Mount Etna is the result of active tectonics within the Mediterranean basin. It is located in the region of the Calabria subduction zone on the hanging wall of the Apennines accretionary prism on the Hyblean plateau (Doglioni et al. 2001; Faccenna et al. 2011). However, the reason for the location of Mount Etna is not as clear as it first seems. Mount Etna is laterally offset from the Calabria subduction zone and south of the Ionian slab. Therefore, the origin of the volcanic activity is not just from a simple subducting plate mechanism (Schellart 2010). This is further supported by the geochemistry of the volcanic rocks, which indicate a deeper mantle origin of the magma (Schellart 2010).

Different mechanisms for the origin of the volcanic activity have been proposed to explain Mount Etna. One of these proposed mechanisms is a mantle plume that originates either from the deep mantle (Schiano et al. 2001) or from the discontinuity in the seismic velocity at 660 km depth in the mantle (Cadoux et al. 2007). However, seismic tomography of the region does not support a plume of a sufficiently deep origin required to support the geochemical mantle signature of the volcanic material (Montelli et al. 2006; Schellart 2010). Another proposed theory is that the volcanic activity is derived from a tectonic origin. Doglioni et al. (2001) suggested that, since Mount Etna is located on a series of tectonic faults, in particular the Malta escarpment, these faults allow the magma to rise, but this does not explain the magma origin (Schellart 2010). However, an asthenospheric window, caused by the rollback of the subducted Ionian slab, would allow for upwelling of the asthenosphere and be the origin of the magma of Mount Etna (Gvirtzman and Nur 1999). Similarly, rollback of the subducted Ionian slab could be causing decompression melting of the upper mantle that then flows upwards and southerly around the edge of the slab. This theory would also explain the origin of the other intra-plate volcanism (e.g., Pantelleria) in the region (Schellart 2010).

Dating of the stratigraphy by ^{40}Ar/^{39}Ar has allowed scientists to reconstruct the formation of Mount Etna (Branca et al. 2008). The formation of the volcano started to occur $\sim$ 500 ka (Branca et al. 2008). This earliest stage consisted of sub-marine volcanism and the erupted material was thoelitic in composition (Branca et al. 2008). At about 300 ka, this volcanic activity became sub-aerial due to tectonic uplift in the region (Di Stefano and Branca 2002; Branca et al. 2008). In this stage, the volcanic activity occurred from fissures on an ancient alluvial plane and resulted in the formation of a lava plateau (Branca et al. 2011). This activity eventually became localised at about 220 ka and built a shield volcano. The volcanism then shifted westwards to the current central position to form the volcanic edifice of Mount Etna today (De Beni et al. 2011).

1.1.2 Recent volcanic activity

During human history, Mount Etna has produced a wide range of different styles of volcanic eruptions (Branca and Del Carlo 2005). These include both effusive eruptions (Andronico and Lodato 2005), such as lava flows (Coltelli et al. 2007; Branca et al. 2013; Branca et al. 2017), and explosive eruptions (Scollo et al. 2007; Andronico et al. 2008b; Andronico et al. 2009a; Andronico et al. 2009b; Andronico et al. 2014b; Calvari et al. 2018; Calvari et al. 2020). The explosive eruptions themselves also vary in style. Many small Strombolian bursts (Branca and Del Carlo 2005; Vergniolle and Ripepe 2008; Pering et al. 2015) occur frequently at Mount Etna, while other eruptions are characterised by long lasting fissures with tephra plumes (Scollo et al. 2007; Andronico et al. 2008b). Larger explosive eruptions, that can be described as sub-Plinian to Plinain, have also occurred from the summit craters (Scollo et al. 2007; Andronico et al. 2008b; Andronico et al. 2009a; Andronico et al. 2009b; Andronico et al. 2014b; Edwards et al. 2018). This large variability in eruption style has been well studied in the literature (Branca and Del Carlo 2005).

Explosive volcanic activity at Mount Etna has increased in the past few decades (Branca and Del Carlo 2005). The majority this explosive volcanic activity at Mount Etna has taken the form of paroxysmal eruptions. These paroxysmal eruptions tend to occur in clusters that last for a period of months and are also known as episodic eruptions (Andronico and Corsaro 2011; Andronico et al. 2015). For example, in 2000, 64 paroxysmal eruptions occurred over a time period of 5 months (Alparone et al. 2003; Andronico and Corsaro 2011). Since then, episodic eruption series have also occurred in 2001 (Scollo et al. 2007), 2006 (Andronico et al. 2009a; Andronico et al. 2009b; Andronico et al. 2014b) and 2011-2013 (Freret-Lorgeril et al. 2018; Calvari et al. 2018). The eruption columns from the paroxysmal eruptions have reached heights of up to 15 km a.s.l (Vulpiani et al. 2016), and generally last for a period of 10s of minutes to a few hours (Freret-Lorgeril et al. 2018; Calvari et al. 2018). Currently, Mount Etna is in a new episodic eruption phase, which started in mid-February 2021, and, by the end of July 2021, it had produced 52 paroxysmal eruptions (https://www.volcanodiscovery.com/photos/etna/2021/paroxysm31jul-1aug/lavafountains.html). Due to the frequency and peculiarity of this recent volcanic activity, the volcanic tephra plumes from these eruptions will be the focus of this thesis.

1.2 Volcanic Plumes

Plumes are defined as vertical, buoyancy-driven flows (Morton et al. 1956; Turner 1969; Woods 2010), where buoyancy is the hydrostatic pressure force which acts on an immersed object in an ambient fluid. Turbulent plumes are characterised by high ($\gtrsim 1000$) Reynolds numbers, a dimensionless parameter that is the ratio of the inertial and viscous forces and governs the resulting flow patterns. Turbulent flows are dominated by the inertial forces that act in the fluid. In plumes, the turbulent nature manifests itself as vortical eddies, which entrain the ambient fluid and mix it into the plume in a process called entrainment. As a result, mixing is effective in the disordered flow and, consequently, unlike laminar flows, these flows are irreversible. Additionally, plumes can be multi-phase and can exist on a wide variety of length scales. This definition can be expanded further when applied to volcanology. Volcanic tephra plumes are turbulent, upward, buoyancy-driven flows that are generated by explosive eruptions (Woods 1988; Sparks et al. 1997; Carey and Bursik 2015). They are initially composed of volcanic gases and tephra and are initially driven by momentum. Many processes occur as they rise including air entrainment, particle fallout, particle re-entrainment and bending due to wind (Woods and Bursik 1991; Sparks et al. 1997; Carey and Bursik 2015). Volcanic plume sizes can vary over orders of magnitude (10s of meters to 10s of kms), with the largest of them being able to reach high into the stratosphere (Sparks et al. 1997; Carey and Bursik 2015). However, despite the large range in size, the underlying fundamental mechanisms remain the same across scales.

A sustained volcanic tephra plume can be split into three regions (Woods 1988; Sparks et al. 1997; Carey and Bursik 2015) (see Figure 1.3). The lowest region of a volcanic plume is known as the gas-thrust region. Here, the tephra plume is being driven by the initial momentum of the eruption. The plume density in this region is greater than that of the surrounding atmosphere meaning the plume is negatively-buoyant. However, as the turbulent volcanic plume entrains air from the ambient, the density of the plume decreases, eventually becoming lower than the ambient density. Buoyancy, as opposed to momentum, is now the driving force of the vertical motion. This region is referred to as the convective region. In this region, the plume continues to entrain air from the surroundings. However, as the plume cools, the plume density starts to increase until it reaches the same density as the ambient. At this neutral buoyancy level (NBL) the plume begins to laterally spread. If the volcanic plume still has some momentum left after the NBL, the plume can continue to rise past this point to form an overshoot. This whole region around the neutral buoyancy level is known as the umbrella cloud region.

Sustained tephra plumes are studied by a variety of methods. Some of these methods come under the umbrella of remote sensing. Remote sensing methods allow for information on volcanic plumes to be determined from a distance. This includes, but is not limited to, information on the plume velocity, the initial MFR, the plume top height, plume dispersion direction and grain-size distribution of the material in the tephra plume (e.g., Montopoli (2016), Freret-Lorgeril et al. (2018), Corradini et al. (2018), Freret-Lorgeril et al. (2021a), and McKee et al. (2021)). Examples of remote sensing methods include satellites (e.g., MODIS, SEVIRI (Corradini et al. 2018)), video cameras (thermal and visible, see Chapter 4.1 for more details) (Sparks and Wilson 1982; Scollo et al. 2009; Scollo et al. 2014; Scollo et al. 2019; Corradino et al. 2020), radar (Donnadieu et al. 2016; Freret-Lorgeril et al. 2018; Mereu et al.

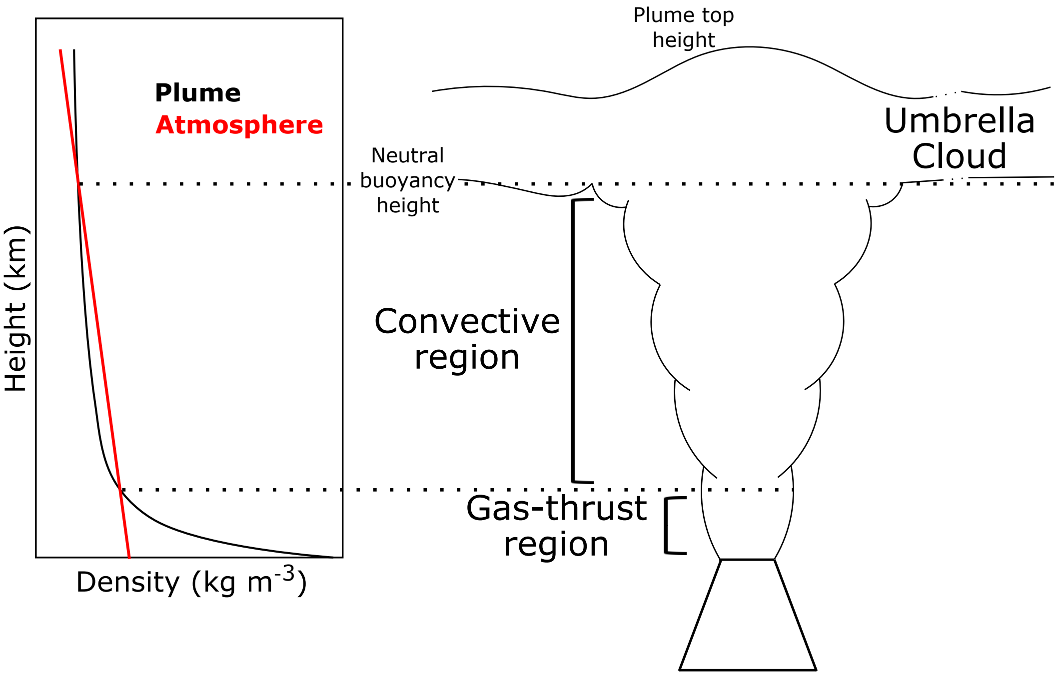

Fig. 1.3 Diagram of the structure of a volcanic plume, based on Figure 29.2, Cioni et al. (2015).

2020), LiDAR (Winker and Osborn 1992; Marenco et al. 2011; Scollo et al. 2012) and infrasound (Lamb et al. 2015; Perttu et al. 2020). Another method to study tephra plumes is via studying the tephra deposit. The tephra deposit is representative of the material that has sedimented out of the tephra plume and can tell us about the initial MFR, the height reached by the tephra plumes (Carey and Sparks 1986; Rossi et al. 2019), the direction of dispersion and even information on fragmentation in the tephra plume (Polacci et al. 2019). More details on how the tephra deposit is analysed to determine such information can be found in Chapter 3.1. Nevertheless, both tephra deposit observations and remote sensing methods can provide vital information on the dynamics of tephra plumes.

1.2.1 Background of Modelling Volcanic Plumes

Further key tools used to study tephra plumes are numerical and analytical models. In this sub-section, I will present a background to the modelling of volcanic tephra plumes, starting with simple analytical expressions, through first-order integral models and finally describing more complicated 3D numerical models.

0th order models

The simplest way that volcanic plumes have been modelled is through the use of analytical expressions, or 0th order models (Costa et al. 2016b; Aubry et al. 2021). These analytical expressions describe the relationship between the source conditions and the height that the plume could reach. They can be divided into two categories: those deriving from physical-based parameterisations and those deriving from observations, where the latter are also known as empirical relationships.

Analytical plume models that are derived from the physics originate from the work of Morton et al. (1956), where the dependency of plume height (H) on the initial buoyancy flux (F) and the density stratification of the surrounding fluid (G) is determined by dimensional analysis (see Appendix A) to be

$$H = 2^{-\frac{7}{8}}\pi^{-\frac{1}{4}}\chi^{-\frac{1}{2}}F^{\frac{1}{4}}G^{-\frac{3}{8}}z_1, \tag{1.1}$$

where z_1 is the maximum dimensionless height of the plume, determined to be 2.8 by Morton et al. (1956), and χ is the radial entrainment coefficient. The constants in this equation are determined empirically (Morton et al. 1956). Since then, other physics-based analytical expressions have been derived for volcanic plumes. Two notable formulations are those of Degruyter and Bonadonna (2012) and Woodhouse et al. (2013). Both of these relationships explicitly account for the effect of wind on plume rise and have been calibrated against standard integral plume models (Degruyter and Bonadonna 2012; Woodhouse et al. 2013; Costa et al. 2016b). The relationship of Degruyter and Bonadonna (2012) also depends on entrainment coefficients (See Section 1.2.1 for definitions), the atmospheric temperature and the source enthalpy of the tephra plumes (Degruyter and Bonadonna 2012). All of these analytical relationships allow for information (either plume height or initial MFR) on a tephra plume to be determined quickly.

The second type of analytical expressions that have been used to provide information on volcanic plumes are empirical relationships that are based on observations. Sparks et al. (1997) investigated the relationship between the rate of material exiting the vent and plume height of an eruption for a number of volcanic eruptions. The rate the material exits the vent is either expressed as a mass (MFR) or as a volume (volumetric flow rate). These values can be determined from the tephra deposit (see introduction of Chapter 3 for further details). The relationship found by Sparks et al. (1997) is

$$H = 1.67\dot{V}^{0.259}, \tag{1.2}$$

where $\dot{V}$ is the volumetric flow rate. This relationship has since been improved and refined to reflect additional data points. For example, Mastin et al. (2009) defined the relationship between H and $\dot{V}$ to be

$$H = 2\dot{V}^{0.241}. \tag{1.3}$$

Integral plume models

Buoyancy-driven plumes have also been modelled using integral plume models. These are based on the theory of turbulent buoyant plumes from a maintained source, first formulated by Morton et al. (1956) who assumed the plume to be sustained with time. This means that, although the turbulent behaviour of a plume on a short timescale is chaotic, over a time period that is longer than the eddy turnover rate, the changes become regular, meaning that the plume can be assumed to be sustained. Morton et al. (1956) made three further assumptions to be able to model a buoyant rising plume in one dimension:

1. the rate of entrainment is proportional to the vertical velocity at all heights,
2. the vertical velocity and buoyancy profile are self-similar at all heights,
3. the largest local fluctuations within the plume column itself are small compared to fluctuations in the surrounding atmosphere.

The first of these assumptions is vital for the way entrainment is treated. As previously mentioned in Section 1.2, entrainment is the process of a turbulent flow, in this case a plume, incorporating the ambient fluid (Morton et al. 1956). The turbulent behaviour manifests itself as turbulent eddies, which range in scale throughout the plume. Turbulent eddies incorporate surrounding ambient air into the plume and causes it to mix with the existing plume material. This process is referred to in the literature as air entrainment. To model this process exactly, the plume turbulence would need to be solved; a non-trivial issue that is not possible to do in integral plume models. However, by making the assumption that the rate of entrainment is proportional to the vertical velocity at all heights (Morton et al. 1956), the entrainment can be modelled while not needing to solve for turbulence itself. The proportionality constant between the plume vertical velocity and the rate of entrainment is given by a coefficient known as the entrainment coefficient, χ. This assumption for integral plume models can be formulated as

$$\mu_\chi = u\chi, \tag{1.4}$$

where μ_χ is the rate of entrainment and u is the plume vertical velocity. From experiments, Morton et al. (1956) determined this entrainment coefficient to be 0.09 ± 0.01. While there has been much discussion on the value of this entrainment coefficient for volcanic plumes (Suzuki and Koyaguchi 2010; Devenish et al. 2010b; Aubry et al. 2017), the value proposed by Morton et al. (1956) has repeatably been shown to be a good fit to describe the rate of entrainment into buoyant plumes (Devenish et al. 2010b; Aubry et al. 2017).

The third of these assumptions made by Morton et al. (1956) is the Boussinesq approximation, which assumes that density differences between the plume and ambient are small, and therefore are negligible unless multiplied by gravitational acceleration. Morton et al. (1956) states that the largest local density fluctuations within the plume column itself are small compared to fluctuations in the surrounding atmosphere and, therefore, these plumes satisfies the Boussinesq approximation. This allowed Morton et al. (1956) to simplify the numerical modelling of a turbulent buoyant plume to a set of ordinary differential equations (ODEs) that can be solved for different source conditions (Hunt and Van den Bremer 2011).

Morton et al. (1956) described the behaviour of a plume rising into a linearly-stratified ambient by deriving the time averaged mass, momentum, and buoyancy flux conservation equations for a control volume for a given time step. These can be defined as:

$$\frac{d(b^2u)}{dz} = 2\mu_\chi b, \tag{1.5}$$

$$\frac{d(b^2u^2)}{dz} = 2b^2g\frac{\rho_a - \rho_p}{\rho_r}, \tag{1.6}$$

$$\frac{d\left(b^2ug\frac{\rho_a-\rho_p}{\rho_r}\right)}{dz} = 2b^2u\frac{g}{\rho_r}\frac{d\rho_a}{dz}, \tag{1.7}$$

where z is the height above the source, ρ_r is the reference density, g is the gravitational acceleration, b is the characteristic length scale, and ρ is the density. The subscripts of ρ refer to the location, where $_r$ refers to a reference, $_a$ to the ambient fluid and $_p$ to the plume. ρ_r is taken to be the ambient fluid density at the source location.

Equations 1.5 to 1.7 can be rewritten by defining $W = b^2u$, $V = bu$, $F^* = b^2ug\left(\frac{\rho_a-\rho_p}{\rho_r}\right)$ and $G = -\frac{g}{\rho_r}\frac{d(\rho_a)}{dx}$ so that

$$\frac{d(W)}{dz} = 2\chi V, \tag{1.8}$$

$$\frac{d(V^4)}{dz} = 4F^*W, \tag{1.9}$$

$$\frac{d(F^*)}{dz} = -2WG. \tag{1.10}$$

Morton et al. (1956) then reduces these equations to a non-dimensional form given by

$$\frac{d(v)}{dz_1} = v, \tag{1.11}$$

$$\frac{d(v^4)}{dz_1} = fw, \tag{1.12}$$

$$\frac{d(f)}{dz_1} = w, \tag{1.13}$$

where the lower-case symbols are scaled dimensionless equivalents to their capitalised counterparts. These equations can then be solved together using a numerical finite-difference technique. A dimensionless solution to these is shown in Figure 1.4. A fourth-order Runge-Kutta solver with a step interval of 0.1 is used and Figure 1.4 represents a plume that develops from an initially

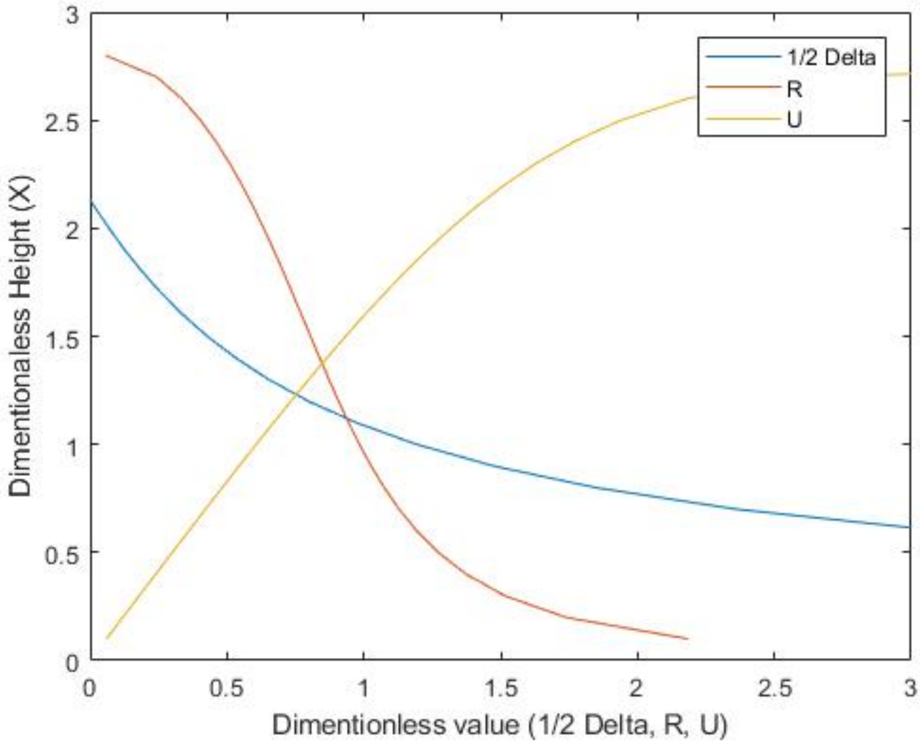

Fig. 1.4 The pure plume solution of Morton et al. (1956). R is defined as w/v, U as v^2/w and Delta as f^*/w.

finite buoyancy flux but zero mass and momentum fluxes. This solution is known as the pure plume solution.

Integral plume models have since been adapted to be more suitable for volcanic plumes. A notable early standard integral model for volcanic plumes was developed by Woods (1988). To be able to better apply an integral model to a volcanic tephra plume, the conservation equations, defined by Morton et al. (1956), were adapted to relax the Boussinesq approximation. Woods (1988) also made the assumption that a volcanic plume is a homogeneous mixture of the ambient gas, volcanic gas (assumed to be water) and solid pyroclasts, which are all in perfect thermal and dynamic equilibrium. The pressure in the plume is assumed to be that of the ambient, which allows the gas properties in the plume to be described by an ideal gas law. As the initial motion of the volcanic plume is controlled by the momentum of the eruption, Woods (1988) accounted for the initial momentum by modelling the gas-thrust region of the plume as a Prandtl jet. Prandtl jet theory was adapted by Woods (1988) for volcanic plumes to account for buoyancy and the entrainment of air. Once the initial momentum reaches zero, buoyant plume theory, developed by Morton et al. (1956), is used to model the evolution of the convecting plume. This model of Woods (1988) now forms the basis of all volcanic integral plume models (Costa et al. 2016b).

Another major step forward in volcanic plume models was the inclusion of wind. Wind increases the entrainment rate, which in turn increase the dilution rate of buoyancy in the plume. This decreases the height that the plume can reach. The effect of wind is more significant for smaller plumes as the entrainment due to wind is a relatively larger contribution to the overall entrainment of air into the plume. Bursik (2001) first included the impact of wind on the modelling of a volcanic plume by following the approach of Hewett et al. (1971) to allow bending of the plume centreline, and entrainment of mass and momentum due to wind. Here, the rate of entrainment (μ_e) can be described as

$$\mu_e = \chi |u - V_w \cos(v)| + \xi |V_w \sin(v)|, \tag{1.14}$$

where V_w is the wind velocity, v in the angle between the plume centreline and the horizontal, and ξ is the wind entrainment coefficient. The value of ξ can be determined from experiments and numerical models but has been subject to much debate. Proposed and used values for ξ range from 0.1 to 1 (Hewett et al. 1971; Huq and Stewart 1996; Bursik 2001; Contini et al. 2011; Degruyter and Bonadonna 2012; Woodhouse et al. 2013; Suzuki and Koyaguchi 2015; Girault et al. 2014; Devenish 2016; Aubry et al. 2017; Michaud-Dubuy et al. 2020).

Today, many integral volcanic plume models have been develop by different research groups to study volcanic plumes (Costa et al. 2016b). Each of these models differ in terms of the processes they consider. For example, the majority of the models consider the effect of wind on the centreline, but not all consider the effect of atmospheric humidity (Mastin 2007; Degruyter and Bonadonna 2012; Mastin 2014; Devenish 2013; Mastin 2014; Folch et al. 2016; Devenish 2016) or the phase change from water to ice on plume rise (Mastin 2007; Mastin 2014). Similarly, not all consider particle sedimentation, although this has been shown to not play a major role on the height that a tephra plume can reach (Woods and Bursik 1991; de'Michieli Vitturi et al.

2015; de'Michieli Vitturi et al. 2016; Macedonio et al. 2016; Pouget et al. 2016). Another difference between the different volcanic integral models is how they handle the rate of entrainment. Many use fixed values for the radial and wind entrainment coefficients (Bursik 2001; Mastin 2007; Degruyter and Bonadonna 2012; Devenish 2013; Woodhouse et al. 2013; Mastin 2014; Pouget et al. 2016; de'Michieli Vitturi et al. 2015; de'Michieli Vitturi et al. 2016; Costa et al. 2016b; Devenish 2016), but the used values of the coefficients vary significantly (See Table 1 in Costa et al. (2016b) for summary). Other models (Girault et al. 2014; Folch et al. 2016; Girault et al. 2016) allow the radial entrainment coefficient to vary depending on the Richardson number to be able to better describe the variation in the rate of entertainment with height in a volcanic plume following the work of Carazzo et al. (2008a). A systematic comparison between these models (Costa et al. 2016b) has shown that these differences do result in a variation in the modelled plume height between the different models.

An example of an integral model for volcanic plumes is that of Degruyter and Bonadonna (2012). The integral model of Degruyter and Bonadonna (2012) is based on the model of Woods (1988) but additionally considers the effect of wind on plume rise by following the approach of Bursik (2001). It solves the conservation equations for the mass of four different phases (dry air, water vapour, liquid water, solid particles) as well as momentum and enthalpy. These equations are defined as

$$
\begin{aligned}
\frac{d(\rho_d u r^2)}{ds} &= 2\mu_e r \rho_{ad}, && (1.15)\\
\frac{d(\rho_v u r^2)}{ds} &= 2\mu_e r \rho_{av} - \tau \rho_v r^2, && (1.16)\\
\frac{d(\rho_l u r^2)}{ds} &= \tau \rho_v r^2, && (1.17)\\
\frac{d(\rho_s u r^2)}{ds} &= 0, && (1.18)\\
\frac{d(\rho_B r^2 u^2)}{ds} &= g(\rho_{aB} - \rho_B) r^2 \sin(v) + V_w \cos(v) \frac{\rho_B u r^2}{ds}, && (1.19)\\
\frac{d(\rho_B r^2 u C_B \theta)}{ds} &= C_{aB} \theta_a \frac{d(M)}{ds} - \rho_B u r^2 g \sin(v) + L \frac{d(\rho_l u r^2)}{ds}, && (1.20)
\end{aligned}
$$

where s is the arc length along the plume centreline, r is the plume radius, τ is the condensation rate, θ is the temperature, L is the latent heat of vaporization and C is the specific heat capacity. The subscripts refer to the phase and location, where $_{aB}$ is the bulk atmosphere and $_{B}$ refers to bulk plume. $_{d}$, $_{v}$, $_{l}$ and $_{s}$ refer to the dry air phase, the water vapour phase, the liquid water phase and the solid phase, respectively. $d(M)/ds$ refers to the total change in mass and is the sum of the change of mass of the four phases considered in the plume. The change in angle between the plume centreline and the horizontal is defined as

$$\frac{d(v)}{dx} = (1/\zeta)\left(g(\rho_{aB} - \rho_B)r^2\cos(v) - V_w\sin(v)\frac{d(M)}{ds}\right), \tag{1.21}$$

where ζ is the momentum flow rate. As the plume centreline is no longer vertical, its position (in the x and y coordinates) can be calculated as

$$\frac{d(x)}{ds} = \cos(v), \tag{1.22}$$

and

$$\frac{d(z)}{ds} = \sin(v). \tag{1.23}$$

In order to parameterise entrainment, equation 1.14 is used, where χ and ξ are set as 0.1 and 0.5, respectively, as supported by Devenish et al. (2010b). The model of Degruyter and Bonadonna (2012) also accounts for entrainment of moisture from the atmosphere and the phase transformation of water vapour to liquid (final terms in equations 1.16, 1.17 and 1.20). A more detailed description of the model, including the closure equation to be able solve equations 1.15 to 1.23, can be found in the supporting information of Degruyter and Bonadonna (2012).

One of the main uses of integral plume models in volcanology is to study the relationship between eruption source parameters (ESPs) and top rise height, neutral buoyancy height and parameter profiles (e.g., temperature, velocity) of tephra plumes (Devenish 2013; Girault et al. 2014; Costa et al. 2016b). They have also been used in operational work. Due to the success of using integral plume models to describe volcanic plumes and their computational efficiency, they are used operationally in volcano observatories to better determine the MFR of the eruption in real-time for an observed plume height (Durig et al. 2015; Scollo et al. 2019). This can then subsequently be used to produce a real-time hazard assessment, a vital tool to mitigate the risks from volcanic plumes.

3D plume models

3D numerical models have also been used to examine volcanic plumes. These models solve the time-dependant Navier-Stokes equations for the conservation of mass, momentum, and energy within a 3D domain (Suzuki et al. 2016a). They explicitly solve the turbulence in a plume by modelling the engulfment and subsequent mixing of the ambient with the plume. While they were first developed in the 1990s (Valentine and Wohletz 1989; Dobran et al. 1993; Oberhuber et al. 1998), recent computational advances have allowed then to become more computationally efficient and more widely used in volcanology (Suzuki et al. 2016a). They have since been used to examine fundamental processes in a volcanic plume, which are lost in a standard integral model. Examples of this include investigating the rate of entrainment from the ambient into the plumes (Suzuki and Koyaguchi 2010; Suzuki and Koyaguchi 2013; Suzuki and Koyaguchi 2015), examining the time-dependant behaviour of co-ignimbrite (Herzog and Graf 2010) and studying the dynamics of tephra plumes (Esposti Ongaro and Cerminara 2016; Cerminara et al. 2016a). They have also been used to reconstruct specific eruptions (e.g., Kelud, Indonesia 2014 eruption, Suzuki and Iguchi (2019)) and examine the relationship between the initial MFR and the height that a plume can reach (Suzuki et al. 2016b). However, it is worth noting that 3D plume models are much more computationally expensive than integral plume models and therefore are not used in an operational capacity.

1.3 Aims and objectives of this thesis

In this thesis, I aim to improve the scientific understanding of tephra plumes from paroxysmal eruptions. Previous work has focused on the study of the tephra deposit (Mannen 2006; Scollo et al. 2007; Andronico et al. 2008b; Andronico et al. 2009a; Andronico et al. 2009b; Andronico et al. 2014a; Andronico et al. 2014b; Andronico et al. 2015; Romero et al. 2018; Edwards et al. 2018; Andronico et al. 2018; Poret et al. 2018b; Freret-Lorgeril et al. 2021b; Freret-Lorgeril et al. 2021a), tephra dispersion (Scollo et al. 2007; Andronico et al. 2008b; Andronico et al. 2014b), source conditions (e.g., Freret-Lorgeril et al. (2018), Poret et al. (2018a), Poret et al. (2018b), and Freret-Lorgeril et al. (2021a) and many more) and the conduit dynamics of paroxysmal eruptions (Calvari et al. 2011; Bonaccorso et al. 2013; Bonaccorso et al. 2014; Pompilio et al. 2017; La Spina et al. 2021). However, only a few studies have focused on understanding the dynamics of the tephra plumes themselves (Stothers et al. 1986; Parfitt and Wilson 1999; Montopoli 2016; Glaze et al. 2017). The tephra plumes are the mechanism by which the tephra can reach high into the atmosphere from where it can disperse to become a hazard over a much larger region. Thus, it is vital to understand the underlying physical processes which govern their dynamics. Therefore, this thesis will focus on understanding the dynamics of tephra plumes that are coupled to lava fountains.

Specifically, I aim to address how lava fountains affect the rise of buoyant plumes. This will first require me to determine if they affect plume rise at all. If so, I aim to quantify their impact on the relationship between the initial MFR and plume height, their influence on the tephra deposit and the mass distribution in the coupled tephra plume - lava fountain. It will then be important to determine what controls the size of the impact that the lava fountain has, and how sensitive the lava fountain effect on plume rise is when varying these controls. By answering these overarching questions, I aim to improve the understanding of the fundamental physical effects of a lava fountain on plume rise.

Since the main motivation of any study of volcanic eruptions is to ultimately contribute towards reducing the risk from the volcanic hazard, the objective of this work will be to achieve my specific aims in such a way that would be the most useful to operational settings. To do this, I will achieve my goals by using integral plume models as described in Section 1.2.1. Standard integral models are widely used operationally as, when used in conjunction with real-time monitoring observations, they can provide valuable information on the source condition of an eruption on a rapid timescale, which is vital for hazard forecasting and mitigation. Such an approach is currently part of the operational set-up of INGV-OE. Therefore, by using an integral model to achieve the aims of this thesis, I will also be able to hopefully provide information and tools that will be beneficial to the operational work of INGV-OE. This approach will also allow me to investigate wider ranges of ESPs compared to what would be achievable when using a 3D numerical model. This is a key benefit as many of these parameters are unconstrained.

Another objective of this thesis is to try and understand how the dynamics of coupled tephra plumes - lava fountains relate to features of the tephra deposit. Since tephra deposits are extensively used to study volcanic eruptions (e.g., Mannen (2006), Scollo et al. (2007), Andronico et al. (2008b), Andronico et al. (2009a), Andronico et al. (2009b), Andronico et al. (2014a), Andronico et al. (2014b), Andronico et al. (2015), Romero et al. (2018), Edwards et al. (2018), Andronico et al. (2018), Poret et al. (2018b), Freret-Lorgeril et al. (2021b), and Freret-Lorgeril et al. (2021a)), it will be important to understand how they relate to the lava fountain and the plume itself. In particular, I aim to determine the relationship between the field-derived MFR and the MFR distribution in the coupled tephra plume - lava fountain. While the link between the field derived MFR, assumed to be the initial MFR, and top plume height is well known (Sparks et al. 1997; Mastin et al. 2009), the effect of a lava fountain in a tephra plume on this relationship is not. So, by better understanding what different portions of the tephra deposit represent in a tephra plume, I can better understand the dynamics of tephra plumes that are coupled to lava fountains.

I also aim to describe the physical characteristics of the coupled tephra plumes - lava fountains. This includes addressing specific questions related to the physical relationship between the tephra plume and the lava fountain, such as what are the geometrical relationships between the lava fountain and the tephra plume? Do both coexist from the volcanic vent, or does the tephra plume originate from the lava fountain itself? Furthermore, is the lava fountain located in the centre of the tephra plume, or are they laterally offset? Similarly, I will aim to characterise the volcanic processes occurring in tephra plumes that are coupled to lava fountains, such as sedimentation from the lava fountain and the tephra plume, entrainment of the ambient into the tephra plume and rotation of the tephra plume. Addressing these questions will clarify the physical characteristics of these plumes in relation to the lava fountain and enable an assessment of how different they are to the processes occurring to standard tephra plumes.

The final objective of this thesis will be to explore the use of plume shape to constrain the solutions of an integral plume model to further the understanding of tephra plumes that are coupled to lava fountains. This will be achieved by using measurements of the shape of the tephra plume from the visible video network of INGV-OE. Typically, integral plume model solutions are only constrained through measurements of the final plume height, but shape measurements will enable better constraints to be placed on the numerical models. This will help to further quantify the source conditions of these eruptions and investigate entrainment into the plumes from the effect of wind. It will also allow me to investigate these parameters for tephra plumes where the top height of the plume cannot be seen by the monitoring cameras, i.e., it goes out of frame. By fulfilling this objective, it will not only allow further knowledge about these plumes to be obtained, but I will also be able to assess the effectiveness of using the plume shape, rather than the top height, to constrain the numerical models.

These aims and objectives will be achieved by focusing on three specific areas, which are:

1. developing a new integral model to explicitly account for the effect of the lava fountain on plume rise, in Chapter 2 - ’A new model for buoyant tephra plumes coupled to lava fountain’,
2. investigating the relationship between the field deposit and the coupled tephra plume - lava fountain in Chapter 3 - ’Understanding the relationship between lava fountains, tephra plume and their deposits at Mount Etna’,
3. examining the use of visible-wavelength camera observation to constrain characteristics of coupled tephra plumes - lava fountains at Mount Etna in Chapter 4 - ’Visible video analysis for the characterisation of tephra plumes: the example of plumes coupled to lava fountains at Mount Etna, Italy’.

Finally, in Chapter 5, I will bring together the findings of this thesis to synthesise an improved understandings of tephra plumes that are coupled to lava fountains. Specifically, I aim to address how and why lava fountains impact tephra plumes, and what the significance of this impact is when comparing to tephra plumes in the absence of lava fountains. I will also focus on what these finding can potentially tell us about what processes are taking place below the vent. Additionally, I will aim to discuss the implications of the findings for the field of volcanology, future studies of these plumes and for operational monitoring. I also aim to outline the direction that future research should take on the research area of tephra plumes that are coupled to lava fountains.

CHAPTER 2

A NEW MODEL FOR BUOYANT TEPHRA PLUMES COUPLED TO LAVA FOUNTAINS

2.1 Introduction

Tephra plumes from explosive basaltic paroxysmal eruptions differ to tephra plumes from large, sustained sub-Plinian to Plinian silicic eruptions in several important ways. Despite this, over the past century, studies have largely focused on characterising the latter. Such studies on these tephra plumes have characterised their dynamics (Mastin et al. 2009; Costa et al. 2018) and have found a relationship between the height that a plume can reach and the initial MFR (Sparks et al. 1997; Mastin et al. 2009; Degruyter and Bonadonna 2012; Woodhouse et al. 2013; Carazzo et al. 2014a; Aubry et al. 2021). However, the applicability of this relationship to tephra plumes from explosive basaltic paroxysmal eruptions needs further investigation due to differences in the observable characteristics of explosive basaltic and silicic volcanism. The most obvious such difference is the presence of a lava fountain. The lava fountain co-exists with the tephra plume and often appears to be inside the tephra plume. While lava fountains themselves are well-studied (Parfitt et al. 1995; Wilson et al. 1995; Houghton and Gonnermann 2008; Stovall et al. 2011; Taddeucci et al. 2015a; Mueller et al. 2019; Namiki et al. 2021), their interaction with a surrounding tephra plume is not. Further to this, due to the difference between basaltic and silicic magmas, tephra plumes from basaltic explosive eruptions are hotter (Ghiorso and Sack 1995; Sparks et al. 1997; Gualda et al. 2012). As a result, it is unknown how a lava fountain affects the dynamics of a tephra plume with which it is coupled.

There has been limited work on the modelling of coupled tephra plumes - lava fountains. Integral plume models have previously been applied to tephra plumes that are coupled to lava fountains through a series of adaptations. One such adaptation is the change from a circular to a linear vent geometry to better model plumes from the fissure fed fountains of the Laki 1783 eruption (Stothers et al. 1986; Woods 1993). However, tephra plumes from paroxysmal eruptions can also occur from a circular summit crater (e.g., Mount Etna (Calvari et al. 2018)). Furthermore, while not directly applied to tephra plumes that are coupled to lava fountains, the inclusion of sedimentation and thermal disequilibrium into plume models (Woods and Bursik 1991; Bursik 2001; Girault et al. 2014; Girault et al. 2016) was a further advance increasing their suitability for modelling volcanic plumes that are composed of coarse material, such as coupled tephra plumes - lava fountains. In particular, Woods and Bursik (1991) found that while sedimentation alone did not significantly affect the plume height, when coupled with accounting for thermal disequilibrium, sedimentation can impact the dynamics of tephra plumes.

Additionally, Parfitt and Wilson (1999) demonstrated the successful ability of applying an integral plume model to match independent measurements of the dynamics of a lava fountain - tephra plume system in Hawaii. By using basaltic ESPs, including a realistic coarse GSD, and accounting for dynamic disequilibrium of different particle sizes at the source (Wilson and Walker 1987; Woods and Bursik 1991), the behaviour of a lava fountain is more accurately represented in the model. These authors were also able to reproduce the height of the lava fountain (maximum height of $\sim$ 570 m above vent level (a.v.l) (Richter et al. 1970)) of the 1959 Kilauea Iki eruptions by assuming that the lava fountain height was equal to the height in the model where the majority ($\sim$ 90%) of the solid phase MFR had been lost. However, the best-fit modelled final plume height (6.7 - 7.5 km a.v.l) was much higher that the observed plume height of $\sim$ 1.4 km (Richter et al. 1970). The authors suggest that this apparent discrepancy can be explained by gasses and very fine particles reaching heights above the visibly-observed plume. This therefore leads back to the question of can an integral plume model fully capture the characteristics of the tephra plume from coupled tephra plume - lava fountain eruptions.

More recent studies have focused on modelling larger sub-Plinian plumes that are coupled to large lava fountains. Glaze et al. (2017) investigated the tephra plume associated with the 1986 eruption of Izu-Oshima, Japan, that was characterised by a 12 - 16 km a.s.l tephra plume and a 1.6 km a.v.l high lava fountain (Sumner 1998), by only modelling the plume portion of the system. The integral model is applied only to the tephra plume above the lava fountain and the ESPs were adapted to account for how much solid mass has been lost from the system in the lava fountain region. This is achieved by defining an effective volatile content, which is determined from a partitioning factor and the bulk volatile content of the magma (Kaminski et al. 2011). The authors then applied the same method to evaluate the plumes and SO_2 mass injection from the ancient flood basalt Roza eruption. However, this approach does not explicitly consider the lava fountain and tephra plume interaction. Therefore, the impact of the lava fountain on plume rise and plume dynamics is not fully determined.

In this Chapter, I aim to explicitly evaluate the impact that a lava fountain has on the rise of a tephra plume through the use of integral plume models. I first evaluate the use of a standard integral model to describe tephra plumes that are coupled to lava fountains in Section 2.2. This is achieved by applying a standard integral model to the tephra plumes that are coupled to lava fountains at Mount Etna, Italy. The model results are then compared to the observed characteristics (e.g., height of the lava fountain, MFR derived from the plume tephra deposit) of the plume (Edwards et al. 2018; Andronico et al. 2015; Corradini et al. 2016; Andronico et al. 2018; de Michele et al. 2019; Poret et al. 2018b; Corradini et al. 2018; Freret-Lorgeril et al. 2021b; Andronico et al. 2014a; Calvari et al. 2011; Andronico et al. 2009b; Andronico et al. 2014b; Andronico et al. 2009a; Andronico et al. 2008b; Scollo et al. 2007). This comparison shows that the use of a standard integral model does not capture the height of the observed lava fountain and confirms that the assumption of the lava fountain height being equal to the height of the gas-thrust region of the tephra plume is not valid (Vulpiani et al. 2016; Calvari et al. 2018). Additionally, it is shown that the MFR derived from a standard integral model that is constrained by the observed plume height is not equal to the MFR derived from the plume tephra deposit. As a result, I conclude that a standard integral model is inadequate to simulate and capture the characteristics of coupled lava fountains - tephra plumes.

To fully investigate the effect of a lava fountain on a volcanic plume, I therefore develop a new, 1D integral coaxial, buoyant plume model that simulates interaction between an inner, circular plume (representing the lava fountain) and an outer, annular-shaped, buoyant plume through the processes of entrainment and particle fallout (Section 2.3). This model will be referred to as the double plume model in what follows. The effect of varying source conditions, such as the initial GSD and the size of a lava fountain, on MFR estimates obtained with the new double plume integral model are then evaluated for two coupling scenarios (Section 2.4.1). I also focus of the impact of a lava fountain on the dynamics of the surrounding tephra plume (Section 2.4.2), and briefly explore the impact of thermal disequilibrium between the gas and solid phases on the height that a coupled tephra plume - lava fountain could reach (Section 2.4.3). Finally, I discuss and summarise the key controls on the rise of tephra plumes that are coupled to lava fountains. The modelling work done in this Chapter highlights that the initial GSD and size of the lava fountain significantly impact the height a coupled tephra plume can reach (Section 2.5.1). The limitations of the methodology of this Chapter on exploring the impact a lava fountain has on a coupled tephra plume are then discussed in Section 2.5.2. The discussion on the limitations focuses on two main sub-topics: parameter uncertainty and unaccounted processes in the double plume model. Future work, which could help tackle the discussed limitations, is then suggested.

2.2 Applicability of a Standard Integral Model to Coupled Lava Fountains - Tephra Plumes

Before applying a new double plume model to plumes coupled with lava fountains from paroxysmal eruptions, the suitability of a standard integral model for simulating these plumes is first determined. The integral model of Degruyter and Bonadonna (2012) is used and has been adapted to account for particle sedimentation during plume rise following the approach of Ernst et al. (1996) and Bursik (2001). Hereinafter, this will be referred to as the standard integral model to distinguish from the double plume model.

To explore the applicability of the standard integral model to tephra plumes that coexist with a lava fountain, I randomly sample the parameter space defined in Table 2.1 to invert the ESPs from the observed plume height. The ESPs that are varied include initial velocity, gas mass fraction, temperature, and MFR. The initial gas mass fraction and exit velocity are treated independent of each other. I keep the entrainment coefficients in the model fixed at 0.1 and 0.5 for the radial and wind entrainment coefficients, respectively as these are the values used in operational modelling by INGV-OE (Scollo et al. 2019) and are also supported by several studies (Devenish et al. 2010b; Aubry et al. 2017; Michaud-Dubuy et al. 2020). The initial GSD used is dependent on the eruption that is being modelled. If a field-derived GSD is available, it is used as the initial GSD. Otherwise, a log-normal GSD is used, which is defined with a median grain-size of 0.5 and a standard deviation of 1.5 in accordance with the values used in operational modelling by INGV-OE (Scollo et al. 2019). Atmospheric conditions (wind, temperature, and pressure) are determined from the ECMWF ERA Interim, Daily data sets (Dee et al. 2011) for each eruption examined in this section. In this section of this Chapter only, the effect of wind on the rise height of the buoyant tephra plume is considered. I follow a similar procedure to the approach of Mastin (2014), Devenish (2016) and Scollo et al. (2019) by calculating the final plume height both in the presence of wind (Z_{wind}) and without wind ($Z_{\text{no wind}}$). When considering the presence of wind, the final plume height, is considered to be the sum of the centreline height and the plume radius. The minimum plume height is chosen to avoid the case of a bent over plume going higher than a plume without wind, which is calculated as

$$Z_{\text{final}} \quad = \quad \min(Z_{\text{wind}}, Z_{\text{no wind}}). \tag{2.1}$$

2.2.1 Gas-thrust region

I first explore the relationship between the lava fountain and the gas-thrust region of a buoyant tephra plume. A lava fountain is defined as a vertical jet of coarse material that is driven by kinetic energy and reaches its final height once this kinetic energy is completely exhausted. This height can be derived from Bernouilli's equation and is given as $u_0^2/(2g)$ where u_0 is the initial velocity and g is gravitational acceleration. This is often referred to as the ballistic height (Head and Wilson 1989; Bonaccorso et al. 2014). In contrast, the gas-thrust region is the negatively buoyant lower region of a

Table 2.1 ESPs for Monte Carlo simulations using the single plume model used in Figure 2.1 and 2.2.

ESP	Standard Integral Model
Total MFR (kg s^{-1})	10^3 - 10^7
Temperature (K)	900 - 1200
Velocity (m s^{-1})	75 - 200
Gas mass fraction	0.01 - 0.03
GSD	Derived from tephra deposit if available or log-normal GSD used in operational modelling

plume that is driven upwards by the initial momentum. Once the buoyancy becomes positive, i.e., where the bulk density of the plume equates to that of the ambient density, the gas-thrust region stops and the convective region begins (Carey and Bursik 2015) (See Section 1.2). Although a lava fountain and the gas-thrust region are different, the terms have sometimes been used interchangeably. Thermal camera images at Mount Etna, show a hot core extending far above the incandescent region seen by the naked eye and this has previously been interpreted as the lava fountain (Calvari et al. 2018). The height of this thermally-saturated region, defined by different thresholds depending on the camera in question (Calvari et al. 2018), has often been equated to the gas-thrust region of the plume (Vulpiani et al. 2016; Calvari et al. 2018). I demonstrate the clear difference between the height of the gas-thrust region and the height of the lava fountain in Figure 2.1. The height of the gas-thrust region is determined with the standard integral model as the height at which the modelled plume becomes less dense than the surrounding fluid (i.e., the point where the modelled plume becomes buoyant) for ESPs that reproduce the observed plume height (9 - 9.9 km a.s.l (Corradini et al. 2018; Freret-Lorgeril et al. 2021b)) of the 29th of August 2011 paroxysmal eruption at Mount Etna. The ballistic heights range between 287 m and 2039 m due to the velocity range in the parameter space. These are consistent with the observed range from thermal camera imaging by Calvari et al. (2018), while the height of the gas-thrust region is significantly lower. This is further supported by recent analyses that have decoupled the gas-thrust region from the vertical ballistic region detected by radar (Mereu et al. 2020). Hence, a standard integral model does not capture the lava fountain height appropriately.

2.2.2 Mass flow rate

Discrepancies exist between initial MFRs determined from tephra deposits and those calculated from observed plume heights (Figure 2.2). Once again, the standard integral model is used as before to show that the MFR calculated from the maximum plume height is greater than, by up to two orders of magnitude, those determined from the field deposits for Etna eruptions between 2000 and 2016. This suggests that the well-established relationship between plume height and initial MFR (Sparks et al. 1997; Mastin et al. 2009; Degruyter and Bonadonna 2012; Woodhouse et al. 2013; Girault et al. 2014; Gouhier et al. 2019) could differ for paroxysmal eruptions at Mount Etna. In the majority of these calculations, the maximum, rather than the mean plume height, was considered owing to a lack of available data. However, for the 29th of August 2011 and the 23rd of November 2013 eruptions of Mount Etna, the results when using the mean plume height are also plotted. Whilst this has partially resolved the conundrum for the 23rd of November 2013 eruption, the discrepancy still exists for the 29th of August 2011 eruption. These discrepancies highlight the need for further investigation of tephra plumes that are coupled to lava fountains and how they differ from more typical plumes. As a result, I develop a model that can be used to simultaneously capture the lava fountain and tephra plume heights and relate these heights to the field deposit.

2.3 Model Description

I present an integral model of a coaxial double plume. The underlying principles follow those of commonly used integral plume models, which are based on the buoyant plume theory developed by Morton et al. (1956) (See Section 1.2.1 for further details). The distinctive feature is to explicitly treat the dynamics of a dense core at the source and how it feeds a tephra-rich outer rim through mass, momentum, and enthalpy exchange. Double plume models, using buoyant plume theory, are used to better represent the complex characteristics of a plume without drastically increasing the computational expense. They are commonly used to better represent turbulence in a plume

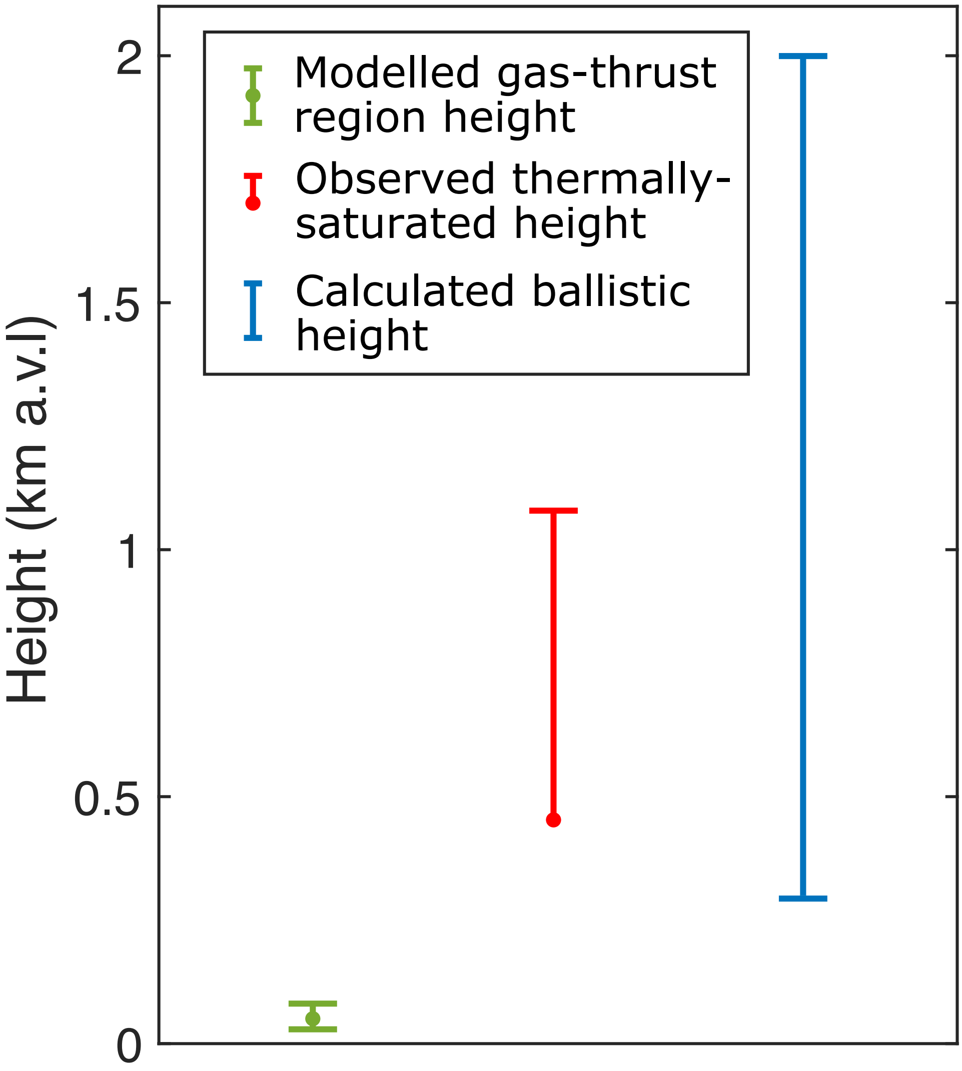

Fig. 2.1 A comparison between the modelled gas-thrust region (green) of a buoyant tephra plume and the observed (red) thermally-saturated region for the 29th of August 2011 paroxysmal eruption of Mount Etna, Italy (Calvari et al. 2018). The calculated ballistic height is also plotted (blue). The error bars are defined with the minimum, average and maximum heights (if available) to show the variability of the height of the feature in question.

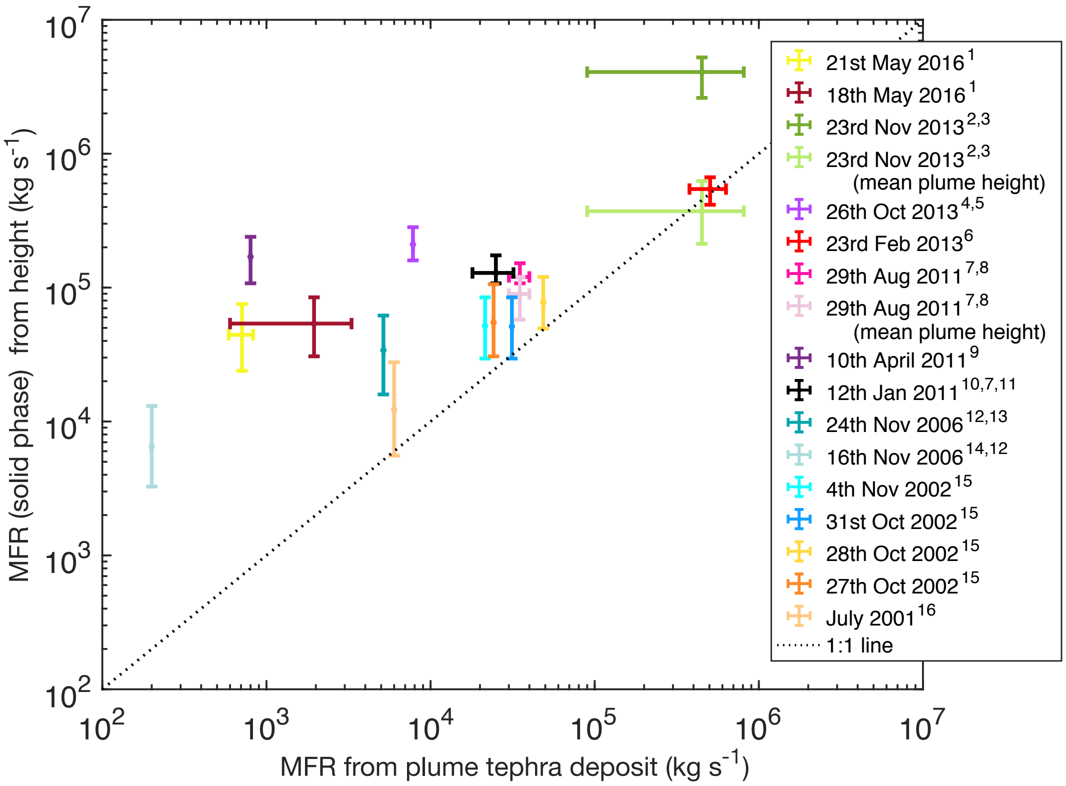

Fig. 2.2 A comparison between the MFRs determined from the tephra deposits associated with plume sedimentation with those determined from the observed plume height, using a standard integral model, for paroxysmal eruptions of Mount Etna between 2000 and 2016, whose tephra deposits have been characterised. The model is that of Degruyter and Bonadonna (2012), but adapted to account for sedimentation from the plume margins. Data sources: [1] Edwards et al. (2018), [2] Andronico et al. (2015), [3] Corradini et al. (2016), [4] Andronico et al. (2018), [5] de Michele et al. (2019), [6] Poret et al. (2018b), [7] Corradini et al. (2018), [8] Freret-Lorgeril et al. (2021b), [9] Andronico et al. (2014a), [10] Calvari et al. (2011), [11] Andronico et al. (2009b), [12] Andronico et al. (2014b), [13] Andronico et al. (2009a), [14] Andronico et al. (2008b) [15] Scollo et al. (2007)

by having a counter-flowing plume surrounding the rising plume (Mcdougall 1978; Mcdougall 1981; Bloomfield and Kerr 2000). A counter-flowing double plume model has been applied to volcanic plumes in a still atmosphere and can better capture complex flow patterns of a volcanic plume and the MFR in the umbrella region of a volcanic plume (Devenish and Cerminara 2018). Such models have also been applied to submarine eruption plumes (Mittal and Delbridge 2019). The study of coaxial plumes ranges from theoretical studies to application to plumes from cooling towers (Morton 1962; Li et al. 2018; Li and Flynn 2020). The model that I present takes inspiration from the coaxial models in the literature (Devenish and Cerminara 2018; Li et al. 2018) to create a coaxial double plume model for a tephra plume that is coupled to a lava fountain.

It is assumed that the plume is composed of two regions; the double plume region where a lava fountain and plume coexist, which transitions into a single plume at higher altitudes (Figure 2.3). The double plume region is treated as two separate plumes that are coupled; an inner circular plume that is surrounded by an outer annular plume, which hereinafter will be referred to as the inner plume and the outer plume. The inner plume is representative of the hot inner core (the lava fountain) and the outer plume is the tephra laden buoyant plume observed in the coupled lava fountain - tephra plume eruptions. This allows for a better description of the different source conditions between a lava fountain and tephra plume compared to a standard integral model. The initial MFR is split at the source into two portions; one for the inner plume (M_{i0}) and one for the outer plume (M_{o0}). The mass partitioning is quantified through the ratio $\varepsilon = M_{i0}/(M_{i0} + M_{o0})$; the greater the value of ε, the greater the relative proportion of MFR in the inner plume. At the height where the rise velocity or the solid phase MFR of the inner plume becomes negligible, i.e., top of the lava fountain, the plume transitions to a single plume description. The initial source conditions of the inner and the outer plume are independent of each other. The initial gas mass fraction and velocity of each plume are also independent of each other as a choked vent (Woods and Bower 1995) is not imposed. A common assumption for large, tephra-rich silicic eruptions is to assume choked vent conditions, whereby the exit velocity is equal to the sound velocity of the mixture (e.g., Girault et al. (2014)). I do not impose this restriction here as this condition is not necessarily met for eruptions with low initial MFRs and for plumes that co-exist with lava fountains. A schematic of the model setup can be seen in Figure 2.3a. To simplify the problem to one-dimension, the following is assumed:

1. The plume rise timescale for both the inner and the outer plume is less than the timescale of mass injection and, therefore, the plume is sustained,
2. The turbulent eddy turnover time is less than the timescale of plume rise,
3. The rate of entrainment into the plume is proportional to the velocity of the plume,
4. The pressure inside the plume is in equilibrium with the atmospheric pressure,
5. Plume properties are self-similar at a given height for which is assumed to be a top-hat profile,
6. The vent is circular.

The plume is considered to consist of three phases - dry air, water vapour and solid mass. These phases are exchanged between the inner and outer plumes, and the surrounding atmosphere via entrainment and particle fallout. Figure 2.3b shows the direction and the type of coupling that can happen between the atmosphere, the inner and the outer plume. The plume velocities are related to the rate of entrainment via a set of entrainment coefficients. The rate of entrainment from the atmosphere to the outer plume and to the single plume is described by λ and χ, respectively. α and β are used to determine the rate of entrainment from the outer plume to the inner plume, and vice-versa, in the double plume region of the model. I follow a similar notation for the entrainment coefficients as Bloomfield and Kerr (2000), who determined the values of α, β and λ as 0.085, 0.147 and 0.147, respectively, for a double plume from the fitting of numerical models to small-scale experiments. The entrainment velocities are calculated as shown by equations 2.2 to 2.4 that have been modified to take into account large density difference between the plume and the surrounding fluid (Ricou and Spalding 1961; Morton 1965; Rooney and Linden 1996; Devenish and Cerminara 2018):

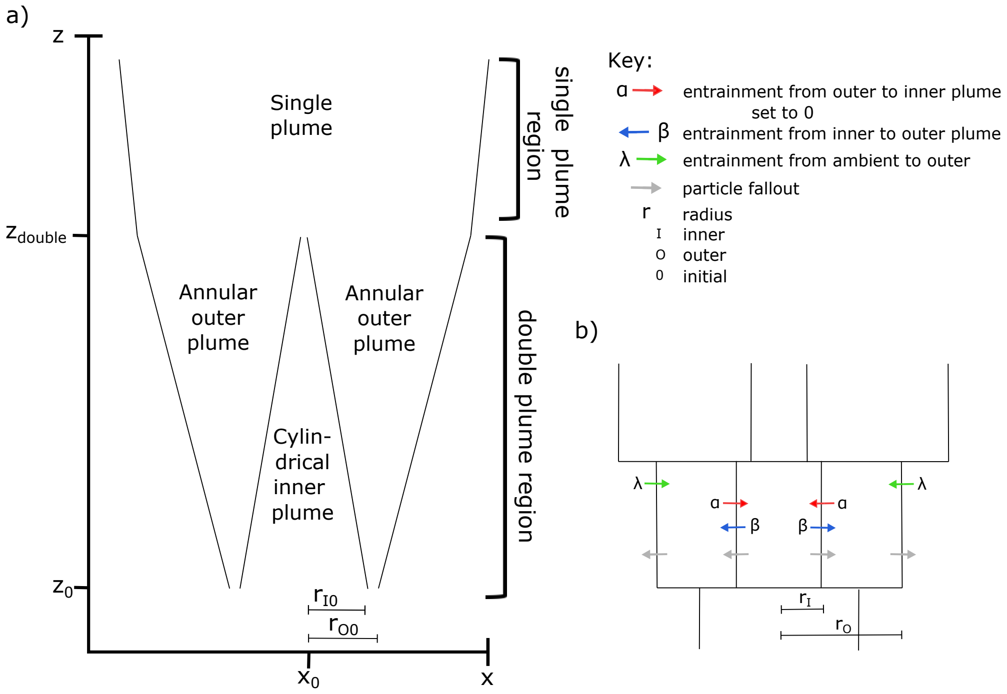

Fig. 2.3 a) Schematic of the double plume model that shows the coordinate system and what each part of the model represents. b) Detailed schematic of the control volume of the double plume model. The coupling of the inner and the outer plumes is highlighted by the arrows.

$$\mu_\lambda = u_o\lambda\left(\frac{\rho_{oB}}{\rho_{aB}}\right)^{0.5}, \tag{2.2}$$

$$\mu_\alpha = (u_i - u_o)\alpha\left(\frac{\rho_{IB}}{\rho_{oB}}\right)^{0.5}, \tag{2.3}$$

$$\mu_\beta = u_o\beta\left(\frac{\rho_{oB}}{\rho_{IB}}\right)^{0.5}, \tag{2.4}$$

where u is the plume velocity and ρ is the bulk plume density (See Table 2.2). Table 2.3 defines the subscripts. The values of 0.147 and 0.147 are used for the β and λ, respectively, from Bloomfield and Kerr (2000) in the double plume region of the double plume model. It is further assumed that re-entrainment of solid particles does not occur, and gas phases are not entrained into the inner plume (α is set to 0). This results in a decrease of the MFR of the inner plume with height, and therefore also a decrease in plume radius with height, which matches the observed structure of lava fountains.

The conservation of mass, momentum and specific enthalpy are solved in the model for the inner, outer and single plume. The definition of each variable is listed in Table 2.2.

2.3.1 Governing Equations of the Double Plume Region

The conservation of mass for dry air (d) and water vapour (v) for the inner plume (denoted by subscript I, see Table 2.3) are defined by equations 2.5 and 2.6, where the left-hand sides are the rate of mass change with height of the respective phase. The sink and sources compose the right-hand sides of the equations. These are the same for both the dry air and vapour phase. The first term is the source of the respective phase of material entrained from the surrounding outer plume, while the second term is the MFR loss of the respective phase from the inner plume due to entrainment to the outer plume.

$$\frac{d(\rho_{Id}u_I r_I^2)}{dz} = 2\rho_{Od}\mu_\alpha r_I - 2\rho_{Id}\mu_\beta r_I \tag{2.5}$$

$$\frac{d(\rho_{Iv}u_I r_I^2)}{dz} = 2\rho_{Ov}\mu_\alpha r_I - 2\rho_{Iv}\mu_\beta r_I \tag{2.6}$$

Table 2.2 Definitions of symbols.

Symbol	Definition	Value	Units
z	vertical coordinate		m
r	radius		m
u	velocity		m s^{-1}
ρ_B	bulk density		kg m^{-3}
ρ_l	density of liquid phase in plume	1000	kg m^{-3}
ρ_s	density of solid phase in plume	2000	kg m^{-3}
μ	entrainment velocity/rate of entrainment		m s^{-1}
w	settling velocity of a particle		m s^{-1}
u_g	Gaussian centreline velocity		m s^{-1}
r_{env}	radius of the support envelope		m
g	gravitational acceleration	9.81	m s^{-2}
C_B	bulk specific heat capacity		J kg^{-1} K^{-1}
C_B	specific heat capacity of dry air	998	J kg^{-1}
C_v	specific heat capacity of water vapour	1952	J kg^{-1}
C_s	specific heat capacity of solids	1250	J kg^{-1} K^{-1}
θ	temperature		K
n	mass fraction		
ε	mass partition ratio between inner and outer plume		
M	mass flow rate		kg s^{-1}
E	Enthlapy flow rate		J s^{-1}
P	pressure (assume plume is at pressure equilibrium with the atmosphere)		Pa
R_g	bulk specific gas content		J kg^{-1} K^{-1}
R_d	specific gas content of dry air	287	J kg^{-1}
R_v	specific gas content of water vapour	461	J kg^{-1}K^{-1}
p	probability of particle fallout for entraining plume	0.27	
p_{gauss}	probability of particle fallout for plume that does not entrain		
D	diameter of grain-size		m
ν	dynamic viscosity		kg m s^{-1}
α	entrainment coefficient describing entrainment from outer to inner plume	0	
β	entrainment coefficient describing entrainment from inner to outer plume	0.147	
λ	entrainment coefficient describing entrainment from ambient to outer plume	0.147	
χ	entrainment coefficient describing entrainment from ambient to single plume	0.1	
H_1	height of the tropopause	11000	m
H_2	height of the stratosphere	20000	m
ω_{trop}	temperature gradient in the troposphere	-0.0065	K m^{-1}
ω_{strat}	temperature gradient in the stratosphere	-0.002	K m^{-1}
θ_{ao}	initial temperature of the atmosphere	280	K

Table 2.3 Definitions of subscripts.

Subscript type	Subscript symbol	Definition
Location	O	outer plume
	I	inner plume
	a	atmosphere
Phase	d	dry air
	v	water vapour
	s	solid
	B	bulk
Entrainment	α	entrainment from outer to inner plume
	β	entrainment from inner to outer plume
	λ	entrainment from ambient to outer plume
	χ	entrainment from ambient to single plume
Grain-size	i	grain-size class i

In the inner plume, the change of the solid MFR is described by equation 2.7. The change of the MFR of the solid mass is described by amount of solid MFR lost from particle fallout. The conservation of mass for the solid phase is solved for each grain-size (m_i) in the model.

$$\frac{d(\rho_{Is} u_I r_I^2)}{dz} = -\sum_{i=1}^{m_i} p_{Gauss} \frac{M_{Isi}}{r_I} \tag{2.7}$$

Grain-sizes from -9 phi to 10 phi are considered, with a spacing of half a phi, where phi is defined as $\log_2 D$ with D being the diameter of the particle in meters. Details of the description of particle fallout from the inner plume can be found further in Section 2.3.3.

For the outer plume (denoted by subscript O) in the double plume region, the processes that control the change in mass are the same as in the inner plume. An additional entrainment term is present in the conservation of mass for dry air and water vapour (third term in equations 2.8 and 2.9) for the entrainment of mass from the atmosphere into the outer plume. An additional term is also present in the conservation of mass of the solid phases as a source term for the particles that move from the inner plume into the outer plume (second term, equation 2.10).

$$\frac{d(\rho_{Od}u_O(r_O-r_I)^2)}{dz} = -2\rho_{Od}\mu_\alpha r_I + 2\rho_{Id}\mu_\beta r_I + 2\mu_\lambda r_O \rho_{ad} \tag{2.8}$$

$$\frac{d(\rho_{Ov}u_O(r_O-r_I)^2)}{dz} = -2\rho_{Ov}\mu_\alpha r_I + 2\rho_{Iv}\mu_\beta r_I + 2\mu_\lambda r_O \rho_{av} \tag{2.9}$$

$$\frac{d(\rho_{Os}u_O(r_O-r_I)^2)}{dz} = -\sum_{i=1}^{n_i} p\frac{w_{Osi}M_{Osi}}{u_O r_O} + \sum_{i=1}^{n_i} p_{Gauss}\frac{M_{Isi}}{r_I} \tag{2.10}$$

The change in the momentum flow rate is described by equation 2.11 for the inner plume and by equation 2.12 for the outer plume. The momentum flow rate is increased from the material added to the plumes via entrainment (for dry air and water vapour) and from buoyancy. For the inner plume, these are described by the first, second and fifth terms in equation 2.11, respectively, and by the third, fourth and fifth terms in equation 2.12, respectively. The outer plume has the additional source of momentum from the solid particles that fall from the inner to the outer plume depending on the relative settling and plume velocities (seventh term, equation 2.12). The loss of momentum flow rate from the plumes is via the processes of entrainment of dry air and water vapour and particle fallout. These refer to the third, fourth and sixth terms in equation 2.11 for the inner plume and the first, second and sixth term in equation 2.12 for the outer plume.

$$\begin{aligned}\frac{d(\rho_{IB}r_I^2u_I^2)}{dz} = {} & 2\rho_{Od}\mu_\alpha r_I u_O + 2\rho_{Ov}\mu_\alpha r_I u_O - 2\rho_{Id}\mu_\beta r_I u_I \\ & -2\rho_{Iv}\mu_\beta r_I u_I + g(\rho_{aB}-\rho_{IB})r_I^2 \\ & +u_I\frac{d(\rho_{Is}u_I r_I^2)}{dz}\end{aligned} \tag{2.11}$$

$$\begin{aligned}\frac{d(\rho_{OB}(r_O-r_I)^2u_O^2)}{dz} = {} & -2\rho_{Od}\mu_\alpha r_I u_O - 2\rho_{Ov}\mu_\alpha r_I u_O \\ & +2\rho_{Id}\mu_\beta r_I u_I + 2\rho_{Iv}\mu_\beta r_I u_I \\ & +g(\rho_{aB}-\rho_{OB})(r_O-r_I)^2 \\ & +u_O\frac{d(\rho_{Os}u_O(r_O-r_I)^2)}{dz} \\ & -u_I\frac{d(\rho_{Is}u_I r_I^2)}{dz}\end{aligned} \tag{2.12}$$

The left-hand sides of equations 2.13 and 2.14 show the variation with respect to height of the enthalpy flow rate of the volcanic mixture of the inner and outer plume, respectively. As in the conservation of momentum for both the inner and the outer plumes (equation 2.11 and 2.12), the change in the enthalpy is caused by the enthalpy gained from the addition of mass flow rate into a plume via entrainment and particle fallout. While the enthalpy flow rate is reduced by entrainment of material from the plume, change due to conversion to gravitational potential energy and particle fallout.

$$\begin{aligned}\frac{d(\rho_{IB} r_I^2 u_I C_{IB} \theta_I)}{dz} &= 2\rho_{Od}\mu_\alpha r_I C_d \theta_O - 2\rho_{Id}\mu_\beta r_I C_d \theta_I \\ &\quad +2\rho_{Ov}\mu_\alpha r_I C_v \theta_O - 2\rho_{Iv}\mu_\beta r_I C_v \theta_I \\ &\quad -\rho_{IB} u_I r_I^2 g \frac{\rho_{aB}}{\rho_{IB}} + C_s \theta_I \frac{d(\rho_{Is} u_I r_I^2)}{dz}\end{aligned} \tag{2.13}$$

$$\begin{aligned}\frac{d(\rho_{OB}(r_O - r_I)^2 u_O C_{OB} \theta_O)}{dz} &= -2\rho_{Od}\mu_\alpha r_I C_d \theta_O + 2\rho_{Id}\mu_\beta r_I C_d \theta_I \\ &\quad +2\rho_{ad}\mu_\lambda r_O C_d \theta_a - 2\rho_{Ov}\mu_\alpha r_I C_v \theta_O \\ &\quad +2\rho_{Iv}\mu_\beta r_I C_v \theta_I + 2\rho_{av}\mu_\lambda r_O C_v \theta_a \\ &\quad -\rho_{OB} u_O (r_O - r_I)^2 g \frac{\rho_{aB}}{\rho_{OB}} \\ &\quad -C_s \theta_I \frac{d(\rho_{Is} u_I r_I^2)}{dz} \\ &\quad +C_s \theta_O \frac{d(\rho_{Is} u_O (r_O - r_I)^2)}{dz}\end{aligned} \tag{2.14}$$

The total MFR and mass fractions for each phase (both for the inner or the outer plumes) are given by equations 2.15 and 2.16 - 2.18, respectively.

$$M = M_d + M_v + M_s \tag{2.15}$$

$$n_d = \frac{M_d}{M_d + M_v + M_s} \tag{2.16}$$

$$n_v = \frac{M_v}{M_d + M_v + M_s} \tag{2.17}$$

$$n_s = \frac{M_s}{M_d + M_v + M_s} \tag{2.18}$$

where M_d, M_v and M_s are the mass flow rates of the dry air, water vapour and solid phases.

The material properties of the plume are described by the following constitutive equations, which once again apply to both the inner and outer plume. The mixture heat capacity (C_B) is

$$C_B = \frac{M_d C_d + M_v C_v + M_s C_s}{M_d + M_v + M_s}. \tag{2.19}$$

From this, the plume temperature (θ) can be found from

$$\theta = \frac{1}{C_B}\frac{E}{M}, \tag{2.20}$$

where E is the enthalpy flow rate.

The bulk density of the plume (equation 2.23) is calculated from the bulk gas constant (equation 2.21) and the density of the gas phase mixture in the plume (equation 2.22) using the ideal gas law.

$$R_g = \left(\frac{n_v}{n_v + n_d} R_v\right) + \left(\frac{1 - n_v}{n_v + n_d} R_d\right) \tag{2.21}$$

$$\rho_g = \frac{P}{R_g \theta} \tag{2.22}$$

$$\rho_B = \left(\frac{(n_v + n_d)}{\rho_g} + \frac{n_s}{\rho_s}\right)^{-1} \tag{2.23}$$

The ode15s solver in MATLAB is used to solve the governing equations for the inner and outer plumes together to be able to include the entrainment of the inner plume to the outer plume and vice-versa (Shampine and Reichelt 1997; Shampine et al. 1999). The ordinary differential equations solved are equations 2.5 to 2.14 along with the closure equations 2.15 to 2.23. The ode15s solver is chosen as the equations being solved are stiff. The MATLAB function created that runs this presented model takes the input of the physical plume properties, i.e., the initial plume temperature, initial gas mass fraction, initial velocity and initial grain-size distribution of the inner and outer plumes. It also requires information on the initial radii of the inner and outer plumes (where the latter is the outer radius of the annulus, see Figure 2.3), or, the overall initial MFR and ε. These values are then used to determine the initial mass (of each grain-size), momentum and enthalpy flow rates for both the inner and outer plumes, which are then the inputs for the ODE solver itself.

2.3.2 Transition from the Double Plume to the Single Plume

The initial double plume of the model stops when the inner plume velocity approaches 0 m s^{-1}. The inner plume is stopped earlier if the solid MFR in the plume becomes negligible. Additionally, in the case where a given grain-size is no longer supported by the inner plume, the simulation is paused, and the corresponding MFR of that grain-size is removed from the system. Associated momentum and enthalpy related to the fallout are also removed. The system of equations is then continued from the height where it was halted. When either of the stopping conditions are met, the inner plume disappears, and the outer plume governing equations change to those of just a single plume.

Two end member situations exist for the treatment of any solid material remaining in the inner plume once it has stopped. The solid phase MFR in the inner plume can either be completely removed from the system or can be added to the single plume. However, due to the dependence on grain-size, it is unlikely that the total solid phase MFR of all sizes present in the plume would be incorporated into the single plume. Therefore, a support envelope approach can be implemented, whereby grain-sizes that can no longer be supported by the plume are removed (Carey and Sparks 1986).

Equations 2.24 to 2.28 are the governing equations of the single plume model.

$$\frac{d(\rho_d u r^2)}{dz} = 2\mu_\chi r \rho_{ad} \tag{2.24}$$

$$\frac{d(\rho_v u r^2)}{dz} = 2\mu_\chi r \rho_{av} \tag{2.25}$$

$$\frac{d(\rho_s u r^2)}{dz} = \sum_{i=1}^{n_i} -p\frac{w_{si} M_{si}}{ur} \tag{2.26}$$

The rate of entrainment from the ambient into the single plume region is described as $\mu_\chi = u\chi\left(\frac{\rho_B}{\rho_{aB}}\right)^{0.5}$, where χ is the entrainment coefficient describing the proportionality between the entrainment rate and plume velocity and is equal to 0.1 (Morton et al. 1956; Devenish et al. 2010a; Degruyter and Bonadonna 2012).

The rate of mass change in the single plume is governed by the entrainment of the ambient fluid (right-hand side, equations 2.24 and 2.25) and particle fallout (right hand-side, equation 2.26). Subsequently, the rate of momentum flow rate change is due to particle fallout and buoyancy (2nd and 1st terms, equation 2.27, respectively).

$$\frac{d(\rho_B r^2 u^2)}{dz} = g(\rho_{aB} - \rho_B)r^2 + u\frac{d(\rho_s u r^2)}{dz} \tag{2.27}$$

In a similar suit as equation 2.27, the rate of enthalpy change is controlled by the change in mass (entrainment, 1st-2nd terms, and particle fallout, 4th term, in equation 2.28) and conversion to gravitational potential (3rd term, equation 2.28).

$$\begin{aligned}\frac{d(\rho_B r^2 u C_B \theta)}{dz} = 2\mu_\chi r \rho_{ad} c_d \theta_a + 2\mu_\chi r \rho_{av} c_v \theta_a - \rho_B u r^2 g \frac{\rho_{aB}}{\rho_B} \\ + C_s \theta \frac{d(\rho_s u r^2)}{dz}\end{aligned} \tag{2.28}$$

This system of governing equations, along with the closure equations 2.15 to 2.23, are solved with the ode45 MATLAB solver and terminate when the plume velocity approaches 0 m s^{-1}. The inputs for this part of the model are the mass (of each grain-size), momentum and enthlapy flow rates from the end of the double plume region part of the model (see Section 2.3.4 for further details).

2.3.3 Particle Sedimentation

To account for sedimentation from the margins of a volcanic plume, I follow the method described in Bursik (2001), Girault et al. (2014), and Girault et al. (2016). The conservation of mass of the solid phase of a buoyant plume (equations 2.10 and 2.26) contains an additional sedimentation term to account for the loss of the solid phase MFR from the plume. The loss of particles from a plume is assumed to be proportional to the MFR of particles (Woods and Bursik 1991; Ernst et al. 1996) and can be mathematically described for each grain-size class (i) as

$$\frac{dM_{Mi}}{dz} = -p\frac{M_{si}}{r}\frac{w_i}{u}, \tag{2.29}$$

where u is the velocity of the plume, r is the plume radius and M_{si} is the MFR of the solid phase (s) at grain-size i at height z. p is defined as the probability of particle fallout from the margins of a plume. This has been previously determined from laboratory experiments and modelling as 0.27 for buoyant plumes (Ernst et al. 1996). The final parameter required to calculate the MFR associated with a grain-size at a given height is the settling velocity of the grain-size (w_i). As the behaviour of settling particles is described by different settling laws in different flow regimes, the settling velocity for a given spherical grain-size is dependent on the Reynolds number as given by Bonadonna et al. (1998) and Bonadonna and Phillips (2003)

$$\left.\begin{array}{ll} \sqrt{\dfrac{3.1d_i g(\rho_s - \rho_B)}{\rho_B}} & \text{for} \quad Re_i \geq 500 \\ d_i\left(\dfrac{4g^2(\rho_s - \rho_B)^2}{225\nu\rho_B}\right)^{\frac{1}{3}} & \text{for} \quad 6 \leq Re_i < 500 \\ \dfrac{d_i^2 g(\rho_s - \rho_B)}{18\nu} & \text{for} \quad Re_i < 6 \end{array}\right\} = w_i. \tag{2.30}$$

The particle Reynolds number is calculated as $Re_i = (D_i w_i \rho_B / \nu)$ where D_i is the diameter of a spherical particle, w_i is the settling velocity of the particle of size i and ν is the dynamic viscosity of the fluid the particle is settling in. I choose to follow the approach of Woods and Bursik (1991) and use ρ_B in the calculation of the Reynolds number and in equation 2.30. This is because the lava fountains and dense tephra plumes in this study are particle-dense and consist of large particles. As a result, the surrounding clasts contribute to the drag exerted on other particles in the plume whilst the material displaced by a particle in the plume is likely to be a mixture of the solid and gas phases.

In the case of a lava fountain, it is assumed that the entrainment of the gas phases from the outer to the inner plume is negligible such that $\alpha = 0$. This causes the radius of the inner plume to reduce with height, which agrees with visual observations. This change in radius geometry results in the sedimentation scheme of Ernst et al. (1996) not being applicable to the inner plume as it would result in no fallout. The Ernst et al. (1996) sedimentation scheme also assumes that the solid particles are fully coupled to the gas. As the GSD of the material composing lava fountains are coarse, this is not a valid assumption. Instead, I use a new method to determine how much MFR is lost from the inner plume from particle fallout based on the particle settling velocity and the Gaussian plume velocity profile. I adapt the approach of Carey and Sparks (1986) to determine when a given grain-size is no longer supported by the plume - the support envelope. The ratio between the area under the Gaussian velocity profile and the area under the Gaussian velocity profile where a clast is no longer supported by the plume is calculated. This replaces the geometrical term and the velocity ratio in equation 2.29 as p_{Gauss}:

$$\frac{dM_{si}}{dz} = -p_{Gauss}\frac{M_{si}}{r}, \tag{2.31}$$

where $-p_{Gauss}$ is

$$-p_{Gauss} = 1 - \operatorname{erf}\left(2\frac{r_{env}}{r}\right), \tag{2.32}$$

with r_{env} being the radius of the support envelope, which is calculated as (Rossi et al. 2019)

$$r_{env} = \frac{r_i}{\sqrt{2}}\ln\left(\frac{u_g}{w_i}\right)^{0.5}. \tag{2.33}$$

The addition of the solid phase material to the outer plume is dependent on the Gaussian centreline velocity (u_g) of the outer plume and the settling velocity of the grain-size in question. The Gaussian centreline velocity is used as that is the highest velocity within the plume. If the Gaussian centreline velocity is greater than the settling velocity of a particle, the MFR of that particular size can be supported by the outer plume. The MFR, along with the associated momentum and enthalpy flow rates, is added to the outer plume. Conversely, if the settling velocity of a given particle size is greater than that of the Gaussian centreline velocity, the mass, momentum, and enthalpy related to it are removed from the whole system. This can be turned on or off in the double plume model.

2.3.4 Coupling Between the Inner and Outer Plumes

The interaction between the two regions of the double plume depends on the degree of coupling between these two flows. Coupling between the lava fountain and the tephra plume is quantified by the amount of mass, momentum and enthalpy that is exchanged between the two. One way this occurs is via entrainment, where gas can be entrained from the ambient to the tephra plume, from the tephra plume to the lava fountain and from the lava fountain to the tephra plume. This mechanism of coupling has been well studied and parameterised for single buoyant plumes (Morton et al. 1956). For coaxial integral plume models, entrainment coefficients have been defined by Bloomfield and Kerr (1998), Bloomfield and Kerr (2000), and Devenish et al. (2010a). Another process that allows for coupling between the lava fountain and the tephra plume is particle fallout. Material falling from the lava fountain can potentially enter the tephra plume. If no coupling is present, the plumes behave independently of each other, and plume dynamics will be very similar to that of a single plume. However, observations suggest a certain level of coupling is present.

The extent of coupling between tephra plumes and lava fountains via particle fallout is not fully understood. Observations of tephra plumes above lava fountains in Hawaii show that wind can affect the finest particle (Head and Wilson 1989). In contrast, the lava fountains at Mount Etna are characterised by much larger quantities of tephra, which co-exist with a lava fountain rather than only originating from above it (Figure 1.1). Additionally, during strong winds, the central portion of the lava fountain appears to not be significantly affected by wind, while the tephra plume can be bent in the direction of the wind. However, a correlation has been suggested between the height of the lava fountain and the height of the volcanic plume (Calvari et al. 2018). Further research is required to understand the extent and the impact of different levels of coupling between a lava fountain and a tephra plume.

To be able to explore the potential range of coupling and its impact on plume dynamics, I examine two end-member scenarios of coupling between the inner and outer regions due to solid mass transfer. For both scenarios, the inner and outer plumes interact by gas being entrained from the inner to the outer plume. Particle fallout from the inner plume is added to the outer plume if the settling velocity of a given size is lower than the Gaussian centreline velocity of the outer plume for both scenarios (See Section 2.3.3 for further details). These scenarios are the following:

1. Fully coupled - Any solid phase MFR remaining in the inner plume once it has stopped is added to the single plume region depending on the ratio between the settling velocity and the outer plume centreline velocity. The MFR related to the gas phases left in the inner plume once it has stopped are also added to the start of the single plume region.
2. Moderately coupled - Any solid phase MFR remaining in the inner plume once it has stopped is not added to the single plume region source, corresponding to the solid MFR sedimenting to the ambient and being removed from the plume system. The MFR related to the gas phases left in the inner plume once it has stopped are not added to the start of the single plume region.

2.3.5 Atmospheric Conditions

The atmospheric conditions that are used in the model include the pressure, density and temperature. It is assumed that the atmosphere is only composed of dry air and there is no humidity. Wind is not accounted for. A representative temperature profile of a standard atmosphere in an intermediate climate is used as defined by Woods (1988),

$$\left.\begin{array}{rll} \theta_{a0} - \omega_{trop} z & \text{for} & z < H_1 \\ \theta_{a0} - \omega_{trop} H_1 & \text{for} & H_1 < z \leq H_2 \\ \theta_{a0} - \omega_{trop} H_1 + \omega_{strat}(z - H_2) & \text{for} & z \geq H_2 \end{array}\right\} = \theta_a, \tag{2.34}$$

where θ_{a0} is the initial atmospheric temperature, H_1 and H_2 are the height of the tropopause and the height of the stratosphere, respectively. ω_{strat} and ω_{trop} are the temperature gradient in the troposphere and the stratosphere, respectively. These are set to the same values used by Woods (1988). The specific heat capacity (C_{aB}) of the atmosphere is equal to C_d, the specific heat capacity of dry air, as the model does not consider the humidity and vapour phase of the atmosphere. Following the same assumption, ρ_{aB} and ρ_{ad} is given in equation 2.35 by using the ideal gas law. The atmospheric hydrostatic pressure is described as

$$\rho_{aB} = \rho_{ad} = \frac{P}{R_d \theta_a}, \tag{2.35}$$

$$\frac{dP}{dz} = -g\rho_{aB}. \tag{2.36}$$

2.4 Results

2.4.1 The Impact of the Lava Fountain on Plume Rise

I present results on the impact of a hotter, coarser-grained inner core, that does not entrain surrounding gas phases, on the overall rise of a volcanic plume. I compare results from the double plume model, where the initial condition of the inner plume resembles the characteristics of a lava fountain, to those of a plume where a lava fountain is not present. The latter is modelled using the standard integral model. The ESPs and atmospheric conditions used are identical to those used for the double plume model.

I randomly sample a parameter space that consists of initial velocity, temperature, gas mass fraction, GSD, MFR and ε, to assess the impact of a lava fountain on plume height. The ranges for each variable are listed in Table 2.4a (Métrich and Rutherford 1998; Parfitt and Wilson 1999; Métrich et al. 2004; Spilliaert et al. 2006; Glaze et al. 2017; Poret et al. 2018b). However, I impose that the inner plume is always hotter, coarser-grained and contains a lower initial gas mass fraction than the outer plume, mimicking lava fountain characteristics (Parfitt 1998). The vent height is set at 0 m a.s.l. As choked vent conditions are not imposed, the initial velocity is allowed to vary, independently of the initial gas mass fraction, between the values of 75 and 200 m s^{-1}. This range agrees with average velocity estimates of tephra plumes that are coupled to lava fountains as determined by radar (Freret-Lorgeril et al. 2018). By allowing the initial source parameters to vary over wide ranges and independently of each other, the whole range of potential implications of a lava fountain on the rise of a tephra plume can be explored.

Figure 2.4 shows the relationship between the initial MFR and the overall plume height in a still standard atmosphere in an intermediate climate. The MFR for the double plume model refers to the combined MFR of both the inner and outer plumes at the vent. The two double plume scenarios are shown by the coloured markers whilst the standard integral model is also plotted (black markers). Regardless of whether the lava fountain and tephra plume are moderately or fully coupled (dark blue and red markers respectively, Figure 2.4), a plume coupled to a lava fountain can reach a greater variation of heights than a standard plume for a given initial MFR. This is indicated by an r^2 of 0.986 for the double plume model (both scenarios) compared to an r^2 of 0.996 for the standard integral model output for the fitting of a power law to the MFR as a function of height. The overall trend between the two coupling scenarios of models is the same. The variation in the initial source parameters allows for a wider range of heights that a plume surrounding a lava fountain can reach compared to the standard integral model for the same initial MFR. This indicates the source conditions are an important control on the height of tephra plumes coupled with lava fountains. However, I do see that, for a higher initial MFR, a plume coupled to a lava fountain can generally reach greater heights than for a plume without a lava fountain. For a plume coupled to a lava fountain with a high initial MFR, the tephra plume could support a greater proportion of the fallout from the lava fountain. The mass partitioning and the GSD introduce two important new degrees of freedom compared to the standard integral model. These are explored separately in the next sections to further investigate their control on plume rise compared to a plume without a lava fountain.

Table 2.4 Source conditions used for the results presented in this work a) ESPs for the general simulations in Section 2.4.1 and b) ESPs for simulations in Section 2.4.1, 2.4.1 and 2.4.2.

ESP	Inner Plume	Outer Plume	Standard Integral Model
a)			
Total MFR (kg s^{-1})	10^3 - 10^7		10^3 - 10^7
Temperature (K)	1200 - 1500	900 - 1200	900 - 1200
Velocity (m s^{-1})	75 - 200	75 - 200	75 - 200
Gas mass fraction	0.01 - 0.03	0.03 - 0.05	0.03 - 0.05
ε	0 - 1		N/A
GSD	log-normal, median between -7 and -1	log-normal, median between inner median and 6	log-normal, median between inner median and 6
b)			
Total MFR (kg s^{-1})	10^5		10^5
Temperature (K)	1500	1200	1200
Velocity (m s^{-1})	100	100	100
Gas mass fraction	0.01	0.03	0.03
ε	$\frac{2}{3}$		N/A
GSD	log-normal, median -7 / -3	log-normal, median 0.5	log-normal, median 0.5

Sensitivity of Plume Rise to the GSD of the Lava Fountain

The effect of the initial GSD of the lava fountain (i.e., the inner plume) on plume rise is important to understand. Firstly, this is because the GSD of a lava fountain is a major characteristic and distinguishes it from typical tephra plumes (Parfitt 1998; Parfitt and Wilson 1999; Mueller et al. 2019). Secondly, GSD is a first order control on the extent of particle fallout (Sparks et al. 1992; Bursik et al. 1992). The size of a particle controls its settling velocity, which in turn contributes to how much solid material falls out and if it is subsequently supported by the surrounding outer plume. Few studies exist of GSDs from field deposits of lava fountains (Parfitt 1998; Andronico et al. 2014a; Edwards et al. 2018). It is not possible to fully constrain this parameter in real time (Scollo et al. 2019). This results in the lava fountain GSD being poorly constrained and a large source of large error.

To explore the sensitivity of the model to different GSDs, the initial GSD of the lava fountain is varied for four different-sized hypothetical eruptions. The eruption sizes that are considered have initial MFRs of 10^3 kg s^{-1}, 10^4 kg s^{-1}, 10^5 kg s^{-1} and 10^6 kg s^{-1}. First, I determine the impact of a GSD composed of a single-size on plume rise to clearly see the effect (Figure 2.5), and then with a log-normal GSD to better represent GSDs observed from real eruptions (Figure 2.6) (Costa et al. 2016a; Pioli et al. 2019). All other ESPs are kept constant (velocity, temperature, gas mass fraction, ε) and are listed in Table 2.4b. The GSD of the outer plume is kept constant as a log-normal distribution with a median grain-size of 0.5 phi and a standard deviation of 1.5 phi, which is similar to the default values that is set to forecast tephra fallout in near real-time (Scollo et al. 2019). This is also used as the initial GSD for the standard integral model. The results from a standard integral model are compared to the double plume model for the two different coupling scenarios previously defined in section 2.3.4.

For a lava fountain where the initial GSD consists of a single particle size, the final plume height is lower than that predicted by the standard integral model for lava fountain composed of grain-sizes coarser than approximately -6 phi (Figure 2.5). An initial coarse single-size GSD leads to significant fallout from the inner plume. Large particles that have fallen out are not supported by the outer plume and are, therefore, completely removed from the system when they fall from the lava fountain. The associated loss of

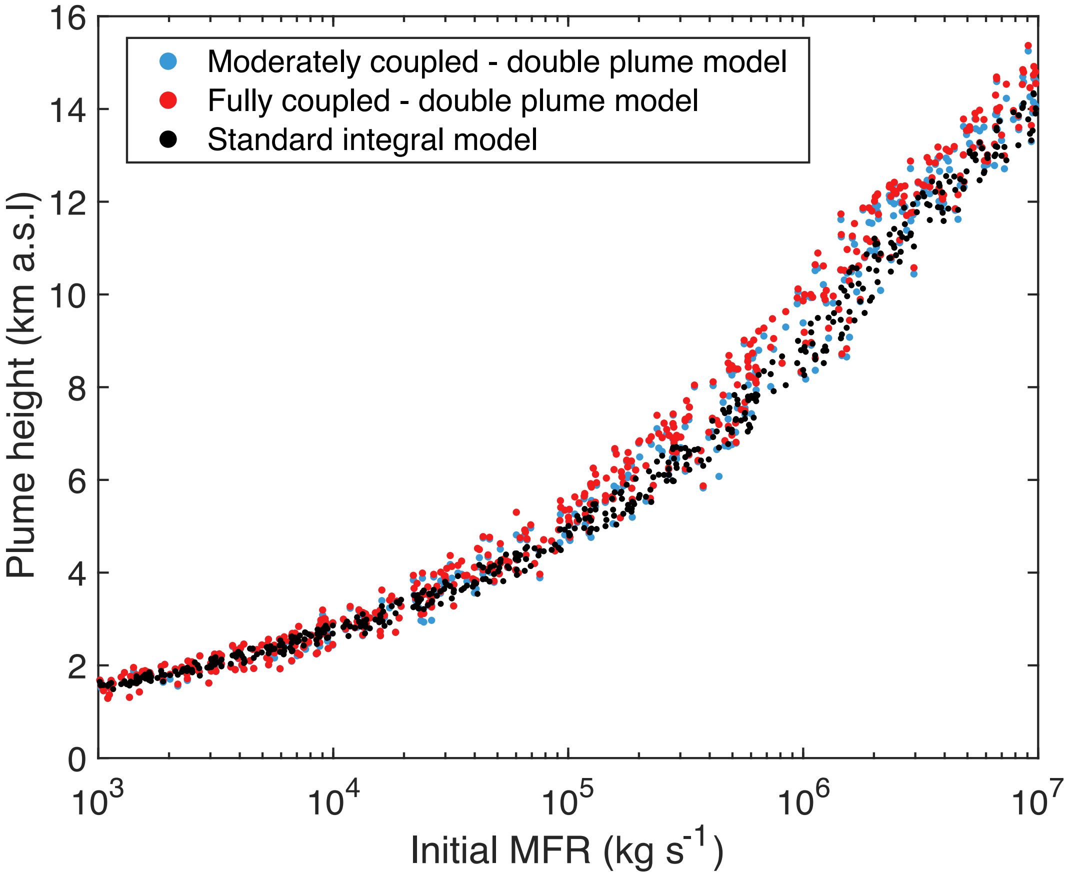

Fig. 2.4 A comparison of the maximum height that plumes with different initial MFRs can reach between a standard integral (black markers) and a double plume model (coloured markers). Two different coupling scenarios of the double plume model are presented; red markers refer to when the MFR is included in the start of the single plume region depending on the velocity (fully coupled) and dark blue markers where any MFR at the top of the lava fountain is completely removed (moderately coupled) (see Section 3.5 for more details).

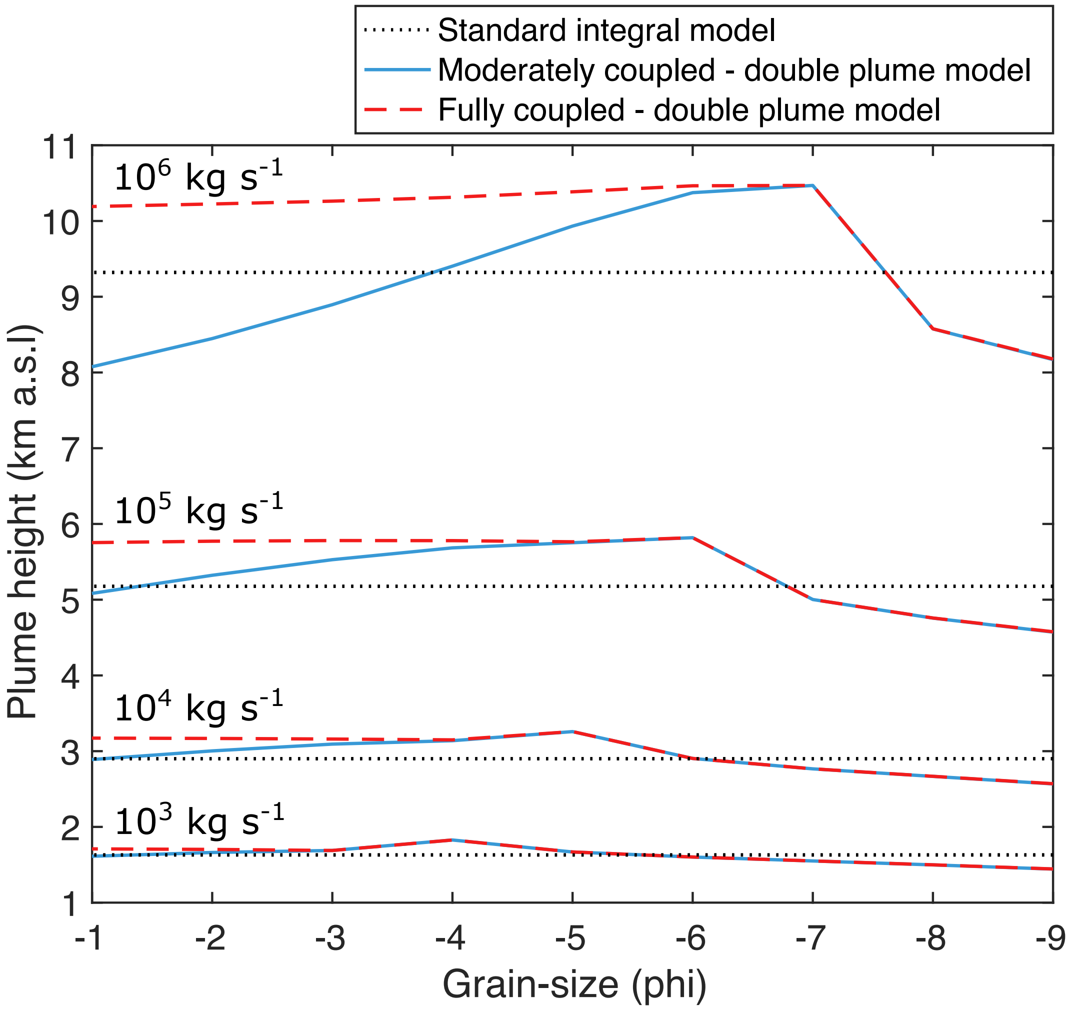

Fig. 2.5 The effect of varying the single-size GSD of the inner plume, where the inner plume is composed of only one grain-size, on the overall plume height for four initial MFRs. For each MFR, the results of the standard integral model (black line) and the two scenarios of the double plume model, listed in section 2.3.4, (dashed red and solid blue, respectively) are shown.

mass, momentum, and enthalpy from this process results in the plume not reaching the same heights as the standard integral model despite having a hotter inner core. As the initial single-size GSD of the inner plume becomes finer, less fallout occurs leaving more mass, momentum, and enthalpy in the whole plume system for it to go higher. The inner plume loses the majority of its solid phase MFR by the time the velocity reaches approximately 0 m s^{-1}. As a result, there is nothing left in the inner plume once it has stopped to add to the start of the single plume region. The different coupling schemes (solid blue and dashed red lines, Figure 2.5), thus become unimportant.

For the case when the lava fountain is composed of a single-size GSD between -6 and -4 phi (depending on the eruption size), with moderate coupling between the lava fountain and tephra plume, the final height of the plume decreases as the GSD becomes finer (solid blue line, Figure 2.5). As the GSD becomes finer, less fallout from the inner plume occurs. This results in the amount of MFR left in the inner plume, once the inner plume has stopped, increasing as the single-size GSD becomes finer. If this MFR is not added to the start of the single plume region, it is lost from the system. As a result, the initial mass, momentum, and enthalpy of the single plume region is reduced. In the case of full coupling between the inner and outer plume (dashed red line, Figure 2.5), the final plume height remains constant, or decreases slightly, depending on the eruption size. This is because the majority of the mass, and related enthalpy and momentum is added to the start of the single plume region. As a result, the overall mass, enthalpy, and momentum flow rates in the whole system is close to constant, so the final height of the plume does not significantly change.

The same behaviour is observed when a log-normal GSD is used, rather than a GSD composed of only one grain-size, for the inner plume. The median of the log-normal GSD of the inner plume is varied between -7 and -2 phi and the standard deviation is kept constant at 0.75 phi (red lines, Figure 2.6 b). The inner plume GSD is kept narrow to agree with observations of ultra-proximal deposits from Hawaiian lava fountains (Parfitt 1998). When the lava fountain GSD is coarse, the double plume final height is lower than that predicted by the standard integral model. As the GSD becomes finer, less material is lost from the system due to lower fallout occurring. This allows the plume to rise higher until the GSD becomes so fine that material which falls out of the inner plume is supported by the outer plume. At this point the coupling mechanism at the top of the plume becomes important. If any material left in the inner plume once it has stopped is not added to the source of the single plume region (moderately coupled scenario), the single plume region starts with the same mass, momentum and enthalpy as the top of the outer plume. The inner plume mass, momentum, and enthalpy flow rates at the point where it stops is lost from the system and the final height of the plume decreases as the GSD becomes finer. On the other hand, if the material of the inner plume is added and can be supported at the top of the double plume region (dashed red line, Figure 2.6) the overall plume height does not significantly vary as the median of the grain-size distribution decreases. The overall mass, momentum, and enthalpy flow rates of the system is generally conserved. The behaviour of the plume from varying the GSD is the same for eruptions of different sizes as defined by the initial MFR.

Impact of Lava Fountain Size on Plume Rise

To vary the size of the lava fountain in the model, the partition ratio, (ε), is varied between 0.25 and 0.9. The bigger ε, the more of the initial MFR partitioned into the inner plume, thus forming a larger lava fountain. The other source conditions (velocity, temperature, gas mass fraction, GSD) are kept constant and can be found in Table 2.4b. I examine the effect of different sizes of lava fountains on the two coupling scenarios; moderately and fully coupled (Section 2.3.4).

An increase in the size of a lava fountain, when the inner plume has a log-normal GSD with a median grain-size of -3 phi, results in the tephra plume rising higher compared to when the lava fountain is small and to a standard tephra plume. This is true for both the moderately and fully coupled scenarios (Figure 2.7a, solid blue and dashed red lines, respectively). As the lava fountain increases in size, the amount of fallout from the inner plume becomes proportionally larger compared to what is in the outer plume. When the fallout is composed of predominately finer particles (Figure 2.7a) the sedimenting particles become a source of mass, momentum, and enthalpy for the outer plume. With larger lava fountains, this contribution of the hot material becomes the dominant component of the solid phase MFR in the outer plume rather than the original solid phase MFR in the outer plume erupted at the vent. The mass, momentum, and enthalpy of the outer plume

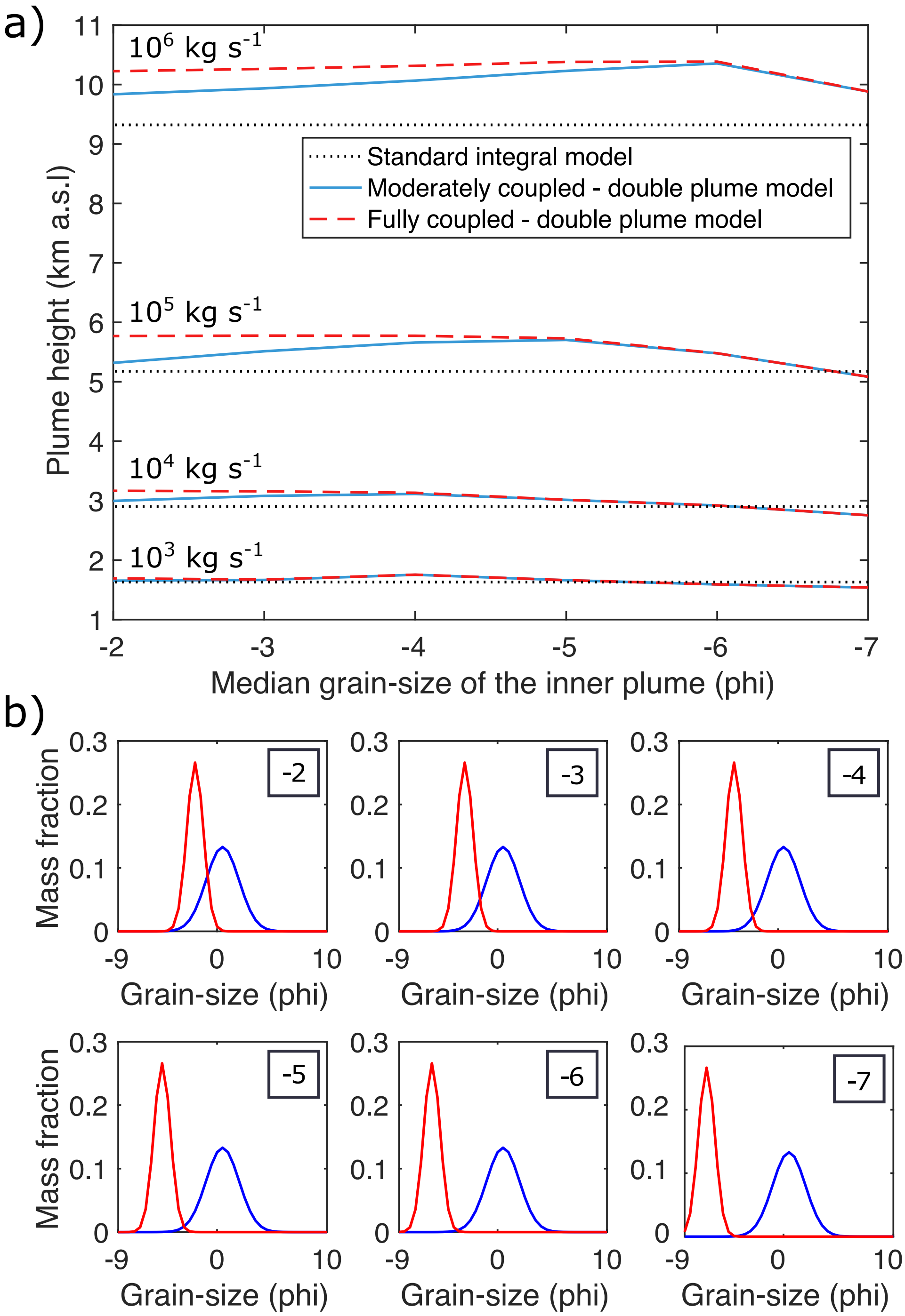

Fig. 2.6 a) The effect of varying the median size of the GSD of the inner plume on the overall plume height for the four initial MFRs investigated. For each MFR, the results from the standard integral model (black line) and the two scenarios of the double plume model, that are listed in section 2.3.4, (dashed red and solid blue, respectively) are shown. b) The GSDs of the inner (red) and the outer (blue) plumes. The median size of the inner plume GSD, which correlates to the x-axis in a), is referenced in the top right corner of each plot.

increases considerably resulting in a higher buoyant plume compared to if a lava fountain was not present.

In contrast, when the initial GSD of the inner plume is coarser (log-normal GSD with a median of -7 phi), a dependence is found on the initial MFR. For initial MFRs $\leq 10^5$ kg s^{-1} an increase in the size of a lava fountain results in the plume rising to lower heights with respect to the standard integral model. If the lava fountain consists of predominately large particles, much of the fallout from the inner plume is not supported by the surrounding plume. The sedimenting particles from the lava fountain are lost from the system, therefore the associated mass, momentum and enthalpy are also lost. The lower levels of mass, momentum and enthalpy being added to the outer plume results in the plume being unable to rise to heights similar to or greater than the standard integral model (Figure 2.7b). The two different coupling approaches are the same as large amounts of fallout results in the majority of the solid phase MFR of the inner plume being lost before the inner plume velocity approaches 0. Little or nothing is present to add to the start of the single plume region and, therefore, the coupling mechanism becomes unimportant. However, when the initial GSD of the inner plume is coarse and the initial MFR is high (i.e., 10^6 kg s^{-1}), the same behaviour as when the GSD of the inner was finer is seen. Plume height increases as the lava fountain size increases because the overall larger initial MFR of the eruption results in the velocity profile of the outer plume decreasing at a slower rate with height compared to an eruption with a lower initial MFR. As a result, more of the fallout from the inner plume can be supported by the outer plume and the lava fountain acts as a source of mass and energy. As lava fountain size increases, this source to the outer plume increases and therefore the plume can reach greater heights. This supports the results of a coupled plume going higher than a standard plume at high initial MFRs as seen in Figure 2.4.

2.4.2 Characteristics of a Coupled Lava Fountain - Tephra Plume

The inclusion of a lava fountain affects not only the rise height of the plume, but also its dynamics. Figures 2.8 and 2.9 show the velocity, temperature, radius, and density profiles for the double and single plume region, respec-

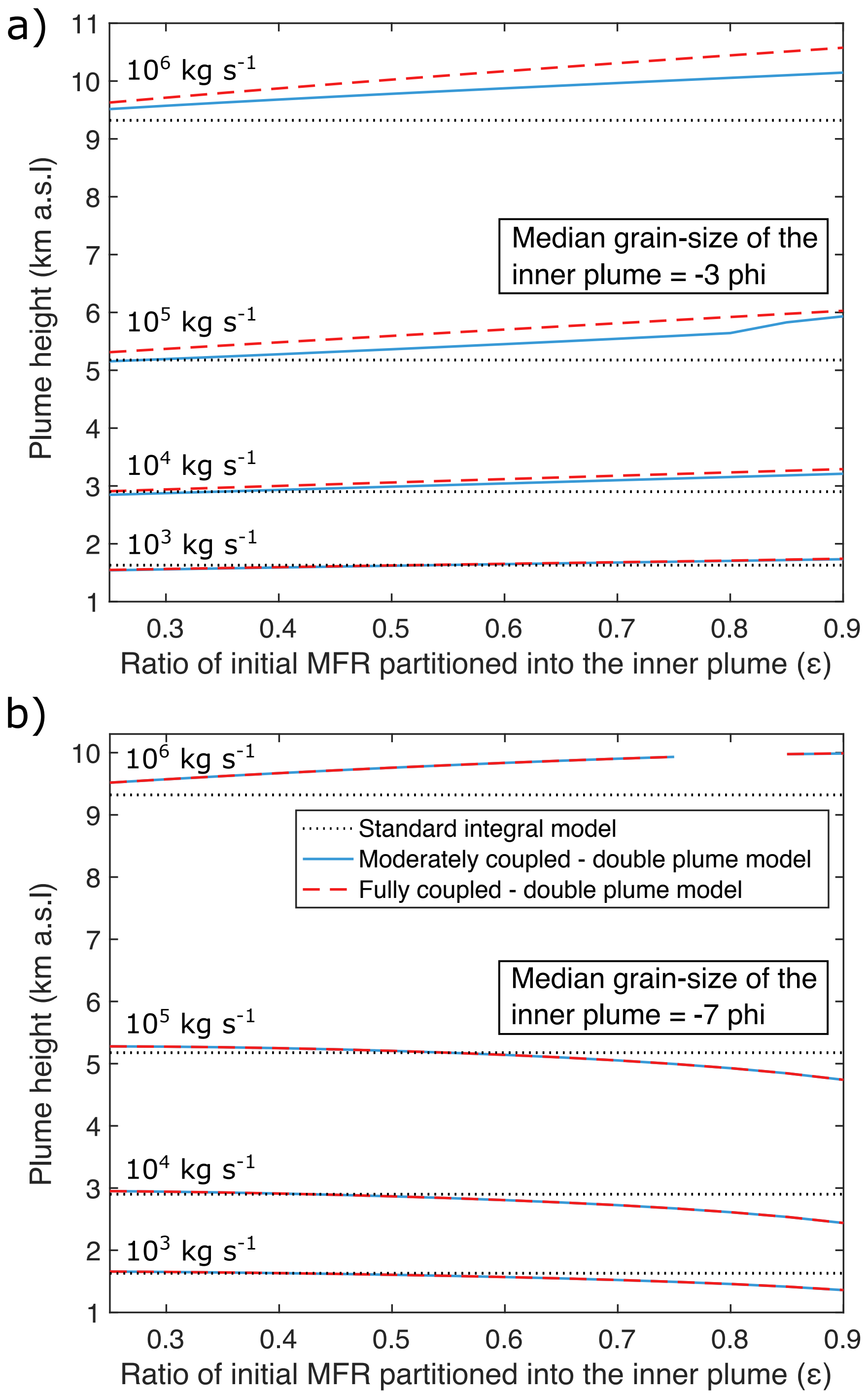

Fig. 2.7 The effect of lava fountain size on the height of the coupled tephra plume (coloured lines) compared to those of a standard integral model (black dotted line) for four different eruption sizes; a) shows the example of when the inner plume is initiated with a fine GSD, b) shows the example of when the inner plume is initiated with a coarse GSD.

tively. I compare two cases: when the GSD of the inner plume is coarse (Figures 2.8b and 2.9b) and when the GSD is fine (Figures 2.8a and 2.9a). Coarse and fine refer to log-normal distributions where the median grain-sizes are -7 and -3 phi, respectively. The standard deviation is kept constant at 0.75 phi. The other source conditions are kept constant and are shown in Table 2.4b. The initial MFR was set to 10^5 kg s^{-1} and 2/3 of this MFR is partitioned into the inner plume. Both the coupling scenarios of the double plume model and the standard integral model are plotted. As both scenarios only differ in the treatment of the initial conditions of the single plume, both scenarios are the same for the double plume region. Reference to the dynamics of the inner and outer plumes in Figure 2.8 refers to both scenarios. I consider representative characteristics for two end-member scenarios and therefore cover the range of plausible outcomes.

The Height of the Double Plume Region

A key feature of the dynamics of the inner plume is that its height is much lower than that of a typical tephra plume. The height of the inner plume (i.e., the lava fountain) is controlled by its initial velocity and the extent of particle fallout. As the lava fountain never becomes buoyant, the maximum height it can reach is the ballistic height. If the inner plume loses the majority of its mass as it rises via the process of particle fallout, the solid phase MFR becomes negligible, and the lava fountain never reaches the ballistic height. When the GSD of the inner plume is fine, the inner plume height is comparable to the ballistic height (Figure 2.8a). The height of the inner plume is 516 m, while the height of the calculated ballistic height is 510 m for the source conditions defined in Table 2.4b. These heights are not comparable to the height of the gas-thrust region (6 - 8 m) of the surrounding tephra plume or to the height of the gas-thrust region in a tephra plume without a lava fountain (25 m). However, when the GSD is coarse, the inner plume stops rising before the ballistic height is reached as the solid material in the plume is depleted (Figure 2.8b). Therefore, the dominant controls on the height of the inner plume (i.e., the lava fountain) differs to those of the surrounding plume, which in turn results in different dynamics between the inner and outer plume.

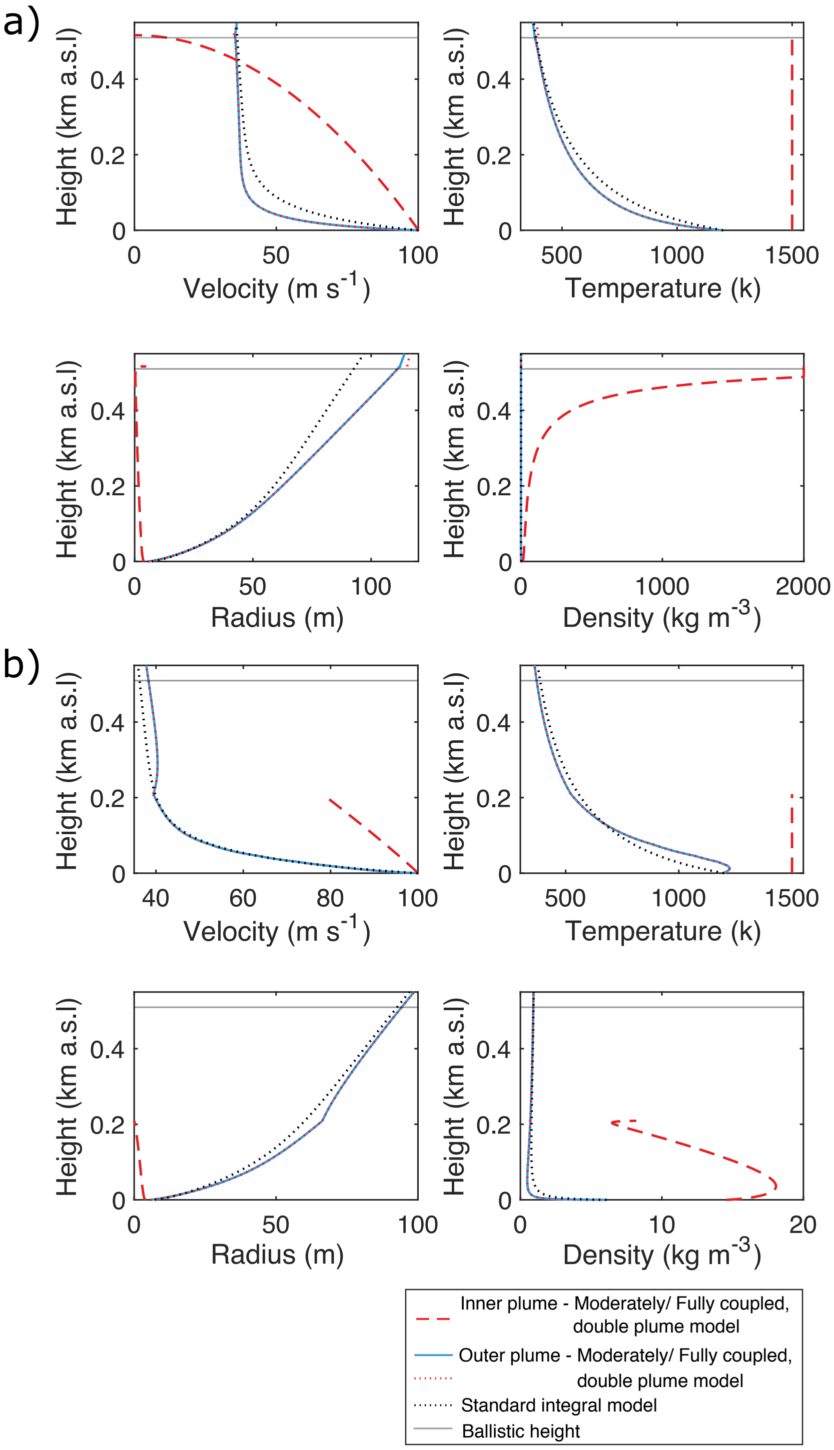

Fig. 2.8 The dynamics (velocity, temperature, radius and density) of the inner and outer plumes (with the moderately and fully coupled scenarios overlapping) in the double plume region compared to those of the standard integral model. a) The example of when the inner plume is initiated with a fine GSD and b) is the case when the inner plume is initiated with a coarse GSD. The standard integral model is shown (dotted black line) for comparison and the modelled surrounding plume in the double plume is also plotted for completeness.

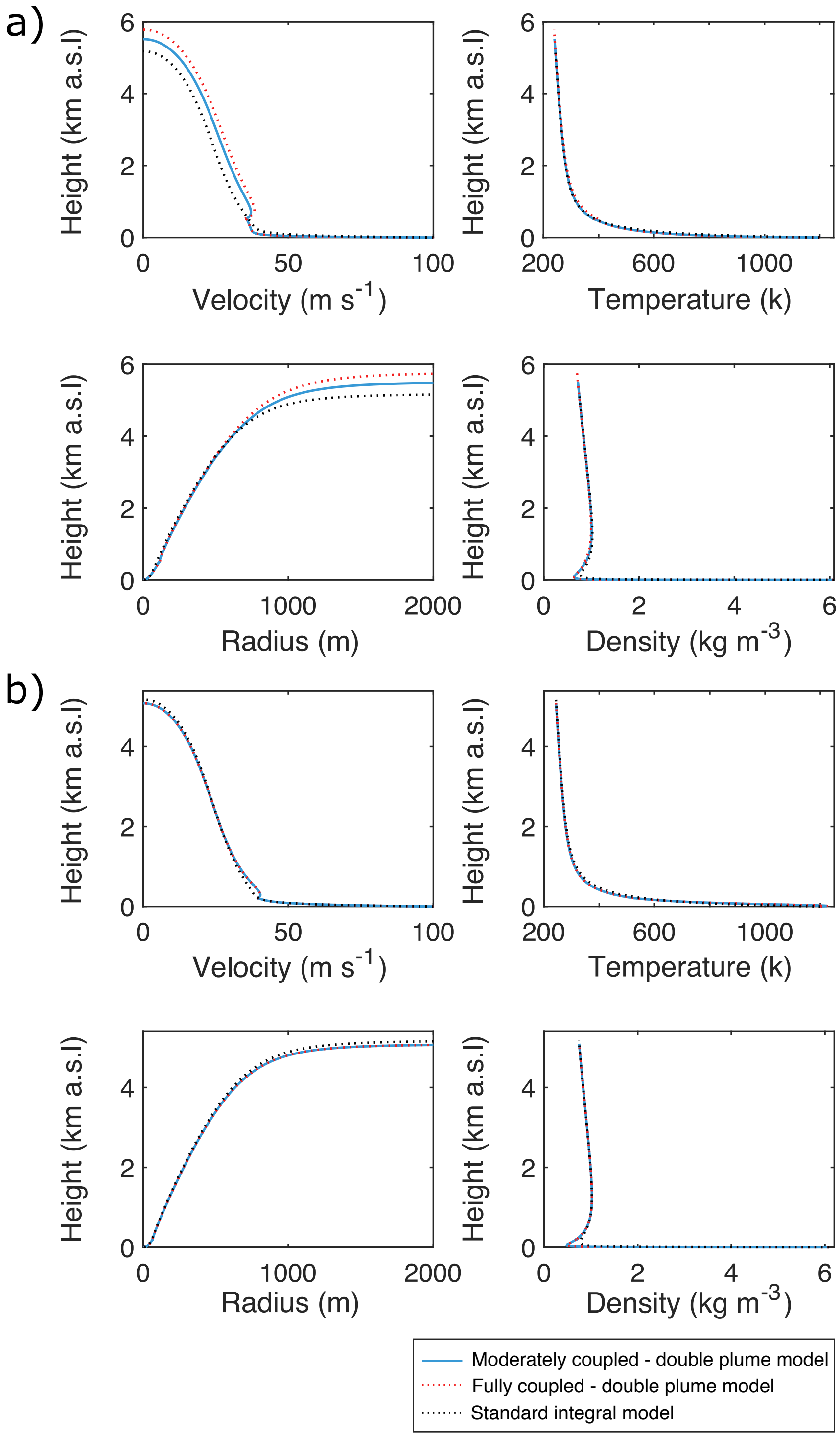

Fig. 2.9 The dynamics (velocity, temperature, radius and density) of the surrounding tephra plume for two examples, where one has a fine and the other has a coarse initial GSD for the inner plume, (a) and b), respectively). The two different coupling scenarios are shown; solid blue line for the moderately coupled case and dotted red line for the fully coupled case. The standard integral model is shown (dotted black line) for comparison.

The Dynamics of the Double Plume Region

The dynamics of a lava fountain differs to those of the surrounding tephra plume (Figure 2.8) as, unlike the outer plume, the inner plume does not entrain the surrounding gas. The inner plume does not become buoyant as its density is always higher than that of the surrounding plume; it is a negatively buoyant plume. The decrease of MFR due to the lack of entrainment into the inner plume and particle fallout results in the radius of the inner plume to decrease with height, while the velocity of the inner plume continuously decreases as it rises. The lack of entrainment of colder gas also causes very little cooling of the inner plume. In contrast the outer plume cools significantly and increases in width as it entrains the colder ambient gas. Once enough gas has been entrained and heated, the buoyancy is reversed causing an increase in the velocity of the outer plume. These characteristics of the outer plume are comparable to those of a standard tephra plume, with a slight difference due to the different entrainment coefficients used in the respective models.

The amount of sedimentation from the inner plume also plays a role in the dynamics of the inner plume and of the surrounding outer plume. When fallout is low (Figure 2.8a), the inner plume stops due to its velocity approaching 0 m s^{-1}, which causes the plume radius to diverge. The gas phase in the inner plume is depleted before all the solid MFR has fallen out of it, causing the bulk plume density to tend towards that of the solid phase. However, when fallout is high (Figure 2.8b), the plume stops before the plume radius diverges as the solid material in the plume has completely fallen out. Initially, before significant amount of entrainment occurs into the outer plume, high fallout from the inner to the outer plume causes the temperature of the surrounding tephra plume to increase. The gas phase becomes the dominant phase of the inner plume, and therefore reduces the bulk density of the inner plume towards that of the gas phase. At the very top of the inner plume, the bulk density appears to increase. This is an artefact caused by the model as the radius of the inner plume becomes narrower than the diameter of the smallest grain-size present in the inner plume. The choice of the initial GSD can result in significant difference in the dynamics of the inner plume and influences the dynamics of the surrounding tephra plume.

The Dynamics of the Single Plume Region

In the single plume region, there is little difference in dynamics between a tephra plume coupled to a lava fountain, for either coupling scenario, and a standard tephra plume (Figure 2.9), with the largest difference seen most strongly just above the lava fountain. There, the velocity of the plume increases before decreasing again. This is because the rate at which momentum in the plume increases is greater than that of the MFR. The radius, temperature and density of the single plume region follows the same general behaviour as the plume without a lava fountain. The radius of the single plume starts wider, before becoming narrower with height, compared to the standard integral model. The density of the outer plume is lower than that of the standard modelled plume.

Depending on the coupling scenario and how much material is left in the inner plume once it has stopped, the dynamics of the single plume varies with respect to the standard integral model. When the initial GSD of the inner plume is coarse (Figure 2.9b), high sedimentation results in the single tephra plume being slightly colder, denser, and wider as it rises compared to the standard integral model. No difference exists between the moderately and fully coupled double plume scenarios (solid dark blue vs dotted red lines, Figure 2.9a) as nothing is left at the top of the inner plume to add to the start of the single plume. In contrast, when the initial inner plume GSD has a median grain-size of -3 phi (Figure 2.9a), the difference between the double plume model and the standard integral model is more significant; especially towards the top of the plume as it rises higher. In the case where the double plume and single plume region are fully coupled, the single plume starts off with higher mass, momentum, and enthalpy flow rates as the majority of the material left at the top of the inner plume is added to the start of the single plume. This results in a discontinuity in the transition of the outer plume to the single plume. The single plume is slightly hotter and less dense than that of the plume without a lava fountain and a surrounding tephra plume that is moderately coupled to a lava fountain.

2.4.3 Thermal Disequilibrium

Thermal disequilibrium can exist to variable extents between particles larger than -2 phi and the gas phase (Woods and Bursik 1991). Much of the erupted material from lava fountains is larger than -2 phi, such as in the example of the 1956 Kilauea Iki (Parfitt 1998), Hawaii eruption, where $\sim$ 98% of the material in the field deposit is larger than -2 phi. This could mean that the heat transfer between the lava fountain and the surrounding plume is overestimated if thermal disequilibrium is not considered. However, as the extent of thermal disequilibrium is dependent on grain-size, and a large amount of the coarse particle are completely removed from the system by particle fallout from the lava fountain, the significance of this reduction in heat transfer has so far been assumed to be negligible and, as a result, is not explicitly considered. In this subsection, however, I consider the role of thermal disequilibrium between solid particles and the gas phase when modelling a plume that is coupled to a lava fountain. I have decided to evaluate this process independently to the previously examined model parameters due to limited work on how to accurately consider thermal disequilibrium between coarse vesicular volcanic clasts throughout the whole eruption column in an integral model.

I evaluate the impact of thermal disequilibrium between solid particles and the gas phase in a plume that is coupled to a lava fountain by considering two different approaches in the double plume model. First, I take an approach where sedimenting particles from the inner plume (i.e., the lava fountain) are not added to the outer plume (i.e., the surrounding tephra plume). This results in no coupling between the inner and the outer plumes and mimics the largest impact of thermal disequilibrium as no coupling prevents any heat transfer through particle fallout from the lava fountain to the surrounding tephra plume. Secondly, I implement the approach of Woods and Bursik (1991), where a thermal coefficient is used to determine the fraction of mass in equilibrium with the solid material. This thermal coefficient is then used to adjust the heat capacity of the solid phase. The thermal coefficient is dependent on the mean of a log-normal grain-size distribution. Woods and Bursik (1991) determined these coefficients by calculating the excess heat content of clasts in the lower 10 km of a tephra plume. Through this approach, I am able to examine the effect of thermal disequilibrium on plume rise as the grain-size distribution becomes coarser and while still allowing coupling between the inner and the outer plume. Both the first and second approaches are investigated by following the same procedure of randomly varying the parameter space to examine the relationship between plume

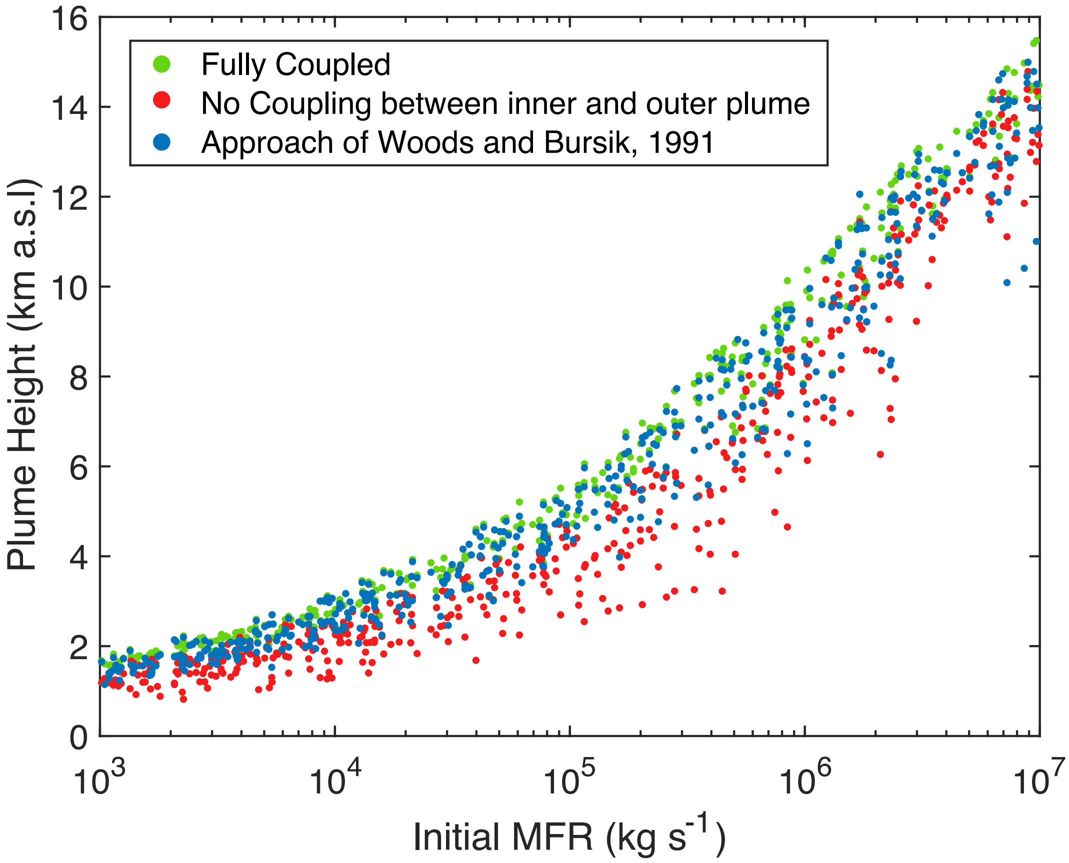

Fig. 2.10 The impact of thermal disequilibrium (red and blue markers) on the relationship between initial MFR and plume height compared to model runs where thermal equilibrium is assumed, and the inner and outer plumes are fully coupled (green markers). The effect from thermal disequilibrium is shown for the two implemented approaches; where it is assumed the inner plume and outer plume are not coupled (red markers), and the approach of Woods and Bursik (1991) (blue markers).

height and the initial MFR as in Section 2.4.1. In both cases, any remaining solid MFR, momentum flow rate and energy flow rate, are added to the start of the single plume region. As a result, I also compare with the fully coupled scenario.

Thermal disequilibrium can reduce the height that a plume can reach for a given overall initial MRF. Figure 2.10 shows the relationship between the overall initial MFR and plume height for the cases where thermal disequilibrium is considered via the approach of allowing no coupling between the inner and outer plumes (red markers) and thermal disequilibrium is considered via the approach of Woods and Bursik (1991) (blue markers). For comparison, I also present the fully-coupled scenario (green markers). For a given initial MFR, when no coupling exists between the lava fountain and the surrounding tephra plume, the final plume height reached is always lower compared to the fully coupled (i.e., no thermal disequilibrium) scenario (red dots compared to green markers). This suggests that if the solid material from the lava fountain is completely out of thermal equilibrium with the surrounding tephra plume, the tephra plume would reach a lower height. However, there are limitations of using the approximation of assuming that no coupling between the inner and outer plumes quantifies the effect of thermal disequilibrium as this approach also prevents mass and momentum transfer through fallout. As a result, this method can only tell us about the end member scenario. Similarly, when considering thermal disequilibrium through the approach of Woods and Bursik (1991), the plume height for a given MFR can potentially be the same or lower than that if thermal disequilibrium was not considered at all (blue versus green markers). This is due to the size of the impact from thermal disequilibrium being dependent on the GSD, and as the initial GSD is allowed to vary, the size of the impact on plume rise also varies. Similarly, this also results in a similar or higher modelled plume height for a given MFR compared to if thermal disequilibrium was considered as the worst-case scenario (blue versus red markers). This is because the degree of thermal disequilibrium is dependent on the GSD.

2.5 Discussion

2.5.1 What controls the effect that a lava fountain has on buoyant plume rise?

The extent to which a lava fountain affects the rise of a buoyant tephra plume depends on the amount of coupling between the tephra plume and the lava fountain. The greater the degree of coupling, the greater amounts of mass, momentum, and enthalpy the lava fountain can provide to the rising tephra plume. This can result in the surrounding tephra plume reaching higher altitudes compared to those without these additional sources. Instances of high coupling include when fallout from the lava fountain is high, and this fallout is incorporated into surrounding plume or is transferred to the single plume region when the lava fountain stops. High fallout generally occurs when the initial GSD is coarse. The larger the solid particles in the plume, the more likely the velocity of the inner plume will not be high enough to support their rise and will subsequently sediment from the plume (Figures 2.5 and 2.6). If there is not any coupling between the lava fountain and the tephra plume, the lava fountain acts as a sink for the system. This occurs when the amount of fallout is really high, and the material is not supported by the surrounding plume, or when the fallout is low and the material is removed from the system when the lava fountain stops. These results lead to the conclusion that the initial GSD of a lava fountain is one of the most important controls on the extent of impact a lava fountain has on the rise of the surrounding tephra plume. Regardless of the type of coupling scenario, the effect on plume rise is greater when more of the overall initial MFR is partitioned into the lava fountain compared to the surrounding tephra plume (Figure 2.7).

Thermal disequilibrium also has a control on the impact that a lava fountain has on a co-existing tephra plume. However, the extent of the impact is uncertain. Depending on the approach used to explore thermal disequilibrium (no coupling versus the use of thermal coefficients (Woods and Bursik 1991)), the overall plume height can be reduced. This, once again, is due to the initial GSD. When modelling thermal disequilibrium with the approach of Woods and Bursik (1991), a coarse initial GSD results in a low thermal coefficient and subsequently a high level of thermal disequilibrium. Similarly, a coarse GSD results in high fallout and therefore none of the energy of the hot lava fountain is transferred to the surrounding tephra plume. However, with the exception of Woods and Bursik (1991), the majority of volcanic plume models do not consider the impact of thermal disequilibrium as the particles are assumed to be fine enough that this process is not important (e.g., Bursik (2001), Woodhouse et al. (2013), Mastin (2014), Girault et al. (2014), de'Michieli Vitturi et al. (2015), and Folch et al. (2016)). As this in not the case for tephra plume-lava fountains, as shown in Section 2.4.3 and due to the fact that the grain-sizes in the plume can reach the order of meters (Parfitt 1998), the impact of thermal disequilibrium on the rise of tephra plumes that are couple to lava fountains should be investigated further.

2.5.2 Limitations of the Model

Unaccounted-for Processes

I focused this study on the coupling of a lava fountain to a tephra plume, but there are of course a series of additional processes that can further influence plume dynamics that were not directly accounted for. I discuss the most important ones and their potential impact here.

Wind could play a vital role on the rise of plumes that contain a lava fountain. Increased entrainment and bending of the plume from wind can reduce the overall height a standard tephra plume can reach. Its effect has been accounted for in standard integral models and has been studied in detail (Bursik 2001; Degruyter and Bonadonna 2012; Degruyter and Bonadonna 2013; Woodhouse et al. 2013; Carazzo et al. 2014b; Girault et al. 2016). While it is reasonable to expect a similar effect for the tephra plume above the lava fountain, the impact of wind on the region of the tephra plume that coexists with the lava fountain is less clear. An increase of entrained fluid from the atmosphere into the tephra plume could affect its ability to support sedimenting material from the inner plume. High wind could also increase the stability of the tephra plume as has been highlight in standard tephra plumes by Degruyter and Bonadonna (2013). Another unaccounted process is secondary fragmentation within the lava fountain, which could result in additional material being added to the surrounding plume.

Consideration should also be given to the potential impact of drag (of the lava fountain and the surrounding tephra plume on each other) on the plume dynamics. Drag is defined as the resistive force that opposes motion. It is a mechanical force that occurs when there is a difference in velocity between an object and the surrounding medium. Currently, the double plume model does not account for this process. However, it could have an important role on the plume rise. While both the inner plume (the lava fountain) and the outer plume (the surrounding tephra plume) start with the same initial velocity, their respective velocities differ with plume rise (see Figure 2.8). If the inner plume was rising faster than the surrounding outer plume, the drag force between the two plumes would result in the inner plume being slowed and the outer plume velocity increasing. Vice-versa, if the outer plume was rising faster than the inner plume, the opposite would be true. Previously drag has been considered in the study of plumes, for instance, when looking at the effect of wind on plume rise (Freitas et al. 2010; Li and Flynn 2020). The implications of drag force on a rising starting plume has also been investigated experimentally (Bhamidipati and Woods 2017). However, the inclusion of drag in the double plume model presented in this Chapter, would face multiple challenges such as defining the drag coefficient term, a key empirical value needed to quantify drag which is difficult to constrain. Given the potential impact from drag on plume rise, future work should determine the effect of drag on the rise of a tephra plume coupled to a lava fountain.

Parameter Uncertainty

Another consideration of this study should be the values of the entrainment coefficients used in the integral plume models. While there has been an extensive amount of research into which values to use in standard integral models (Devenish et al. 2010b; Suzuki and Koyaguchi 2015; Aubry et al. 2017; Aubry and Jellinek 2018), including using varying entrainment coefficients that are dependent on the Richardson number (Kaminski et al. 2005; Carazzo et al. 2008b), considerable uncertainty on their values remains. Entrainment coefficients for double plumes have been determined from large eddy simulation of Boussinesq plumes (0.05, 0.8 and 0.01 for α, β and λ, respectively) (Devenish et al. 2010a). They have also been calculated from the fitting of theoretical modelling to experiments of Boussinesq fountains (0.085, 0.147 and 0.147 for α, β and λ, respectively) (Bloomfield and Kerr 2000). The coefficients from these different studies differ to each other and therefore lead to a difference in plume dynamics (Devenish and Cerminara 2018). The plume height modelled by a double plume model is sensitive to the values chosen for the entrainment coefficients as shown in Li et al. (2018) and Li and Flynn (2020). Given the importance of the value of the entrainment coefficients, and the structure of a coupled lava fountain - tephra plume being different to experimental Boussinesq fountains (hotter, coarser, co-flowing), further experiments and analysis of real eruptions are needed to better constrain their values.

Even though the source conditions are a major control on the extent of coupling between a lava fountain and a tephra plume, the characterisation of the GSD and lava fountain size of a coupled lava fountain - tephra plume system are poorly constrained. Such source parameters are difficult to determine.

Field analysis of the proximal deposit is challenging after an eruption due to the difficult accessibility and deposit correlation (Andronico et al. 2014a; Behncke et al. 2014). Frequent eruptions at volcanoes such as Mount Etna, make it difficult to determine one eruption deposit from another in the very proximal region. As a result, analysis of the GSDs and of the erupted material has not been carried out on the very proximal deposits of fallout forming the scoria cone from the lava fountains that occurred between 2011 and 2016. Further information on the GSDs of the inner plume would provide a better description of the initial grain-size characteristics of the lava fountain and would improve the reconstruction of coupled lava fountain - tephra plumes. It would also allow for a better exploration of the role that thermal disequilibrium can have on plume rise. Field studies of proximal cones produced by coupled lava fountains - tephra plumes should be carried out to determine the GSD of the lava fountain. To better determine the amount of erupted mass of the lava fountain, remote sensing methods, such as radar, could also be used to define the MFR partition ratio ε between the lava fountain and the surrounding tephra plume (Freret-Lorgeril et al. 2018). High accuracy Lidar surveys (Fornaciai et al. 2010; Scollo et al. 2012; Scollo et al. 2015) and Unmanned Aerial Vehicles investigations (De Beni et al. 2019) after individual eruptions could also provide details on the characteristics and the volume of the cone deposits to better estimate the partition ratio of the initial MFR.

2.6 Conclusion

In this Chapter, I have examined the issue of how to model tephra plumes that are coupled to lava fountains. This was first achieved by evaluating if a standard integral model can reproduce the observations of tephra plumes that are coupled to lava fountains at Mount Etna, Italy. Results show that a standard integral model cannot capture the height of the lava fountain. Furthermore, the height of the gas-thrust region of a tephra plume, that is modelled with a standard integral model, is not equal to the ballistic height since the plume becomes buoyancy driven before the latter is reached. These findings highlighted the need of a new model to be able to capture the observed features of tephra plumes that are coupled to lava fountains.

To improve the modelling of tephra plume that are coupled to lava fountains so that the impact of a lava fountain on plume rise can be investigated, I have developed a novel model for buoyant tephra plumes associated with a lava fountain. My results indicate that lava fountains do affect the characteristics of buoyant tephra plumes. In particular, the type and extent of the effect on a plume from a coupled lava fountain is predominantly dependent on the proportion of the initial MFR that is partitioned into the lava fountain and the GSD of the lava fountain. The presence of a lava fountain increases the variability of the MFR-plume height relationship, compared to the case without one. This relationship is altered further when thermal disequilibrium is considered. When a greater fraction of the overall initial MFR is partitioned into the lava fountain and, if the fountain is composed of coarse material, the lava fountain acts as a sink of mass, momentum, and enthalpy of the overall plume system. In this scenario, a higher MFR at the source is required to reach the same height as a plume without a lava fountain.

Despite the advances presented in this Chapter, much work is still left to do to be able to use integral models to study tephra plumes that are coupled to lava fountain. Specifically, a better characterisation of the initial GSDs is required. The initial GSD of the lava fountain controls how much MFR, momentum flow rate and energy flow rate from the lava fountain are transferred to the surrounding tephra plume. It also controls the size of the impact of thermal disequilibrium on plume rise. However, studies of the size of the deposited material from lava fountains is limited. Moreover, it is essential that further work is focused on determining the entrainment coefficients of co-flowing buoyant plumes. Much of the previous work has determined the entrainment coefficients for counter-flowing plumes by fitting numerical models to experimental data (Bloomfield and Kerr 2000). In contrast, the plumes of the focus of this study are large, particle rich and co-flowing. To be able to use integral models to examine the dynamics of tephra plumes coupled to lava fountains, a better understanding of parameter such entrainment coefficients used in the double plume model are required.

CHAPTER 3

UNDERSTANDING THE RELATIONSHIP BETWEEN LAVA FOUNTAINS, TEPHRA PLUMES AND THEIR DEPOSITS AT MOUNT ETNA

3.1 Introduction

Volcanic tephra deposits have been used extensively to study the volcanic eruptions that generate them. They can provide information about many of the eruption characteristics including, but not limited to, the eruption source parameters, for example, total grain size distributions (TGSDs) (Bonadonna et al. 2015; Costa et al. 2016a; Pioli et al. 2019), the height that a plume reached (Carey and Sparks 1986; Rossi et al. 2019) and the eruption style (e.g., magmatic or phreatomagematic, Osman et al. (2019)). One of the most widely used pieces of information that can be derived from the study of a tephra deposit is the MFR at the vent. As mentioned in Chapter 1, MFRs derived from tephra deposits have been used to determine the relationship between plume height and the MFR (Sparks et al. 1997; Mastin et al. 2009). The MFR is also a vital input parameter for plume, volcanic tephra dispersal and hazard models. Effective forecasting and hazard assessment of eruptions requires a sufficiently accurate determination of ESPs and particularly the MFR (Scollo et al. 2008; Devenish et al. 2012; Bonadonna et al. 2015).

The MFR can be derived from the erupted mass and the duration of the eruption. The erupted mass is estimated from the tephra deposit based on how the deposit changes along its dispersal axis. First, the erupted volume or mass has to be calculated from the creation of an isopach (contours of equal thickness) or isomass (contours of equal mass load) map (Bonadonna et al. 2015; Biass et al. 2019). These maps can be used to determine how the deposit thickness, or mass load, changes along the dispersal axis. This data is then plotted as a semi-log plot of log(thickness) or log(mass load) versus the square root of the area enclosed within a contour. Fitting a line to this and integrating under the curve allows for an erupted volume or mass to be determined. Different fittings have been proposed including an exponential (Pyle 1989), multiple segments (Fierstein and Nathenson 1992), a power-law (Bonadonna and Houghton 2005a) and a Weibull function (Bonadonna and Costa 2012). An erupted mass (or volume converted to mass by using an estimate of the deposit density) can then be used to compute a MFR by combining it with an estimation of eruption duration.

Many studies have used the tephra deposits of the paroxysmal eruptions of Mount Etna, Italy, to determine MFR estimates (Scollo et al. 2007; Andronico et al. 2009a; Andronico et al. 2009b; Andronico et al. 2014a; Andronico et al. 2014b; Andronico et al. 2015; Andronico et al. 2018; Edwards et al. 2018; Poret et al. 2018b; Freret-Lorgeril et al. 2021b). However, as shown in Section 2.2.2, a discrepancy exists between deposit-derived MFR estimates and those derived from direct observations of the plume height. Based on my findings in Chapter 2, I hypothesise that this discrepancy is the result of high fallout from the lava fountain that causes a significant amount of the initially-erupted material to not reach the top of the eruption column. Instead, the tephra from the lava fountain sediments to form the proximal cone deposit (Taddeucci et al. 2015b; Behncke et al. 2014; De Beni et al. 2015). This results in the solid phase MFR at the top of the tephra plume being less than that at the vent. To test this theory, a better understanding of the relationship between the plume dynamics with respect to the tephra deposits is required, specifically on the mass distribution in the tephra plumes.

The plume tephra deposit also holds vital clues on the coupling between the tephra plume and the lava fountain of paroxysmal eruptions. But little is known about the coupling between the lava fountain and the surrounding tephra plume, i.e., the mass, momentum, and energy exchange between the lava fountain and the tephra plume, and its impact on the resulting tephra deposit. Previous studies have shown that a significant amount of erupted material from the lava fountain is deposited in the cone (Behncke et al. 2014; De Beni et al. 2015; Andronico et al. 2018). This is evidence of low coupling between the lava fountain and the surrounding tephra plume. I hypothesise that the degree of coupling determines the extent of the discrepancy between the MFR derived from the observed plume height (through empirical formulas or standard integral models) and that determined from analysis of the field deposit. While MFR estimates from the observed plume height tell us about what is erupted at the vent, not all of this material reaches the top of the surrounding tephra plume and becomes dispersed. The degree of coupling and the role it has on the dispersal of the erupted material and on the characteristics of the tephra deposit needs to be quantified.

Due to the high frequency of occurrence and availability of relevant data, the paroxysmal eruptions of Mount Etna provide an excellent opportunity the study the effect of tephra plume - lava fountain coupling on plume tephra deposits. Such data includes plume height estimates (Bonaccorso et al. 2014; Andronico et al. 2014a; Sellitto et al. 2016; Poret et al. 2018a; Corradini et al. 2018; Freret-Lorgeril et al. 2021b) and plume tephra deposit characterisations (Andronico et al. 2014a; Andronico et al. 2015; Freret-Lorgeril et al. 2021b; Edwards et al. 2018).

I have selected five eruptions between 2011 and 2013 of which clear plume heights have been determined and the tephra deposits have been analysed. These are the 12th of January 2011, 29th of August 2011, 23rd of February 2013, 26th of October 2013 and 23rd of November 2013. Each eruption is examined with the double plume model, that was presented in Chapter 2, to determine the MFR profiles in the plume. These are then compared to the MFR derived from the analysis of the field deposits reported in the literature. I show that the deposit-derived MFR better correlates with the modelled solid phase MFR at the start of the single plume, rather than the modelled solid phase MFR at the source. This indicates that the high fallout in the double plume region leads to a significant reduction of solid material in the tephra plume with height.

I then quantify the extent of coupling between the tephra plume and lava fountain for the five selected eruptions and demonstrate how it controls the discrepancy between the plume tephra deposit- and plume height-derived MFRs. When the extent of coupling is low, I find that this discrepancy is higher. This is because when coupling is low, fallout from the lava fountain to the ambient is higher and forms the cone deposit. This results in less material reaching the top of the buoyant tephra plume, and subsequently less material being dispersed to form the plume tephra deposit. This work therefore shows that coupling between the tephra plume and the lava fountain affects the relationship between MFR and plume height.

I then go on to discuss the impact of these findings on the understanding of the relationships between the tephra deposit, the lava fountain, and the tephra plume. I also offer thoughts on what MFR estimates should be used as a source parameter for dispersion and hazard models. Finally, I discuss the importance of coupling on the understanding of tephra plumes coupled to lava fountains at Mount Etna, Italy. This includes a discussion on the uncertainty related to the results, why there is a difference in coupling between the different eruptions and suggestions on how to better further quantify the extent of coupling.

3.2 Methods

3.2.1 The model

I examine the characteristics of sustained tephra plumes that are coupled to lava fountains at Mount Etna using the coaxial plume integral model, referred to as the double plume model, that was presented in Chapter 2, where in-depth details on the formation and characteristics of the model can be found. As in Chapter 2, it is assumed that no entrainment of the gas phases into the inner plume occurs to ensure that the radius of the inner plume decreases with height to reproduce the characteristic shape of a lava fountain. The values of the entrainment coefficients that describe entrainment from the inner plume to the outer plume, and from the ambient to the outer plume are also kept the same as to those used in the previous Chapter. The coupling between the double plume region and the single plume region is set as fully coupled (see Chapter 2.3.4). This is because I assume this approach is the most realistic as the addition of material from the lava fountain is dependent of the size of the material rather than assuming that all material is removed as explored in Chapter 2.

Compared to the model presented in Chapter 2, I make the adaptation of including the effect of wind on the rise of the single plume region. Figure 3.1

shows a schematic of the model, where the effect of wind is accounted for in the single plume region. This adaptation is made as many real eruptions are affected by wind, so this change allows for these eruptions to be explored with the double plume model. However, I do not include the effect of wind in the double plume region as it is assumed that wind plays only a minor role on lava fountain dynamics. To make this adaptation, the governing equations of the single plume region become the same as those of Degruyter and Bonadonna (2012), which are presented in Chapter 1. A complication of including wind in the single plume region is that an intermediate plume can be predicted to have a higher top plume height (height of the centreline plus the plume radius) than when modelled in the absence of wind. Since this is a clearly unphysical result, simulations are run both with and without wind as in Chapter 2.2. Then, following Mastin (2014), Devenish (2016), and Scollo et al. (2019), wind is only accounted for if the height predicted by the model with wind (Z_{wind}) is less than that predicted when wind is not accounted for ($Z_{\text{no wind}}$), i.e.,

$$Z_{\text{final}} = \min(Z_{\text{wind}}, Z_{\text{no wind}}). \tag{3.1}$$

I also make use of a standard integral model developed in Degruyter and Bonadonna (2012) for calculating a MFR estimate from plume height. As with the double plume model, the effect of wind on the rise of a tephra plume is considered. Similarly, to above, simulations are ran with and without wind, and the case with wind is only considered if the modelled top plume height, defined as the top modelled centreline height plus the radius at the top of the plume, is less than the top plume height when wind is not considered (see equation 3.1).

3.2.2 Modelling approach

The ESPs of the eruptions are inverted by randomly sampling the model parameter space and matching observations of both the lava fountain height and the plume height to the model. This Monte Carlo approach is taken for both the standard integral model and the double plume model. For each run of the Monte Carlo simulation, the unknown ESPs (initial values of velocity, gas mass fraction, temperature, MFRs of the outer and inner

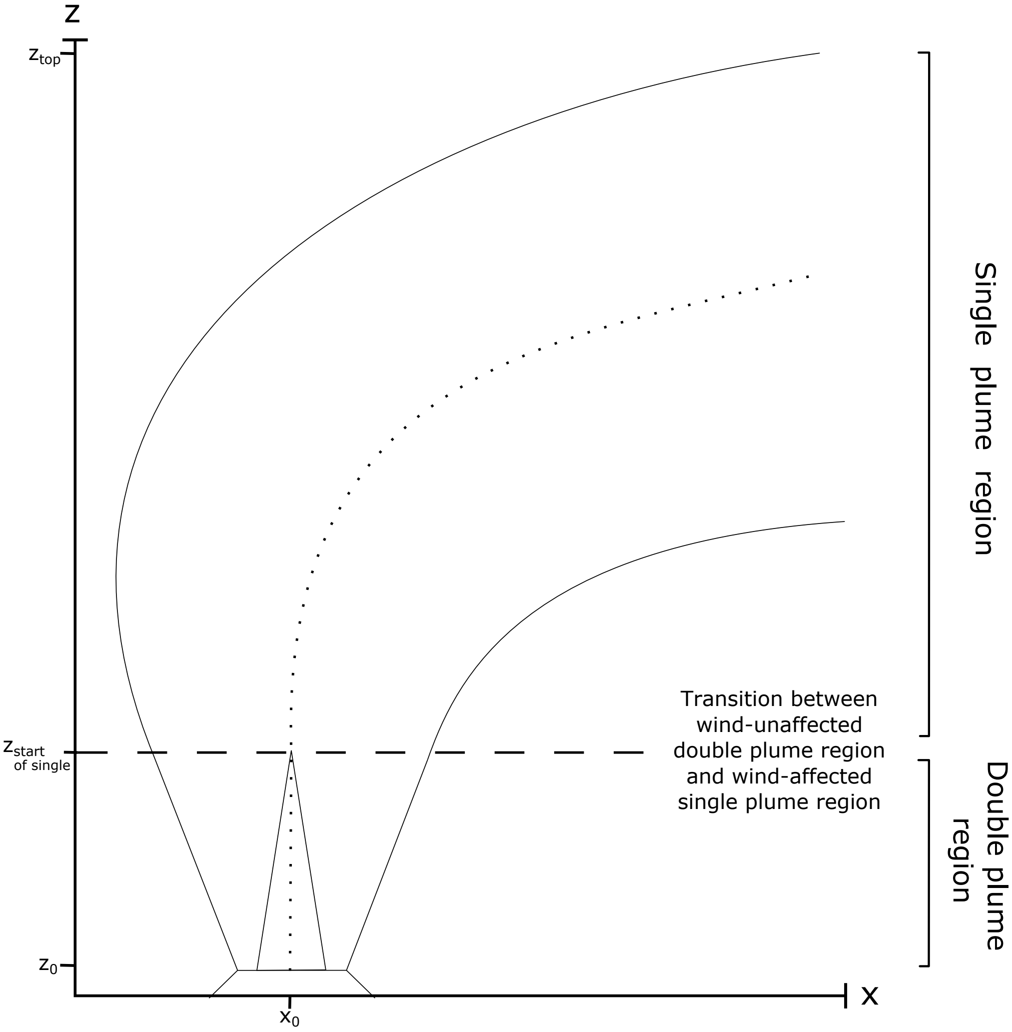

Fig. 3.1 Schematic of the double plume model, where the single plume region considers the effect of wind.

plumes) are varied. The source parameter ranges are given in Table 3.1 and the parameters are varied independently of each other. I also impose that the initial velocities of the inner and outer plumes are equal in the double plume model. For the Monte Carlo simulations using the double plume model, the simulated top plume height and double plume region height are then compared to the observed heights of the tephra plume and lava fountain, respectively. In the case of the Monte Carlo simulations using the standard integral model, only the top modelled plume height can be compared to the observed plume height.

The observed plume height and lava fountain heights used to constrain the Monte Carlo simulations can be found in Table 3.2 (Scollo et al. 2014; Corradini et al. 2018; Andronico et al. 2014a; Freret-Lorgeril et al. 2021b; Calvari et al. 2018). For the 23rd of February 2013 eruption, the observed plume height was calculated by INGV-OE from analysis of SEVIRI data using the dark pixel approach (Prata and Grant 2001). If the modelled heights are both within error of these observed heights, it is recorded as a match. For each constrained solution of the Monte Carlo simulation using the double plume model, the MFR of the solid phase at the source, the start of the single plume, the NBL and at the top of the plume are recorded for further comparison to other MFR estimates. Similarly, the initial MFR of the solid phase is recorded from the constrained solutions of the Monte Carlo simulation using the standard integral model. In the case of the double plume model, I also note the extent of coupling between the lava fountain and the surrounding tephra plume, which is defined as the percentage of the initial solid MFR of the inner plume that is transferred to the surrounding tephra plume during plume rise

$$\text{Extent of coupling (\%)} = \frac{MFR_{i\to o} + MFR_{i\to s}}{MFR_{i0}} \times 100, \tag{3.2}$$

where $MFR_{i\to o}$ is the total solid phase MFR transferred from the inner plume to the outer plume due to particle fallout, $MFR_{i\to s}$ is the solid phase MFR transferred from the inner plume to the single plume once the inner plume has terminated and MFR_{i0} is the initial solid phase MFR of the inner plume.

Table 3.1 ESPs for the plume model Monte Carlo runs.

ESP	Inner Plume	Outer Plume	Standard Integral Model
MFR (kg s^{-1})	Dependent on eruption	10^2 - 10^6	9×10^3 - 10^7
Temperature (K)	1250 - 1500	900 - 1250	900 - 1250
Velocity (m s^{-1})	50 - 200	50 - 200	50 - 200
Gas mass fraction	0.01 - 0.03	0.03 - 0.05	0.03 - 0.05
GSD	Hawaiian TGSD	Deposit-derived or Operational TGSD	Deposit-derived or Operational TGSD

Table 3.2 The height constraints for the case studies in the Monte Carlo simulations. Data sources: [1] Andronico et al. (2014a), [2] Freret-Lorgeril et al. (2021b) and Corradini et al. (2018), [3] Sellitto et al. (2016), [4] Bonaccorso et al. (2014) and Poret et al. (2018a).

Eruption date	Plume Height Range (km)	Lava Fountain Height Range (m) (Calvari et al. 2018)
12th January 2011	8.5 - 9.5 [1]	334 - 830
29th August 2011	9 - 9.9 [2]	453 - 1080
23rd February 2013 (calculated from satellite)	10 - 11	590 - 1350
23rd February 2013 (best-match)	11.5 - 12.5	590 - 1350
26th October 2013	6.5 - 7.5 [3]	430 - 1100
23rd November 2013	9.5 - 11 [4]	1075 - 3400

Some of the ESPs in the Monte Carlo simulations are kept fixed. The initial GSDs of the inner and outer plumes are kept constant. The field-derived TGSD is used as the initial GSD of the outer plume if available. This is under the assumption that the field deposit does not include significant fallout from the lava fountain. Otherwise, a log-normal GSD, with a mode of 0.5 phi and a standard deviation of 1.5 phi, is used (Scollo et al. 2019). The TGSD from the 1959 Kiluea Iki, Hawaiian eruption from Parfitt (1998) is used as the initial GSD of the inner plume as in Chapter 2. All these GSDs can be seen in Figure 3.2. The atmospheric conditions used in the double plume model (i.e., wind profile, pressure, and temperature) are sourced from interim-ECWMF data (Berrisford et al. 2011) for the specific eruption in question.

Calculation of the initial inner plume MFR

Unlike the standard integral model, the double plume model explicitly models the tephra plume and the lava fountain separately. As a result, the double plume model requires information on how the total initial MFR is partitioned between the inner and outer plumes (i.e., the lava fountain and the tephra plume). To determine this parameter, I used MFR estimates from field measurements of the cone. De Beni et al. (2015) and Behncke et al. (2014) have estimated the total volume of the cone deposit from paroxysmal eruptions at the New South East Crater (NSEC) of Mount Etna between 2011 and 2014. To estimate how much of this volume derives from each individual eruption, I use the volume estimates along with the total erupted mass proxy (TEM*) calculated with Doppler radar measurements (Freret-Lorgeril et al. 2018). TEM* allows us to determine how much an individual eruption contributed to the summated TEM*. I then use the relative contribution of an individual eruption to estimate how much of the volume of the cone derives from each eruption. The MFR of the cone material for each eruption is derived from the cone volume for each eruption, density measurements and eruption duration (Behncke et al. 2014; De Beni et al. 2015; Mulas et al. 2016; Freret-Lorgeril et al. 2018). These values will be referred to as the MFR from the lava fountain tephra deposit (MFR_{LFTD}) from now on under the assumption that they are composed of only material that has fallen from the lava fountain and can be found in Table 3.3. As a result, this examination is restricted to the period between 2011 and 2014, as this is the only time period where an estimate of the volume of the cone is made (Behncke et al. 2014; De Beni et al. 2015).

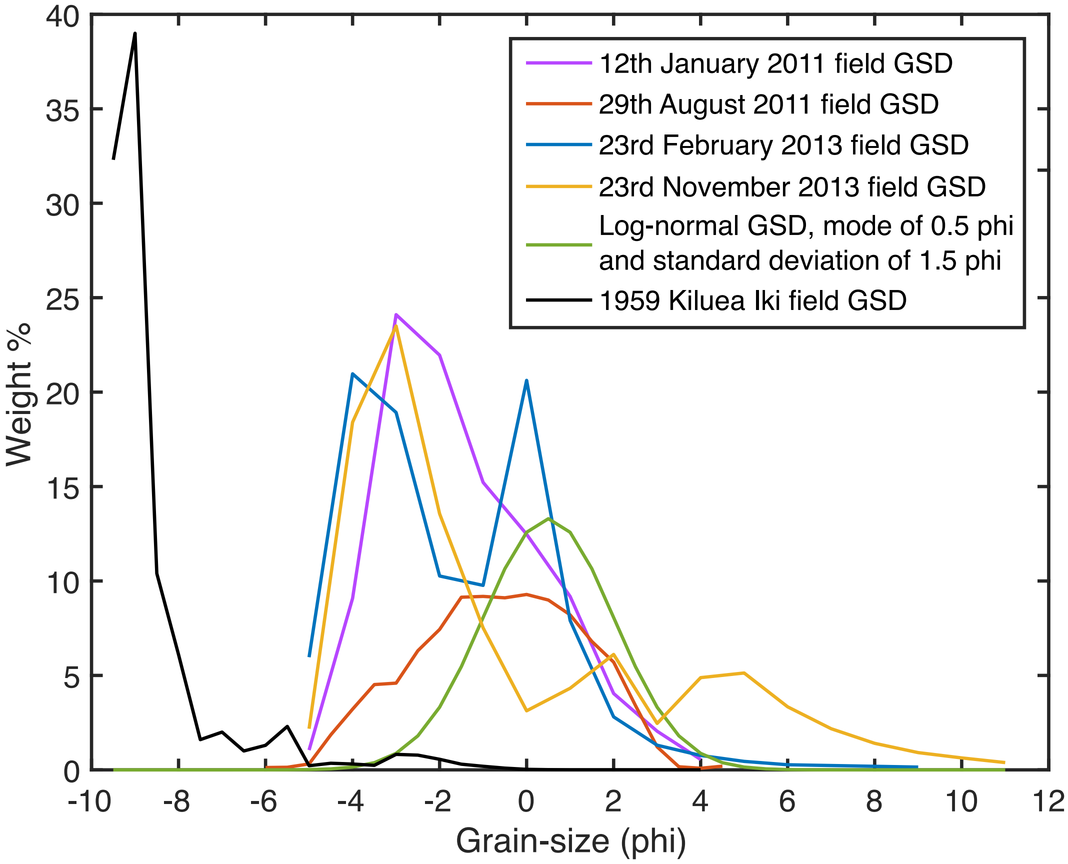

Fig. 3.2 GSDs of Etna Cases studies that are used in numerical modelling. Data sources: 12th January 2011, Andronico et al. (2014a), 29th August 2011, Freret-Lorgeril et al. (2021b), 23rd February 2013, Poret et al. (2018b), 23rd November 2013, Poret et al. (2018a), Log-normal GSD, Scollo et al. (2019) and 1959 Kiluea Iki, Parfitt (1998).

Table 3.3 Table of the cone volume related to each eruption (column 2), the field-derived MFRs from the literature (column 3) and the MFRs derived in this study for the lava fountain deposit (column 4). Data sources: [1] Andronico et al. (2014a), [2] Freret-Lorgeril et al. (2021b), [3] Poret et al. (2018b), [4] Andronico et al. (2018), [5] Andronico et al. (2015).

Eruption date	Cone volume (m^3)	MFR_{PTD} (kg s^{-1})	MFR_{LFTD} (kg s^{-1})
12th January 2011	1.3×10^6	2.5×10^4 [1]	2.97×10^5
29th August 2011	3.97×10^5	3.7×10^4 [1]	1.28×10^5
23rd February 2013 (best-match)	5.03×10^6	5.05×10^5 [3]	1.31×10^6
23rd February 2013 (reported)			
26th October 2013	8.29×10^5	7.81×10^3 [4]	3.12×10^4
23rd November 2013	4.18×10^5	4.5×10^5	4.41×10^5

Further to this, as there is no uncertainty analysis reported with the data that I use (volumes estimates and total erupted mass proxy), I allow the calculated MFR from the lava fountain to vary between ± 10 % when used as the initial MFR of the inner plume.

3.2.3 Comparison of model results to field data

The relationship between the tephra plume dynamics and the resulting tephra deposits are examined by comparing MFRs from the field tephra deposit from the literature to MFR estimates from the integral plume models (standard and double). The MFR estimated from the field tephra deposit will be referred to as the MFR from the *plume* tephra deposit (MFR_{PTD}) to distinguish it from the material that has deposited into the *cone* deposit, which is generally not included in the calculation of the field derived MFR (Behncke et al. 2014; Andronico et al. 2015; De Beni et al. 2015; Freret-Lorgeril et al. 2021a).

3.3 Results

3.3.1 Comparison of modelled and field-derived MFR estimates

In this section, I investigate the relationship between deposit-derived and modelled MFR estimates (from the double and standard integral models) at different heights in a tephra plume when the model is constrained by the observed plume and lava fountain heights. First, it can be seen that the

Table 3.4 Table of the modelled mean total initial MFR and modelled extent of coupling for the examined case-studies.

Eruption date	Mean MFR$_{model,source}$ (kg s^{-1})	Mean Extent of coupling (%)
12th January 2011	3.24×10^5	12.6
29th August 2011	1.78×10^5	25.6
23rd February 2013 (best-match)	1.77×10^6	27.4
23rd February 2013 (reported)	1.4×10^6	16.1
26th October 2013	4.53×10^4	26
23rd November 2013	9.96×10^5	49.6

double plume model requires a slightly higher initial MFR to reach the same height as the standard integral model (Figure 3.3). The exact values for each case-study can be found in Table 3.4. This is because the inner plume, i.e., the lava fountain, is initiated with a coarse GSD. This results in high fallout from the inner plume that is not supported by the outer plume (see Chapter 2), so is subsequently removed from the system. This results in the plume reaching lower heights than the standard integral model, which does not account for the lava fountain material. This is despite the double plume simulations starting with more initial enthalpy than the standard plume simulations, due to the temperature of the inner plume. In fact, much of this extra enthalpy is completely removed from the system by fallout.

Despite these differences in the initial MFR determined from the double and standard integral models, for four of the five examined eruptions (12th of Janurary 2011, 29th of August 2011, 26th of October 2013 and 23rd of November 2013), neither correspond with the MFR derived from the plume tephra deposit (Figure 3.3). Indeed, Figure 3.3 shows that the MFR derived from the plume tephra deposit is significantly lower than those modelled at the source (MFR$_{model,source}$) (Figure 3.4a). Double plume model simulations, initiated with MFR values equal to that derived from the plume tephra deposit, do not reach the observed heights of the examined plumes. This suggests that the additional heat from the hotter inner core (the lava fountain) does not result in the tephra plume going higher for a given MFR compared to a plume that does not have a lava fountain. However, the modelled MFR at the source, for the double plume model, best fits the sum of the MFRs derived from the cone and plume tephra deposits. This suggests that a considerable amount of erupted material for these eruptions is deposited in the proximal cone.

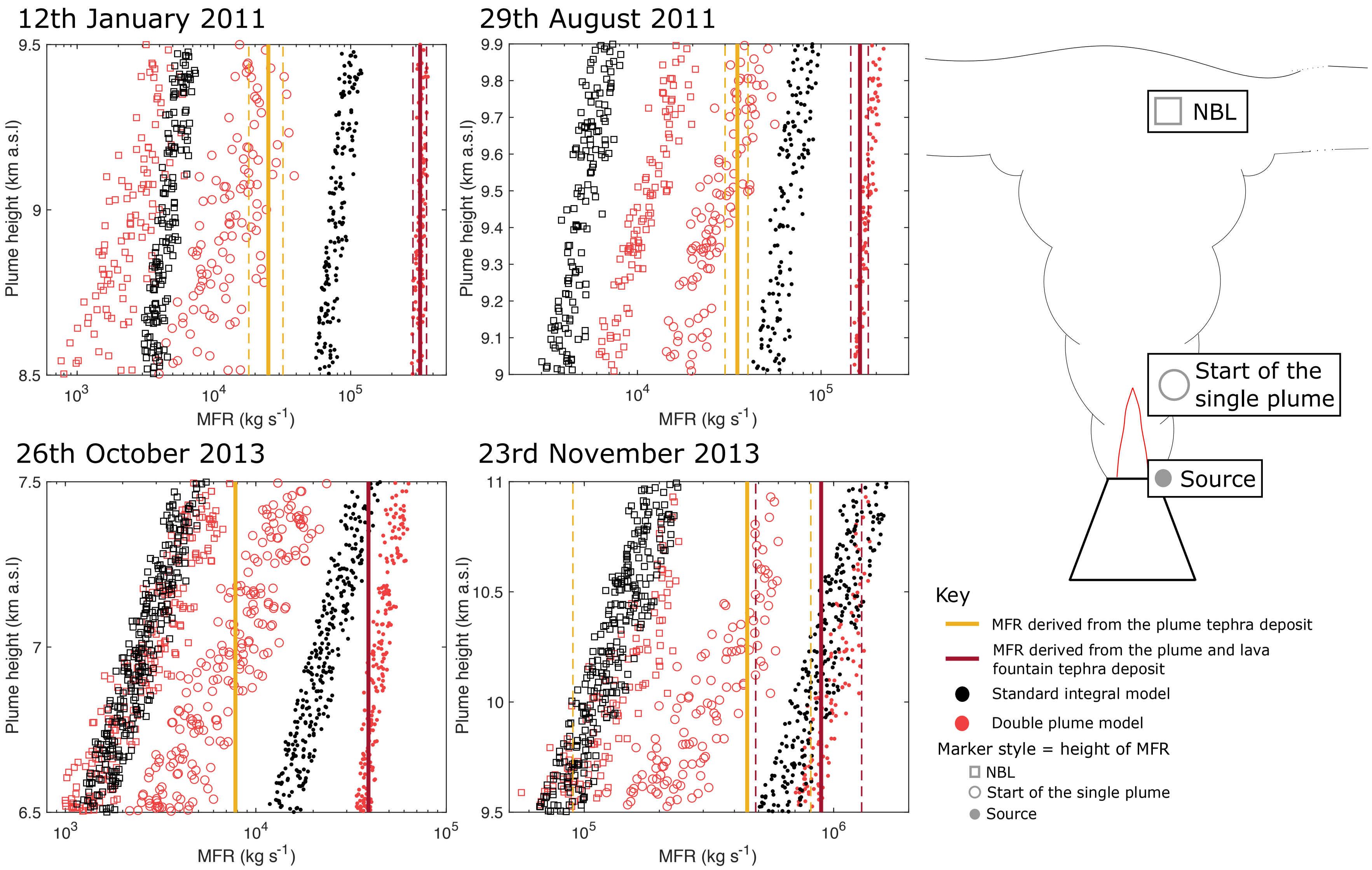

Fig. 3.3 Subplots showing the modelled MFRs at different heights in a plume the eruptions of 12th of January 2011, 29th of August 2011, 26th of October 2013 and 23rd of November 2013, compared with field-derived estimates of the MFR (solid lines). A schematic is located next to the key defining the different heights in the plume that each marker and line refers to. The dashed lines correspond to the uncertainty limits on the solid line of the same colour, if available. The range of plume heights on the vertical axis is constrained by observations of plume heights (see Table 3.2).

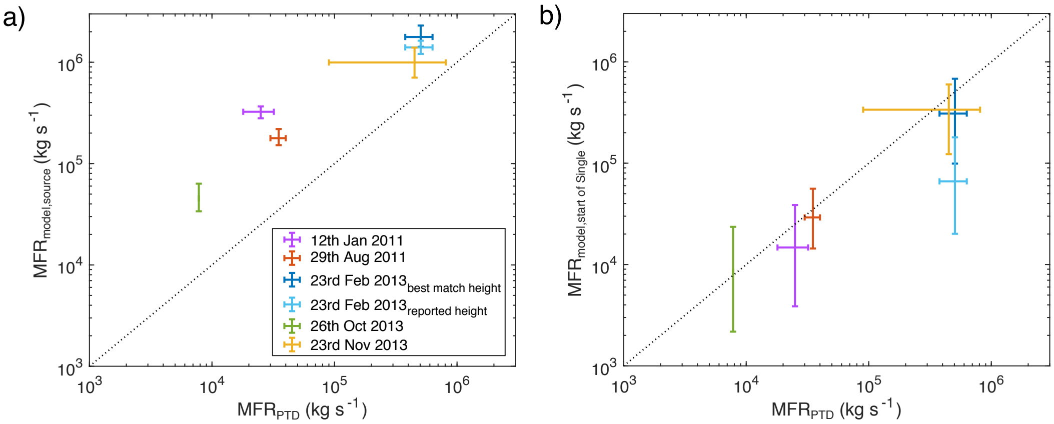

Fig. 3.4 Comparison of the plume tephra deposit-derived MFRs reported in the literature (Andronico et al. 2014a; Andronico et al. 2015; Andronico et al. 2018; Poret et al. 2018b; Freret-Lorgeril et al. 2021b). a) the best match initial MFRs from the double plume model, and b) the best match MFRs at the start of the single plume in the double plume model. The error bars in the x-axis direction signify the minimum and maximum estimates of the MFRs from the Monte Carlo modelling, while the error bars in the y-axis direction signify the minimum and maximum plume tephra deposit-derived MFRs reported in the literature.

Consistent with this result is the fact that the MFRs from the plume tephra deposits are more similar to the modelled MFRs in the buoyant tephra plume above the lava fountain (orange line compared with the hollow circle and square markers, Figure 3.3). As there is not a source of solid MFR in this region of the system, the overall solid phase MFR in the double plume can only remain constant or decrease with plume rise. Significant levels of fallout occur of coarse material in the region where a lava fountain is present. This causes the solid phase MFR to decrease drastically in this zone to a value that is comparable to the MFR determined by the field deposit analysis. This indicates that the MFRs derived from the plume tephra deposits are capturing the deposition of material from just the tephra plume. Accordingly, good agreement can be found between the values of the modelled MFR at the start of the single plume and the MFR derived from the plume tephra deposits (Figure 3.4b).

In contrast to the above results, I find that the MFR derived from the plume tephra deposit of the paroxysm of the 23rd of February 2013 is not comparable to the modelled MFR at the start of the single plume. This is despite the fact that, as with the other eruptions, the model runs have been constrained with the observed lava fountain (Calvari et al. 2018) and calculated plume height of 10 - 11 km a.s.l (Figure 3.5). While the modelled MFR at the source is comparable to the total MFR derived from the sum of the plume and lava fountain tephra deposit volumes, the modelled MFR at the start of the single plume is lower than the MFR derived from the plume tephra deposit by an order of magnitude. In order to reconcile these two values, the plume height constraint used in the Monte Carlo simulation would need to be increased from 10 - 11 km a.s.l to $\sim$ 12 km asl (Figure 3.5b). This could be due to either uncertainty in the observational data used to constrain the model or additional processes that remain unaccounted for within the double plume model. For example, the calculated plume height could be an underestimate of the top plume height (Scollo et al. 2019) or the recorded eruption duration of the eruption could have been an overestimate (Poret et al. 2018b). As the eruption occurred during poor weather conditions and at night, these factors could have hindered observations of the plume. Uncertainty could also lie in the value of the MFR derived from the plume tephra deposit. Many factors, such as poor sampling, can affect volume estimates from the plume tephra deposit (Bonadonna and Houghton 2005b; Bonadonna and Costa 2012; Bonadonna and Costa 2013; Costa et al. 2016a), which affect the comparison between numerical models and measurements from the field data. Since the plume was affected by the wind (Poret et al. 2018b), it is also possible that so was the lava fountain, meaning that tephra from the lava fountain may have deposited further than just into the cone deposit and thus could have been included as part of the plume tephra deposit MFR estimate. Finally, unmodelled phenomena could also result in the MFR derived from the plume tephra deposit not actually corresponding to the modelled MFR at the start of the single plume. While I have assumed that the numerical model does consider all the first order processes, not all secondary processes are accounted for. For instance, even though we have accounted for the effect of wind on the single plume region, the effect of wind on the lower, double plume region remains neglected.

3.3.2 Examination of the extent of coupling between the lava fountain and tephra plume

Figure 3.4a highlights that the size of the discrepancy between the estimates of the MFR at the source derived from plume height (using the Monte Carlo

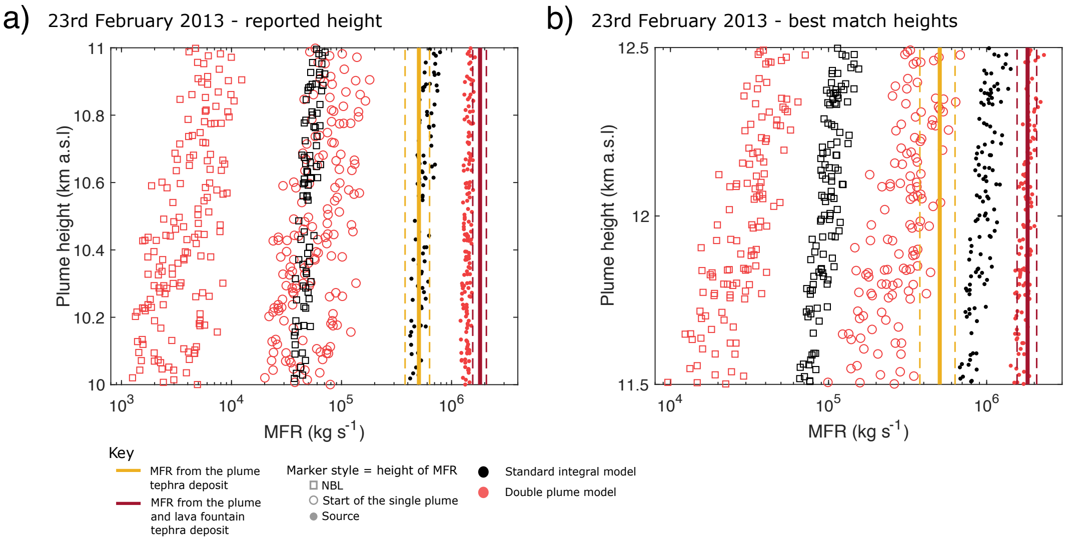

Fig. 3.5 a) The modelled MFRs at four heights within the plume (source, start of the single plume region and NBL)) plotted against the top height of the modelled buoyant plume for 'successful' runs of the Monte Carlo simulation when the height is constrained with calculated plume heights of 10 - 11 km a.s.l for the 23rd of February 2013 paroxysmal eruption of Mount Etna. The MFRs derived from the plume tephra deposit and the sum of the plume and lava fountain tephra deposits are plotted as solid lines for comparison, with dashed lines showing the uncertainty. b) The same parameters, but for when the Monte Carlo simulations were constrained to plume heights between 11 and 12.5 km a.s.l..

results of the double plume model) and the MFR derived from the plume tephra deposit varies between eruptions. For example, the eruption of the 12th of January 2011 lies further from the one-to-one line than the eruption of the 23rd of November 2013. This is also shown in Figure 3.3, as the separation between the MFR at the source (solid red circles) and the MFR at the start of the single plume (hollow red circles) varies for each of the different case-studies. To understand what controls the size of the discrepancy, I explore the relationship between the tephra deposits and the extent of coupling between the lava fountain and the surrounding tephra plume.

I first examine the relationship between the partitioning of the MFR into the lava fountain and plume tephra deposits and the extent of coupling (see Table 3.4) using the results from the double plume model. The inset to Figure 3.6a shows the extent of coupling of each Monte Carlo simulation as a function of the ratio of the MFR that is lost from the inner plume to the ambient through sedimentation and the MFR that reaches the start of the single plume. This ratio is defined as $MFR_{\text{sedimented from inner to ambient}}/MFR_{\text{start of single}}$. It is clear that as the extent of coupling increases, relatively less solid phase MFR is lost by sedimentation from the inner plume to the ambient and relatively more solid phase MFR reaches the single plume. This relationship can be explained by examining the source conditions of the lava fountain. The size of the lava fountain, i.e., the amount of MFR that is initially partitioned into the inner plume, controls the ratio of the MFR that is lost from the inner plume to the ambient through sedimentation and the MFR that reaches the start of the single plume. The larger the lava fountain, the lower the extent of coupling as less of the material that is sedimented by the lava fountain is supported by the surrounding tephra plume. Additionally, as one would expect, with a larger lava fountain, more of the overall initial tephra is deposited into the lava fountain deposit. If the partition ratio is fixed (i.e., by keeping the outer plume initial MFR and the inner plume initial MFR fixed), there is little variation in the ratio of the MFR that is lost from the inner plume to the ambient through sedimentation and the MFR that reaches the start of the single plume (pink markers, Figure 3.7a). Another major control is the initial velocity, which controls the extent of coupling. The initial velocity is one of the major controls of particle sedimentation (red markers, Figure 3.7b). Therefore, it is also a major control on the extent of coupling. In contrast, the initial temperature and gas mass fraction do not significantly

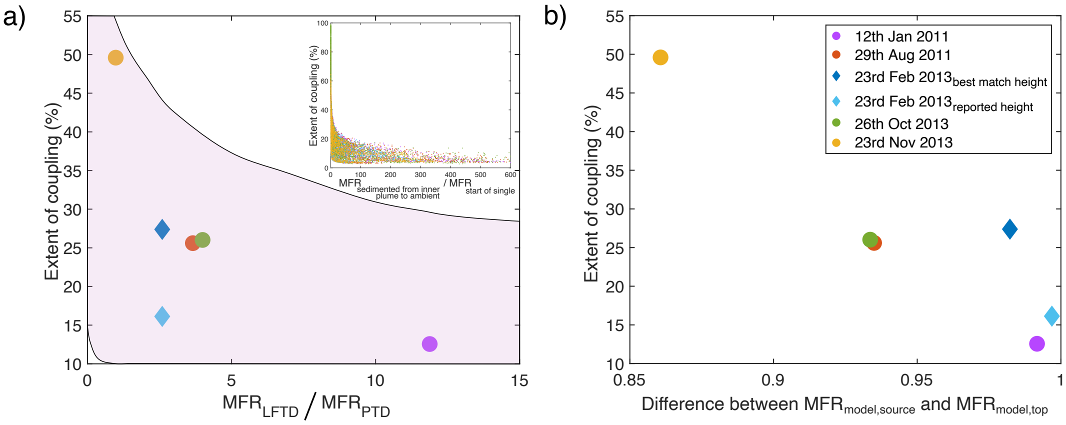

Fig. 3.6 a) Markers show modelled average estimates of the extent of coupling (%) for each eruption plotted as a function of the ratio of the MFR derived from the lava fountain tephra deposit (MFR_{LFTD}) and the MFR derived from the plume tephra deposit (MFR_{PTD}). The inset shows the coupling extents produced by each run of the Monte Carlo simulations plotted against the ratio of the MFR that sediments from the inner plume to the ambient and the MFR that reaches the start of the single plume. The span of these data has been used to define the purple field in the main figure. b) Modelled average estimates of the extent of coupling (%) plotted as a function of the difference between the initial solid MFR and the solid MFR at the top of the buoyant plume, where this difference is calculated as $MFR_{model,source}$ - $MFR_{\mathrm{model,\ top}}$ / $MFR_{\mathrm{model,\ source}}$.

affect the extent of coupling or the ratio of the MFR that is lost from the inner plume to the ambient through sedimentation and the solid phase MFR that reaches the start of the single plume (yellow and green markers, Figure 3.7b).

I can now relate this relationship to the observations. The extent of coupling is an average from the Monte Carlo simulations of the double plume model that are constrained by both the observed lava fountain and tephra plume heights. As demonstrated in Section 3.3.1, the mass of the plume tephra deposit divided by the eruption duration can be approximated by the solid phase MFR at the start of the single plume region. Similarly, the mass of the lava fountain tephra deposit divided by the eruption duration can be approximated by the solid phase MFR that sediments out of the inner plume directly to the ground. Using these approximations, the tephra deposit partitioning of each of the case studies and their relative relationship can be understood as a function of the extent of coupling (individual points in Figure 3.6). The modelled relationship between the ratio of the MFR that is lost from the inner plume to the ambient through sedimentation and the

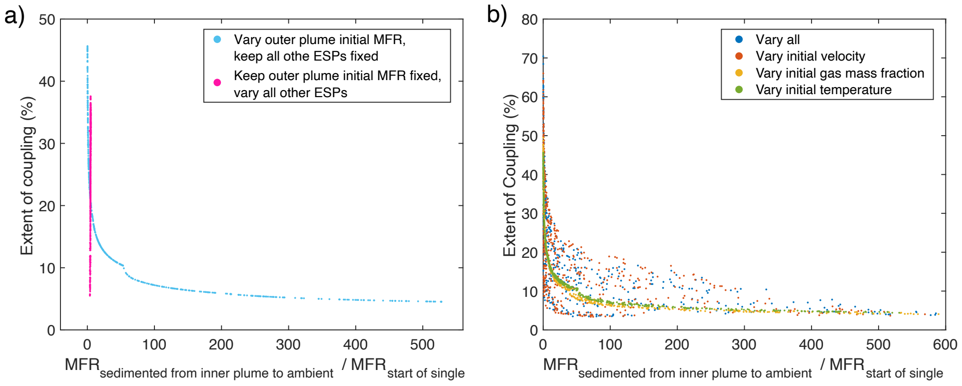

Fig. 3.7 Examination of the impact of the ESPs on the relationship between the ratio between the MFR that is lost from the inner plume to the ambient through sedimentation and the MFR that reaches the start of the single plume, and the extent of coupling (%). a) examines the impact of varying the amount of initial MFR partitioned into the outer plume (blue markers) compared to when it is kept fixed and all other ESPs are varied (pink markers). In both cases, the inner plume initial MFR is kept fixed. b) examines the impact of varying the initial velocity (red markers), temperature (green markers) and gas mass fraction (yellow markers) of the inner plume compared to when all are allowed to vary (blue markers). The inner plume initial MFR is kept fixed and the outer plume initial MFR is allowed to vary.

MFR that reaches the start of the single plume, and the extent of coupling is shown as a purple field in Figure 3.6. It can be seen that each case-study lies within this field, including the eruption of the 23rd of February 2013. As a result, while this eruption appears anomalous when comparing with just the field data of the other examined eruptions, the 23rd of February 2013 eruption does lie within the range of the limits of the relationship between the extent of coupling and the mass distribution between the lava fountain deposit and plume tephra deposit as predicted by the double plume model.

To further understand what the relationship between the ratio of the MFRs derived from the lava fountain and plume tephra deposits and the extent of coupling physically means for mass distribution in a volcanic plume, I investigate how much of the initial overall (lava fountain plus tephra plume) solid phase MFR reaches the top of the buoyant plume (Figure 3.6b). When coupling between the inner and outer parts of the plume is low, by definition, much of the initial MFR comprising the inner plume is completely lost from the plume system and, therefore, does not contribute to the surrounding tephra plume. As a result, the amount of solid MFR remaining at the top of the buoyant plume is lower compared to cases where coupling is high. This would result in a greater proportion of the initially-erupted solid MFR being deposited into the lava fountain tephra deposit (within $\sim$ 0.6 km (Behncke et al. 2014) under the assumption that the cone deposit is composed of tephra fallout from the lava fountain) rather than reaching the top of the buoyant plume and thus being dispersed more widely. This is demonstrated by the high ratio between the MFR from the lava fountain and plume tephra deposits when the extent of coupling is low in Figure 3.6a. In contrast, when the extent of coupling is high, a greater proportion of the initial solid MFR of the lava fountain can reach the top of the buoyant plume and subsequently be dispersed into the plume tephra deposit (Figure 3.6).

Based on this understanding of the mass distribution in the volcanic plume, the tephra deposits, and the extent of coupling, I am able to explain the size of the discrepancy between the MFR estimated using plume height and the MFR derived from the plume tephra deposit. This discrepancy is calculated as the difference between the averaged modelled MFR at the source (derived from the range given by the double plume model Monte Carlo simulations) and that of the MFR derived from the plume tephra deposit divided by the average modelled MFR at the source to normalise for the size of the eruption. This is given by

$$\text{Discrepancy} = \frac{MFR_{model,source} - MFR_{PTD}}{MFR_{model,source}}. \tag{3.3}$$

As the discrepancy between the MFR derived from the plume tephra deposit and the average modelled MFR at the source increases, the average extent of coupling between the lava fountain and the surrounding tephra plume is generally reduced (Figure 3.8). Only the case of the 23rd of February of 2013, where the Monte Carlo simulation was constrained with the observed plume height, diverges from this trend (light blue diamond marker, Figure 3.8). The extent of coupling increases as the discrepancy decreases since, when coupling is high, proportionally more of the fallout from the lava fountain enters the surrounding tephra plume rather than depositing into the ambient to form the lava fountain tephra deposit (Figures 3.6a, b). This results in a larger proportion of the initial MFR forming the plume tephra deposit rather than the lava fountain tephra deposit. Conversely, when the discrepancy is larger, the extent of coupling is lower, indicating that more of the fallout from the lava fountain is depositing out of the plume system completely and,

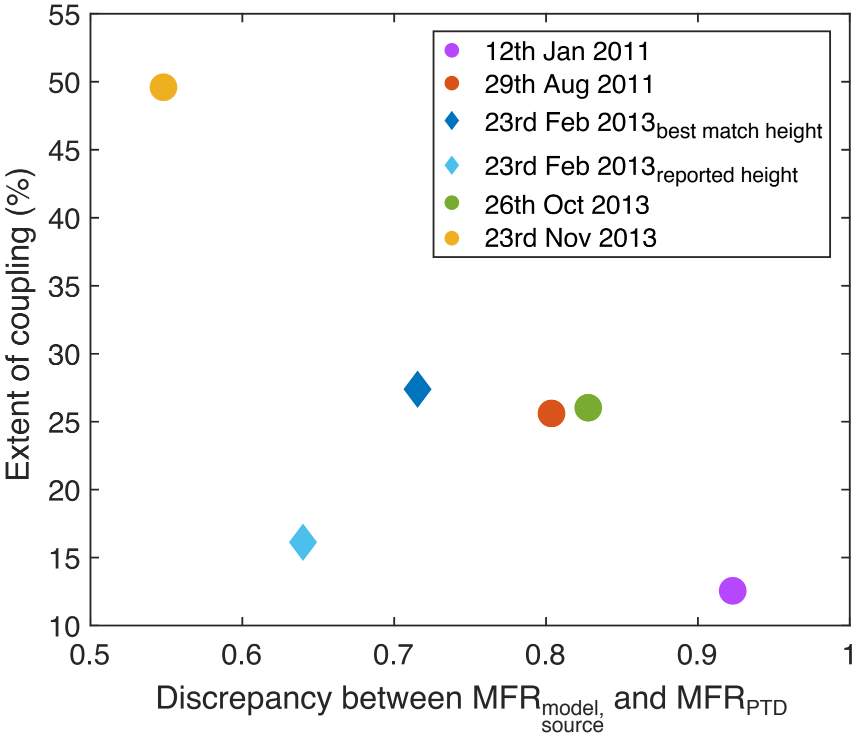

Fig. 3.8 Extent of coupling for each examined paroxysm plotted against the discrepancy between the averaged modelled MFR at the source (MFR$_{model,source}$) and the MFR derived from the plume tephra deposit (MFR$_{PTD}$).

therefore, forming a larger lava fountain tephra deposit. This suggests that the extent of coupling is an important control on how much of the initial solid MFR of a paroxysmal eruption can reach the atmosphere.

These results indicate that there is a difference between the five examined eruptions. The eruption of the 23rd of November 2013 shows the highest extent of coupling, while that of the 12th of January shows the lowest. This difference is also reflected in the tephra deposit (Figure 3.6a) and mass flow rate distribution in the plume (Figure 3.6b). The other three examined eruptions (29th of August 2011, 23rd of February 2013 and 26th of October 2013) lie in between these two extremes and the extents of coupling are all very similar to each other. This indicates that at least one of the controls on the extent of coupling (i.e., the GSD, initial velocity and/or the size of the lava fountain) must differ between the eruptions.

3.4 Discussion

3.4.1 What is the relation between tephra deposits and coupled lava fountain - tephra plumes?

My results have shown that the MFR at the vent of a tephra plume coupled to a lava fountain, when determined from the numerical modelling, is different from the MFR calculated from the plume tephra deposit. Indeed, for the case studies explored, the modelled MFRs at the vent, from both the double plume and standard integral models, are an order of magnitude larger than the MFR determined from analysis of the plume tephra deposit. The same pattern is seen with multiple other eruptions at Mount Etna, Italy (Figure 2.2). However, as Figure 3.3 highlights, use of the double plume model has shown that the plume tephra deposit MFRs better correlate with modelled MFR values at the start of the single plume, just above the lava fountain (Figure 3.3). This indicates that the double plume region produced a significant fallout in proximal region.

The difference between the modelled MFR at the source and the MFR derived from the plume tephra deposit has important consequences for modelling atmospheric dispersion of tephra. This is because the MFR is a key input in volcanic tephra dispersion models (Bonadonna et al. 2012). Significant uncertainty is associated with determining its value for an eruption (e.g., Bonadonna et al. (2015)). The results presented here show that the MFR determined by a standard integral model overestimates the amount of tephra that reaches the top of the plume and thus can be dispersed. The same is true for the source MFR determined through use of the double plume model. It would be more suitable to use the solid MFR at the NBL, as determined from the double plume model, as a source term for modelling distal atmospheric dispersion, as this represents the erupted material that reaches the umbrella cloud. This value can be similar to the value derived from the plume tephra deposit but is different from both the total initial MFR as determined from the standard integral model or from the combined cone and plume tephra deposit, which heavily depends on the spatial distribution of the tephra samples (Andronico et al. 2014a). However, the MFR from the plume tephra deposit can also be an overestimation of what reaches the top of the plume as seen in Figure 3.3 due to the likelihood that it also contains some material that has sedimented from the plume above the lava fountain. Therefore, while the new double plume model offers more insight into the MFR distribution in the tephra plume, care is required when using this to further investigate distal tephra dispersion.

3.4.2 The importance of coupling between the lava fountain and the tephra plume

There is a first order relationship between the extent of coupling between the lava fountain and the surrounding tephra plume, and how much of the erupted MFR is injected into the atmosphere. I have highlighted the control of the extent of coupling between the lava fountain and the surrounding tephra plume and the size of the discrepancy between the MFR derived from the plume tephra deposit and the modelled MFR at the vent (Figure 3.8). However, a number of caveats need to be considered when interpreting the results. While I have made maximum use of the available data, this trend is based on a limited amount of eruptions. For the time period considered (2011-2013), only a handful of paroxysmal eruptions have had their plume tephra deposits analysed. Only eruptions in this time period could be analysed as it is the only time period for which there is an estimate of the lava fountain tephra deposit (Behncke et al. 2014; De Beni et al. 2015). Field deposits are difficult to characterise due to both physical challenges (e.g., accessibility and/or quality of exposure (Bonadonna and Houghton 2005b; Bonadonna and Costa 2012; Costa et al. 2016a; Bonadonna and Costa 2013)) and access to resources to be able to go and collect data from the whole region of deposition (Behncke et al. 2014; De Beni et al. 2015; Freret-Lorgeril et al. 2021a). These limitations make it challenging to determine the eruptive volume/mass, and to subsequently determine the MFR of the tephra deposit.

3.4.3 Insights into fragmentation and the cause of the discrepancy between eruptions

While it is known that the MFR partitioning, the initial velocity and GSD of the lava fountain controls the extent of coupling with the tephra plume (Chapter 2 and Section 3.3.2), a large outstanding question that remains is what controls these? In particular, what parameters govern the initial GSD and velocity, which in turn govern the partitioning of the initial MFR into the lava fountain and tephra plume? And why do these quantities vary between eruptions? An explanation could lie in details of the fragmentation processes. Through the use of an integral conduit model, La Spina et al. (2021) showed that fragmentation during paroxysmal eruptions at Mount Etna is likely occurring above the vent rather than in the conduit. The generation of tephra in the lava fountain therefore depends on the conditions at the vent. If the magma at the vent level is over-pressurised and ejected at high velocity (leading to a lava fountain that is > 50 m), brittle fragmentation could occur at the margins of the lava fountain and generate large amounts of tephra, such as in the case of Mount Etna's paroxysms, in contrast to fountains from Hawaii (La Spina et al. 2021). However, while this may answer how the tephra is generated, it does not explain the variation in lava fountain GSDs between events. In the conduit, more energetic and explosive eruptions lead to higher fragmentation efficiencies resulting in a finer GSD (Cashman and Scheu 2015). However, the efficiency of fragmentation in a lava fountain is less clear. Fluidal fragmentation has previously been reported in lava fountains and generates coarse pyroclasts (Jones et al. 2019). Recent work has also offered further insights into how brittle fragmentation can occur in lava fountains. Namiki et al. (2021) showed that, under certain conditions (gas-rich vesicular magma and rapid adiabatic cooling of the gas phase), brittle fragmentation can occur to generate fine tephra from lava fountains in Hawaii. Moreover, secondary fragmentation, i.e., further fragmentation of already-fragmented clasts above the vent, in low-intensity mafic explosions can also lead to a finer GSD, with the shift to finer sizes increasing with jet velocity (Edwards et al. 2020). These studies suggest that secondary fragmentation is greater in gas-rich lava fountains that have a high exit velocity. These are both factors that also control the height of a lava fountain. An increase in gas content of a magma leads to an increase in exit velocity (Wilson et al. 1980; Wilson 1980; Wilson and Head III 1981), which, assuming lava fountain height scales with the ballistic height (Chapter 2), in turn results in a higher lava fountain (Head and Wilson 1987). As a result, a higher lava fountain could signify a greater amount of secondary fragmentation occurring and could potentially lead to a greater coupling between the lava fountain and surrounding tephra plume. This can be demonstrated by plotting the observed lava fountain height, as reported by Calvari et al. (2018), against the ratio of the MFR derived from the plume tephra deposit and that derived from the lava fountain deposit. Figure 3.9 shows that as

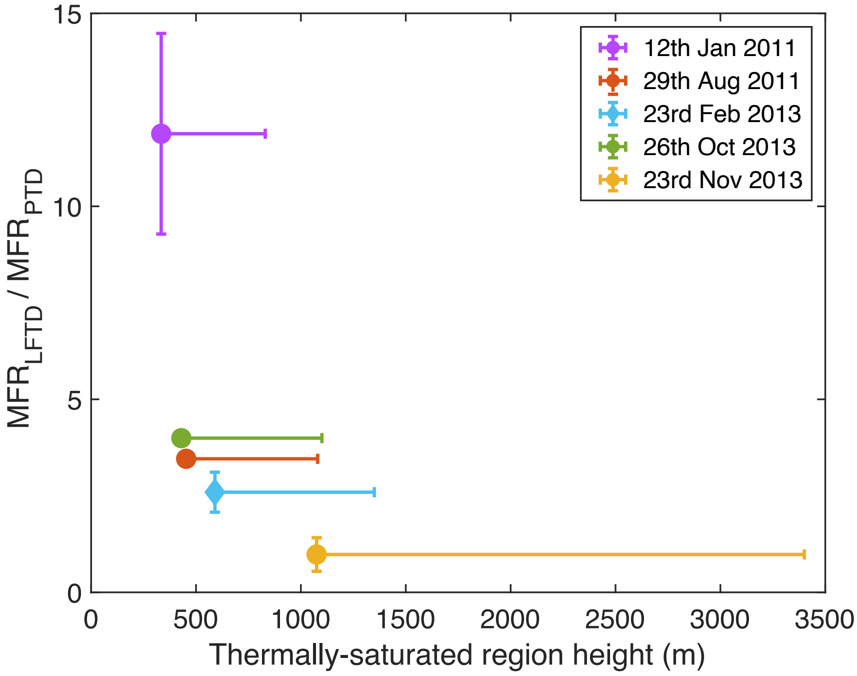

Fig. 3.9 Comparison between the thermally-saturated region height, assumed to be the height of the lava fountain, from Calvari et al. (2018), and the ratio between the MFR_{LFTD} and MFR_{LFTD}. The error bars in the x-axis direction reflect the average and maximum thermally-saturated region heights as reported in Calvari et al. (2018). The error bars in the y-axis direction reflect the uncertainty of the MFR_{PTD} that are reported in the literature.

the lava fountain height, assumed to be equal to the thermally-saturated region height, increases, the partitioning of material into the plume tephra deposit relative to the lava fountain deposit also increases. This signifies that the coupling between the lava fountain and the surrounding tephra plume is greater for higher lava fountains. It needs to be noted that these recent studies have focused on examining fragmentation in much smaller basaltic explosive eruptions that generate smaller levels of fine tephra compared to the lava fountain eruptions at Mount Etna. However, since increasing both the initial gas content and exit velocity seem to lead to brittle fragmentation occurring (Edwards et al. 2018; Namiki et al. 2021), as well as increasing the fountain height (Head and Wilson 1987), it is reasonable to assume that there would be a positive correlation between the fountain height and GSD. Additionally, since this thesis Chapter shows that the lava fountain GSD controls the extent of coupling with the surrounding plume, there is also a relationship between this coupling and the fountain height.

Another observation that distinguishes the paroxysmal eruptions of Mount Etna from smaller-scale basaltic fountaining eruptions (e.g., Hawaii, Piton de la Fournaise) is that they coexist with a tephra plume which is seen to start at the vent (see Chapter 4). Generally, tephra plumes associated with lava fountains could either be sourced from fragmentation occurring at the margins of the lava fountain or from fragmentation in the conduit. As it is observed that the lava fountain and tephra plume co-exist at the vent at Mount Etna, some fragmentation must be occurring in the conduit. This could be reflecting the fact that the magma ascent is not spatially homogeneous in the conduit. For example, friction at the conduit walls could result in fragmentation at the conduit margins even if it does not occur in the centre of the conduit (Gonnermann and Manga 2003). Moreover, differences in the overall magma ascent conditions could result in a greater amount of fragmentation happening in the conduit compared to in the lava fountain, which would affect the amount of the initial MFR partitioned in the lava fountain, and hence affect the extent of coupling between the lava fountain and surrounding tephra plume. Further investigations into the efficiency of fragmentation in a lava fountain and fragmentation in explosive basaltic eruptions, such as by using remote sensing methods (e.g., (Gouhier and Donnadieu 2008; Pioli and Harris 2019)), could help explain the differences that are seen in the extent of coupling for different paroxysmal eruptions at Mount Etna.

Another explanation for the difference in coupling between the examined case-studies could directly or indirectly come from wind effects. Increased entrainment into the plume from interaction with wind could affect the ability of the surrounding tephra plume to support fallout from the lava fountain, hence directly affecting the coupling between the lava fountain and the surrounding tephra plume. However, as the double plume model currently does not consider the impact of wind on the co-flowing region, I am unable to determine significance of this process on the extent of coupling. Wind could also indirectly affect the extent of coupling by altering the location of deposition of the material from the lava fountain. The trajectories of ballistic fallout from the lava fountain are influenced by the wind (Rossi et al. 2019; Osman et al. 2019). Depending on the size of the fallout and the strength of the wind, the sedimenting material from the lava fountain could be deposited further away from the vent than the cone deposit (i.e., what is typically thought of as the lava fountain deposit). This could lead to part of the material that I have been referring to as the lava fountain tephra deposit appearing to be part of the plume tephra deposit. Hence, this would appear to alter the extent of coupling when solely determined by looking at the deposit. This could be the case for the 23rd of February 2013 eruption, where the wind was strong (Poret et al. 2018b), as the MFR derived from the plume tephra deposit is higher than the modelled MFR at the start of the single plume when constrained with the observed lava fountain and plume heights (see Figure 3.5a). However, it is unlikely this is the explanation for the differences in the extent of coupling between all of case-studies as the values of extent of coupling that I discuss come directly from modelling the plume.

3.4.4 Perspectives for future study of the deposits from coupled lava fountains-tephra plumes

Full characterisation of not only the tephra-fallout deposit but also of the tephra plume would be beneficial to the understanding of the dynamics of eruptions that produce tephra plumes coupled to lava fountains. One way to achieve this would be by changing the way field deposits from an eruption are characterised. At Mount Etna, the majority of erupted material ($\sim 92\%$) from a paroxysmal eruption is deposited in the ultra-proximal cone ($\sim <0.6$ km from the vent). However, this is the least studied part of the deposit (Behncke et al. 2014; De Beni et al. 2015) despite it containing essential clues on the eruption dynamics. The GSD of this material and the erupted volume, specific to each eruption, would help validate the use of radar TEM* and cone volume estimates to derive the initial MFR of the lava fountain and offer vital insights into the efficiency of fragmentation. Technological advancements could also help reduce observational uncertainties such that the influence of coupling on the plume dynamics can be uncovered. Higher temporal resolution measurements of plume height during an eruption should be striven for, as well as further study into how height measurements using different methods (e.g., satellite, thermal camera, radar) relate to each other (Pailot-Bonnétat et al. 2020; Freret-Lorgeril et al. 2021a). Uncertainty on the height measurements themselves should also be better characterised as well as the information on where the height measurement has been made (e.g., distance from the vent, measurement of the plume or the cloud) (Bonadonna et al. 2012). While gathering the data from the literature for this work, it was not always clear what the height measurement was of, or what the errors associated with it were. This led to challenges in deciding what observations to use to constrain the Monte Carlo modelling. In conclusion, further study of future eruptions that are characterised by coexisting lava fountains and tephra plumes would allow the amplitude of the control coupling has on mass injection into the atmosphere to be fully determined.

3.5 Conclusion

This Chapter has offered an insight into the relationship between the tephra deposit, the lava fountain, and the surrounding tephra plume. I show that coupling between a lava fountain and a corresponding tephra plume during basaltic explosive eruptions is a first-order control on the mass injection into the atmosphere. As coupling increases between the lava fountain and tephra plume, more of the initial MFR of the lava fountain sediments completely from the plume system and forms the cone deposit. This results in the amount of solid erupted material reaching the top of the buoyant plume being reduced compared to what was originally erupted and to what would be expected for a standard tephra plume. For the majority of the eruptions that I have examined (12th of January 2011, 29th of August 2011, 26th of October 2013 and 23rd of November 2013), the deposit-derived MFR corresponds to the erupted material that reaches the single plume region, while the MFR that reaches the NBL is significantly smaller than that initially erupted. Therefore, less tephra contributes to the plume tephra deposit. Modelling tephra plumes at Mount Etna with a plume model that captures the effect of the lava fountain better quantifies the amount of tephra that is injected into the atmosphere and is, therefore, better suited than a standard integral model to determine the amount of tephra that could be dispersed and generates their resulting deposits. Lava fountain height could be used as a vital ESP for tephra dispersion models, as well as to provide information on end-member eruption scenarios used for forecasting. More observations, particularly on the cone deposit, are required to reduce uncertainty in determining the magnitude of the effect of coupling.

CHAPTER 4

VISIBLE VIDEO ANALYSIS FOR THE CHARACTERISATION OF TEPHRA PLUMES: THE EXAMPLE OF PLUMES COUPLED TO LAVA FOUNTAINS AT MOUNT ETNA, ITALY

4.1 Introduction

Observations of volcanic plumes are key sources of data that volcanologists can use to study an explosive eruption. While they allow for the basic features of an eruptions to be determined (e.g., start, duration, style), these observations can also provide key information about the eruption dynamics. For instance, information on the plume height can be used to calculate an estimated erupted mass (see Chapters 2 and 3) - a parameter that is a key input for dispersion models (Sparks et al. 1997; Mastin et al. 2009; Folch 2012). Observations can also be used to study the complex processes occurring in a volcanic plume such as entrainment of ambient air into the volcanic plume (Sparks and Wilson 1982; Patrick 2007; Aubry et al. 2017). This has led to an improved understanding of plume rise (Sparks and Wilson 1982; Formenti et al. 2003), sedimentation (Manzella et al. 2015; Houghton et al. 2020), entrainment (Patrick 2007), and many other processes. These observations can be performed with a variety of remote sensing methods (e.g., satellite observations, Corradini et al. (2018), radar, Freret-Lorgeril et al. (2018) or thermal cameras, Bombrun et al. (2016)). However, in this Chapter, I focus on the observations of tephra plumes coupled to lava fountains from visible-wavelength video recordings.

Visible video analysis has been utilised around the world to study volcanic eruptions. It is a method that allows for observations of the eruptive style and dynamics. They were first used to study the dynamics of multiple explosions during the 1979 eruption of La Soufrière volcano, St Vincent (Sparks and Wilson 1982). From three minutes of footage, ascent velocities, plume spatial dimensions, heights and spreading angles of the volcanic plume were determined. These observations were then integrated with a theoretical plume model to infer the ESPs (e.g., discharge rates). Since this initial study, visible video analysis has continued to be used to study multiple different eruption styles. In particular, they have been used extensively to study low-intensity short-lived, frequent volcanic explosions, i.e., Strombolian and Vulcanian. Such studies have characterised the source conditions and morphology of transient explosions (Formenti et al. 2003; Terada and Ida 2007; Suwa et al. 2014; Tournigand et al. 2017; Tournigand et al. 2019) and identified patterns in eruption style (Andronico et al. 2008a; Taddeucci et al. 2013). Additionally, visible-wavelength videos have also been used to examine low intensity lava fountaining eruptions. Examples include using visible-wavelengths videos to examine fountaining dynamics during the 2018 eruption of the lower East Rift Zone of Kilauea, Hawaii (Houghton et al. 2020). Houghton et al. (2020) were able to determine information such as erupted mass, ejection velocities and even grain-size distributions (GSDs) of airborne clasts within the lava fountain. Further to this, Witt and Walter (2017) also used visible-wavelength imagery to study the relationship between lava fountain dynamics and the lava fountain position in a series of aligned vents during the March 2011 Pu'u'Ō'ō eruption of Kiluea. Observations of lava fountains have also been made with visible video imagery at other volcanoes around the world (e.g., the 2014–2015 eruption of Holuhraun, Iceland (Witt et al. 2018)).

In addition to being used to study the dynamics of different eruption styles, visible-wavelength imagery has also been used extensively to study specific volcanic processes. One such process is sedimentation. High-speed and high-resolution visible-wavelength videos have frequently been used to study the trajectories of ballistic particles (Taddeucci et al. 2012; Gaudin et al. 2014; Dürig et al. 2015; Gaudin et al. 2016; Taddeucci et al. 2017; Kelfoun et al. 2020; Houghton et al. 2020), whilst they have also been used to examine sedimentation streaks, or fingers, from tephra plumes (Manzella et al. 2015). Additionally, analysis of visible-wavelength videos has also provided information on processes such as secondary fragmentation (Edwards et al. 2020), lava lake dynamics (Pering et al. 2019) and even volcanic lighting (Aizawa et al. 2016). Moreover, recent advances have focused on the automation of volcanic activity detection in the visible-wavelength (Valade et al. 2014; Witsil and Johnson 2020) and the imaging of volcanic plumes in 3D using cameras mounted on drones (Albadra et al. 2020).

Similarly, many studies have used thermal videos, rather than visible-wavelength videos, to analyse volcanic activity. Thermal videos have been used in a similar way to visible-wavelength videos, such as being used to study lava lakes (Valade et al. 2018; Pering et al. 2019), lava fountains (Calvari et al. 2018) and eruption dynamics (Calvari et al. 2006; Bombrun et al. 2016; Giudicepietro et al. 2019). They have also been used much more extensively to study volcanic plumes, although the majority of these studies have focused on small transient plumes and vulcanian explosions (e.g., Patrick (2007), Yamamoto et al. (2008), Sahetapy-Engel and Harris (2009), Harris et al. (2013), Tournigand et al. (2017), Bombrun et al. (2018), Wood et al. (2019), and Pioli and Harris (2019)). They are also used heavily for volcano monitoring (Spampinato et al. 2011; Calvari et al. 2018). Thermal cameras have the advantage of being able to clearly distinguish the volcanic plume from the ambient due to the temperature contrast with the surroundings. However, these cameras are expensive and direct temperature measurements of the plume cannot be made due to the atmospheric conditions and the radiative properties of the material in the plume (Sawyer and Burton 2006; Harris et al. 2013). As a result, visible-wavelength video analysis could be further utilised to study volcanic plumes.

Despite many studies on the use of visible-wavelength videos to study volcanic processes, few have focused on sustained volcanic plumes, especially those that are coupled to lava fountains. At Mount Etna, a volcano that frequently produces sustained volcanic plumes that are coupled to lava fountains, INGV-OE, the observatory responsible for monitoring the volcano, have a well-established video network that is used for volcano monitoring (Scollo et al. 2014; Scollo et al. 2019). It is composed of eight visible-wavelength cameras and three thermal cameras located at distances from the volcanic vent that range from 3 to 27 km (Calvari et al. 2011; Coltelli et al. 2017; Scollo et al. 2019). The camera network's main purpose is for the monitoring of Mount Etna in real-time e.g., to detect variations in volcanic activity and to estimate the plume height (Scollo et al. 2014; Scollo et al. 2019). However, these videos have also been used to study Mount Etna's tephra plumes, mainly by using estimated measurements of the top plume height (e.g., Freret-Lorgeril et al. (2021a)). As a result, the video network of INGV-OE has recorded many of the paroxysmal eruptions of Mount Etna Italy over the past decade.

In this Chapter, I utilise the extensive dataset of sustained tephra plumes coupled to lava fountains at Mount Etna to demonstrate the use of visible-wavelength videos for improving the understanding of tephra plumes that are coupled to lava fountains. This includes the objective of describing, both quantitatively and qualitatively, key processes and characteristics of the tephra plumes. Some of the issues that I aim to address include are tephra plumes that co-exist with lava fountains the same as those without and what is the relationship between the lava fountain and surrounding tephra plume. Answers to these questions will help to understand the dynamics of tephra plumes that are coupled to lava fountains.

I also aim to investigate how information from the visible-wavelength videos can be coupled with modelling of sustained tephra plumes. This is to achieve the objective of ultimately providing even more information on the tephra plumes than by just using the visible videos alone. Past studies have coupled plume models to visible observations (Sparks and Wilson 1982; Formenti et al. 2003), however, many of these have focused on short-lived volcanic plumes. I aim to examine how this can be applied to sustained tephra plumes that are coupled to lava fountains at Mount Etna and evaluate how plume shape derived from video analysis can constrain numerical models. Specifically, I want to determine source parameters, and important integral model coefficients (radial and wind entrainment coefficients). This will help refine the use of integral models to determine source parameters that are used in subsequent hazard modelling.

I first provide an overview of the methodology to analyse the visible-wavelength videos of tephra plumes that are coupled to lava fountains at Mount Etna (Section 4.2). After first providing information about the cameras used, I then give details on the how the visible-wavelength videos are calibrated. This includes the presentation of a new methodology which adjusts the geometrical calibration to account for the effect of wind in Section 4.2.1. I then summarise in further detail the approaches that are taken to quantify the rotation rate of the tephra plumes (Section 4.2.2), and how the results of the video analysis are then integrated with a standard integral model (Section 4.2.3).

The results are then presented. I first present qualitative descriptions of interesting features that were observed in Section 4.3.1. This includes descriptions of the sedimentation, the origin of the tephra plumes and the entrainment of material from the surrounding ground into the tephra plumes. Following on from this, a qualitative description of the observed feature of rotation is then provided (Section 4.3.2). Here, details such as which eruptions show rotation, the direction of rotation, when during the eruption does rotation occur and the reduction in rotation with height in the plume are noted. This section is then concluded by quantitative analysis of the rotation (Section 4.3.2). I find the frequency of the rotation, and then calculate Rossby numbers to quantify the extent of the effect of rotation on the plume dynamics.

I then present my findings on the coupling of visible-wavelength video analysis with modelling of volcanic plumes. I calculate radial entrainment coefficients from the observed gradient of the margins of strong plumes (Section 4.3.3) and show that the obtained values are within the expected range for sustained tephra plumes (Aubry et al. 2017). I also show that the value of the entrainment coefficients are slightly lower for the lower plume region compared to the whole plume. I then present work on using the plume shape, determined by the visible video analysis, to constrain a standard integral model in the same section. By using the shape of the plume and the standard integral model, I am able to infer information on the entrainment of air due to the wind and the source conditions that resulted in the observed tephra plume. Furthermore, I then evaluate the benefits of using plume shape, rather than using just the top height of the tephra plume, for the determination of the initial conditions and final height of an observed tephra plume.

Finally, Section 4.4 discusses what interpretations these observations can provide on the volcanic processes that occur at tephra plumes coupled to lava fountains. This includes discussions on the dynamics of sedimentation, the relationship between the tephra plume and lava fountain, and the origin and importance of rotation on the plume rise. I also discuss more broadly

Table 4.1 Information related to the different cameras of the INGV-OE visible camera network, which are used in this Chapter. Data sourced from Calvari et al. (2011), Coltelli et al. (2017), and Calvari et al. (2018).

Camera Code	Latitude (°)	Longitude (°)	Distance to Vent (km)	Altitude (m a.s.l)	Camera
ECV	37.514	15.044	27	35	Canon VC-C4R
ENV	37.614	15.019	15	730	Canon VC-C4R
EMOV	37.719	15.004	3	2600	Canon VC-C4R
EMOH	37.719	15.004	3	2600	Vivotek IP8172

the successes and limitations of this type of approach and the uncertainty on the information that visible-wavelength videos can provide (Section 4.4.3). Suggestions are also provided to help maximise the benefit of using visible-wavelength video analysis to study tephra plumes, specifically those that are coupled to lava fountains, in the future.

4.2 Methods

Visible-wavelength video analysis is used to investigate the dynamics of tephra plumes that are coupled to lava fountains. The videos are sourced from the official video network of INGV-OE, specifically the ECV, ENV, EMOH and EMOV cameras. The locations of these cameras are shown in Figure 4.1. Table 4.1 provides information on the physical properties of these cameras. The camera locations range from a distance of 3 to 27 km from the vent. Two different camera models are used. The ECV, ENV and EMOV cameras are Cannon VC-C4R cameras, while the EMOH camera is a VIVOTEK IP8172. The frame rate of the ECV and ENV cameras is 1 frame per 2 seconds, and for the EMOV and EMOH cameras it is 1 frame per second. The details on the properties of these cameras can be found in Table 4.2.

In total, I examine 23 of the paroxysmal eruptions of Mount Etna between 2011 and 2013. These are the majority of the eruptions that occurred during daylight hours in this time period. Each eruption is qualitatively examined and interesting features and conditions on visibility are recorded. For seven of these eruptions, no information could be recorded due to poor weather conditions. Out of all the eruptions analysed, 7 are further quantitatively

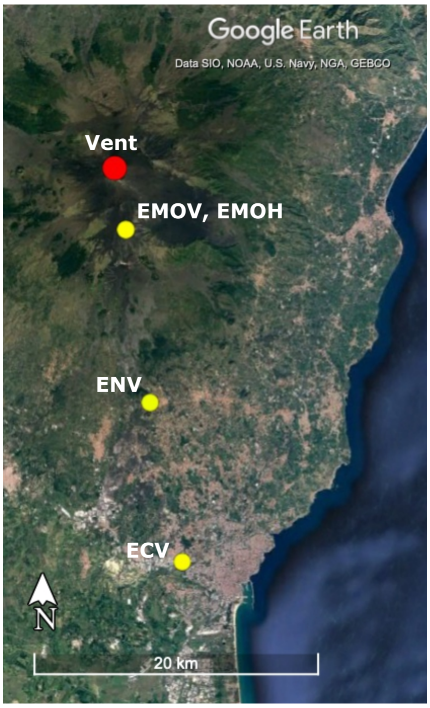

Fig. 4.1 A map that shows the locations of the cameras used in this study from the INGV-OE camera network.

Table 4.2 Information related to the different camera models. Horizontal field of view data is sourced from Calvari et al. (2011) and Coltelli et al. (2017).

Camera Type	Pixel Dimensions	Horizontal Field of View Range (°)	Vertical Field of View Range (°)
Canon VC-C4R	704 x 608	3-47.5	2.5-40.7
Vivotek IP8172	704 x 608	33–93	24–68

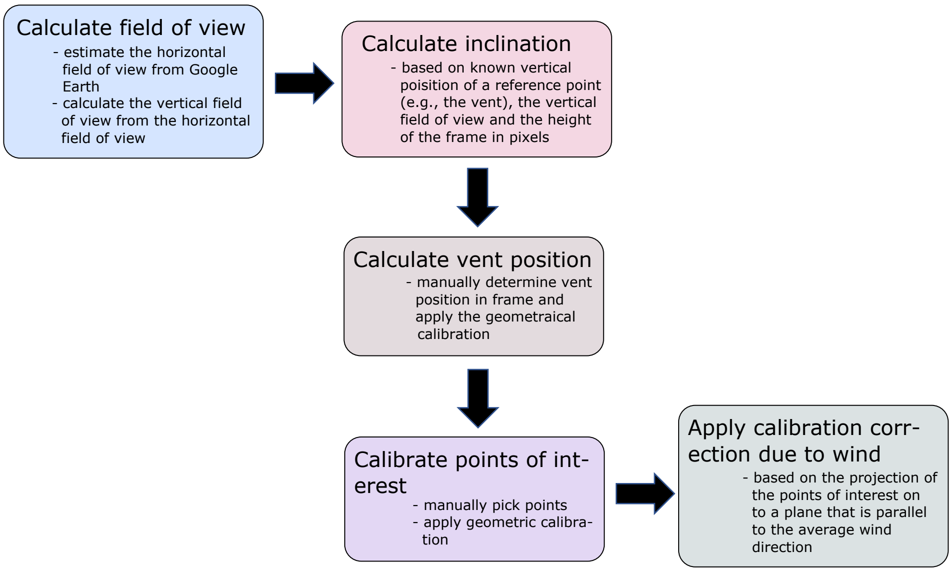

Fig. 4.2 A flowchart that denotes the workflow process to calibrate the visible-wavelength videos used in this study.

analysed to extract information such as the rotation rate of the plume or the radial and wind entrainment coefficients. The methodology of this further analysis is described below.

4.2.1 Camera Calibration

Despite the fact that INGV-OE stores all the videos that they record, information related to the used camera properties is, unfortunately, unknown because the setting can be modified by the operator and are not recorded. This includes parameters such as the optical zoom, which in needed to calculate the horizontal and vertical fields of view (θ_h and θ_v, respectively), and the camera inclination (ϕ). For the cameras that I use in this Chapter, a camera calibration only exists for the ECV camera (Scollo et al. 2014). As a result, to calibrate the visible videos, I develop and follow the workflow that is shown in Figure 4.2. Each component of the workflow is detailed in the subsequent text.

Calculation of Field of Views

While the possible ranges of θ_h are found in the literature (Calvari et al. 2011; Coltelli et al. 2017), the specific values of θ_h and θ_v, which depend on to the optical zoom used by the operator, for each recording is unknown. In turn,

Table 4.3 Table of the estimated horizontal field of views used in this study.

Eruption Date	Camera Code	Estimated θ_h
All eruptions	ECV	16 - 18
29th August 2011	ENV	14 - 16
29th August 2011	EMOV	29.2 - 29.5
4th March 2012	EMOV	29.2 - 29.5
18th March 2012	ENV	14 - 16
18th March 2012	EMOV	23.5 - 26
26th October 2013	EMOH	40.7 - 42.9

the optical zoom applied to a specific video of interest is also unknown. As a result, I need to estimate θ_h for the videos that I use in this analysis. I do this by first drawing a horizontal line in Google Earth from the camera location to a recognisable point at the centre of the image. This is the horizontal projection of the centreline of the image and, for all the considered videos, connects the camera position with the summit crater area of Mount Etna. A vertical plane, that is perpendicular to this line and goes through the region of interest (i.e., the New South East Crater (NSEC)), can then be drawn and will hereon be referred to as the image plane. By positioning oneself at the camera location within Google Earth and adjusting the view to be similar to the one in the videos, it is possible to estimate and mark the right-, and/or left-hand margins of the video. A line can then be drawn connecting this point and the camera position. The angle this line makes with the horizontal projection of the centreline is equal to $\theta_h/2$. Therefore, θ_h is calculated by doubling this calculated value. An example of this can be seen for the EMOV video of the 4th of March 2012 paroxysmal eruption (Figure 4.3). This procedure enabled calculation of θ_h for the EMOV and EMOH cameras (see Table 4.3), which match well with those of the thermal cameras located in the same locations whose field of views are known to be similar to those of the visible cameras. After θ_h has been estimated, it can then be used to calculate θ_v using

$$\theta_v = \theta_h \frac{N}{M}, \tag{4.1}$$

where N is the height of the frame in pixels and M is the width of the frame in pixels.

Fig. 4.3 An example of how the field of view (horizontal) was calculated by determining the left and right margins of the image frame (left and right green lines) on Google Earth.

For the ECV camera, this approach is slightly modified as the greater distance between the camera and the vent (Table 4.1) made it difficult to precisely determine the position of the right-hand or left-hand margins of the frame in Google Earth. This is because the right-hand side of the frame does not intersect with the volcanic edifice, so it is difficult to precisely determine θ_h. However, it is possible to constrain the minimum value to be 16 °. Given the uncertainty on this value though, the value of θ_h for the ECV camera is allowed to vary. Given that the INGV-OE have a calibration for the ECV camera only, it is possible to compare results with the calibration procedure described here with that used operationally. As will be seen in Section 4.3.3, Figure 4.15, best agreement between the two procedures is obtained for $\theta_h = 18°$. I therefore choose to use a range of θ_h = 16-18° for the ECV camera. A similar approach is taken for the ENV camera, where the minimum value of θ_h is determined to be 14° and I allow to vary to 16°.

Calculation of the camera inclination

Once θ_h and θ_v have been determined, the camera inclination (ϕ), which is specific to each of the recorded videos of interest, can then also be estimated. This can be calculated using knowledge of the camera properties and the known vertical location of a reference point in the image frame, which I take to be the summit of the volcano.

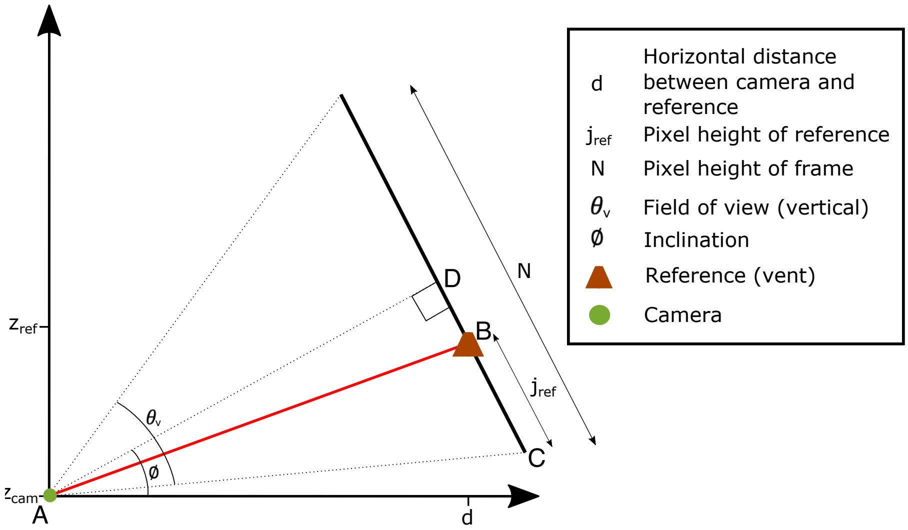

Fig. 4.4 Diagram defining the length scales and angles used to calculate the camera inclination.

First, ψ is defined as the angle denoted by the line between the camera (A) and the reference point (B) and the horizontal (see Figure 4.4 for a sketch showing positions A and B). It can be calculated as

$$\psi = \tan^{-1}\left(\frac{z_{ref} - z_{cam}}{d}\right), \tag{4.2}$$

where d is the horizontal distance between the camera and the reference point in the image frame. The angles denoted by BAC and ACB (see Figure 4.4), where C in the lowest vertical point in the image frame, can then be defined as $\frac{\theta_v}{2} - (\phi - \psi)$ and $90 - \frac{\theta_v}{2}$, respectively. Using these angles in the sine rule allows the length AB to be calculated as

$$AB = \cos\left(\frac{\theta_v}{2}\right)\left[\sin\left(\frac{\theta_v}{2} - (\phi - \psi)\right)\right]^{-1} j_{ref}. \tag{4.3}$$

However, since there are multiple unknown quantities in this equation, a further expression for AB is required to be able to determine the value of ϕ. By writing the angle DAB, where D defines the vertical midpoint in the image frame, as

$$DAB = \phi - \psi, \tag{4.4}$$

and the length DB as

$$DB = \frac{N}{2} - j_{ref}, \tag{4.5}$$

the length AB can also be written as

$$AB = \frac{\frac{N}{2} - n}{\sin(\phi - \psi)}, \tag{4.6}$$

and rearranged to be

$$AB = \frac{N - 2n}{2\sin(\phi - \psi)}. \tag{4.7}$$

Equations 4.3 and 4.7 can now be set equal to each other as

$$\cos\left(\frac{\theta_v}{2}\right)\left[\sin\left(\frac{\theta_v}{2} - (\phi - \psi)\right)\right]^{-1} j_{ref} = \frac{N - 2n}{2\sin(\phi - \psi)}, \tag{4.8}$$

which can be rearranged to determine ϕ

$$\phi = \tan^{-1}\left(\frac{z_{ref} - z_{cam}}{d}\right) + \tan^{-1}\left(1 - \frac{2j_{ref}}{N}\tan\left(\frac{\theta_v}{2}\right)\right). \tag{4.9}$$

Geometrical Calibration

I can then use the estimated field of views and camera inclination to calibrate the visible videos with a geometrical calibration. The calibration used here is based on that of Bombrun et al. (2018) and assumes that the points of interest, i.e., features in the plume, are in a vertical plane perpendicular to the line of sight of the camera (see Figure 4.5) called the image plane. As with calculating θ_h, the plane is placed at a distance from the camera (l) where it crosses the volcanic vent (i.e., where the points of interest are located). A right-hand coordinate system is defined such that the x direction is horizontal in the image plane, the y is the direction is along the camera orientation and the z direction is vertical.

For a given pixel at pixel height j, the height of a point of interest with respect to the camera ($\delta z(j)$) is given as

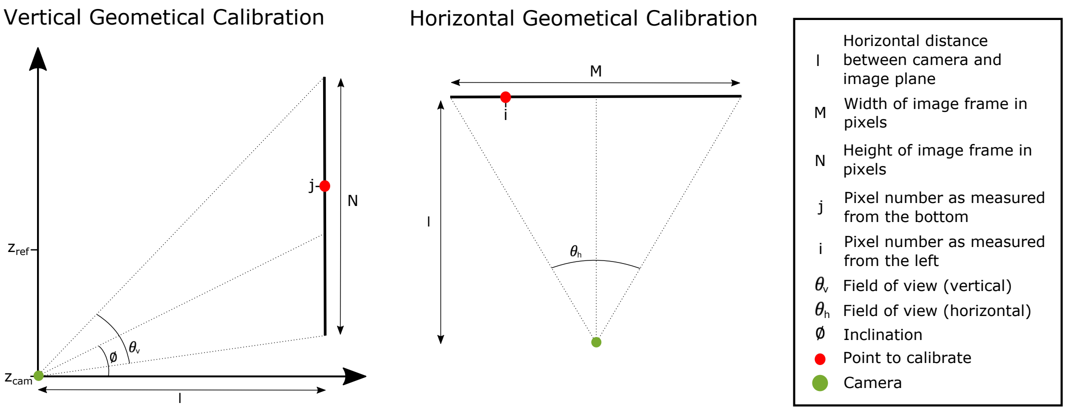

Fig. 4.5 Diagram defining the length scales and angles used to apply the geometrical calibration.

$$\delta z(j) = \frac{l}{2}\left[\tan\left(\phi - \frac{\theta_v}{2} + (j-1)\delta\theta_v\right) + \tan\left(\phi - \frac{\theta_v}{2} + j\delta\theta_v\right)\right], \tag{4.10}$$

where $\delta\theta_v = \theta_v/N$ is the angle subtended in the vertical direction by an individual pixel. The height z_c of the point of interest above sea level can then be calculated as

$$z_c(j) = z_{cam} + \delta z(j), \tag{4.11}$$

where z_{cam} is the height of the camera.

A similar procedure can be applied to perform the calibration in the horizontal direction. In this case, the horizontal location δx of pixel i with respect to the camera is given by

$$\delta x(i) = \frac{l}{2}\left[\tan\left(-\frac{\theta_h}{2} + (i-1)\delta\theta_h\right) + \tan\left(-\frac{\theta_h}{2} + i\delta\theta_h\right)\right], \tag{4.12}$$

where $\delta\theta_h = \theta_h/M$ is the angle subtended by an individual pixel in the horizontal direction. If δx is known for the pixel that contains the vent, the horizontal distance b between the vent and the point of interest can then be calculated as

$$b = |\delta x - \delta x_v|, \tag{4.13}$$

where δx_v is the horizontal position of the pixel containing the vent with respect to the camera.

Adjustment for wind

Finally, an adjustment has to be made to a calibrated point to correct for the effect of wind. For instance, if the wind direction is towards the camera, the point of interest would be closer to the camera compared to the corresponding point on the image plane. This is because a weak plume would be bending into the direction of the wind. Therefore, the plume would be located in a plane parallel to the wind direction rather than in a plane perpendicular to the camera orientation and a correction is required for the calibration when a plume is weak. This correction is only applied to plumes that are weak, as determined by reports in the literature and visual observations of the shape of the eruption column. This is because even if a plume is strong (i.e., the eruption column is vertical), there will always be some wind present. As a result, if the wind correction was applied, it would wrongly adjust calibrated points of interest to be not in the original image plane. Therefore, the correction is only applied to bent plumes.

The correction is made by defining a new plane that passes through the vent and is parallel to the orientation of the average wind direction above the vent. The exact calculation for the correction to the calibration is dependent on two things: the relative alignment of the wind direction and the camera orientation, and the location of the point of interest with respect to the vent.

In the following, I demonstrate how to determine the wind correction for the case that the point of interest is to the left of the vent (from the camera's perspective), and the wind is directed towards the upper left quadrant of x, y plane of the right-handed coordinate system defined above (i.e., where the camera orientation determines the positive y direction) (see Figure 4.6). An entirely analogous derivation can be performed for cases where the point of interest is to the right of the vent and/or the wind is directed elsewhere. First P1 is defined as the calibrated point of interest on the image plane and the angle $\alpha = i\delta\theta_h$ is defined as its horizontal angular position. P1 is then projected onto the new plane that is parallel to the wind direction to define P2. The points P1, P2 and the volcanic vent form a triangle that is shown in more detail in Figure 4.6b. The horizontal distance (h) between P1 and P2 can now be calculated using the sine rule

$$\frac{h}{\sin(\lambda)} = \frac{b}{\sin\left(90 - \frac{\theta_h}{2} + \alpha - \lambda\right)}, \tag{4.14}$$

where λ is the acute angle between the image and wind-oriented planes. Thus, h can be written as

$$h = \frac{b\sin(\lambda)}{\sin\left(90 - \frac{\theta_h}{2} + \alpha - \lambda\right)}. \tag{4.15}$$

By expanding the denominator using the angle addition formula, this can be rewritten as

$$h = \frac{b\sin(\lambda)}{\sin(90)\cos\left(\alpha - \frac{\theta_h}{2} - \lambda\right) + \cos(90)\cos\left(\alpha - \frac{\theta_h}{2} - \lambda\right)}, \tag{4.16}$$

and since $\sin(90) = 1$ and $\cos(90) = 0$,

$$h = \frac{b\sin(\lambda)}{\cos\left(\alpha - \frac{\theta_h}{2} - \lambda\right)}. \tag{4.17}$$

Once h has been calculated, the wind-correction in the x and y directions, Δ_x and Δy, respectively, can be determined with Pythagoras's theorem. First the acute angle that is defined by the intersection of the line P1-P2 with the original image plane is calculated as $180 - \left(90 + \frac{\theta_h}{2} - \alpha\right) = 90 - \frac{\theta_h}{2} + \alpha$. Then Δx and Δy can be defined as

$$\Delta x = h\cos\left(90 - \frac{\theta_h}{2} + \alpha\right), \tag{4.18}$$

and

$$\Delta y = h\sin\left(90 - \frac{\theta_h}{2} + \alpha\right). \tag{4.19}$$

Again, using the angle addition formulae, these can then both be rewritten as

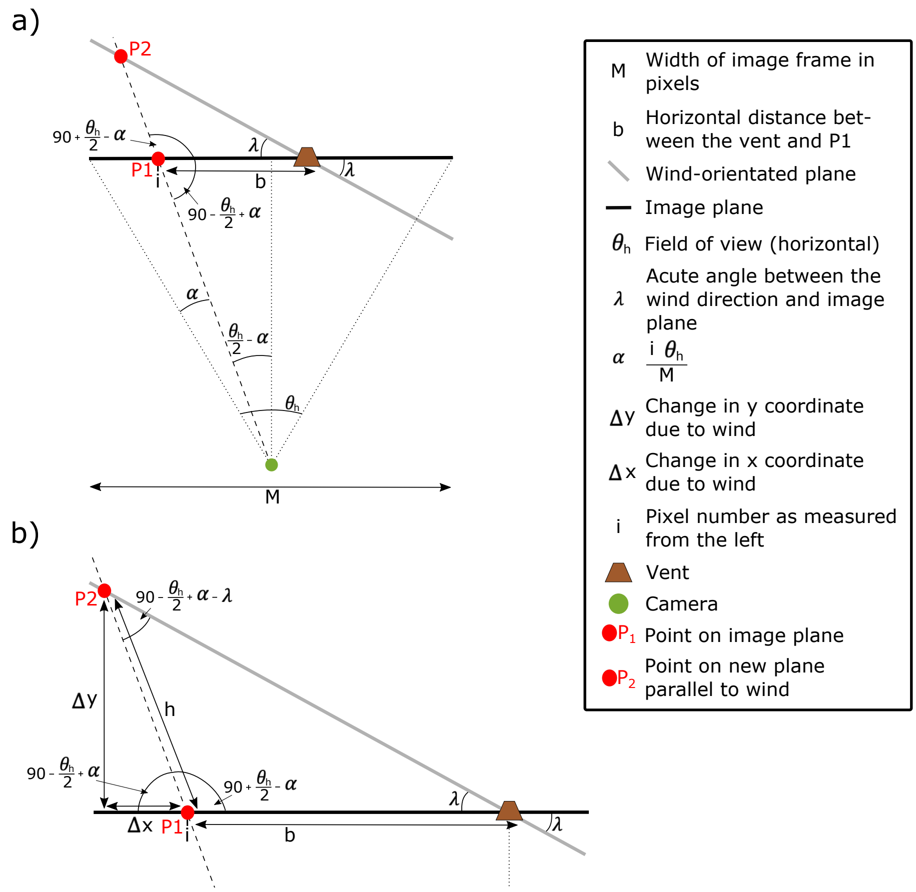

Fig. 4.6 Diagram defining the length scales and angles used to apply the wind correction to determine the horizontal change in position. a) shows the whole region of interest and b) shows a zoom in of the upper left region of a).

$$\Delta x = h\left[\cos(90)\cos\left(\alpha - \frac{\theta_h}{2}\right) - \sin(90)\sin\left(\alpha - \frac{\theta_h}{2}\right)\right], \tag{4.20}$$

and

$$\Delta y = h\left[\sin(90)\cos\left(\alpha - \frac{\theta_h}{2}\right) - \cos(90)\sin\left(\alpha - \frac{\theta_h}{2}\right)\right]. \tag{4.21}$$

These can then be simplified to

$$\Delta x = -h\sin\left(\frac{\theta_h}{2} - \alpha\right), \tag{4.22}$$

and

$$\Delta y = h\cos\left(\frac{\theta_h}{2} - \alpha\right). \tag{4.23}$$

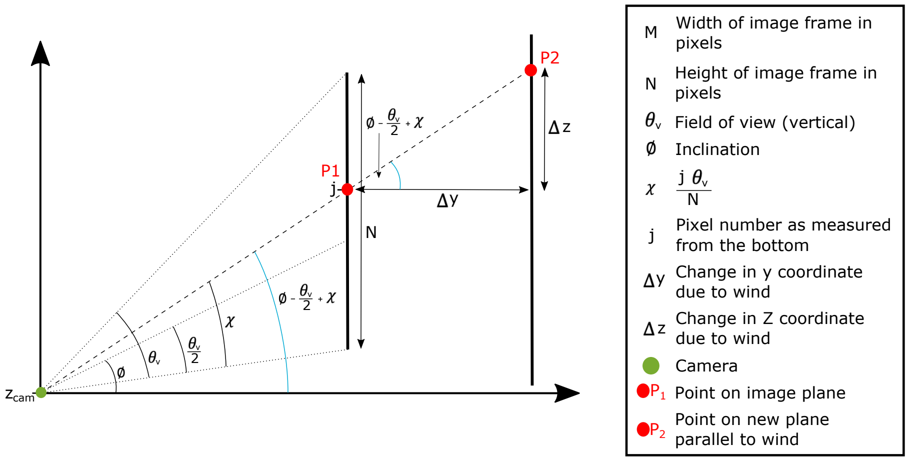

Fig. 4.7 Diagram defining the length scales and angles used to apply the wind correction to determine the vertical change in position.

To determine the vertical wind-correction Δz, the angle between the horizontal and the line connecting the camera to P1 is first defined as χ and is given by

$$\chi = \frac{j\theta_v}{N}. \tag{4.24}$$

χ, ϕ and θ_v can then be used to determine the angle defined by P1, the camera and the horizontal (Figure 4.7). This angle is the same as the angle defined by P2, P1 and the horizontal and, therefore, can be used, along with Δy, to calculate Δz

$$\Delta z = \Delta y \tan\left(\phi - \frac{\theta_v}{2} + \chi\right). \tag{4.25}$$

Although the expressions for Δx, Δy and Δz derived here are only valid for a point of interest to the left of the vent and for wind directed into the upper-left quadrant, analogous expression can be derived for all possible scenarios and are given in Table 4.4. These can then be used to calculate the height z_{cW} of the wind-corrected calibrated point above sea level as

$$z_{cW} = z_c + \Delta z. \tag{4.26}$$

These values can then be also used to determine the horizontal displacement (x_{cW}) between the corrected calibrated point and the vent. If the point of interest lies to the left of the vent, x_{cW} is given by

$$x_{cW} = -\sqrt{(b + \Delta x)^2 + \Delta y^2}. \tag{4.27}$$

Conversely, if the point of interest lies to the right of the vent, x_{cW} is defined as

$$x_{cW} = \sqrt{(b + \Delta x)^2 + \Delta y^2}. \tag{4.28}$$

Table 4.4 The equations for the correction to the geometrical calibration due to wind where λ is the acute angle between wind direction and image plane, $\alpha = i\delta\theta_h$ and $\chi = j\delta\theta_v$. The schematics in the first column show the wind direction (double ended arrow) with respect to the camera plane (solid line).

Wind direction in the image	h	P1 to the right of the vent	P1 to the left of the vent
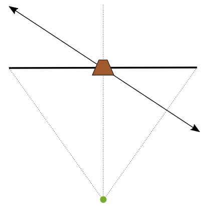	$\frac{b\sin(\lambda)}{\cos(\alpha-\frac{\theta_h}{2}-\lambda)}$	$\Delta x = h\sin\left(\frac{\theta_h}{2}-\alpha\right)$ $\Delta y = -h\cos\left(\frac{\theta_h}{2}-\alpha\right)$ $\Delta z = \Delta y\tan\left(\phi-\frac{\theta_v}{2}+\chi\right)$	$\Delta x = -h\sin\left(\frac{\theta_h}{2}-\alpha\right)$ $\Delta y = h\cos\left(\frac{\theta_h}{2}-\alpha\right)$ $\Delta z = \Delta y\tan\left(\phi-\frac{\theta_v}{2}+\chi\right)$
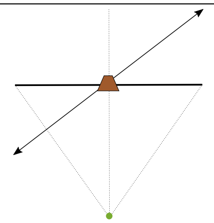	$\frac{b\sin(\lambda)}{\cos(\alpha-\frac{\theta_h}{2}+\lambda)}$	$\Delta x = -h\sin\left(\frac{\theta_h}{2}-\alpha\right)$ $\Delta y = h\cos\left(\frac{\theta_h}{2}-\alpha\right)$ $\Delta z = \Delta y\tan\left(\phi-\frac{\theta_v}{2}+\chi\right)$	$\Delta x = h\sin\left(\frac{\theta_h}{2}-\alpha\right)$ $\Delta y = -h\cos\left(\frac{\theta_h}{2}-\alpha\right)$ $\Delta z = \Delta y\tan\left(\phi-\frac{\theta_v}{2}+\chi\right)$

4.2.2 Rotation Analysis

To examine the rotation present in tephra plumes that are coupled to lava fountains at Mount Etna I quantify the frequency of the rotation. This frequency is defined as the number of rotations that occur within a given time period and I use the units of rotations per second. I use videos from the ENV and EMOH visible cameras to calculate this frequency. The frequency can then be used to calculate the Rossby number

$$Ro = \frac{u}{\pi L F}, \tag{4.29}$$

where u is the characteristic velocity, L is the characteristic length scale, and F is the frequency of the rotation. The Rossby numbers describes the ratio of inertial and Coriolis forces. Here, the Coriolis force refers to that arising from the plumes' own rotation rather than the Coriolis force that arise from the Earth's rotation (i.e., the Coriolis effect), which would only be important for plumes with large horizontal length scales. The greater the value of the Rossby number, the less significant the Coriolis force arising from the rotation. As a result, by calculating the frequency of rotation, I can make quantitative interpretations of the significance of the rotation of the tephra plumes.

The frequency is calculated from the visible videos via two approaches. The first approach involved manually tracking visible coherent structures within the plume. By measuring the time it takes for such a feature to first appear (Figure 4.8, left), move laterally across the plume due to rotation (Figure 4.8, centre), and then disappear (Figure 4.8, right), I can estimate how long it takes for the plume to complete half a rotation. The features that were manually tracked were white coherent structure that generally appeared towards the base of the plume, which I suspect to be regions of high volcanic gas (e.g., water vapour) content.

For the second approach, I also explored estimating the rotation of tephra plumes by using optical flow analysis. Optical flow is the estimation of apparent velocities between different frames of a video by which the speed and the direction of an object can be tracked. The approach of the Lukas-Kande method was used, which determines the flow parameters by splitting the image into small sections within which the local flow is assumed constant

Fig. 4.8 An example of how a coherent structure is manually tracked to determine rates of plume rotation. The coherent structure is marked (red marker) in each frame from when it first appears (left panel) until it can last be seen (right panel).

(Barron et al. 1994). The optical flow equations are then solved using a least squares fit criterion (Barron et al. 1994). This procedure was performed using the built-in optical flow functions (estimateFlow,OpticalFlowLK) in the Computer Vision Toolbox in MATLAB. The opticalFlowLK function requires a noise threshold to filter background noise. As there is no prior information as to what this value should be, due to not knowing the speed at which the plume is rotating relative to other simultaneous movements (e.g., lateral motion due to wind, vertical motion due to plume rise), several different values were explored. The speed determined from the optical flow analysis is finally converted to frequency.

4.2.3 Integrating visible video analysis with plume modelling

In this section, I present the methodology of linking visible-wavelength video analysis with a standard integral model to maximise the information that can be inferred about tephra plumes coupled to lava fountains. I first present results analysing the shape of strong volcanic plumes, defined as plumes which visibly appear as vertical and are not significantly bent due to wind, to determine the radial entrainment coefficient - a key parameter in integral plume models that determines the rate of entrainment into a buoyant plume (see Chapter 1.2.1). I then investigate weak-intermediate plumes, defined as plumes which are bent due to wind, by presenting results directly linking observations from the video analysis with a standard integral model, i.e., that of Degruyter and Bonadonna (2012). This is done by using the observed plume shape to constrain Monte Carlo simulations to infer plume characteristics that include the ESPs, the top plume height and the coefficient that governs the link between entrainment due to wind and the plume velocity.

Calculation of the Radial Entrainment Coefficient

Radial entrainment coefficients are determined from the visible-wavelength videos for two eruptions. These eruptions are the 29th of August 2011 and the 18th of March 2012, which occurred from 03:50 UTC to 04:53 UTC and 07:46 UTC to 09:50 UTC, respectively (Freret-Lorgeril et al. 2018). These eruptions were chosen because they are characterised by a strong eruption column, i.e., the volcanic plume itself is not bent, and the plume was visible (e.g., not covered by cloud coverage, occurred during daylight). This allows for the rate of radial entrainment into the plume to be constrained and excludes the influence on entrainment from the wind.

To determine entrainment coefficients of the eruptions that I analyse, I first create a series of time-averaged images for the sustained part of the eruption. The sustained part of the eruption is determined by plotting a plume height time-series from the videos of the eruption of interest. This is done automatically in MATLAB by first subtracting the red channel from the blue channel, and then detecting the highest height in the frame where 10 vertically connected pixels all have a pixel value of below 0.2. If the automatic plume top height detection fails, e.g., due to high levels of background cloud, the top plume height is determined by manually selecting the top plume height in the image frame. The region of the eruption where the plume is sustained, i.e., where the top plume height is more or less constant, can then be identified and selected to be the period of the eruption that will be used for further analysis. But for both of the eruptions analysed in this section, the plume goes out of the frame of the ECV camera as the plume rises above the vertical view of the ECV camera. As a result, I assume that this part of the eruption is the part which is ’sustained’. Only the sustained part of the eruption is selected as the standard integral model assumes that a plume is sustained.

A series of time-averaged images are then created, starting from the moment that the eruption is classed as sustained according to the above definition. Time-averaged images are necessary because the standard integral model assumes that the turbulent eddy turnover timescale is less than the timescale of plume rise (Morton et al. 1956). As a result, time-averaging is required to remove turbulent fluctuations in plume shape that the model is unable to resolve. The result of the time-averaging is an image of the eruption over a timescale that is longer than the eddy turnover timescale. To determine the minimum window over which time-averaging is necessary for each eruption, I first generated different time-averaged images at the start of the sustained period using different time windows ranging from 30 seconds to 14 minutes. These images are converted to grey-scale and stored as matrices σ_n, where n is the number of time-averaged frames. By then evaluating $\max(\sigma_n - \sigma_{n-1})$ as a function of n, one can identify the value of n at which convergence is achieved. This value of n is then used throughout the eruption. This procedure allows for a set of time-averaged images to be created that start when the eruption becomes sustained to when the eruption stops or is no longer sustained.

Points demarking the plume margin in the time-averaged images are then manually selected using ImageJ (Schindelin et al. 2012). The number of points used depend on the eruption but are placed frequently enough on the plume margin to cover any changes in it. Because of the time-averaging, the plume margin boundaries are not sharply defined. Therefore, the uncertainty associated with this is accounted for by delimiting the position of the margin and obtaining results with both the minimum and maximum possible extents for the plume margin. This is done for both the left- and right-hand plume margins. However, it is sometimes the case that one margin of the plume is obscured due to more tephra fallout on one side or lighting conditions, e.g., if the eruption occurred during sunrise. This is more often than not the case for the right plume margin as, generally, the wind at Mount Etna is towards the right of the field of view.

Before the entrainment coefficients can be calculated for the observed plume margins, a geometrical conversion needs to be applied to enable comparison with the standard integral model. The manually selected plume margins are those of the visibly-observed plume margin. However, the standard integral model assumes that the properties of a plume exhibit a top-hat profile. As a result, the visibly-observed plume margin has to be converted to a top-hat plume margin. To do this, I follow the same procedure as Patrick (2007) who converted a visibly-observed radius (r) to a Gaussian radius (R) using

$$R = 0.5r. \tag{4.30}$$

This conversion was based on observations of the velocity of a volcanic plume (Sparks and Wilson 1982). R can then be converted to a top-hat radius (b) using

$$b = \sqrt{2}R, \tag{4.31}$$

as stated in Turner (1979). This results in the conversion of r to b of

$$b = 0.71r, \tag{4.32}$$

which I use to convert the visibly-observed plume margins to a top-hat plume margin.

These top-hat plume margins can now be used to calculate the radial entrainment coefficient (ψ). To do this, I first fit a straight line through each of the plume margins. The gradient of this line, db/dz represents the spreading rate of the buoyant plume and can be related to ψ as

$$\frac{db}{dz} = \frac{6}{5}\psi, \tag{4.33}$$

for steady plumes (Morton et al. 1956). By rearranging equation 4.33, ψ can be calculated as

$$\psi = \frac{5}{6}\frac{db}{dz}. \tag{4.34}$$

This is done for both the left and right, minimum and maximum selected plume margins.

Constraining an integral model with the plume shape

In this part of the analysis, the use of the observed plume shape to help constrain a standard integral model is investigated. Here, multiple eruptions are investigated. These are the 4th of March 2012, the 12th of April 2012, the 12th of April 2013 and the 23rd of November of 2013. All of these eruptions produced a weak tephra plume (Scollo et al. 2019). I choose to only investigate weak plumes in this section as one of the key parameters of interest is the wind entrainment coefficient. To do this analysis, the videos that are used are those from the ECV camera (Table 4.1) as this camera allows for the maximum vertical view of the eruptions column and thus enables the best constraints to be placed on the overall plume shape.

As for the case of strong plumes, images of the observed plume have to be time-averaged to be able to compare the shape of an observed plume with that of the standard integral model. A similar procedure to that presented earlier is therefore followed. First, the time period where the plume is sustained is defined as the time interval where the plume height is more or less constant (i.e., the mass injection timescale is greater than that of the plume rise timescale). However, when the plume is weak, the fluctuations in the observed maximum plume height are greater compared to those of strong plumes as discussed in the previous sub-section. This is due to the highest part of the plume leaving the field of view. A series of time-averaged images are then created, starting from the beginning of the identified time region where the plume is sustained. Determining the time window required for time-averaging follows an identical procedure to that described above for the analysis of the radial entrainment coefficients. However, due to the large fluctuations in the top plume height, the upper and lower plume margins are not as sharply defined as for the strong plume case, even after time-averaging.

The plume shape is then extracted for each of the time-averaged images. To account for the uncertainty from the time-averaging (i.e., the lack of sharply defined plume margins), the top and bottom limits of the region where the plume margin appears to lie is selected for both the upper and lower plume margin. This is done for three points along the plume at fixed points along the width of the image (as shown on Figure 4.9). These points are selected manually with ImageJ (Schindelin et al. 2012). While attempts were made, it was not possible to automate the identification of the plume margin region. This was due to multiple factors that include difficulties with distinguishing meteorological clouds from the plume, the varying contrast between the background of the image and the plume (e.g., during sunrise and sunset), and variation of the colour of the plume with height due to condensation of the water phase in the plume. The uncertainties on each

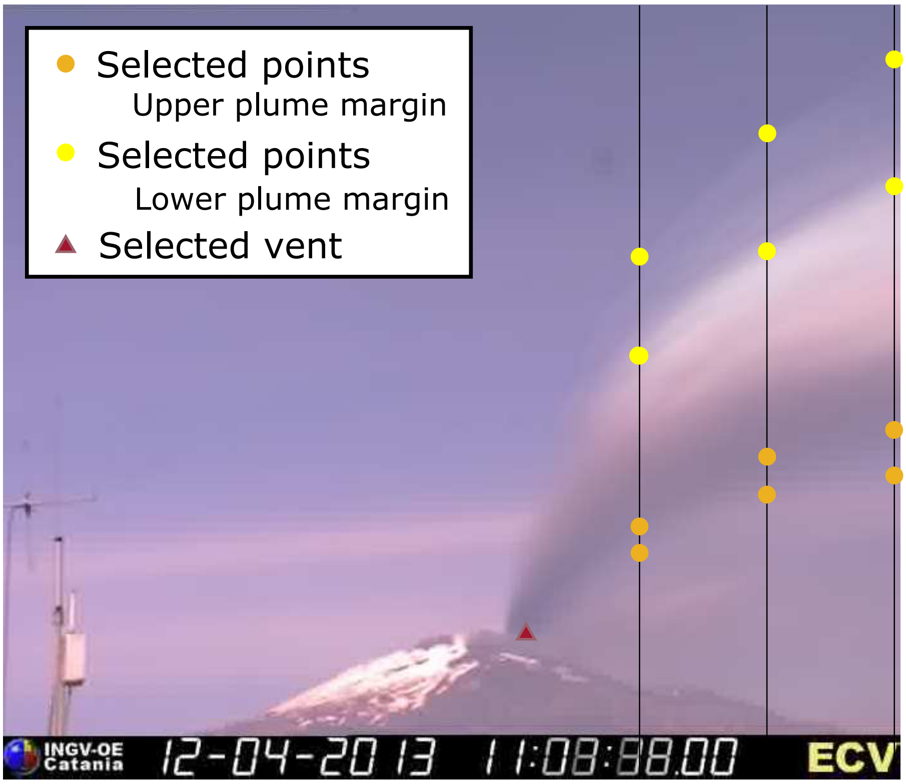

Fig. 4.9 An example of the points selected from an image to define the shape of a time-averaged plume. This example is of the 12th of April 2012 eruption.

of the selected points are also determined. This uncertainty is potentially from three different sources; using only the average wind direction in the wind-corrected calibration, the pixel resolution and the range of potential values of θ_h (Figure 4.10). The maximum and minimum possible vertical and horizontal of each selected point is taken to be the maximum and minimum vertical and horizontal uncertainty. From these uncertainties, a rectangular region can be defined around each point. This procedure allows for an estimate of the shape of the plume that can be used to compare with the modelled plume.

The extracted plume shape is then used to constrain a Monte Carlo simulation of the standard integral model. For each model run in the Monte Carlo simulation, the initial source conditions are varied (see Table 4.5). The modelled plume margin then has to be converted to be comparable to the observed visible-wavelength plume margin. To do this, the modelled plume radius is converted from a top-hat radius to a visible radius by using equation 4.32. The resulting modelled upper and lower plume margins are then checked to see if they match the observed upper and lower plume margins. This

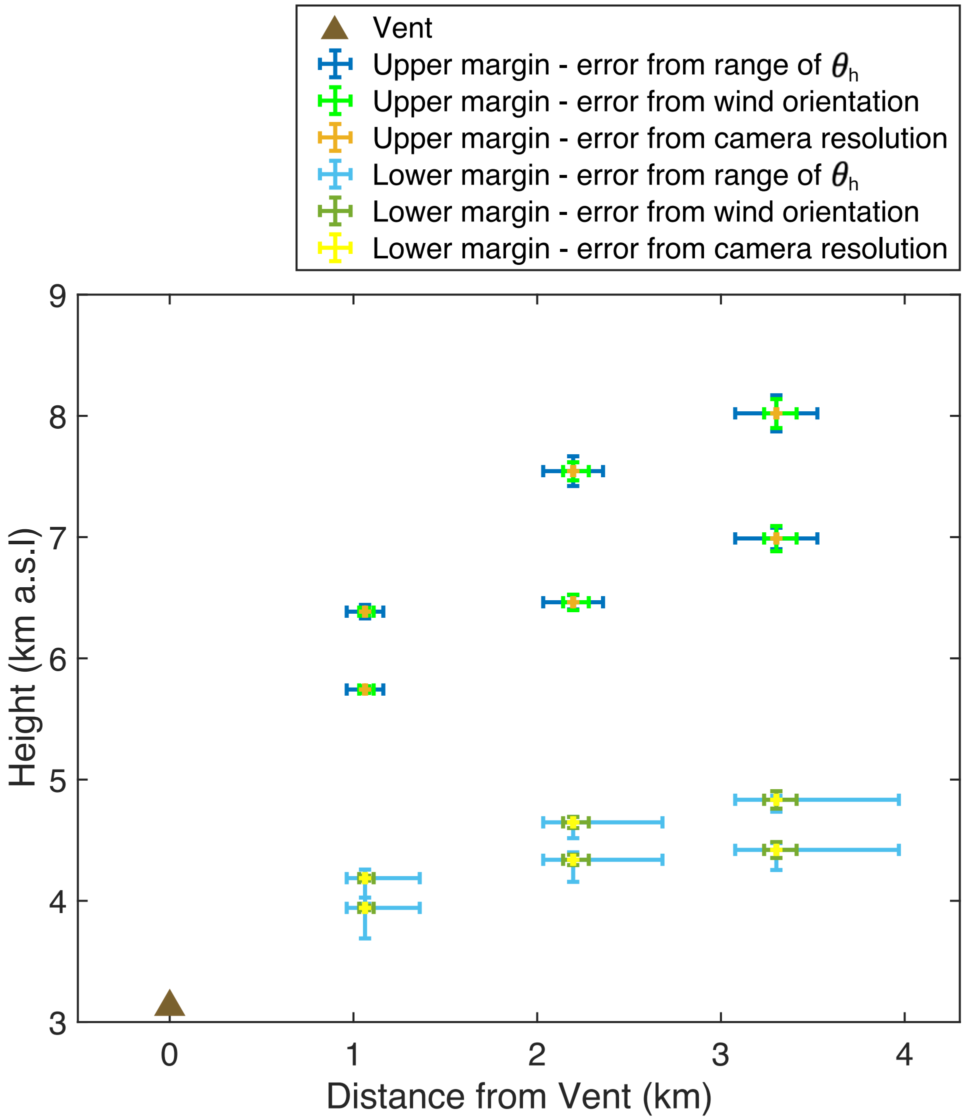

Fig. 4.10 An example of the errors associated with the selected points from three sources; the uncertainty form the field of view, the camera resolution and from the wind orientation used in the wind-correction calibration. This example is of the 12th of April 2012 eruption.

Table 4.5 The ESPs for Monte Carlo simulations using the single plume model used to calculate the wind entrainment coefficient. [1] 10^7 was used for the eruption of the 23rd of November 2013 as initial model runs showed the matches between the model and the observations were possible at the top end of the explored parameter space.

ESP	Standard Integral Model
Total MFR (kg s^{-1})	10^2 - 10^6 or 10^7 [1]
Temperature (K)	900 - 1500
Velocity (m s^{-1})	50 - 200
Gas mass fraction	0.01 - 0.05

check is done by comparing the modelled upper and lower plume margin to the observed upper and lower plume region at the each of the three points where the observed plume margin measurements were made. For each of the points, the modelled plume margin is checked to see if it lies within the rectangle that is defined by the minimum height and minimum distance from vent of the bottom bound of the plume margin, and the maximum height and maximum distance from vent of the top bound of the plume margin. If the modelled margin passes through all of these rectangles, or just enters the last rectangle at the edge of the image, the simulation is recorded as a match. The initial ESPs, value of the wind entrainment coefficient and the top height of the matched modelled plumes are recorded and are presented in Section 4.3.3.

4.3 Results

In this section, I first qualitatively describe observations of the dynamics of the tephra plumes and the source environment that I observe from the EMOV and EMOH cameras (Section 4.3.1). I then go on to describe, qualitatively and quantitatively, the rotation observed in these plumes (Section 4.3.2). Finally, I present results from the coupling of the video observations with plume modelling (Section 4.3.3).

4.3.1 Qualitative Descriptions

The videos from the EMOH and EMOV cameras allow for the physical relationship between the lava fountain and the tephra plume to be examined.

Fig. 4.11 Images of the proximal region of paroxysmal eruptions. a) and b) show the tephra plume surrounding the lava fountain on the 29th of August 2011 during the night, so the lava fountain can be seen, and during the day, respectively. c) shows the tephra plume to the right of the lava fountain during the 12th of April 2012 eruption and d) also shows the tephra plume to the right of the lava fountain during the 12th of April 2013 eruption.

From these videos it is clear to see that the spatial relationship is not the same for all eruptions. In many eruptions, the tephra plume surrounds the entire lava fountain. This is the case for many of the eruptions as shown in Figures 4.11a and b for the 29th of August 2011, where at sunrise (Figure 4.11a) the lava fountain is seen in the centre of the tephra plume and, during the day (Figure 4.11b), only the tephra plume can be seen. However, for other eruptions, such as the 12th of April 2012, the tephra plume is mainly on downwind side of the lava fountain (Figures 4.11c and d). In both cases, the tephra plume is present from the base of the lava fountain, rather than originating solely from the margins of the lava fountain.

Sedimentation from the margins of the tephra plumes can be seen with the naked eye in the videos from the EMOV and EMOH cameras. Details of which eruptions show sedimentation from the tephra plumes can be found in Table 4.6. The tephra fallout appears as streaks, i.e., material appears to be concentrated in bands, as can be seen in Figure 4.12. These streaks are observed on the downwind side of the tephra plume. In some cases, the lower portion of the streak appears to join up with the rising tephra plume. In the videos, the streak fallout is present at all the heights seen by the EMOV and EMOH cameras, even in the region where the tephra plume and lava fountain co-exist.

Table 4.6 Summary table of the eruptions examined and the presence of the analysed features in each eruption. The shaded regions refer to the eruptions no observations where made.

Eruption Date	Observed Features			Linking to standard integral model	
	Sedimentation	Rotation	Entrainment from ground	Via calculation of radial entrainment coefficient	Via plume shape
10/04/2011	x				
09/07/2011					
25/07/2011	x				
12/08/2011	x		x		
20/08/2011	x				
29/08/2011		x	x	x	
08/09/2011			x		
08/10/2011					
15/11/2011			x		
05/01/2012			x		
09/02/2012					
04/03/2012		x	x		x
18/03/2012	x			x	
10/04/2012					
12/04/2012	x		x		x
28/02/2013	x				
03/04/2013	x				
12/04/2013	x				x
18/04/2013					
20/04/2013					
27/04/2013	x				
26/10/2013	x	x	x		
23/11/2013	x	x			x

Sedimentation from the lava fountain can also be clearly seen in the videos from the EMOV and EMOH cameras. Fallout from the lava fountain is characterised as individual large clasts, which appear red during the night. Due to the low resolution of the video imagery, the finer material, if present, cannot be seen. Unlike the sedimentation from the tephra plume, the rate of fallout from the lava fountain is not continuous. Instead, the amount of fallout pulsates, with fallout of larger material seeming to correlate with pulses of lava fountaining that goes higher. This fallout can be seen to occur simultaneously with the fallout from the tephra plume, such as during the eruption of the 26th of October 2013 eruption (Figure 4.12). It also occurs on both the upwind and downwind side of the lava fountain.

Another interesting feature that was observed was the entrainment of material other than air into the tephra plumes. During eight eruptions (see Table 4.6 for further details), white gas from the surrounding region (i.e., areas in the image other than the vent) can be seen being incorporated into the rising tephra plume (Figure 4.13). In addition, brown clouds, which are assumed to be composed of tephra, can also be seen to be swept into the tephra plume. I suspect the source of this material could be from loose material on the ground of the area around the vent. But I expect that the impact of this process is likely to not play a major role on the dynamics of tephra plumes coupled to lava fountain as it is volumetrically insignificant compared to the volume of the tephra plume.

4.3.2 Rotation

Visual Description

Rotation of the tephra plume is observed during the paroxysmal eruptions of the 29th of August 2011, 4th of March of 2012, and the 26th of October 2013 as shown in Figure 4.14. It is potentially also present, as the rotation appears very weak, in the 23rd of November 2013 eruption. The rotation appears to be the clearest on the 26th of October 2013. For this event, the rotation is observed for the majority of the climax of the paroxysmal eruption. Conversely, for the 4th of March 2012, it is only observed for a period of a few minutes when a white gas-rich pulse occurs next to the main lava fountain. Moreover, the direction of rotation is not constant. On the 29th of August 2011, the 4th of March 2012 and, potentially, the 23rd of November

Fig. 4.12 Selection of video frames from the EMOV camera, that show examples of particle fallout as streaks from the tephra plumes that are coupled to lava fountains. Example are from the eruptions of the 18th of March 2012 (top left) and the 26th of October 2013 (top right, bottom left and bottom right).

Fig. 4.13 Selection of video frames from the EMOV and EMOH cameras, that show examples of entrainment of ground material into coupled lava-fountains - tephra plumes (highlighted in the white boxes). Examples are from the eruptions of the 8th of August 2011 (top left), the 15th of November 2011 (top right), the 4th of March 2012 (bottom left) and the 26th of October 2013 (bottom right).

Fig. 4.14 Selection of video frames from the EMOV and EMOH cameras, that show the rotation of tephra plumes that are coupled to lava fountains. Black arrows denote the inferred direction of rotation. Images are from the eruptions of the 29th of August 2011 (left), the 4th of March 2012 (middle) and the 26th of October 2013 (right).

2013, the rotation of the plume is in an anti-clockwise direction when looking upwards from the camera position. In contrast, the direction of rotation of the tephra plume from the 26th of October eruption is clockwise. In all cases, the rotation is present from the base of the tephra plume. It is also worth noting that at greater heights in the tephra plume, as the turbulent eddies expand, the frequency of rotation appears to decrease, likely a consequence of angular momentum conservation. To better describe these observations, a more quantitative approach is required.

Frequency of Rotation and Rossby Number

To be able to better examine the impact of rotation on plume rise, I examine the calculated frequency of rotation for the eruptions of the 4th of March 2012 and the 26th of October 2013. It was not possible to carry out the same procedure for the 29th of August 2011 as the eruption occurred during sunrise, which made it difficult to distinguish coherent structures in the plume. I also do not quantify rotation for the 23rd of November 2013 eruption due to the uncertainty on the presence of any rotation. The range of calculated frequencies from the manual tracking method can be seen in Table 4.7.

Table 4.7 Extracted data from the manual analysis of the rotation of the tephra plumes. Each tracked structure is given a marker and the times at which the structure appears and disappears are noted.

Eruption	Camera	Marker	Marker 1st seen	Marker last seen	Full rotation duration (s)	Frequency (s^{-1})
26th Oct 2011	ENV	1	07:54:20	07:54:36	32 ± 0.5	0.0313 (0.0308-0.0317)
		2	07:57:36	07:57:58	44 ± 0.5	0.0227 (0.0225-0.0230)
		3	07:58:38	07:58:56	36 ± 0.5	0.0278 (0.0274-0.0282)
	EMOH	4	07:46:48	07:47:03	30 ± 0.5	0.0333 (0.0328-0.0339)
		5	07:47:42	07:47:55	26 ± 0.5	0.0385 (0.0377-0.0392)
		6	07:49:34	07:49:52	36 ± 0.5	0.0278 (0.0274-0.0282)
		7	07:52:06	07:52:25	38 ± 0.5	0.0263 (0.0260-0.0267)
		8	07:54:49	07:55:07	36 ± 0.5	0.0278 (0.0274-0.0274)
		9	07:57:34	07:57:51	34 ± 0.5	0.0294 (0.0290-0.0299)
		10	08:03:39	08:03:57	36 ± 0.5	0.0278 (0.0274-0.0282)
		11	08:06:51	08:07:12	42 ± 0.5	0.0238 (0.0235-0.0241)
		12	08:07:32	08:07:50	36 ± 0.5	0.0278 (0.0274-0.0282)
		13	08:08:37	08:08:59	44 ± 0.5	0.0227 (0.0225-0.0230)
		14	08:13:59	08:14:10	22 ± 0.5	0.0455 (0.0444-0.0465)
		15	08:19:53	08:20:14	42 ± 0.5	0.0238 (0.0235-0.0241)
		16	08:27:25	08:27:26	22 ± 0.5	0.0455 (0.0444-0.0465)
		17	08:29:49	08:29:58	18 ± 0.5	0.0556 (0.0541-0.0571)
4th March 2012	EMOV	18	07:53:26	07:53:47	42 ± 0.5	0.0238 (0.0235-0.0241))
		19	07:53:38	07:53:49	24 ± 0.5	0.417 (0.0408-0.426)

The range of calculated frequencies from manual tracking vary between 0.0227 and 0.0556 s^{-1}. I do not present results from the optical flow analysis as a very large range of values were determined. I hypothesise that the larger range from the optical flow analysis could be reflecting the sensitivity to the noise threshold parameter, while the greater values could be due to the optical flow analysis also detecting the plume's lateral motion due to wind. As it seems that it is difficult to isolate just the rotation from the optical flow analysis, I decide not to pursue or present these results any further and use the frequency estimates from the manual tracking going forward.

In order to calculate the Rossby number, it is necessary to define values for the characteristic velocity and length scales of the plume. For the length-scale, I take the visible horizontal distance travelled by the tracked coherent structure from when it first appeared until it was last seen. For the velocity, I divide the vertical distance the structure travelled by the time taken. I apply this procedure only to frequency estimates determined from the EMOV camera. The measured plume widths and vertical velocities, along with the calculated Rossby numbers can be found in Table 4.8. The velocity estimates range from 0.74 to 34.67 m s^{-1}, and the calculated widths range from 141.15 to 389.23. However, the minimum recorded velocity of 0.74 m s^{-1} appears to be an outlier and, when excluding this data point, the average vertical velocity is 21.53 m s^{-1}. When using these values for the characteristic velocity and length scale, the Rossby numbers associated with these plumes range from 0.04 to 2.32 (when once again excluding the previously mentioned outlier).

Table 4.8 Table showing the extracted data from the manual analysis of the rotation of the tephra plumes. Values reported inside the brackets are the minimum and maximum values based on uncertainty. The values outside the brackets are the average. [1] Velocity from radar range from Freret-Lorgeril et al. (2018) and [2] velocity range from exit velocity estimations from Calvari et al. (2011), Bonaccorso et al. (2014), Carbone et al. (2015), and Vulpiani et al. (2016).

Marker Number	Measured Width (m)	Measured Vertical U ($m\ s^{-1}$)	Radar U[1] (av - max) ($m\ s^{-1}$)	Exit U[2] (min - max) ($m\ s^{-1}$)	Rossby Number		
					(Measured U)	(Radar U)	(Exit U)
4	295.92 (270.44 - 321.44)	13.29 (12.35 - 14.27)	- 341	- 341	0.43 (0.36 - 0.51)	(- 12.24)	(0.96 - 9.26)
5	332.86 (307.55 - 358.22)	34.67 (32.59 - 36.83)			0.86 (0.74 - 1.01)	(- 9.35)	(0.75 - 7.08)
6	289.03 (262.51 - 315.58)	24.73 (23.27 - 26.24)			0.98 (0.83 - 1.16)	(- 15.09)	(1.18 - 11.42)
7	389.23 (368.80 - 409.70)	27.09 (25.80 - 28.43)			0.84 (0.75 - 0.94)	(- 11.33)	(0.96 - 8.57)
8	361.31 (338.03 - 384.62)	23.41 (22.23 - 24.63)			0.74 (0.65 - 0.85)	(- 11.72)	(0.97 - 8.87)
9	276.41 (251.09 - 301.75)	18.47 (17.70 - 19.26)			0.72 (0.63 - 0.84)	(- 14.91)	(1.17 - 11.28)
10	303.44 (277.74 - 329.17)	21.70 (20.81 - 22.62)			0.82 (0.71 - 0.95)	(- 14.26)	(1.13 - 10.79)
11	316.98 (293.75 - 340.24)	18.30 (17.23 - 19.40)			0.77 (0.67 - 0.89)	(- 15.70)	(1.28 - 11.88)
12	273.79 (248.13 - 299.49)	25.02 (23.94 - 26.14)			1.05 (0.90 - 1.22)	(- 15.97)	(1.25 - 12.08)
13	266.11 (241.07 - 291.17)	24.38 (23.36 - 25.42)			1.28 (1.11 - 1.49)	(- 20.04)	(1.57 - 15.16)
14	185.47 (158.21 - 212.75)	19.61 (18.15 - 21.13)			0.74 (0.58 - 0.96)	(- 15.44)	(1.06 - 11.68)
15	177.85 (151.22 - 204.50)	30.90 (29.44 - 32.39)			2.32 (1.90 - 2.90)	(- 30.51)	(2.13 - 23.08)
16	148.30 (121.28 - 175.35)	32.96 (30.98 - 35.03)			1.56 (1.21 - 2.07)	(- 20.14)	(1.29 - 15.24)
17	141.15 (113.08 - 169.24)	24.44 (23.09 - 25.88)			0.99 (0.76 - 1.35)	(- 17.76)	(1.09 - 13.44)
18	275.70 (271.46 - 279.95)	0.74 (0.64 - 0.84)	180 - 432	33 - 258	0.04 (0.03 - 0.04)	8.73 (- 21.53)	(1.56 - 12.86)
19	224.12 (220.15 - 228.09)	4.72 (4.43 - 5.03)			0.16 (0.15 - 0.18)	6.14 (- 15.30)	(1.08 - 9.14)

It is important to note that the vertical velocity of a feature on the margin of a plume may not be representative of the characteristic velocity of the plume. Therefore, I alternatively explore using vertical velocity estimates from radar, as well as exit velocities determined from lava fountain heights, as the characteristic velocity of the plume. Doppler radar has recorded the velocity of Etna plumes in the region above the vent (1.2km a.v.l) (Freret-Lorgeril et al. 2018). I therefore use the maximum and, if available, the average velocity estimates from Freret-Lorgeril et al. (2018) as the characteristic velocities. Further to this, I also examine the use of the exit velocity derived from the lava fountain heights using the ballistic formula. Exit velocities from this method vary from 33 to 258 s^{-1} (Calvari et al. 2011; Bonaccorso et al. 2014; Carbone et al. 2015; Vulpiani et al. 2016). As a result, I use a velocity range of 33 and 258 m s^{-1} that represents both end members of the exit velocity reported in the literature as the characteristic velocity in the Rossby number calculations. The resulting Rossby numbers, using velocity estimates derived from both radar and lava fountain height measurements, are given in Table 4.8 along with the corresponding velocities. I use the same characteristic length scale (i.e., the width of the plume at the height of the coherent feature) as in the previous paragraph. The Rossby numbers from both of these approaches are generally much higher than those calculated with the vertical velocity of the coherent features, except those calculated with the low-end member exit velocity of 33 m s^{-1}. These values are more comparable to the Rossby numbers calculated with the velocity estimates of the coherent features.

4.3.3 Visible video analysis and plume modelling

Calculation of the radial entrainment coefficients

Radial entrainment coefficients have been calculated from the videos of two of the eruptions (29th of August 2011 and 18th of March 2012) that were examined. Based on the methodology presented in Section 4.2.3, the sustained parts of these eruptions were identified as lasting from 04:18:38 UTC to 04:50:00 UTC, and 08:31:18 UTC to 09:36:36 UTC for the 29th of August 2011 and 18th of March 2012, respectively (Figure 4.15). These times represent the time at which the whole top region of the plume is no longer in frame. Similarly, the number of frames required to produce a sufficient time-averaged image were 270 frames and 210 frames (9 and 7 minutes)

a) 29th August 2011

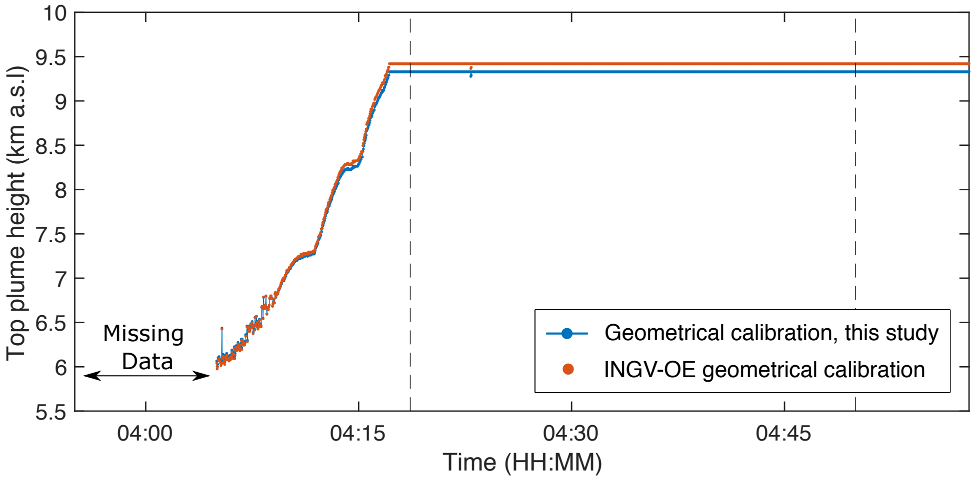

b) 18th March 2012

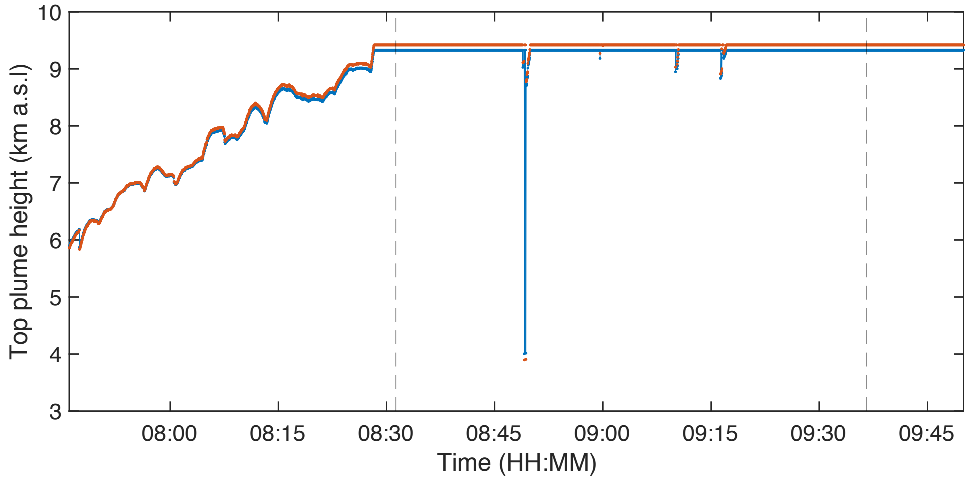

Fig. 4.15 Plume height times-series for the eruptions used to calculate the radial entrainment coefficient. The dashed lines the mark the beginning and the end of the time range used in the radial entrainment coefficient analysis.

for the 29th of August 2011 and 18th of March 2012, respectively (Figure 4.16). These both lead to 3 time-averaged images for the 29th of August 2011 eruption and 9 time-averaged images for 18th of March 2012 eruption from which the radial entrainment coefficients are calculated.

The range of the calculated radial entrainment coefficients for each eruption, and for each camera, are shown as error bars on Figure 4.17. The calculated radial entrainment coefficients range in value between 0.02and 0.18. As a result, the majority of the calculated radial entrainment coefficients lie within the range reported in the literature (Morton et al. 1956; Woods 1988; Suzuki and Koyaguchi 2010; Devenish et al. 2010b; Aubry et al. 2017), which is

a) 29th August 2011

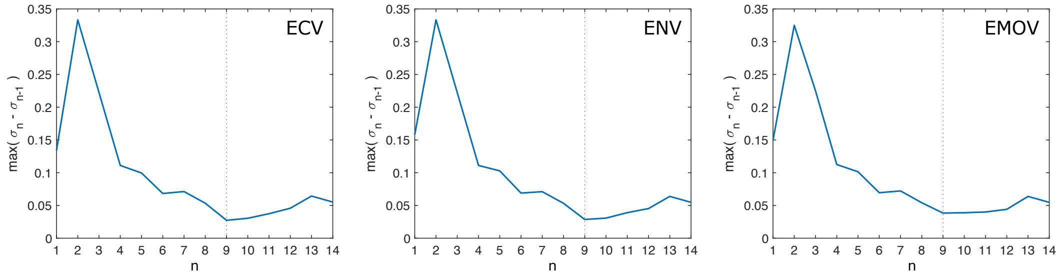

b) 18th March 2012

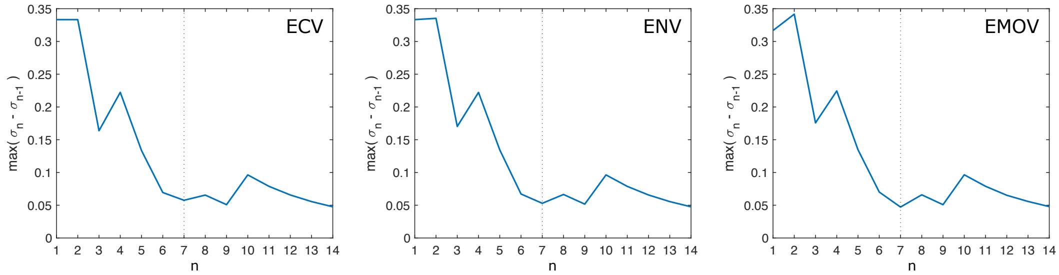

Fig. 4.16 Cumulative plots used to determine the number of frames required for the time-averaging for the eruptions analysed to calculate the radial entrainment coefficient. The dotted lines mark the number of frames that were selected.

indicated by the dashed lines in Figure 4.17. Moreover, the average calculated radial entrainment coefficient (0.1) determined from the ECV and ENV cameras from both eruptions is the same as the commonly used value of 0.1 (Morton et al. 1956; Woods 1988; Degruyter and Bonadonna 2012; Devenish et al. 2010b).

Variation does exist between the calculated radial entrainment coefficients measured using different cameras. As Figure 4.17 shows, the radial entrainment coefficients calculated from the EMOV videos, where the average of both eruption is 0.06, are lower than those calculated from the ECV or the ENV cameras (average value of 0.1). The EMOV camera is much closer to the vent than ECV or ENV, and therefore, as the maximum height seen by the EMOV camera is ∼1km a.v.l, the proportion of the plume that is seen is only that which co-exists with the lava fountain. However, the average radial entrainment coefficients determined from the EMOV camera still lie within the range of values reported in the literature.

Coupling of an integral model with plume shape measurements

To examine the use of the observed plume shape to constrain standard integral models, I focus on the eruptions of the 4th of March 2012, 12th of

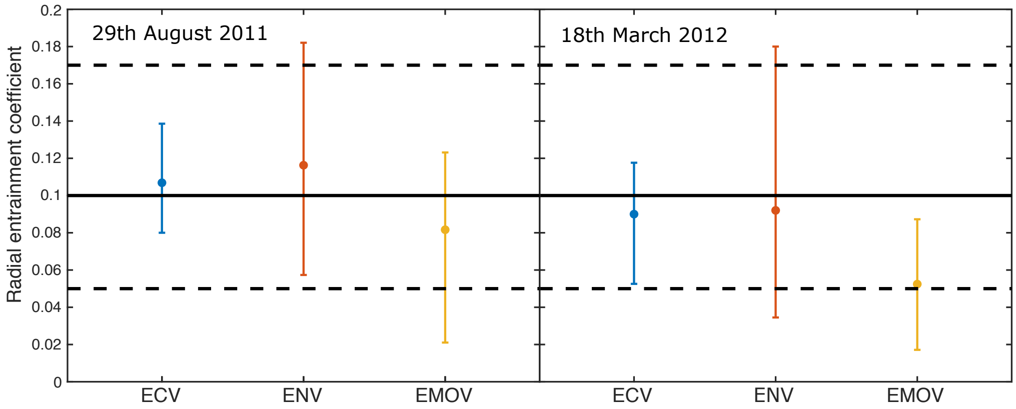

Fig. 4.17 The calculated radial entrainment coefficients for the two eruptions analysed. The dashed lines mark the minimum and maximum radial entrainment coefficients reported in the literature (Morton et al. 1956; Woods 1988; Suzuki and Koyaguchi 2010; Devenish et al. 2010b; Aubry et al. 2017), and the solid line marks the commonly used value of 0.1 of the radial entrainment coefficients (Morton et al. 1956; Woods 1988; Degruyter and Bonadonna 2012; Devenish 2016).

April 2012 and the 12th of April 2013 and the 23rd of November 2013. These eruptions were chosen as they are all weak plumes and are not obscured by cloud. Using the method presented in Section 4.2.3, I identified the sustained part of these eruptions as occurring between 07:57:12 UTC and 08:59:38 UTC, 14:33:00 UTC and 15:13:30, 11:02:22 UTC and 11:59:12 UTC, and 09:56:44 UTC and 10:26:48 UTC for the 4th of March 2012, the 12th of April 2012, the 12th of April 2013, and the 23rd of November 2013, respectively (Figure 4.18). The number of frames used to create the time-averaged images are 330, 210, 210 and 330 frames for the eruptions of the 4th of March 2012, 12th of April 2012, 12th of April 2013 and 23rd of November 2013, respectively (Figure 4.19). 210 frames correspond to 7 minutes and 330 correspond to 11 minutes. This resulted in 5, 5, 8 and 1 time-averaged images for the eruptions of the 4th of March 2012, 12th of April 2012, 12th of April 2013 and 23rd of November 2013, respectively, which are used in the subsequent results.

First, I present results on the calculated wind entrainment coefficients. Figure 4.20 shows the range and average best fit values from the Monte Carlo modelling, that is constrained by the observed plume shape, for the examined eruptions. Considering all eruptions, the range of the calculated wind entrainment coefficient is 0.1- 0.4, and the average is 0.23. These calculated wind entrainment coefficients are very similar between the different analysed

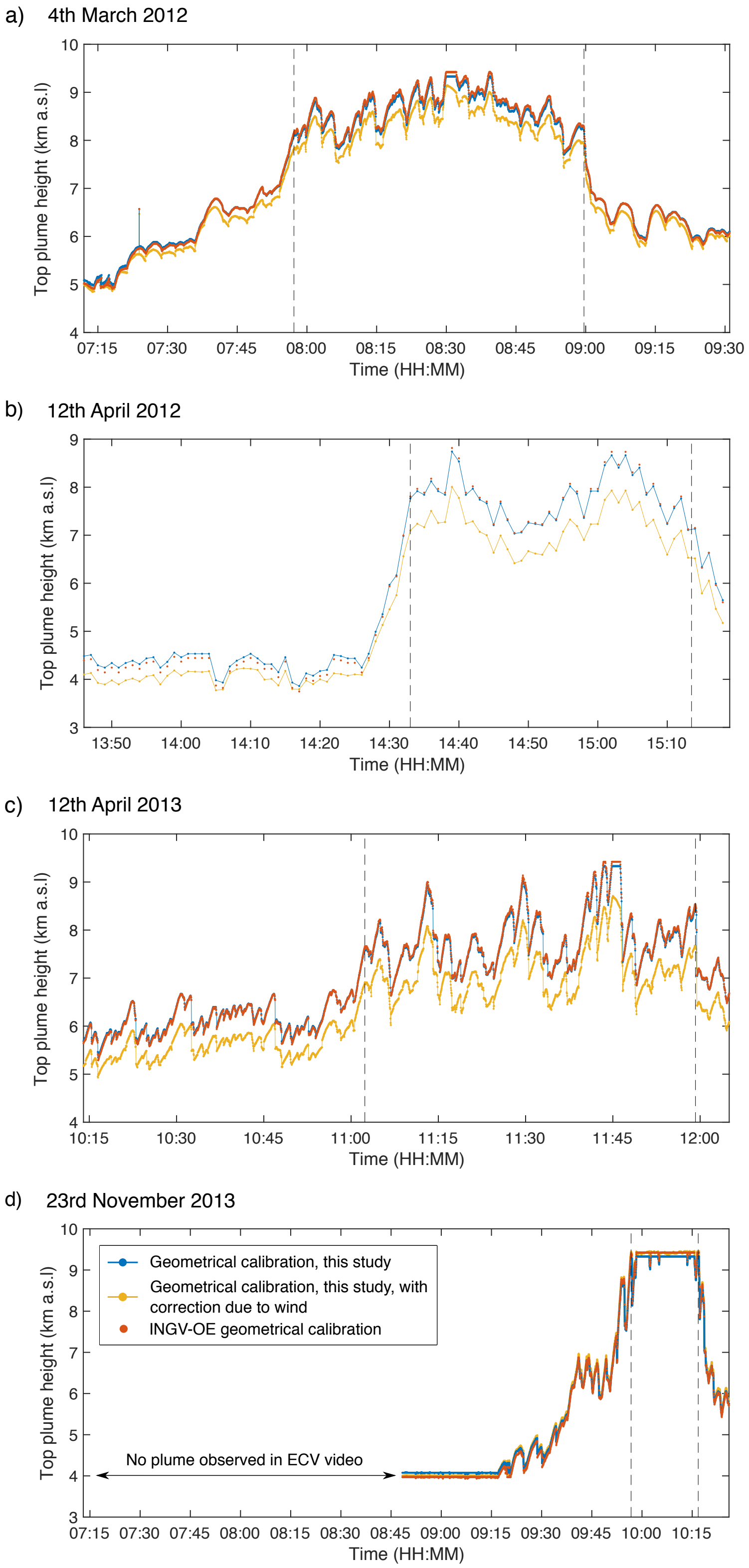

Fig. 4.18 Plume height times-series for the eruptions used in the plume shape analysis using the standard integral model, where the dashed lines the mark the beginning and the end of the time range used.

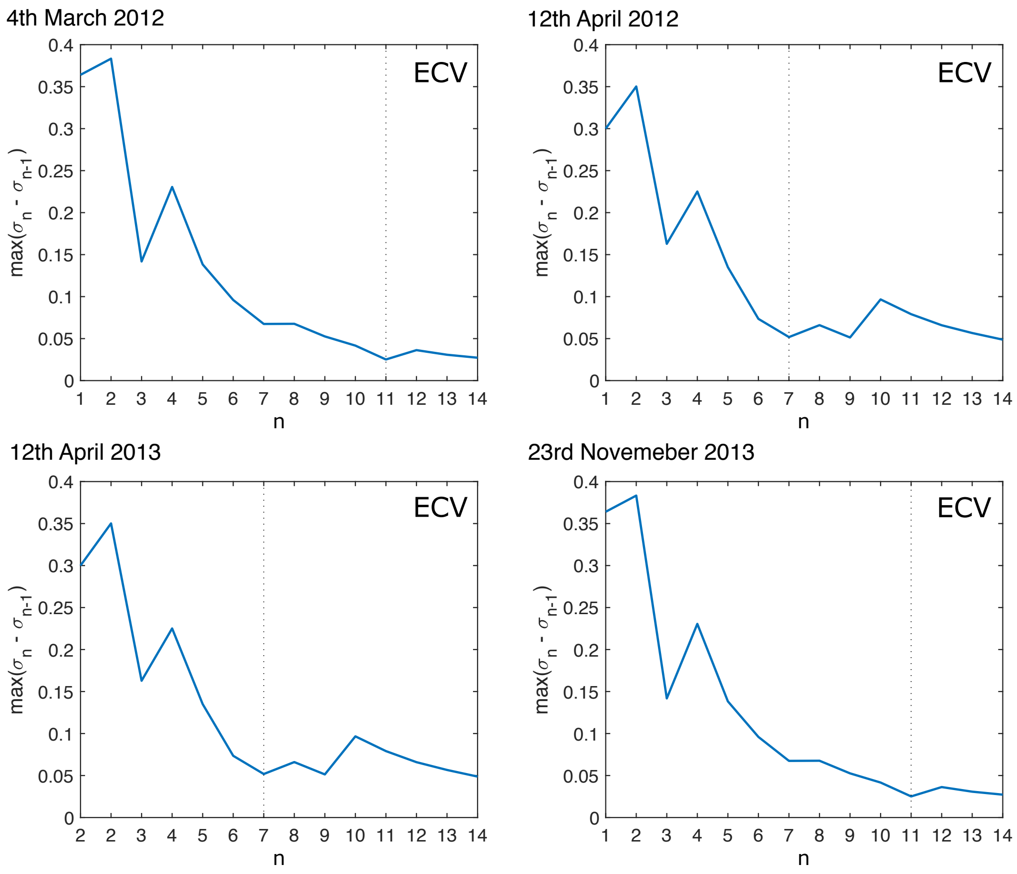

Fig. 4.19 Cumulative plots used to determine the number of frames required for the time-averaging for the eruptions analysed to be able to compare model simulations to plume shape observations. The dotted lines mark the number of frames that were selected.

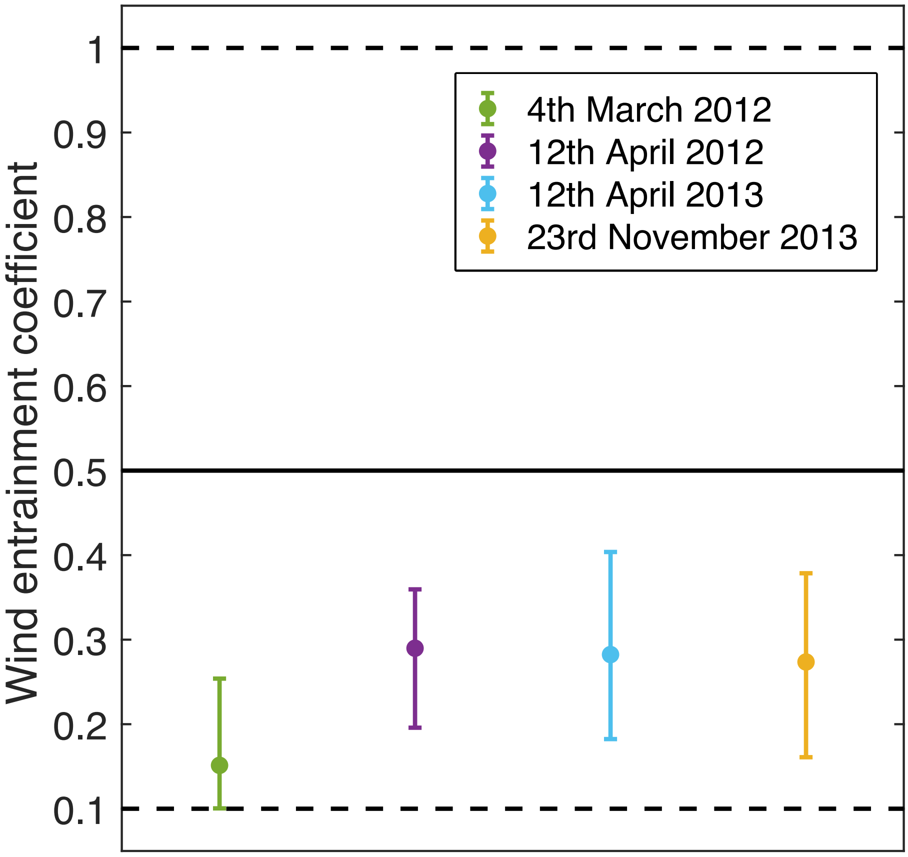

Fig. 4.20 The calculated wind entrainment coefficients for the eruptions analysed. Values are reported as the average from every model run of every analysed time-averaged image. The error bars signify the minimum and maximum. The dashed lines mark the minimum and maximum wind entrainment coefficients reported in the literature (Hewett et al. 1971; Devenish et al. 2010b; Suzuki and Koyaguchi 2015; Aubry et al. 2017; Michaud-Dubuy et al. 2020), and the solid line marks the commonly used value of 0.5 for the wind entrainment coefficient (Devenish et al. 2010b; Degruyter and Bonadonna 2012; Aubry et al. 2017; Michaud-Dubuy et al. 2020).

eruptions. However, their values lie in the lower end of the range reported in the literature and below the often used value of 0.5 (solid line, Figure 4.20). For the 12th of April 2012 eruption, it is worth noting that very few matches were achieved between the modelled plume margins and the observed plume margins and, as a result, caution is required when examining the model results for this eruption. However, the obtained values are consistent with the range of wind entrainment coefficient from the other examined eruptions.

Secondly, I compare the results of Monte Carlo model simulations of the examined case-studies when the simulations are constrained by the observed plume height from the ECV camera with the case when the simulations are constrained by the plume shape. To do this, I start by comparing the range of modelled top plume heights produced by matched simulations in the Monte Carlo. For the 4th of March 2012 eruption, the range obtained from the two approaches is very similar (Figure 4.21a). One difference is that, for the 3rd time-averaged frame analysed, the maximum modelled plume height when the simulations are constrained by the plume shape is slightly higher than that when the simulations are constrained only by the maximum observed plume height. The same can be seen for the eruption of the 12th of April 2013 (Figure 4.21c). Although the maximum plume height from the Monte Carlo simulations constrained with top height in the ECV video, from the Monte Carlo simulations constrained with the plume shape and from satellite measurements (green lines, end panel, Figure 4.21c) are all broadly in agreement for this eruption. However, for the eruption of the 23rd of November 2013 (Figure 4.21d), the maximum modelled plume height from when the Monte Carlo simulations are constrained by the plume shape is much higher than when the Monte Carlo simulations are constrained by the maximum observed plume height in the ECV video but is similar to the top plume height determine by satellite (green lines (Corradini et al. 2018)).

Another key feature is that for some time-averaged images, the range of maximum modelled plume height from when the Monte Carlo simulations are constrained with the plume shape is narrower than when the range from the Monte Carlo simulations constrained by the maximum observed plume height. Examples of this include the eruptions of the 12th of April 2013 and the 12th of April 2012. But, once again, it is worth noting that caution is needed when examining the results of the 2nd and 3rd time-averaged image of the 12th of April 2012 because very few matches were achieved in the Monte Carlo simulations that are constrained by plume shape.

These results for the modelled maximum plume heights are reflected in the source parameters that resulted in these matches. In the cases where the maximum plume height from the Monte Carlo simulation constrained with plume shape are similar to those when the Monte Carlo simulation are constrained with the maximum observed plume height in the image frame, the range of matching MFRs from these two cases are similar (e.g.,

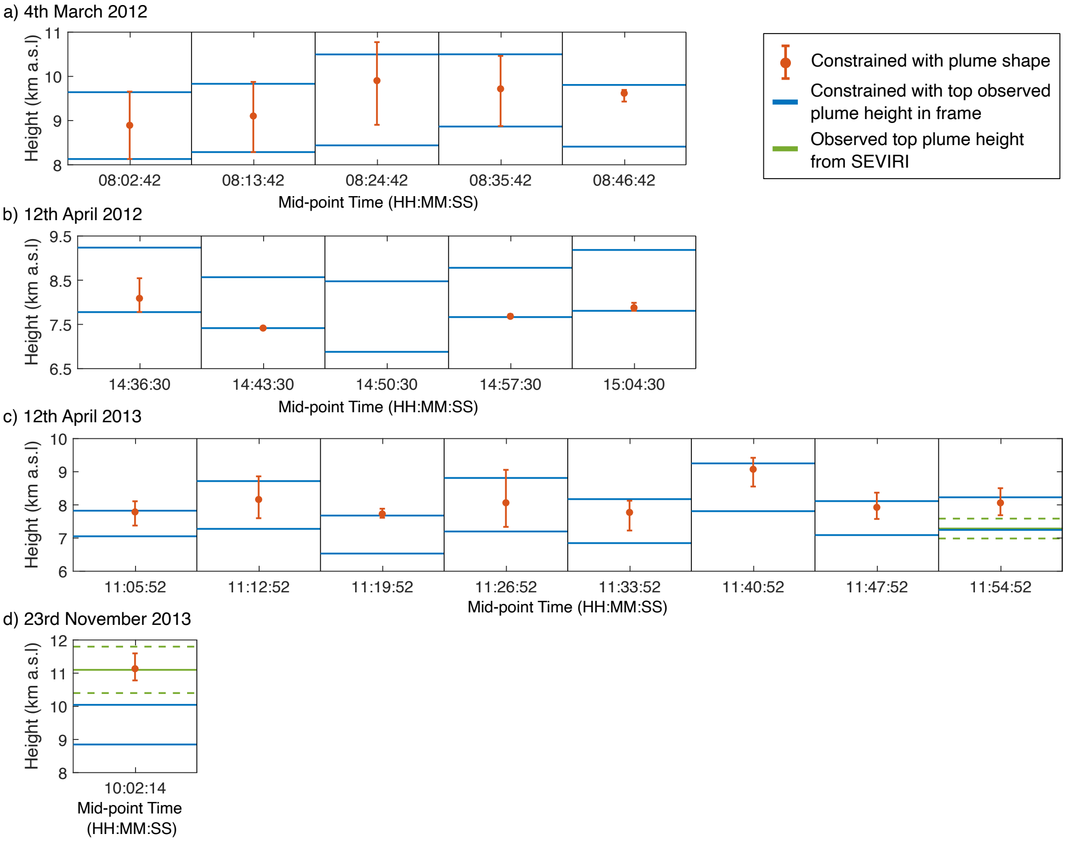

Fig. 4.21 Comparison of the maximum modelled plume heights for Monte Carlo simulations that are constrained by the plume shape (red error bars) versus when constrained by the maximum observed plume height for each time-averaged frame from the ECV videos of the four examined eruptions (a) 4th of March 2012, b) 12th of April 2012, c) 12th of April 2013 and d) 23rd of November 2013). The solid green lines refer to the maximum plume height determined from the SEVIRI satellite reported in the literature, and the dashed green lines mark the uncertainty on this measurement. Data sources: 12th April 2013, Scollo et al. (2019), 23rd November 2013, Corradini et al. (2018).

4th of March 2012, Figure 4.22a). However, if the plume shape is used to constrain the Monte Carlo simulation, the best-fit initial modelled MFRs are generally more constrained. This is shown by the narrower range of the initial modelled MFRs from the Monte Carlo simulations that are constrained by the plume shape (red error bars) compared the those constrained by the maximum observed plume height (blue error bars) in Figure 4.22. This is particularly evident in Figure 4.22d for the eruption of the 23rd of November 2013 and correlates with the fact the biggest discrepancy in the maximum modelled plume height between the two ways to constrain the Monte Carlo simulations (Figure 4.21d).

It is also worth stating that neither constraining the Monte Carlo simulations with plume shape or the maximum observed plume height helps to constrain the other ESPs (velocity, temperature, gas mass fraction). This is not unexpected as the parameter range that is explored in the Monte Carlo modelling is large and the modelled plume height is not very sensitive to these parameters (Woodhouse et al. 2015; Woodhouse et al. 2016).

4.4 Discussion

In this discussion, I first discuss points related to the different processes that have been observed and analysed in this Chapter. This includes the origin of the lava fountain, sedimentation, rotation and both the wind and radial entrainment coefficients. I then review the use of plume shape to constrain integral plumes models of real eruptions, before finally discussing the usefulness of visible video analysis to study volcanic processes that occur during the rise of coupled tephra plumes - lava fountains.

4.4.1 Discussion of the individual features

Origin of the tephra plumes that are coupled to lava fountains

One uncertainty surrounding tephra plumes that are coupled to lava fountains is their height of origin. Previously, Glaze et al. (2017) assumed that the tephra plume originated from 2/3 of the height of the lava fountain due to dynamic separation (i.e., fine tephra and gas separate from the remaining coarse material of the lava fountain) based on images of the Pùù o ō Hawaii 1984 eruption. Others (Vulpiani et al. 2016) have assumed that the lava foun-

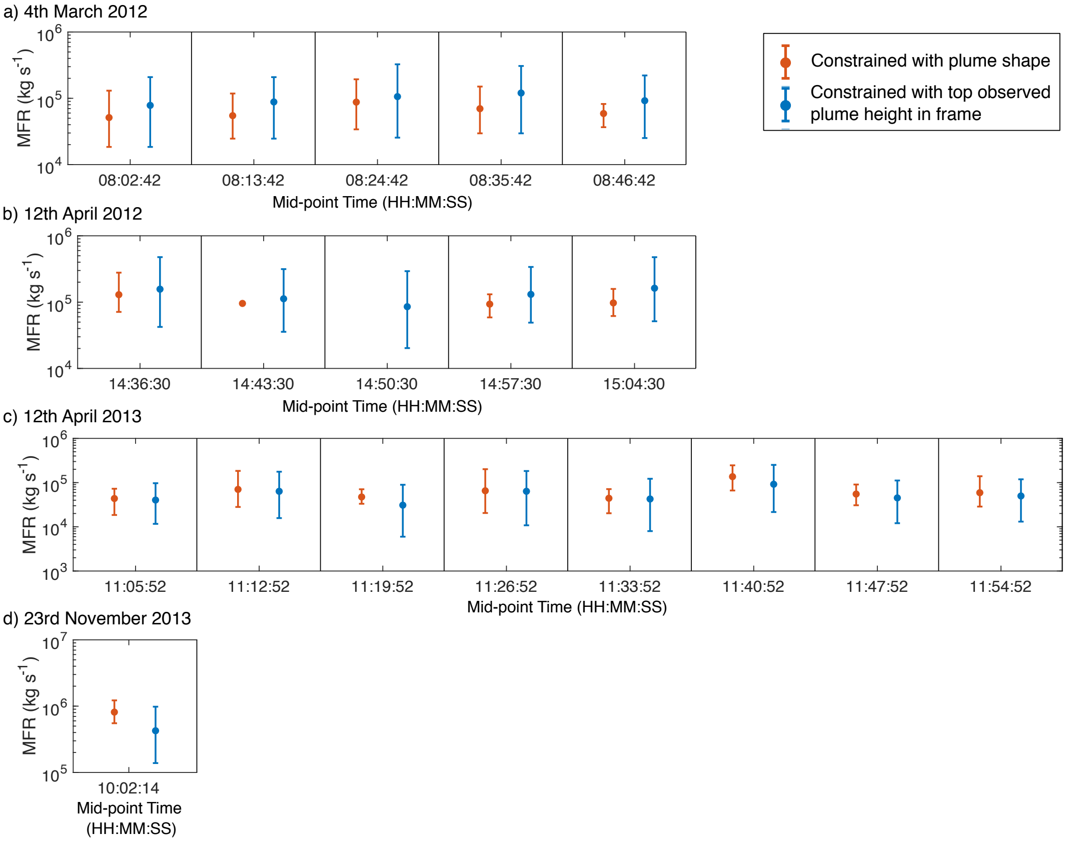

Fig. 4.22 Comparison of the initial MFR from the Monte Carlo simulations that are constrained by the plume shape and from when constrained by the maximum observed plume height for each time-averaged frame of the four examined eruptions (a) 4th of March 2012, b) 12th of April 2012, c) 12th of April 2013 and d) 23rd of November 2013).

tain is the gas-thrust region of the tephra plume, which has already been shown to not be valid in Chapter 2. In this Chapter, specifically Section 4.3.1, I have identified that the tephra plume is always present from the base of the lava fountain for paroxysmal eruptions of Mount Etna. This suggests that at least some component of the tephra plume originates from the conduit and, therefore, some fragmentation must be occurring in the conduit to generate this initial plume material. As some tephra plumes can be seen to surround the whole lava fountain, I hypothesise that the fragmentation resulting in some of the finer material of the initial tephra plume is occurring around the margins of the conduit, potentially due to the increased friction here between the magma and the conduit walls (Gonnermann and Manga 2003). Additionally, when the wind is high, this resulting tephra plume is affected by the wind and results in it appearing to be on only one side of the lava fountain.

Sedimentation from coupled tephra plumes - lava fountains

Despite the fact that no quantitative information on the sedimentation from the coupled tephra plumes - lava fountains could be extracted due to the low resolution of the visible videos, it is possible to obtain a qualitative insight into the dynamics of the sedimentation. Sedimentation from the tephra plume can be seen to be sometimes occurring as concentrated bands rather than as individual clasts. These bands have been referred to as fingers in the literature and impact the expected rate of sedimentation (Carazzo and Jellinek 2012; Manzella et al. 2015; Scollo et al. 2017; Freret-Lorgeril et al. 2020; Fries et al. 2021). The mechanism for their formation is likely to be different compared to those that form in the dispersing tephra clouds (Manzella et al. 2015; Scollo et al. 2017; Fries et al. 2021) as they originate from a vertical boundary between the atmosphere and the tephra plume. Instead, they could be formed from interactions between the wind and the tephra plume (Ernst 1998; Park and Park 2021). Finally, the presence of fingers on the downwind side of the tephra plume reflects the fact that the lateral motion of the sedimentation is wind-driven.

The presence of two different types of sedimentation, streak from the tephra plume and pulsating fallout of large clasts from the lava fountain, that co-exist from tephra plume - lava fountain eruptions can tell us about the relationship between the tephra plume and the lava fountain. As the lava fountain pulsates, large clasts fall to the ground rather than being entrained into the surrounding tephra plume. Although the fraction of the original material that sediments to ground rather than being entrained into the surrounding tephra plume is unknown. I also cannot conclude what happens to any finer material, defined as the material that cannot be seen in the videos due to the low resolution, of the lava fountain. The fallout of large clasts from the lava fountain indicates that this component of the lava fountain material is not coupled to the tephra plume. The impact on the reduction of the extent of coupling cannot be determined from the analysis of the visible video imagery. However, I can conclude the lava fountain and the tephra plume are not fully coupled. This has implications on the dynamics of the plume rise as with a reduction in the extent of coupling between the lava fountain and the tephra plumes, the less of a role that the lava fountain plays on contributing to the final height that the plume reaches (see Chapter 2 for further detail).

Rotation

Many plumes in different geophysical systems have been observed to rotate. Large weather systems with a central convective column are well known to rotate (Davies-Jones 1984) whilst vorticity of plumes from large oil spills in the ocean has also been noted (Fabregat Tomàs et al. 2016; Fabregat et al. 2017). Investigations into the cause of the rotation in these large-scale plumes have shown that the vorticity originates from the Earth's rotation and is due to the Coriolis effect (Deremble 2016). In a volcanic context, the spreading of large volcanic plumes from super eruptions has also been shown to be controlled by the Earth's rotation (Baines and Sparks 2005). Similary, rotation of the volcanic plume associated with the 1991 Pinatubo eruption, which was on a much smaller scale compared to the plumes previously discussed that can be affected by the rotation of the Earth, has been identified as the reason behind volcanic meso-cyclones (Chakraborty et al. 2009). Here, Chakraborty et al. (2009) argued that the rotation of the tephra plume was due to the wind, Kelvin - Helmholtz instabilities, and shearing between the atmosphere and the tephra plume. The rotating plumes that I have described in this Chapter are much smaller than those affected by the Earth's rotation and even than the rotating plume of the 1991 Pinatubo eruption. As a result, I examine the potential causes of rotation of tephra plumes that are coupled to lava fountains below.

Rotation could be intrinsic or due to the ambient conditions. From the limited eruptions that I have examined, I note that the plume rotates in a clockwise direction with respect to the camera field of view when the wind direction is to the west (26th of October 2013), and vice-versa when the wind direction is to the east (29th of August 2011 and 4th of March 2012). This suggests rotation could be due to the ambient conditions, specifically the wind field. This situation could be analogous to weather systems or volcanic meso-cyclones, where wind shear drives the rotation (Davies-Jones 1984; Chakraborty et al. 2009). However, I do not see rotation at many of the tephra plumes at Etna even when these plumes are affected by varying amounts of wind. This is further supported by the fact that rotation of the tephra plume is only seen for a limited time period in the eruption of the 4th of March 2012. As the wind behaviour is unlikely to change significantly during one eruption, wind is unlikely to be the sole cause of rotation in these tephra plumes. Another possible explanation for the rotation is that it is intrinsic to the tephra plumes. For example, the rotation could be due to the angle of ejection of the tephra plume or asymmetry of the lava fountain. An intrinsic origin is supported by the observation that the rotation is observed, and is in fact the strongest, at the base of the plume. Moreover, the rotation could be due to the interaction of multiple plumes. During the 4th of March 2012 eruption, rotation is only observed after an ejection of a more gas-rich plume from one side of the vent next to the lava fountain, therefore indicating that the rotation is linked to this phenomenon. Multiple plumes were also observed during the 26th of October 2013 eruption. In this case, the additional plume originated from the neighbouring Bocca Nuova crater (Sellitto et al. 2016; Andronico et al. 2018). This further supports the hypothesis that the rotation is caused by the complex source characteristics of tephra plumes that are coupled lava fountains, but it does not account for why the direction of rotation appears to correlate with wind direction. As a result, the cause of rotation of the tephra plumes coupled to lava fountains that I examine is unclear. Further investigation into the characteristics of rotation would be required to determine its source. Higher resolution videos would allow for a better understanding of how rotation changes with plume rise, while experimental work would enable an increased understanding of how multiple plumes interact and on how wind shear affects plume rotation.

Regardless of the source of the rotation, it is important to determine if the rotation significantly impacts plume rise. I evaluate the importance of rotation on tephra plume rise by comparing the calculated Rossby number to those of rotating plumes in the literature. Pham et al. (2006b), Pham et al. (2006a), and Pham et al. (2011) experimentally and numerically investigated the impact of rotation on the rise of thermally-driven plumes. Pham et al. (2006b) determined that below a Rossby number threshold of around 1.82, the impact of rotation on the structure of the plume was considerable. For plumes that have a Rossby number below this threshold, rotation of the plume results in an increase in mixing between the ambient and the plume. This results in a reduction of the temperature field of the plume which, in turn, dampens the buoyancy forces. An increase in mixing between the ambient and the plume can also increase the degree of entrainment into the lower region of the plume close to the heat source (Pham et al. 2006a). Rotation can also cause the plume to be wider and the greater the rotation, the greater the proportion of the plume (with height) that is affected by the rotation (Pham et al. 2006b). However, with increasing distance from the source, the characteristics of a rotating plume (e.g., structure, rate of entrainment) converge to that of a non-rotating plume (Pham et al. 2006b). These previous findings form the basis of my evaluation of the significance of rotation on the rise of the rotating tephra plumes that I examined.

I find that the Rossby numbers associated with the rotating tephra plumes of this study are generally above the threshold, as determined by Pham et al. (2006b), below which rotation has an important effect on plume rise. This indicates that rotation has little impact on the plume structure. If the calculated vertical velocities from the video analysis are considered to be the characteristic velocity, the resulting Rossby numbers can be lower than this threshold. However, as briefly mentioned in Section 4.3.2, these velocities are unlikely to be characteristic of the vertical velocity of the plumes. These velocities are the vertical component of velocity for coherent features on the margins on the plume. They do not represent the bulk upwards motion and will be much lower than than the characteristic velocity as the velocity at the margins of the plume will be much lower than the centreline velocity. Exit velocities (either from radar or estimating from the lava fountain height) were also used as the characteristic velocities. The majority of the features that I use to determine the frequency of the rotation in the plumes are within the first 1km of the vent. Hence, while the exit velocity is not the velocity at the height of the features of interest, it can be used as a good approximation for the velocity in the lower plume region, based on the examination of plume velocity profiles from radar, which agree to those from a standard integral model, as presented by Montopoli (2016). Using these velocities, the corresponding Rossby numbers are well above the threshold defined by (Pham et al. 2006b). While rotation is observed, it is therefore unlikely to affect the degree of entrainment, or the structure of the tephra plume. As a result, I conclude that while rotation of these plumes is interesting, it does not have a significant effect on the rise of the tephra plume and does not need to be considered when studying the dynamics of tephra plumes that are coupled to lava fountains.

Entrainment coefficients

As mentioned in Section 4.3.3, the calculated radial entrainment coefficients (0.02 to 0.18) are comparable with ranges reported in the literature (Morton et al. 1956; Woods 1988; Devenish et al. 2010b; Suzuki and Koyaguchi 2010; Aubry et al. 2017). The average estimated radial entrainment coefficient (0.1) of the whole plume (i.e., from the ECV and ENV cameras) for both examined eruptions is similar to the commonly used value of 0.1 (Morton et al. 1956; Woods 1988; Devenish et al. 2010b; Degruyter and Bonadonna 2012). While I did calculate lower entrainment coefficient values for lower regions of the plumes (i.e., from the EMOV camera, which sees a maximum height of $\sim$ 1km a.v.l), this is not completely unexpected as radial entrainment coefficients have been estimated to be lower in the negatively buoyant plume region (Kaminski et al. 2005; Carazzo et al. 2008a). This is because the rate of entrainment is reduced in regions of high density, such as the lower region of a volcanic plume, and it has therefore been allowed to vary depending in the Richardson number (Carazzo et al. 2008a). Richardson numbers in a volcanic plume can vary and correspond to a range of entrainment coefficients between 0 (imposed when the Richardson number is negative) and 0.17 (Carazzo et al. 2006; Girault et al. 2016). Altogether, these findings in this section of the Chapter suggest that entrainment into these plumes is similar to that of standard plumes, even for the eruption of the 29th of August 2011, which shows rotation.

The estimated wind entrainment coefficients determined in Section 4.3.3 are also comparable to values reported in the literature. In particular, the estimated ranges are comparable to the range of 0.1 to 0.3 reported by Suzuki and Koyaguchi (2015). But it is worth noting that these values are lower than the often-used value of 0.5 (Degruyter and Bonadonna 2012; Girault et al. 2014; Devenish 2016) that has recently been further supported by theoretical models (Michaud-Dubuy et al. 2020) and by comparison of integral models to observed volcanic plume trajectories (Aubry et al. 2017). It is also much lower than the higher range of wind entrainment coefficients that are used in some standard integral models (Bursik 2001; Woodhouse et al. 2013). These differences reflect the large uncertainty on the value of the wind entrainment coefficient. Future work should focus on trying to understand the reason for these difference by examining more volcanic tephra plumes to determine its value. It should also focus on trying to determine more details on the plume dynamics, such as velocity profiles of a volcanic plume and the characteristics of turbulent eddies in a windy environment, to determine if this variation is due to uncertainty or is it reflecting different conditions in different volcanic plumes. However, as the estimated value from this study lie within the reported range of 0.1 to 1 (Aubry et al. 2017) and are very similar to those reported by Suzuki and Koyaguchi (2015), it suggests that the effect on entrainment rates from wind on tephra plumes that are coupled to lava fountains are similar to standard tephra plumes as previously suggested by the calculated radial entrainment coefficients.

4.4.2 What observations to use to constrain integral plume models

When performing Monte Carlo simulations with a standard integral model of a volcanic plume, the observed maximum plume height is typically used to constrain the model (Costa et al. 2016b). However, by using visible-wavelength observations from the video network of INGV-OE at Mount Etna, I was able to relatively easily determine much more information about these plumes, such as the plume shape. This can also be used to constrain the ESPs when using a plume model. My work has attempted to determine whether using the plume shape as a constraint has any advantages over just using the maximum observed plume height. In theory, the more restrictive the constraints, the smaller the range of source conditions which would result in a match between the model and the observations. Thus, since multiple points (i.e., different heights at different distances from the vent) are being used to constrain the integral model when using the plume shape, the range of the initial conditions that lead to a match between the model and the observation should be smaller compared to using the observed maximum plume height. From the results presented in Section 4.3.3, neither using the plume shape or only the observed maximum plume height constrains the majority of the source parameters (velocity, temperature, gas mass fraction). This is because the modelled plume is not overly-sensitive to such initial parameters (Woodhouse et al. 2015; Woodhouse et al. 2016). However, using the plume shape does help to constrain the initial MFR by reducing the range for which matches are achieved (e.g., 12th of April 2013 and 23rd of November 2013, Figure 4.22c and d). And while for most of the eruptions examined, the difference in the initial MFR is minimal between the two approaches to constrain the model, for the 23rd of November 2013, using the plume shape increases the average initial MFR by 30% compared to the initial MFR from when the modelling is constrained by the maximum observed plume height in the image frame.

One advantage of using the plume shape to constrain an integral model is that the maximum plume height does not need to be known. If the maximum plume height is out of the frame of the camera, the shape of the plume could be used instead to constrain an integral model. This was the case for the 23rd of November 2013 eruption that was investigated in Section 4.3.3. The modelled maximum plume height was greater when constrained with the plume shape, and more comparable to the maximum plume height determined from previous satellite observations and modelling studies (Figure 4.21) (Andronico et al. 2015; Corradini et al. 2018). However, if the maximum plume height can be seen, e.g., 4th of March 2012 and 12th of April 2013, then using the plume shape produces a very similar modelled maximum plume height and initial MFR. Therefore, using the plume shape to constrain a plume model can be useful to better estimate the actual height a plume reached and the initial MFR of the eruption.

4.4.3 The benefits and disadvantages of Visible-wavelength Videos

In this Chapter, I have used visible-wavelength videos to study tephra plumes that are coupled to lava fountains. This has identified multiple benefits of using such sensors to study these plumes. Firstly, one big advantage is the high spatial and temporal resolution of the data. High spatial resolution allows for information on the plume shape to be extracted. This is useful data that can be coupled to a standard integral model to refine source parameters (Section 4.3.3). High temporal resolution is also a useful benefit of visible-wavelength video analysis. The videos of INGV-OE that were used in this study capture an image every 1 or 2 seconds (depending on the camera). This allows for a high-resolution plume height time-series of the eruption and the creation of time-averaged images at a much higher frequency than compared to satellite data. For example, the SEVIRI satellite, which is commonly used to examine the tephra plumes of Mount Etna (Corradini et al. 2018; Scollo et al. 2019), has a spatial resolution of $\sim 3 \times 3$ km and a temporal resolution of 10 minutes, which are both much coarser than that of the visible-wavelength videos. Therefore visible-wavelength videos allow for much more detail on the characteristics and development of tephra plumes.

Another clear advantage of visible-wavelength videos to study volcanic plumes is that they are low-cost. A visible camera is much cheaper than a thermal camera for instance (e.g., £100-£1000’s, https://www.jessops.com/videography/camcorders, compared to £1000-£10000, https://www.tester.co.uk/thermal-night-vision-optics/th ermal-cameras/scientific-research-development-thermal-cameras). Even the relatively low-resolution (spatial and temporal) visible-wavelength cameras used in this study, compared to many on the market today, can provide vital information on the characteristics, processes and even the source conditions of tephra plumes. This has led to them being a very common tool at volcano observatories (e.g., INGV, Scollo et al. (2019), Alaska volcano observatory, Cameron et al. (2018), GNS, NZ, Miller and Jolly (2014) and many more), which results in a large data set of visible-wavelength videos of volcanic eruptions around the world. As they are low cost, multiple cameras could be bought and used in conjunction together, as has been done with thermal cameras (Wood et al. 2019), to provide a 3D picture of the plume in question. The low-cost of visible-wavelength cameras compared to other remote sensors, would also allow for them to be a useful tool for those studying volcanic plumes in developing countries.

Despite the benefits of visible-wavelength videos, there are limitations and disadvantages to their use. One obvious limitation is that they can only be used when the plume can be seen (Scollo et al. 2014). This requires an eruption to occur during the day and for there to be limited cloud cloud. These requirements limit the use of visible-wavelength video analysis to study a volcanic tephra plume. In this work, this limitation reduced the number of eruptions that I could examine between 2011 - 2013 from 44 (Freret-Lorgeril et al. 2018) to 23. While more videos of eruptions would always be a benefit as they would provide more evidence of the claims made in the results of this Chapter, it was not a debilitating limitation of this study. However, this would not be the case for a volcano observatory who require information on every eruption. Therefore, visible-wavelength videos cannot be solely relied upon for real-time monitoring (Scollo et al. 2014; Scollo et al. 2019).

Visible-wavelength videos are also harder to analyse than videos from thermal cameras. This is because there are bigger contrasts in the thermal videos between different features, such as between the lava fountain and the surrounding tephra plume, and the surrounding tephra plume and the ambient. This has resulted in a number of studies that have automated the analysis of volcanic plumes and other eruptive activity from thermal videos (Valade et al. 2014; Gaudin et al. 2017; Bombrun et al. 2018). In this Chapter, I was able to have some success in automatically detecting the plume height (see Section 4.2.3 for further details), but the method failed if there was heavy cloud or clouds above the top height of the volcanic plume in the field of view. I was also unable to develop a reliable approach to automatically detect the whole plume due to the plume itself changing colour as it rises due to condensation, the contrast between the plume and the background changing at sunrise/sunset and atmospheric cloud being similar in colour to parts of the volcanic cloud. As a result, analysis of visible videos from different days and times can be a time-consuming process.

There are also difficulties when trying to compare information from visible-wavelength videos with plume models. Many assumptions are required to make such a comparison such as time-averaging and the conversion from the observed visible plume margin to a top-hat plume margin. However, there is little research (Sparks and Wilson 1982) behind the conversion from observed visible radius to a Gaussian radius. There are also large uncertainties associated with the time-averaging of the eruptions due to large fluctuation in the plume height even in the identified sustained part of the eruption. Despite this, the values that have been calculated for both the radial and wind entrainment coefficients are within the reported ranges in the literature (Morton et al. 1956; Hewett et al. 1971; Woods 1988; Devenish et al. 2010b; Suzuki and Koyaguchi 2010; Suzuki and Koyaguchi 2015; Aubry et al. 2017; Michaud-Dubuy et al. 2020). Therefore, while caution and understanding of the uncertainty should be had, overall, the coupling of visible-wavelength video analysis to integral plume models provides additional information on the tephra plumes that are hard to access with other methods making it a valuable tool in the array of instruments used to observe tephra plumes.

4.5 Conclusion

Visible-wavelength video analysis of paroxysmal eruptions at Mount Etna have offered a unique insight into the characteristics and dynamics of tephra plumes that are coupled to lava fountains. Many interesting observations can be made from even low resolution visible-wavelength video analysis. Analysis of the visible-wavelength videos has allowed for processes that have rarely been recorded in volcanic plumes, to not only be qualitatively described, but also to be quantitatively assessed for their potential impact on plume rise. Key findings include:

1. The tephra plume and lava fountain are not fully coupled, at least for the largest particles.
2. A component of the tephra plume must originate from primary fragmentation, possibly due to the friction between the rising magma and the conduit, as it surrounds the entirety of the lava fountain.
3. Volcanic gas and particles from the surrounding region can be entrained into a tephra plume.
4. Rotation of tephra plumes is observed, but it is likely to not have a significant impact on the plume dynamics and its origin is uncertain.

5. Entrainment of the ambient fluid (both radial and wind) into these plumes is similar to those of standard tephra plumes.

By analysing these eruptions, it has also allowed for a new strategy for the analysis of tephra plumes from visible-wavelength videos that includes a workflow to calibrate videos of wind-affected plumes for when information on the camera set-up is limited.

Despite these findings, a number of limitations prevented more quantitative results from being obtained. If a high-definition visible-wavelength camera could be used, information on the rate of sedimentation and the size of the clasts could be obtained (Houghton et al. 2020). This could offer vital information of the GSD of the lava fountain. In addition, if there were further eruptions that could be analysed, it would allow for more support of the findings. Even though there were 44 (Freret-Lorgeril et al. 2018) eruptions in the time period that was analysed, many of these occurred during the night or during bad weather. This prevented analysis, especially any quantitative analysis, of the eruptions. Because of this, I suggest future work should focus on using visible-wavelength video analysis to study not only tephra plumes that are coupled to lava fountains, but all sustained tephra plumes as many volcano observatories around the world have a webcam system (e.g., Alaska volcano observatory, Cameron et al. (2018), GNS, NZ, Miller and Jolly (2014)). Many videos of volcanic eruption are also recorded by local residents, which should also be explored to determine if these videos can be a useful to study tephra plumes. This initial work has proven what even low-resolution visible-wavelength videos can tell us about the complex dynamics and processes of coupled tephra plumes - lava fountains. Specifically, questions such as do volcanic plumes have a significant rotation component, and what is the GSD of lava fountains should be answered. Further work should also be combined with integral models to better determine the wind entrainment coefficient - a major source of uncertainty in integral models. Therefore visible-wavelength video analysis is a useful tool for volcanologists in the future to further understand tephra plumes.

CHAPTER 5

CONCLUSIONS

In this thesis, I have studied tephra plumes that are coupled to lava fountains via three approaches. These approaches are:

1. the development of a novel co-axial integral model to study the effect of a lava fountain on plume dynamics (Chapter 2),
2. applying this new model to multiple paroxysmal eruptions at Mount Etna, Italy, to understand the relationships amongst the deposit, the tephra plume and the lava fountain (Chapter 3),
3. examining visible-wavelength camera observation to constrain characteristics of coupled tephra plumes - lava fountains at Mount Etna (Chapter 4).

Each of these studies have individually contributed to an improved understanding of tephra plumes that are coupled to lava fountains. In Chapter 2, I first evaluated the suitability of a standard integral model (Degruyter and Bonadonna 2012) to model such plumes (Section 2.2). Through this, I clarified how the lava fountain relates to the surrounding tephra plume by showing, with the standard integral model, that the observed lava fountain height does not equate to the height of the modelled gas-thrust region (Section 2.2.1). The result clarifies any assumption on using the lava fountain height as the height of the gas-thrust region in the literature. Further to this, I also highlighted a discrepancy between the MFR derived from the tephra deposit and the MFR inverted from the observed plume height by a standard integral model (Section 2.2.2). This led to the development of a new co-axial integral model (Section 2.3), called the double plume model, that explicitly considers the effect of a lava fountain on plume rise. The results have indicated that the height reached by a tephra plume that has a hot, coarse inner core (e.g., a lava fountain), that I defined as having a log-normal grain-size distribution with a median grain-size of -7 phi, is reduced compared to a tephra plume that either has no inner core or an inner core composed of fine material (Sections 2.2.2 and 2.4.1). I have also shown that the size of the lava fountain, defined as the proportion of the initial MFR in the lava fountain compared to the surrounding tephra plume, also governs the size of the impact it has on the final plume height reached (Section 2.4.1). If the lava fountain is large with respect to the surrounding tephra plume, and the inner plume is coarse, much of the initial MFR from the plume system is lost through sedimentation and results in a lower plume height compared to the same plume modelled with the standard integral model. However, if the initial GSD of the inner plume is finer, this additional material contributes to an overall higher plume height being reached. These findings form a fundamental basis to the understanding of how lava fountains effect the rise of a surrounding tephra plume.

Although the model results in Chapter 2 marked significant progress in understanding the dynamics of coupled tephra plumes - lava fountains, an outstanding question was why there remained a discrepancy between the MFR derived from the tephra deposit and the MFR inverted from the observed plume height. Indeed, this discrepancy was present when using both the standard and newly-developed double plume models to look at the initial MFRs (Figure 2.2 and Figure 3.4a). To address this required coupling model results with field observations. I therefore focused on understanding the relationship between the mass in the coupled tephra plume - lava fountain and the deposited mass on the ground for five different eruptions of Mount Etna, Italy. In these case studies, the modelled initial MFR, as determined by constrained Monte Carlo simulations performed using the double plume model, could be up to an order or magnitude larger than the tephra deposit-derived MFR (Chapter 3.3.1). However, by comparing the field-derived MFR to the modelled MFRs at different heights in the double plume model, I showed that the modelled MFR at the start of the single plume region (i.e., above the lava fountain) was comparable to the field deposit-derived MFR (Figure 3.4b). This indicates that much of the initially-erupted material is deposited into the proximal cone deposit.

Another key observation was that the size of the discrepancy between the initial MFR inverted from the plume height and that determined from the plume tephra deposit varied between eruptions. I therefore investigated which parameters control the size of this discrepancy. In particular, I looked at the extent of coupling between the modelled lava fountain and the modelled tephra plume (Section 3.3.2), where the coupling extent is defined as the fraction of initial solid MFR of the inner plume that is transferred to the outer plume during plume rise. From this, I concluded that a large discrepancy correlates with a lower extent of coupling (Figure 3.8). When coupling is low, much of the initially erupted material sediments directly from the lava fountain and results in less material reaching the top of the tephra plume. This could result in a reduction in the expected mass injected into the atmosphere from a tephra plume that is coupled to a lava fountain.

Finally, I investigated coupled lava fountains - tephra plumes at Mount Etna through analysis of visible-wavelength videos of different eruptions. In total, I qualitatively examined 23 eruptions and further quantitatively analysed 7 of these to examine different features. Key findings from the qualitative analysis include the observation of rotation of the plumes, two sedimentation regimes, information on the plume origin with respect to the lava fountain, and the identification of the entrainment of surrounding gases and particles into the plume (Section 4.3.1). I then move on to a more quantitative analysis where I first quantify how much rotation is occurring by calculating Rossby numbers in Section 4.3.2 - a key value to determine whether the rotation is having a significant effect on the plume rise (Pham et al. 2006b; Pham et al. 2006a; Pham et al. 2011). I determine the rotation that is observed is likely not significantly effecting the plume rise or entrainment into the tephra plumes and speculate on the cause of the rotation (Section 4.4.1). I then explore using information from the visible-wavelength videos to infer entrainment coefficients used in integral plume models (Section 4.3.3) and to help constrain a standard integral model to help determine the best-fit wind entertainment coefficients and source parameters (Section 4.3.3). To conclude, I offer thoughts on the benefits and limitations of using visible-wavelength videos to study tephra plumes in Section 4.4.3.

5.1 Implications of This Work on the Understanding of Coupled Tephra Plumes - Lava Fountains

Together, these three Chapters have formed a picture of the dynamics of tephra plumes that are coupled to lava fountains. I can conclude that tephra plumes that are coupled to lava fountains have multiple significant differences to standard tephra plumes. This is because lava fountains affect the rise of a coupled tephra plume. High fallout from the co-existing tephra plume - lava fountain region, that can even be visibly seen (Section 4.3.1), results in a loss of mass, momentum and enthlapy from the plume that causes a reduction in plume height (Sections 2.4.1, 2.4.1 and 2.4.1). This also results in much of the initially erupted material to be deposited in the cone deposit (Chapter 3) rather than in the plume tephra deposit, which is the part that is commonly analysed. This is especially the case when coupling between the lava fountain and the surrounding tephra plume is low (Chapter 3).

These findings could have significant impact on how volcanologists study the deposits of these eruptions. For instance, much of the erupted material deposits in the ultra-proximal regions (i.e., the cone deposit) of these eruptions. The ultra-proximal region is rarely sampled (Behncke et al. 2014; Andronico et al. 2014a; De Beni et al. 2015), partly due to the hazards associated with being so close to an active volcanic vent (Andronico et al. 2014a). It is also the region that is poorly characterised by fitting of lines to deposit thinning data that are used to calculate volume estimates (Bonadonna and Houghton 2005a). As this ultra-proximal region is so important for tephra plumes that are coupled to lava fountains, it will be one of the most important regions of the deposit to characterise in future field deposit characterisations.

Similarly, as much of the erupted material deposits from the plume before it reaches high in the atmosphere, my findings will also have an impact of hazard forecasting of these eruptions. Rather than using MFR estimates of what was initially erupted for a recorded plume height, either derived from numerical models or empirical formulations (e.g., Mastin et al. (2009) and Degruyter and Bonadonna (2012)), it may be better to use the MFR that has reached above the neutral buoyancy level, or even the MFR distribution in the plume, depending on the tephra dispersion model. Otherwise, using the

MFR at the source, could result in an overestimation of mass injection into the atmosphere, and a less accurate forecast of the tephra dispersion from tephra plumes that are coupled to lava fountains.

Furthermore, an improved understanding of the coupled tephra plume - lava fountain allows insights on the fragmentation that results in them. Based on the results in Chapter 3, I discuss potential causes of the different extents of coupling between a lava fountain and tephra plume - specifically that it could relate to fragmentation. I hypothesise that with a larger lava fountain, more efficient fragmentation could be occurring. Similarly, based on the observations of the origin of the tephra plume (Chapter 4), I discuss that fragmentation in the conduit is not uniform, with potentially more fragmentation happening at the margins of the conduit, which results in the initial tephra plume. These discussions show that fragmentation in paroxysmal eruptions could be complex.

Despite these differences, which have been the focus of much of this thesis, many of the characteristics of tephra plume that are coupled to lava fountains are similar to those of standard tephra plumes. While a lava fountain does affect the dynamics and mass distribution in a coupled plume, for a given overall initial MFR, plumes with a lava fountain can reach similar heights to those without (Section 2.4.1). We also find that entrainment of air from the ambient to the tephra plume can be described by a radial entrainment coefficient which is very similarly to those previously reported (Section 4.3.3) (Morton et al. 1956; Aubry et al. 2017). Another example of these similarities includes sedimentation from the plume as streaks or 'fingers' (Section 4.3.1), which have been observed during many different styles of volcanic activity (Carazzo and Jellinek 2012; Manzella et al. 2015; Scollo et al. 2017; Freret-Lorgeril et al. 2020; Fries et al. 2021).

There are also some observations of the coupled tephra plumes - lava fountains of Mount Etna for which I am unable to say if they are unique to these plumes. For instance, while we observe and discuss rotation in these plumes, I can not say, or expect, it to be unique to just tephra plumes that are coupled to lava fountains. Rotation occurs in many plume in nature (e.g., Helfrich and Battisti (1991), Jones and Marshall (1993), and Holland and Feltham (2006)), and the origin of the rotation may not be due to the presence of the lava fountain. Similarly, I also demonstrate that air entrainment from the ambient to the tephra plume in the region where the plume and lava fountain co-exist might be described by a lower radial entrainment coefficient than in the single plume region (Section 4.3.3). While this once again may be due to the presence of a lava fountain, reduced rates of entrainment have long been reported in the negatively-buoyant lower plume region (Carazzo et al. 2008a) and may depend on the local Richardson number. Finally, I have shown that coupled lava fountain - tephra plumes can produce volumetrically-significant ultra-proximal deposits, e.g., the cone deposit at Mount Etna. However, it is uncertain how much material is deposited in similarly proximal regions for other eruption styles. Often referred to as segment 0 (Bonadonna et al. 1998; Bonadonna and Phillips 2003), the most proximal part of the tephra deposit is often unaccounted for due to under sampling (e.g., Andronico et al. (2014a)). However, I do not expect the size of the most proximal deposit in comparison to the plume tephra deposit to be as large for other volcanic eruption styles as they are characterised by GSDs that are finer than those from lava fountains (Cashman and Scheu 2015; Girault et al. 2014).

Moreover, the development of a simple and new double plume model (Chapter 2), and its proven suitability to model tephra plumes that are coupled to lava fountain (Chapter 3), provides an important new tool for the volcanology community. It is fast and not computationally expensive. It can also provide key constraints on source parameters such as the initial MFR and MFR distribution in a plume if the plume height and lava fountain heights are known. These key features make it suitable to be used in real-time and provide better constraints on key ESPs compared to the standard integral model that is currently in use operationally (Scollo et al. 2019). Therefore, this new double plume model could be implemented operationally in the future at volcano observatories that monitor volcanoes with paroxysmal eruptions, such as INGV-OE, to aid with real-time estimates of how much MFR is reaching the atmosphere.

5.2 Limitations and Future Work

In this Section, I will discuss the major limitations of the work presented in this thesis. This will include an explanation of why it was not possible to overcome, and its potential implications on the results. I will then suggest future work in Section 5.2.2 that would help to overcome these limitations and improve the understanding of tephra plume that are coupled to lava fountains.

5.2.1 Limitations of the presented work

Despite the advances I have made on the understanding of tephra plumes that are coupled to lava fountains, multiple questions about them remain. One of these remaining questions is how do additional processes or assumptions that I have not been able to consider affect the dynamics of these plumes. One such example is the assumption that drag force between the inner plume and the outer plume in the modelling of tephra plumes that are coupled to lava fountain is not important, hence it was not considered in this work. However, since its impact on plume rise is uncertain (see Section 2.5.2 for discussion), it should be investigated and its impact quantified. Another example is the assumption of dynamic disequilibrium. Dynamic disequilibrium is the disconnect between the particle motion and fluid motion. While it has been considered in volcanic models before (Parfitt and Wilson 1999), it was done so by adjusting the source parameters to calculate a true gas exit velocity. To fully account of dynamic dis-equilibrium, this process would have to be modelled throughout plume rise. Similarly, while I briefly investigated the effect of thermal disequilibrium between the solid and gas phases on plume rise in Chapter 2, this was through an approximate parameterisation (Woods and Bursik 1991) and not a complete model of the physical process itself. This could have implications on reducing the energy and momentum transfer between the large clasts of the lava fountain that have fallen, and are supported, by the surrounding tephra plume. As a result, the effect of these processes on the dynamics of coupled lava fountains - tephra plume needs to be further investigated.

Another remaining question is how does strong wind affect the region where the tephra plume and lava fountain co-exist. Throughout this thesis, I have assumed that wind does not significantly impact this region, since this is frequently the case when looking at videos of paroxysmal eruptions of Mount Etna. Therefore, the effect of wind in this region is not accounted for in the double plume model. However, whilst often valid, this may not always be the case. For example, in the eruption of the 12th of April 2012, the tephra plume does not surround the entire of the lava fountain. Rather, the tephra plume is offset to the lava fountain as it rises. This could result in a reduction of coupling between the lava fountain and the tephra plume and could result in a reduction in height that the plume could reach. The new simple double plume integral model presented in Chapter 2 of this thesis is unable to model such cases as this plume violates the axisymmetric assumption of the model. As a result, other more complex models, ones that model in more than one-dimension, would be required to understand the effect of wind on the double plume region.

Moreover, in some eruptions, the lava fountain is sourced from a linear fissure rather than as a circular vent (Personal communication, INGV-OE). The model that I have developed in Chapter 2, and was used in Chapter 3, assumes that the lava fountain occurs from a point source and is therefore not applicable to those lava fountains that originate from a fissure. This approach was chosen as the length scale of the lava fountains that originate from fissures are on a much smaller scale than the length scale of the plume. While these fissures are on a much shorter length scale compared to many of the previously modelled fissure eruptions (e.g., Laki, Stothers et al. (1986)) and also a much shorter length scale than the height that the plumes reach, the impact of this difference in vent geometry on plume dynamics should be investigated. This could be done in a similar way as to Stothers et al. (1986) and Woods (1993).

5.2.2 Future Work

One avenue for future work that could partially address these complexities would be to use 3D numerical plume models to study tephra plumes that are coupled to lava fountains. 3D numerical models (Suzuki et al. 2016a) would allow for the symmetry in the double plume region to be broken. As a result, the effect of wind could then be explored as the geometries of the inner and outer plumes would no longer be imposed. A 3D numerical model would also allow additional more complex processes occurring in tephra plume that are coupled to lava fountains to be explored. For instance, the effect of thermal and dynamic disequilibrium (Cerminara et al. 2016b) on the coupling between the inner and outer plume, and on overall plume rise could be explored. The impact of drag could also be investigated. 3D numerical models would enable a more accurate physical description of the disequilibrium, rather than relying on an approximate parameterisation as in simple integral models (Woods and Bursik 1991).

Future work should also focus on improving the visible observations of tephra plumes that are coupled to lava fountains. While visible videos have provided vital clues on the dynamics of tephra plumes that are coupled to lava fountains (Chapter 4), higher spatial and temporal resolution cameras would allow for even more details to be captured. A higher spatial resolution would allow for smaller details in the plume to be seen, such as smaller particles and more detailed plume margin. While a higher temporal resolution would allow the better tracking of features with time such as rotation and sedimenting particles to get better estimates of rates of sedimentation from the tephra plume and the lava fountain, plume velocities and characteristics of the turbulent eddies (especially in the tephra plume -lava fountain co-existing region). Furthermore, these observations could be further utilised with modelling to further extract information on the dynamics of these plumes as in Chapter 4. Examples includes using velocity estimates to compare to modelled velocities and comparing sedimentation loss from the modelled plume to observed sedimentation rates from the plume margin. Similarly, much more could be done in terms of integrating the data from visible-wavelength videos and plume modelling with other data types. An obvious example of this is plume height. In Chapter 4, I have shown how information on shape from visible-wavelength video can be compared to a modelled plume. But how can plume data from radar or satellite be further used with plume modelling? And in turn, are all these different remote sensing methods seeing the same thing as each has varying sensitivities to different grain-sizes? This is one of many areas future work should focus on to not only help us understand tephra plumes that are coupled to lava fountains, but also how different methods can work together to understand volcanic plumes in general.

Finally, I recommend that further studies of these plumes are carried out at other volcanoes around the world. Mount Etna is not the only volcano the produces eruptions characterised by coupled lava fountains and tephra plumes. As mentioned in Chapter 1, Izu Oshima, Japan (Mannen 2006) and Villarrica, Chile (Romero et al. 2018), have also had eruptions that produced coupled tephra plumes - lava fountains. Due to the extensive data sets on plume height and information of MFRs derived from the tephra deposits of some eruptions from frequent eruptions of Mount Etna over the past decade, much of my findings are based on Mount Etna. As shown in Chapter 2, the impact of a lava fountain on plume rise depends on initial GSD and size of the lava fountain relative to the surrounding tephra plume. Therefore, to do a similar analysis at other volcanoes, characteristics of multiple eruptions for different volcanoes such as plume height estimates, lava fountain height estimates, and deposit characterisation would be required. I have also highlighted how differences in coupling between the lava fountain and tephra plume also play a major role in mass transfer with the plume and how this differs between different eruptions at Mount Etna. This leads to question on how does coupling between lava fountains and tephra plumes differ at other volcanoes that have paroxysmal eruptions. Given the potential impact on mass injection into the atmosphere from such eruptions, it will be essential to evaluate the dynamics of these eruptions around the world to ensure they are fully understood by the next time that they erupt.

REFERENCES

Aiuppa, A., Moretti, R., Federico, C., Giudice, G., Gurrieri, S., Liuzzo, M., Papale, P., Shinohara, H., and Valenza, M. (2007). Forecasting Etna eruptions by real-time observation of volcanic gas composition. *Geology* **35**, 1115–1118.

Aizawa, K., Cimarelli, C., Alatorre-Ibargüengoitia, M. A., Yokoo, A., Dingwell, D. B., and Iguchi, M. (2016). Physical properties of volcanic lightning: Constraints from magnetotelluric and video observations at Sakurajima volcano, Japan. *Earth and Planetary Science Letters* **444**, 45–55.

Albadra, A., Wood, K., Berthoud, L., Calway, A., Watson, M., Thomas, H., Richardson, T., Liu, E., and Chigna, G. (2020). Determining the three-dimensional structure of a volcanic plume using Unoccupied Aerial System (UAS) imagery. *Journal of Volcanology and Geothermal Research* **407**, 106731.

Alparone, S., Andronico, D., Lodato, L., and Sgroi, T. (2003). Relationship between tremor and volcanic activity during the Southeast Crater eruption on Mount Etna in early 2000. *Journal of Geophysical Research - Solid Earth* **108**.

Alparone, S., Andronico, D., Sgroi, T., Ferrari, F., Lodato, L., and Reitano, D. (2007). Alert system to mitigate tephra fallout hazards at Mt. Etna Volcano, Italy. *Natural Hazards* **43**, 333–350.

Andronico, D., Behncke, B., De Beni, E., Cristaldi, A., Scollo, S., Lopez, M., and Lo Castro, M. D. (2018). Magma Budget From Lava and Tephra Volumes Erupted During the 25-26 October 2013 Lava Fountain at Mt Etna. *Frontiers in Earth Science* **6**, 116.

Andronico, D., Branca, S., Calvari, S., Burton, M., Caltabiano, T., Corsaro, R. A., Del Carlo, P., Garfì, G., Lodato, L., Miraglia, L., et al. (2005). A multi-disciplinary study of the 2002–03 Etna eruption: insights into a complex plumbing system. *Bulletin of Volcanology* **67**, 314–330.

Andronico, D., Cantarero, M., Corsaro, R. A., Cristaldi, A., Castro, M. D. L., Messina, L., and Scollo, S. (2013). *L'attività parossistica del 23 Novembre 2013 al Nuovo Cratere di SE: dispersione del deposito di caduta e caratteristiche dei prodotti eruttati [in italian], Rapporto UFVG del 28 Novembre 2013, Rapporti, Vulcanologia*.

Andronico, D. and Corsaro, R. A. (2011). Lava fountains during the episodic eruption of South–East Crater (Mt. Etna), 2000: insights into magma-gas dynamics within the shallow volcano plumbing system. *Bulletin of volcanology* **73**, 1165–1178.

Andronico, D., Corsaro, R. A., Cristaldi, A., and Polacci, M. (2008a). Characterizing high energy explosive eruptions at Stromboli volcano using multidisciplinary data: An example from the 9 January 2005 explosion. *Journal of Volcanology and Geothermal Research* **176**, 541–550.

Andronico, D. and Lodato, L. (2005). Effusive activity at Mount Etna volcano (Italy) during the 20th century: A contribution to volcanic hazard assessment. *Natural Hazards* **36**, 407–443.

Andronico, D., Scollo, S., Caruso, S., and Cristaldi, A. (2008b). The 2002-03 Etna explosive activity: Tephra dispersal and features of the deposits. *Journal of Geophysical Research: Solid Earth* **113**.

Andronico, D., Scollo, S., and Cristaldi, A. (2015). Unexpected hazards from tephra fallouts at Mt Etna: The 23 November 2013 lava fountain. *Journal of Volcanology and Geothermal Research* **304**, 118–125.

Andronico, D., Scollo, S., Cristaldi, A., and Ferrari, F. (2009a). Monitoring ash emission episodes at Mt. Etna: The 16 November 2006 case study. *Journal of Volcanology and Geothermal Research* **180**, 123–134.

Andronico, D., Scollo, S., Cristaldi, A., and Lo Castro, M. D. (2014a). Representivity of incompletely sampled fall deposits in estimating eruption source parameters: a test using the 12-13 January 2011 lava fountain deposit from Mt. Etna volcano, Italy. *Bulletin of Volcanology* **76**, 861.

Andronico, D., Scollo, S., Lo Castro, M. D., Cristaldi, A., Lodato, L., and Taddeucci, J. (2014b). Eruption dynamics and tephra dispersal from the 24 November 2006 paroxysm at South-East Crater, Mt Etna, Italy. *Journal of Volcanology and Geothermal Research* **274**, 78–91.

Andronico, D., Spinetti, C., Cristaldi, A., and Buongiorno, M. F. (2009b). Observations of Mt. Etna volcanic ash plumes in 2006: An integrated approach from ground-based and polar satellite NOAA-AVHRR monitoring system. *Journal of Volcanology and Geothermal Research* **180**, 135–147.

Aubry, T. J., Carazzo, G., and Jellinek, A. M. (2017). Turbulent entrainment into volcanic plumes: new constraints from laboratory experiments on buoyant jets rising in a stratified crossflow. *Geophysical Research Letters* **44**, 10–198.

Aubry, T. J., Engwell, S., Bonadonna, C., Carazzo, G., Scollo, S., Van Eaton, A. R., Taylor, I. A., Jessop, D., Eychenne, J., Gouhier, M., et al. (2021). The Independent Volcanic Eruption Source Parameter Archive (IVESPA, version 1.0): A new observational database to support explosive eruptive column model validation and development. *Journal of Volcanology and Geothermal Research*, 107295.

Aubry, T. J. and Jellinek, A. M. (2018). New insights on entrainment and condensation in volcanic plumes: Constraints from independent observations of explosive eruptions and implications for assessing their impacts. *Earth and Planetary Science Letters* **490**, 132–142.

Baines, P. G. and Sparks, R. S. J. (2005). Dynamics of giant volcanic ash clouds from supervolcanic eruptions. *Geophysical Research Letters* **32**.

Bani, P., Harris, A. J. L., Shinohara, H., and Donnadieu, F. (2013). Magma dynamics feeding Yasur's explosive activity observed using thermal infrared remote sensing. *Geophysical Research Letters* **40**, 3830–3835.

Barnard, S. T. (2004). Results of a reconnaissance trip to Mt. Etna, Italy. *Bulletin of the New Zealand Society for Earthquake Engineering* **37**, 47–61.

Barron, J. L., Fleet, D. J., and Beauchemin, S. S. (1994). Performance of optical flow techniques. *International journal of computer vision* **12**, 43–77.

Behncke, B., Branca, S., Corsaro, R., De Beni, E., Miraglia, L., and Proietti, C. (2014). The 2011-2012 summit activity of Mount Etna: Birth, growth and products of the new SE crater. *Journal of Volcanology and Geothermal Research* **270**, 10–21.

Berrisford, P., Dee, D., Poli, P., Brugge, R., Fielding, K., Fuentes, M., Kallberg, P., Kobayashi, S., Uppala, S., and Simmons, A. (2011). The ERA-Interim archive, version 2.0.

Bertagnini, A., Di Roberto, A., and Pompilio, M. (2011). Paroxysmal activity at Stromboli: lessons from the past. *Bulletin of Volcanology* **73**, 1229–1243.

Bhamidipati, N. and Woods, A. W. (2017). On the dynamics of starting plumes. *Journal of Fluid Mechanics* **833**.

Biass, S., Bonadonna, C., and Houghton, B. F. (2019). A step-by-step evaluation of empirical methods to quantify eruption source parameters from tephra-fall deposits. *Journal of Applied Volcanology* **8**, 1–16.

Bloomfield, L. J. and Kerr, R. C. (1998). Turbulent fountains in a stratified fluid. *Journal of Fluid Mechanics* **358**, 335–356.

Bloomfield, L. J. and Kerr, R. C. (2000). A theoretical model of a turbulent fountain. *Journal of Fluid Mechanics* **424**, 197–216.

Bombrun, M., Jessop, D., Harris, A., and Barra, V. (2018). An algorithm for the detection and characterisation of volcanic plumes using thermal camera imagery. *Journal of Volcanology and Geothermal Research* **352**, 26–37.

Bombrun, M., Spampinato, L., Harris, A., Barra, V., and Caltabiano, T. (2016). On the transition from strombolian to fountaining activity: a thermal energy-based driver. *Bulletin of volcanology* **78**, 15.

Bonaccorso, A., Bonforte, A., Calvari, S., Del Negro, C., Di Grazia, G., Ganci, G., Neri, M., Vicari, A., and Boschi, E. (2011). The initial phases of the 2008–2009 Mount Etna eruption: A multidisciplinary approach for hazard assessment. *Journal of Geophysical Research: Solid Earth* **116**.

Bonaccorso, A., Calvari, S., Currenti, G., Del Negro, C., Ganci, G., Linde, A., Napoli, R., Sacks, S., and Sicali, A. (2013). From source to surface: Dynamics of Etna's lava fountains investigated by continuous strain, magnetic, ground and satellite thermal data. *Bulletin of volcanology* **75**, 1–12.

Bonaccorso, A., Calvari, S., Linde, A., and Sacks, S. (2014). Eruptive processes leading to the most explosive lava fountain at Etna volcano: The 23 November 2013 episode. *Geophysical Research Letters* **41**, 4912–4919.

Bonadonna, C., Biass, S., and Costa, A. (2015). Physical characterization of explosive volcanic eruptions based on tephra deposits: Propagation of uncertainties and sensitivity analysis. *Journal of Volcanology and Geothermal Research* **296**, 80–100.

Bonadonna, C. and Costa, A. (2012). Estimating the volume of tephra deposits: a new simple strategy. *Geology* **40**, 415–418.

Bonadonna, C. and Costa, A. (2013). Modeling tephra sedimentation from volcanic plumes. In: *Modeling Volcanic Processes: The Physics and Mathematics of Volcanism*. Ed. by S. A. Fagents, T. K. P. Gregg, and R. M. C. Lopes. Cambridge University Press, 173–202.

Bonadonna, C., Ernst, G. G. J., and Sparks, R. S. J. (1998). Thickness variations and volume estimates of tephra fall deposits: the importance of particle Reynolds number. *Journal of Volcanology and Geothermal Research* **81**, 173–187.

Bonadonna, C., Folch, A., Loughlin, S., and Puempel, H. (2012). Future developments in modelling and monitoring of volcanic ash clouds: outcomes from the first IAVCEI-WMO workshop on Ash Dispersal Forecast and Civil Aviation. *Bulletin of Volcanology* **74**, 1–10.

Bonadonna, C. and Houghton, B. F. (2005a). Total grain-size distribution and volume of tephra-fall deposits. *Bulletin of Volcanology* **67**, 441–456.

Bonadonna, C. and Houghton, B. F. (2005b). Total grain-size distribution and volume of tephra-fall deposits. *Bulletin of Volcanology* **67**, 441–456.

Bonadonna, C. and Phillips, J. C. (2003). Sedimentation from strong volcanic plumes. *Journal of Geophysical Research: Solid Earth*.

Branca, S., Coltelli, M., De Beni, E., and Wijbrans, J. (2008). Geological evolution of Mount Etna volcano (Italy) from earliest products until the first central volcanism (between 500 and 100 ka ago) inferred from geochronological and stratigraphic data. *International Journal of Earth Sciences* **97**, 135–152.

Branca, S., Coltelli, M., and Groppelli, G. (2011). Geological evolution of a complex basaltic stratovolcano: Mount Etna, Italy. *Italian Journal of Geosciences* **130**, 306–317.

Branca, S., De Beni, E., Chester, D., Duncan, A., and Lotteri, A. (2017). The 1928 eruption of Mount Etna (Italy): Reconstructing lava flow evolution and the destruction and recovery of the town of Mascali. *Journal of Volcanology and Geothermal Research* **335**, 54–70.

Branca, S., De Beni, E., and Proietti, C. (2013). The large and destructive 1669 AD eruption at Etna volcano: reconstruction of the lava flow field evolution and effusion rate trend. *Bulletin of Volcanology* **75**, 1–16.

Branca, S. and Del Carlo, P. (2005). Types of eruptions of Etna volcano AD 1670–2003: implications for short-term eruptive behaviour. *Bulletin of Volcanology* **67**, 732–742.

Bursik, M. I. (2001). Effect of wind on the rise height of volcanic plumes. *Geophysical Research Letters* **28**, 3621–3624.

Bursik, M. I., Sparks, R. S. J., Gilbert, J. S., and Carey, S. N. (1992). Sedimentation of tephra by volcanic plumes: I. Theory and its comparison with a study of the Fogo A plinian deposit, Sao Miguel (Azores). *Bulletin of Volcanology* **54**, 329–344.

Cadoux, A., Blichert-Toft, J., Pinti, D. L., and Albarède, F. (2007). A unique lower mantle source for Southern Italy volcanics. *Earth and Planetary Science Letters* **259**, 227–238.

Calvari, S., Bilotta, G., Bonaccorso, A., Caltabiano, T., Cappello, A., Corradino, C., Del Negro, C., Ganci, G., Neri, M., Pecora, E., et al. (2020). The VEI 2 Christmas 2018 Etna eruption: A small but intense eruptive event or the starting phase of a larger one? *Remote Sensing* **12**, 905.

Calvari, S., Cannavò, F., Bonaccorso, A., and Pellegrino, A. G. (2018). Paroxysmal Explosions, Lava Fountains and Ash Plumes at Etna Volcano: Eruptive Processes and Hazard Implications. *Frontiers in Earth Science* **6**, 1–20.

Calvari, S., Salerno, G. G., Spampinato, L., Gouhier, M., La Spina, A., Pecora, E., Harris, A. J. L., Labazuy, P., Biale, E., and Boschi, E. (2011). An unloading foam model to constrain Etna's 11-13 January 2011 lava fountaining episode. *Journal of Geophysical Research: Solid Earth* **116**.

Calvari, S., Spampinato, L., and Lodato, L. (2006). The 5 April 2003 vulcanian paroxysmal explosion at Stromboli volcano (Italy) from field observations and thermal data. *Journal of Volcanology and Geothermal research* **149**, 160–175.

Cameron, C. E., Prejean, S. G., Coombs, M. L., Wallace, K. L., Power, J. A., and Roman, D. C. (2018). Alaska volcano observatory alert and forecasting timeliness: 1989–2017. *Frontiers in Earth Science* **6**, 86.

Carazzo, G., Girault, F., Aubry, T., Bouquerel, H., and Kaminski, E. (2014a). Laboratory experiments of forced plumes in a density-stratified crossflow and implications for volcanic plumes. *Geophysical Research Letters* **41**, 8759–8766.

Carazzo, G., Girault, F., Aubry, T., Bouquerel, H., and Kaminski, E. (2014b). Laboratory experiments of forced plumes in a density-stratified crossflow and implications for volcanic plumes. *Geophysical Research Letters* **41**, 8759–8766.

Carazzo, G. and Jellinek, A. M. (2012). A new view of the dynamics, stability and longevity of volcanic clouds. *Earth and Planetary Science Letters* **325**, 39–51.

Carazzo, G., Kaminski, E., and Tait, S. (2006). The route to self-similarity in turbulent jets and plumes. *Journal of Fluid Mechanics* **547**, 137–148.

Carazzo, G., Kaminski, E., and Tait, S. (2008a). On the dynamics of volcanic columns: A comparison of field data with a new model of negatively buoyant jets. *Journal of Volcanology and Geothermal Research* **178**, 94–103.

Carazzo, G., Kaminski, E., and Tait, S. (2008b). On the rise of turbulent plumes: Quantitative effects of variable entrainment for submarine hydrothermal vents, terrestrial and extra terrestrial explosive volcanism. *Journal of Geophysical Research: Solid Earth* **113**.

Carbone, D., Zuccarello, L., Messina, A., Scollo, S., and Rymer, H. (2015). Balancing bulk gas accumulation and gas output before and during lava fountaining episodes at Mt. Etna. *Scientific reports* **5**, 1–11.

Carey, S. and Bursik, M. (2015). Volcanic plumes. In: *The Encyclopedia of Volcanoes*. Ed. by H. Sigurdsson, B. Houghton, S. R. McNutt, H. Rymer, and J. Stix. Elsevier, 571–585.

Carey, S. and Sparks, R. S. J. (1986). Quantitative models of the fall. *Bulletin of Volcanology* **48**, 109–125.

Carlsen, H. K., Gislason, T., Benediktsdottir, B., Kolbeinsson, T. B., Hauksdottir, A., Thorsteinsson, T., and Briem, H. (2012a). A survey of early health effects of the Eyjafjallajökull 2010 eruption in Iceland: a population-based study. *BMJ open* **2**, e000343.

Carlsen, H. K., Hauksdottir, A., Valdimarsdottir, U. A., Gíslason, T., Einarsdottir, G., Runolfsson, H., Briem, H., Finnbjornsdottir, R. G., Gudmundsson, S., Kolbeinsson, T. B., et al. (2012b). Health effects following the Eyjafjallajökull volcanic eruption: a cohort study. *BMJ open* **2**, e001851.

Cashman, K. V., Mangan, M. T., and Poland, M. (2014). A century of studying effusive eruptions in Hawai'i. *Characteristics of Hawaiian volcanoes. US Geol Surv Prof Pap* **1801**, 357–94.

Cashman, K. V. and Scheu, B. (2015). Magma fragmentation. In: *The encyclopedia of volcanoes*. Ed. by H. Sigurdsson, B. Houghton, S. R. McNutt, H. Rymer, and J. Stix. Academic Press, 459–471.

Cerminara, M., Esposti Ongaro, T., and Neri, A. (2016a). Large Eddy Simulation of gas–particle kinematic decoupling and turbulent entrainment in volcanic plumes. *Journal of Volcanology and Geothermal Research* **326**, 143–171.

Cerminara, M., Esposti Ongaro, T., and Berselli, L. C. (2016b). ASHEE-1.0: a compressible, equilibrium–Eulerian model for volcanic ash plumes. *Geoscientific Model Development* **9**, 697–730.

Chakraborty, P., Gioia, G., and Kieffer, S. W. (2009). Volcanic mesocyclones. *Nature* **458**, 497–500.

Cioni, R., Pistolesi, M., and Rossi, M. (2015). Plinian and Subplinian eruptions. In: *The Encyclopedia of Volcanoes*. Ed. by H. Sigurdsson, B. Houghton, S. R. McNutt, H. Rymer, and J. Stix. Elsevier, 519–535.

Coltelli, M., d'Aranno, P. J. V., De Bonis, R., Guerrero Tello, J. F., Marsella, M., Nardinocchi, C., Pecora, E., Proietti, C., Scifoni, S., Scutti, M., et al. (2017). The use of surveillance cameras for the rapid mapping of lava flows: an application to Mount Etna Volcano. *Remote Sensing* **9**, 192.

Coltelli, M., Del Carlo, P., and Vezzoli, L. (1998). Discovery of a Plinian basaltic eruption of Roman age at Etna volcano, Italy. *Geology* **26**, 1095–1098.

Coltelli, M., Proietti, C., Branca, S., Marsella, M., Andronico, D., and Lodato, L. (2007). Analysis of the 2001 lava flow eruption of Mt. Etna from three-dimensional mapping. *Journal of Geophysical Research: Earth Surface* **112**.

Contini, D., Donateo, A., Cesari, D., and Robins, A. G. (2011). Comparison of plume rise models against water tank experimental data for neutral and stable crossflows. *Journal of wind engineering and industrial aerodynamics* **99**, 539–553.

Corradini, S., Guerrieri, L., Lombardo, V., Merucci, L., Musacchio, M., Prestifilippo, M., Scollo, S., Silvestri, M., Spata, G., and Stelitano, D. (2018). Proximal Monitoring of the 2011–2015 Etna Lava Fountains Using MSG-SEVIRI Data. *Geosciences* **8**, 140.

Corradini, S., Montopoli, M., Guerrieri, L., Ricci, M., Scollo, S., Merucci, L., Marzano, F. S., Pugnaghi, S., Prestifilippo, M., Ventress, L. J., Grainger, R. G., Carboni, E., Vulpiani, G., and Coltelli, M. (2016). A Multi-Sensor Approach for Volcanic Ash Cloud Retrieval and Eruption Characterization: The 23 November 2013 Etna Lava Fountain. *Remote Sensing* **8**, 58.

Corradino, C., Ganci, G., Cappello, A., Bilotta, G., Calvari, S., and Del Negro, C. (2020). Recognizing eruptions of Mount Etna through machine learning using multiperspective infrared images. *Remote Sensing* **12**, 970.

Corsaro, R. A., Cristofolini, R., and Patanè, L. (1996). The 1669 eruption at Mount Etna: chronology, petrology and geochemistry, with inferences on the magma sources and ascent mechanisms. *Bulletin of Volcanology* **58**, 348–358.

Costa, A., Pioli, L., and Bonadonna, C. (2016a). Assessing tephra total grain-size distribution: Insights from field data analysis. *Earth and Planetary Science Letters* **443**, 90–107.

Costa, A., Suzuki, Y. J., Cerminara, M., Devenish, B. J., Ongaro, T. E., Herzog, M., Van Eaton, A. R., Denby, L. C., Bursik, M., Vitturi, M. D., Engwell, S., Neri, A., Barsotti, S., Folch, A., Macedonio, G., Girault, F., Carazzo, G., Tait, S., Kaminski, E., Mastin, L. G., Woodhouse, M. J., Phillips, J. C., Hogg, A. J., Degruyter, W., and Bonadonna, C. (2016b). Results of the eruptive column model inter-comparison study. *Journal of Volcanology and Geothermal Research* **326**, 2–25.

Costa, A., Suzuki, Y. J., and Koyaguchi, T. (2018). Understanding the plume dynamics of explosive super-eruptions. *Nature communications* **9**, 1–6.

Damby, D. E., Horwell, C. J., Larsen, G., Thordarson, T., Tomatis, M., Fubini, B., and Donaldson, K. (2017). Assessment of the potential respiratory hazard of volcanic ash from future Icelandic eruptions: a study of archived basaltic to rhyolitic ash samples. *Environmental Health* **16**, 1–15.

Davies-Jones, R. (1984). Streamwise vorticity: The origin of updraft rotation in supercell storms. *Journal of Atmospheric Sciences* **41**, 2991–3006.

De Beni, E., Behncke, B., Branca, S., Nicolosi, I., Carluccio, R., Caracciolo, F. D., and Chiappini, M. (2015). The continuing story of Etna's New Southeast Crater (2012-2014): Evolution and volume calculations based on field surveys and aerophotogrammetry. *Journal of Volcanology and Geothermal Research* **303**, 175–186.

De Beni, E., Branca, S., Coltelli, M., Groppelli, G., and Wijbrans, J. R. (2011). 40Ar/39Ar isotopic dating of Etna volcanic succession. *Italian Journal of Geosciences* **130**, 292–305.

De Beni, E., Cantarero, M., and Messina, A. (2019). UAVs for volcano monitoring: A new approach applied on an active lava flow on Mt. Etna (Italy), during the 27 February–02 March 2017 eruption. *Journal of Volcanology and Geothermal Research* **369**, 250–262.

de Michele, M., Raucoules, D., Corradini, S., Merucci, L., Salerno, G., Sellitto, P., and Carboni, E. (2019). Volcanic Cloud Top Height Estimation Using the Plume Elevation Model Procedure Applied to Orthorectified Landsat 8 Data. Test Case: 26 October 2013 Mt. Etna Eruption. *Remote Sensing* **11**, 785.

de'Michieli Vitturi, M., Engwell, S. L., Neri, A., and Barsotti, S. (2016). Uncertainty quantification and sensitivity analysis of volcanic columns models:

Results from the integral model PLUME-MoM. *Journal of Volcanology and Geothermal Research* **326**, 77–91.

de'Michieli Vitturi, M., Neri, A., and Barsotti, S. (2015). PLUME-MoM 1.0: A new integral model of volcanic plumes based on the method of moments. *Geoscientific Model Development* **8**, 2447–2463.

Dee, D. P., Uppala, S. M., Simmons, A. J., Berrisford, P., Poli, P., Kobayashi, S., Andrae, U., Balmaseda, M. A., Balsamo, G., Bauer, P., et al. (2011). The ERA-Interim reanalysis: Configuration and performance of the data assimilation system. *Quarterly Journal of the royal meteorological society* **137**, 553–597.

Degruyter, W. and Bonadonna, C. (2012). Improving on mass flow rate estimates of volcanic eruptions. *Geophysical Research Letters* **39**.

Degruyter, W. and Bonadonna, C. (2013). Impact of wind on the condition for column collapse of volcanic plumes. *Earth and Planetary Science Letters* **377**, 218–226.

Del Negro, C., Cappello, A., Bilotta, G., Ganci, G., Hérault, A., and Zago, V. (2020). Living at the edge of an active volcano: Risk from lava flows on Mt. Etna. *Bulletin* **132**, 1615–1625.

Deremble, B. (2016). Convective plumes in rotating systems. *Journal of Fluid Mechanics* **799**, 27–55.

Devenish, B. J. (2013). Using simple plume models to refine the source mass flux of volcanic eruptions according to atmospheric conditions. *Journal of Volcanology and Geothermal Research* **256**, 118–127.

Devenish, B. J. (2016). Estimating the total mass emitted by the eruption of Eyjafjallajökull in 2010 using plume-rise models. *Journal of Volcanology and Geothermal Research* **326**, 114–119.

Devenish, B. J. and Cerminara, M. (2018). The Transition From Eruption Column to Umbrella Cloud. *Journal of Geophysical Research: Solid Earth* **123**, 10418–10430.

Devenish, B. J., Rooney, G. G., and Thomson, D. J. (2010a). Large-eddy simulation of a buoyant plume in uniform and stably stratified environments. *Journal of Fluid Mechanics* **652**, 75.

Devenish, B. J., Rooney, G. G., Webster, H. N., and Thomson, D. J. (2010b). The Entrainment Rate for Buoyant Plumes in a Crossflow. *Boundary-Layer Meteorology* **134**, 411–439.

Devenish, B. J., Thomson, D. J., Marenco, F., Leadbetter, S. J., Ricketts, H., and Dacre, H. F. (2012). A study of the arrival over the United Kingdom in April 2010 of the Eyjafjallajökull ash cloud using ground-based lidar and numerical simulations. *Atmospheric Environment* **48**, 152–164.

Di Stefano, A. and Branca, S. (2002). Long-term uplift rate of the Etna volcano basement (southern Italy) based on biochronological data from Pleistocene sediments. *Terra Nova* **14**, 61–68.

Dietterich, H. R., Diefenbach, A. K., Soule, S. A., Zoeller, M. H., Patrick, M. P., Major, J. J., and Lundgren, P. R. (2021). Lava effusion rate evolution and erupted volume during the 2018 Kīlauea lower East Rift Zone eruption. *Bulletin of Volcanology* **83**, 1–18.

Dingwell, A. and Rutgersson, A. (2014). Estimating volcanic ash hazard in European airspace. *Journal of volcanology and geothermal research* **286**, 55–66.

Dobran, F., Neri, A., and Macedonio, G. (1993). Numerical simulation of collapsing volcanic columns. *Journal of Geophysical Research: Solid Earth* **98**, 4231–4259.

Doglioni, C., Innocenti, F., and Mariotti, G. (2001). Why Mt Etna? *Terra Nova* **13**, 25–31.

Donnadieu, F., Freville, P., Hervier, C., Coltelli, M., Scollo, S., Prestifilippo, M., Valade, S., Rivet, S., and Cacault, P. (2016). Near-source Doppler radar monitoring of tephra plumes at Etna. *Journal of Volcanology and Geothermal Research* **312**, 26–39.

Duncan, A. M., Dibben, C., CHESTER, D. K., and Guest, J. E. (1996). The 1928 eruption of Mount Etna Volcano, Sicily, and the destruction of the town of Mascali. *Disasters* **20**, 1–20.

Durig, T., Gudmundsson, M. T., Karmann, S., Zimanowski, B., Dellino, P., Rietze, M., and Buttner, R. (2015). Mass eruption rates in pulsating eruptions estimated from video analysis of the gas thrust-buoyancy transition-a case study of the 2010 eruption of Eyjafjallajokull, Iceland. *Earth Planets and Space* **67**, 180.

Dürig, T., Gudmundsson, M. T., and Dellino, P. (2015). Reconstruction of the geometry of volcanic vents by trajectory tracking of fast ejecta-the case of the Eyjafjallajökull 2010 eruption (Iceland). *Earth, Planets and Space* **67**, 1–8.

Edwards, M. J., Pioli, L., Andronico, D., Scollo, S., Ferrari, F., and Cristaldi, A. (2018). Shallow factors controlling the explosivity of basaltic magmas: The 17–25 May 2016 eruption of Etna Volcano (Italy). *Journal of Volcanology and Geothermal Research* **357**, 425–436.

Edwards, M. J., Pioli, L., Harris, A. J. L., Gurioli, L., and Thivet, S. (2020). Magma fragmentation and particle size distributions in low intensity mafic explosions: the July/August 2015 Piton de la Fournaise eruption. *Scientific reports* **10**, 1–14.

Ernst, G. G. J. (1998). Dynamics of sediment-laden plumes. PhD thesis. University of Bristol.

Ernst, G. G. J., Sparks, R. S. J., Carey, S. N., and Bursik, M. I. (1996). Sedimentation from turbulent jets and plumes. *Journal of Geophysical Research: Solid Earth* **101**, 5575.

Esposti Ongaro, T. and Cerminara, M. (2016). on-equilibrium processes in ash-laden volcanic plumes: new insights from 3D multiphase flow simulations. *Journal of Volcanology and Geothermal Research* **326**, 127–142.

Fabregat, A., Deremble, B., Wienders, N., Stroman, A., Poje, A., Özgökmen, T. M., and Dewar, W. K. (2017). Rotating 2d point source plume models with application to Deepwater Horizon. *Ocean Modelling* **119**, 118–135.

Fabregat Tomàs, A., Poje, A. C., Özgökmen, T. M., and Dewar, W. K. (2016). Effects of rotation on turbulent buoyant plumes in stratified environments. *Journal of Geophysical Research: Oceans* **121**, 5397–5417.

Faccenna, C., Molin, P., Orecchio, B., Olivetti, V., Bellier, O., Funiciello, F., Minelli, L., Piromallo, C., and Billi, A. (2011). Topography of the Calabria subduction zone (southern Italy): Clues for the origin of Mt. Etna. *Tectonics* **30**.

Fierstein, J. and Nathenson, M. (1992). Another look at the calculation of fallout tephra volumes. *Bulletin of volcanology* **54**, 156–167.

Fisher, R. V. (1961). Proposed classification of volcaniclastic sediments and rocks. *Geological Society of America Bulletin* **72**, 1409–1414.

Folch, A. (2012). A review of tephra transport and dispersal models: Evolution, current status, and future perspectives. *Journal of Volcanology and Geothermal Research* **235**, 96–115.

Folch, A., Costa, A., and Macedonio, G. (2016). FPLUME-1.0: An integral volcanic plume model accounting for ash aggregation. *Geoscientific Model Development* **9**, 431–450.

Formenti, Y., Druitt, T. H., and Kelfoun, K. (2003). Characterisation of the 1997 Vulcanian explosions of Soufrière Hills Volcano, Montserrat, by video analysis. *Bulletin of Volcanology* **65**, 587–605.

Fornaciai, A., Behncke, B., Favalli, M., Neri, M., Tarquini, S., and Boschi, E. (2010). Detecting short-term evolution of Etnean scoria cones: a LIDAR-based approach. *Bulletin of Volcanology* **72**, 1209–1222.

Freitas, S. R., Longo, K. M., Trentmann, J., and Latham, D. (2010). Sensitivity of 1-D smoke plume rise models to the inclusion of environmental wind drag. *Atmospheric Chemistry and Physics* **10**, 585–594.

Freret-Lorgeril, V., Bonadonna, C., Corradini, S., Donnadieu, F., Guerrieri, L., Lacanna, G., Marzano, F. S., Mereu, L., Merucci, L., Ripepe, M., et al. (2021a). Examples of Multi-Sensor Determination of Eruptive Source Parameters of Explosive Events at Mount Etna. *Remote Sensing* **13**, 2097.

Freret-Lorgeril, V., Bonadonna, C., Corradini, S., Guerrieri, L., Lemus, J., Donnadieu, F., Scollo, S., Gurioli, L., and Rossi, E. (2021b). Tephra characterization and multi-disciplinary determination of Eruptive Source Parameters of a weak paroxysm at Mount Etna (Italy). *Journal of Volcanology and Geothermal Research*, 107431.

Freret-Lorgeril, V., Donnadieu, F., Scollo, S., Provost, A., Fréville, P., Guéhenneux, Y., Hervier, C., Prestifilippo, M., and Coltelli, M. (2018). Mass Eruption Rates of Tephra Plumes During the 2011–2015 Lava Fountain Paroxysms at Mt. Etna From Doppler Radar Retrievals. *Frontiers in Earth Science* **6**, 73.

Freret-Lorgeril, V., Gilchrist, J., Donnadieu, F., Jellinek, A. M., Delanoë, J., Latchimy, T., Vinson, J.-P., Caudoux, C., Peyrin, F., Hervier, C., et al. (2020). Ash sedimentation by fingering and sediment thermals from wind-affected volcanic plumes. *Earth and Planetary Science Letters* **534**, 116072.

Fries, A. A., Lemus, J., Jarvis, P., Clarke, A. B., Phillips, J. C., Manzella, I., and Bonadonna, C. (2021). The Influence of Particle Concentration on the Formation of Settling-Driven Gravitational Instabilities at the Base of Volcanic Clouds. *Frontiers in Earth Sciences* **9**.

Ganci, G., James, M. R., Calvari, S., and Negro, C. D. (2013). Separating the thermal fingerprints of lava flows and simultaneous lava fountaining using ground-based thermal camera and SEVIRI measurements. *Geophysical Research Letters* **40**, 5058–5063.

Gaudin, D., Taddeucci, J., Houghton, B. F., Orr, T. R., Andronico, D., Del Bello, E., Kueppers, U., Ricci, T., and Scarlato, P. (2016). 3-D high-speed imaging of volcanic bomb trajectory in basaltic explosive eruptions. *Geochemistry, Geophysics, Geosystems* **17**, 4268–4275.

Gaudin, D., Taddeucci, J., Scarlato, P., Harris, A., Bombrun, M., Del Bello, E., and Ricci, T. (2017). Characteristics of puffing activity revealed by ground-based, thermal infrared imaging: the example of Stromboli Volcano (Italy). *Bulletin of Volcanology* **79**, 24.

Gaudin, D., Taddeucci, J., Scarlato, P., Moroni, M., Freda, C., Gaeta, M., and Palladino, D. M. (2014). Pyroclast Tracking Velocimetry illuminates bomb ejection and explosion dynamics at Stromboli (Italy) and Yasur (Vanuatu) volcanoes. *Journal of Geophysical Research: Solid Earth* **119**, 5384–5397.

Ghiorso, M. S. and Sack, R. O. (1995). Chemical mass transfer in magmatic processes IV. A revised and internally consistent thermodynamic model for the interpolation and extrapolation of liquid-solid equilibria in magmatic systems at elevated temperatures and pressures. *Contributions to Mineralogy and Petrology* **119**, 197–212.

Girault, F., Carazzo, G., Tait, S., Ferrucci, F., and Kaminski, É. (2014). The effect of total grain-size distribution on the dynamics of turbulent volcanic plumes. *Earth and Planetary Science Letters* **394**, 124–134.

Girault, F., Carazzo, G., Tait, S., and Kaminski, É. (2016). Combined effects of total grain-size distribution and crosswind on the rise of eruptive volcanic columns. *Journal of Volcanology and Geothermal Research* **326**, 103–113.

Giudicepietro, F., Calvari, S., Alparone, S., Bianco, F., Bonaccorso, A., Bruno, V., Caputo, T., Cristaldi, A., D'Auria, L., De Cesare, W., et al. (2019). Integration of ground-based remote-sensing and in situ multidisciplinary monitoring data to analyze the eruptive activity of Stromboli volcano in 2017–2018. *Remote Sensing* **11**, 1813.

Glaze, L. S., Self, S., Schmidt, A., and Hunter, S. J. (2017). Assessing eruption column height in ancient flood basalt eruptions. *Earth and Planetary Science Letters* **457**, 263–270.

Gonnermann, H. M. and Manga, M. (2003). Explosive volcanism may not be an inevitable consequence of magma fragmentation. *Nature* **426**, 432–435.

Gouhier, M. and Donnadieu, F. (2008). Mass estimations of ejecta from Strombolian explosions by inversion of Doppler radar measurements. *Journal of Geophysical Research: Solid Earth* **113**.

Gouhier, M., Eychenne, J., Azzaoui, N., Guillin, A., Deslandes, M., Poret, M., Costa, A., and Husson, P. (2019). Low efficiency of large volcanic eruptions in transporting very fine ash into the atmosphere. *Scientific reports* **9**, 1–12.

Gualda, G. A. R., Ghiorso, M. S., Lemons, R. V., and Carley, T. L. (2012). Rhyolite-MELTS: a modified calibration of MELTS optimized for silica-rich, fluid-bearing magmatic systems. *Journal of Petrology* **53**, 875–890.

Gudmundsson, G. (2011). Respiratory health effects of volcanic ash with special reference to Iceland. A review. *The clinical respiratory journal* **5**, 2–9.

Guffanti, M., Mayberry, G. C., Casadevall, T. J., and Wunderman, R. (2009). Volcanic hazards to airports. *Natural hazards* **51**, 287–302.

Gvirtzman, Z. and Nur, A. (1999). The formation of Mount Etna as the consequence of slab rollback. *Nature* **401**, 782–785.

Harris, A. J. L., Delle Donne, D., Dehn, J., Ripepe, M., and Worden, A. K. (2013). Volcanic plume and bomb field masses from thermal infrared camera imagery. *Earth and Planetary Science Letters* **365**, 77–85.

Head, J. W. and Wilson, L. (1989). Basaltic pyroclastic eruptions: Influence of gas-release patterns and volume fluxes on fountain structure, and the formation of cinder cones, spatter cones, rootless flows, lava ponds and lava flows. *Journal of Volcanology and Geothermal Research* **37**, 261–271.

Head, J. W. and Wilson, L. (1987). Lava fountain heights at Pu'u'O'o, Kilauea, Hawaii: Indicators of amount and variations of exsolved magma volatiles. *Journal of Geophysical Research: Solid Earth* **92**, 13715–13719.

Heggie, T. W. (2009). Geotourism and volcanoes: health hazards facing tourists at volcanic and geothermal destinations. *Travel medicine and infectious disease* **7**, 257–261.

Helfrich, K. R. and Battisti, T. M. (1991). Experiments on baroclinic vortex shedding from hydrothermal plumes. *Journal of Geophysical Research: Oceans* **96**, 12511–12518.

Herzog, M. and Graf, H.-F. (2010). Applying the three-dimensional model ATHAM to volcanic plumes: Dynamic of large co-ignimbrite eruptions and associated injection heights for volcanic gases. *Geophysical Research Letters* **37**.

Hewett, T. A., Fay, J. A., and Hoult, D. P. (1971). Laboratory experiments of smokestack plumes in a stable atmosphere. *Atmospheric Environment (1967)* **5**, 767–789.

Holland, P. R. and Feltham, D. L. (2006). The effects of rotation and ice shelf topography on frazil-laden ice shelf water plumes. *Journal of physical oceanography* **36**, 2312–2327.

Houghton, B. F. and Gonnermann, H. M. (2008). Basaltic explosive volcanism: constraints from deposits and models. *Geochemistry* **68**, 117–140.

Houghton, B. F., Tisdale, C. M., Llewellin, E. W., Taddeucci, J., Orr, T. R., Walker, B. H., and Patrick, M. R. (2020). The Birth of a Hawaiian Fissure Eruption. *Journal of Geophysical Research: Solid Earth*, e2020JB020903.

Hunt, G. R. and Van den Bremer, T. S. (2011). Classical plume theory: 1937–2010 and beyond. *IMA journal of applied mathematics* **76**, 424–448.

Huq, P. and Stewart, E. J. (1996). A laboratory study of buoyant plumes in laminar and turbulent crossflows. *Atmospheric Environment* **30**, 1125–1135.

Jones, H. and Marshall, J. (1993). Convection with rotation in a neutral ocean: A study of open-ocean deep convection. *Journal of Physical Oceanography* **23**, 1009–1039.

Jones, T. J., Reynolds, C. D., and Boothroyd, S. C. (2019). Fluid dynamic induced break-up during volcanic eruptions. *Nature communications* **10**, 1–7.

Kaminski, E., Tait, S., and Carazzo, G. (2005). Turbulent entrainment in jets with arbitrary buoyancy. *Journal of Fluid Mechanics* **526**, 361.

Kaminski, E., Tait, S., Ferrucci, F., Martet, M., Hirn, B., and Husson, P. (2011). Estimation of ash injection in the atmosphere by basaltic volcanic plumes: The case of the Eyjafjallajokull 2010 eruption. *Journal of Geophysical Research - Solid Earth* **116**.

Kelfoun, K., Harris, A., Bontemps, M., Labazuy, P., Chausse, F., Ripepe, M., and Donnadieu, F. (2020). A method for 3D reconstruction of volcanic bomb trajectories. *Bulletin of Volcanology* **82**, 1–15.

La Spina, G., Arzilli, F., Llewellin, E. W., Burton, M. R., Clarke, A. B., de'Michieli Vitturi, M., Polacci, M., Hartley, M. E., Di Genova, D., and Mader, H. M. (2021). Explosivity of basaltic lava fountains is controlled by magma rheology, ascent rate and outgassing. *Earth and Planetary Science Letters* **553**, 116658.

Lamb, O. D., De Angelis, S., and Lavallée, Y. (2015). Using infrasound to constrain ash plume rise. *Journal of Applied Volcanology* **4**, 1–9.

Li, S. and Flynn, M. R. (2020). Coaxial plumes in a windy ambient with applications to cooling towers. *Journal of Wind Engineering and Industrial Aerodynamics* **196**, 104054.

Li, S., Moradi, A., Vickers, B., and Flynn, M. R. (2018). Cooling tower plume abatement using a coaxial plume structure. *International Journal of Heat and Mass Transfer* **120**, 178–193.

Macedonio, G., Costa, A., and Folch, A. (2016). Uncertainties in volcanic plume modeling: A parametric study using FPLUME. *Journal of Volcanology and Geothermal Research* **326**, 92–102.

Mannen, K. (2006). Total grain size distribution of a mafic subplinian tephra, TB-2, from the 1986 Izu-Oshima eruption, Japan: An estimation based on a theoretical model of tephra dispersal. *Journal of Volcanology and Geothermal Research* **155**, 1–17.

Manzella, I., Bonadonna, C., Phillips, J. C., and Monnard, H. (2015). The role of gravitational instabilities in deposition of volcanic ash. *Geology* **43**, 211–214.

Marenco, F., Johnson, B., Turnbull, K., Newman, S., Haywood, J., Webster, H., and Ricketts, H. (2011). Airborne lidar observations of the 2010 Eyjafjallajökull volcanic ash plume. *Journal of Geophysical Research: Atmospheres* **116**.

Mastin, L. G. (2007). A user-friendly one-dimensional model for wet volcanic plumes. *Geochemistry, Geophysics, Geosystems* **8**.

Mastin, L. G. (2014). Testing the accuracy of a 1-D volcanic plume model in estimating mass eruption rate. *Journal of Geophysical Research: Atmospheres* **119**, 2474–2495.

Mastin, L. G., Guffanti, M., Servranckx, R., Webley, P., Barsotti, S., Dean, K., Durant, A., Ewert, J. W., Neri, A., Rose, W. I., Schneider, D., Siebert, L., Stunder, B., Swanson, G., Tupper, A., Volentik, A., and Waythomas, C. F. (2009). A multidisciplinary effort to assign realistic source parameters to models of volcanic ash-cloud transport and dispersion during eruptions. *Journal of Volcanology and Geothermal Research* **186**, 10–21.

Mcdougall, T. J. (1978). Bubble plumes in stratified environments. *Journal of Fluid Mechanics* **85**, 655–672.

Mcdougall, T. J. (1981). Negatively buoyant vertical jets. *Tellus* **33**, 313–320.

McKee, K., Smith, C., Reath, K., Snee, E., Maher, S., Matoza, R. S., Carn, S., Mastin, L., Anderson, K., Damby, D., et al. (2021). Evaluating the state-of-the-art in remote volcanic eruption characterization Part I: Raikoke volcano, Kuril Islands. *Journal of Volcanology and Geothermal Research*, 107354.

Mereu, L., Scollo, S., Bonadonna, C., Freret-Lorgeril, V., and Marzano, F. S. (2020). "Multisensor Characterization of the Incandescent Jet Region of Lava Fountain-Fed Tephra Plumes".

Métrich, N., Allard, P., Spilliaert, N., Andronico, D., and Burton, M. (2004). 2001 flank eruption of the alkali- and volatile-rich primitive basalt responsible for Mount Etna's evolution in the last three decades. *Earth and Planetary Science Letters* **228**, 1–17.

Métrich, N., Bertagnini, A., and Pistolesi, M. (2021). Paroxysms at Stromboli volcano (Italy): source, genesis and dynamics. *Frontiers in Earth Science* **9**, 45.

Métrich, N. and Rutherford, M. J. (1998). Low Pressure Crystallization Paths of H2O-Saturated Basaltic-Hawaiitic Melts from Mt Etna: Implications for Open-System Degassing of Basaltic Volcanoes. *Geochimica et Cosmochimica Acta* **62**, 1195–1295.

Michaud-Dubuy, A., Carazzo, G., and Kaminski, E. (2020). Wind entrainment in jets with reversing buoyancy: Implications for volcanic plumes. *Journal of Geophysical Research: Solid Earth* **125**.

Miller, C. A. and Jolly, A. D. (2014). A model for developing best practice volcano monitoring: a combined threat assessment, consultation and network effectiveness approach. *Natural hazards* **71**, 493–522.

Mittal, T. and Delbridge, B. (2019). Detection of the 2012 Havre submarine eruption plume using Argo floats and its implications for ocean dynamics. *Earth and Planetary Science Letters* **511**, 105–116.

Montelli, R., Nolet, G., Dahlen, F. A., and Masters, G. (2006). A catalogue of deep mantle plumes: New results from finite-frequency tomography. *Geochemistry, Geophysics, Geosystems* **7**.

Montopoli, M. (2016). Velocity profiles inside volcanic clouds from three-dimensional scanning microwave dual-polarization Doppler radars. *Journal of Geophysical Research: Atmospheres* **121**, 7881–7900.

Morton, B. R. (1962). Coaxial turbulent jets. *International Journal of Heat and Mass Transfer* **5**, 955–965.

Morton, B. R. (1965). Modeling fire plumes. *Symposium (International) on Combustion* **10**, 973–982.

Morton, B. R., Taylor, G. I., and Turner, J. S. (1956). Turbulent gravitational convection from maintained and instantaneous sources. *Proceedings of the Royal Society of London. Series A. Mathematical and Physical Sciences* **234**, 1–23.

Mueller, S. B., Houghton, B. F., Swanson, D. A., Poret, M., and Fagents, S. A. (2019). Total grain size distribution of an intense Hawaiian fountaining event: case study of the 1959 Kīlauea Iki eruption. *Bulletin of Volcanology* **81**, 43.

Mulas, M., Cioni, R., Andronico, D., and Mundula, F. (2016). The explosive activity of the 1669 Monti Rossi eruption at Mt. Etna (Italy). *Journal of volcanology and geothermal research* **328**, 115–133.

Namiki, A., Patrick, M. R., Manga, M., and Houghton, B. F. (2021). Brittle fragmentation by rapid gas separation in a Hawaiian fountain. *Nature Geoscience* **14**, 242–247.

Neri, M., Casu, F., Acocella, V., Solaro, G., Pepe, S., Berardino, P., Sansosti, E., Caltabiano, T., Lundgren, P., and Lanari, R. (2009). Deformation and eruptions at Mt. Etna (Italy): A lesson from 15 years of observations. *Geophysical Research Letters* **36**.

Neri, M., Mazzarini, F., Tarquini, S., Bisson, M., Isola, I., Behncke, B., and Pareschi, M. T. (2008). The changing face of Mount Etna's summit area documented with Lidar technology. *Geophysical Research Letters* **35**.

Oberhuber, J. M., Herzog, M., Graf, H.-F., and Schwanke, K. (1998). Volcanic plume simulation on large scales. *Journal of Volcanology and Geothermal Research* **87**, 29–53.

Osman, S., Rossi, E., Bonadonna, C., Frischknecht, C., Andronico, D., Cioni, R., and Scollo, S. (2019). Exposure-based risk assessment and emergency management associated with the fallout of large clasts at Mount Etna. *Natural Hazards and Earth System Sciences*.

Pailot-Bonnétat, S., Harris, A. J. L., Calvari, S., De Michele, M., and Gurioli, L. (2020). Plume Height Time-Series Retrieval Using Shadow in Single Spatial Resolution Satellite Images. *Remote Sensing* **12**, 3951.

Parfitt, E. A. (1998). A study of clast size distribution, ash deposition and fragmentation in a Hawaiian-style volcanic eruption. *Journal of Volcanology and Geothermal Research* **84**, 197–208.

Parfitt, E. A. and Wilson, L. (1999). A Plinian treatment of fallout from Hawaiian lava fountains. *Journal of Volcanology and Geothermal Research* **88**, 67–75.

Parfitt, E. A., Wilson, L., and Neal, C. A. (1995). Factors influencing the height of Hawaiian lava fountains: implications for the use of fountain height as an indicator of magma gas content. *Bulletin of Volcanology* **57**, 440–450.

Park, J. and Park, H. (2021). Particle dispersion induced by vortical interactions in a particle-laden upward jet with a partial crossflow. *Journal of Fluid Mechanics* **915**.

Patrick, M. R. (2007). Dynamics of Strombolian ash plumes from thermal video: Motion, morphology, and air entrainment. *Journal of Geophysical Research: Solid Earth* **112**.

Pedersen, G. B. M., Höskuldsson, A., Dürig, T., Thordarson, T., Jonsdottir, I., Riishuus, M. S., Óskarsson, B. V., Dumont, S., Magnússon, E., Gudmundsson, M. T., et al. (2017). Lava field evolution and emplacement dynamics of the 2014–2015 basaltic fissure eruption at Holuhraun, Iceland. *Journal of Volcanology and Geothermal Research* **340**, 155–169.

Pering, T. D., Ilanko, T., Wilkes, T. C., England, R. A., Silcock, S. R., Stanger, L. R., Willmott, J. R., Bryant, R. G., and McGonigle, A. J. S. (2019). A rapidly convecting lava lake at Masaya Volcano, Nicaragua. *Frontiers in Earth Science* **6**, 241.

Pering, T. D., Tamburello, G., McGonigle, A. J. S., Aiuppa, A., James, M. R., Lane, S. J., Sciotto, M., Cannata, A., and Patanè, D. (2015). Dynamics of mild strombolian activity on Mt. Etna. *Journal of volcanology and geothermal research* **300**, 103–111.

Perttu, A., Taisne, B., De Angelis, S., Assink, J. D., Tailpied, D., and Williams, R. A. (2020). Estimates of plume height from infrasound for regional volcano monitoring. *Journal of Volcanology and Geothermal Research* **402**, 106997.

Pham, M. V., Plourde, F., and Kim, S. D. (2006a). Effect of swirl on pure turbulent thermal plume development. *International journal of heat and fluid flow* **27**, 502–513.

Pham, M. V., Plourde, F., and Kim, S. D. (2011). Unstable process identification in a pure thermal plume under forced rotating conditions. *Experimental Heat Transfer* **24**, 151–167.

Pham, M. V., Plourde, F., Kim, S. D., and Balachandar, S. (2006b). Large-eddy simulation of a pure thermal plume under rotating conditions. *Physics of Fluids* **18**, 015101.

Pioli, L., Bonadonna, C., and Pistolesi, M. (2019). Reliability of Total Grain-Size Distribution of Tephra Deposits. *Scientific Reports* **9**, 10006.

Pioli, L. and Harris, A. J. L. (2019). Real-time geophysical monitoring of particle size distribution during volcanic explosions at Stromboli volcano (Italy). *Frontiers in Earth Science* **7**, 52.

Polacci, M., Andronico, D., Taddeucci, J., Cristaldi, A., et al. (2019). Mechanisms of ash generation at basaltic volcanoes: the case of Mount Etna, Italy. *Frontiers in Earth Science* **7**, 193.

Pompilio, M., Bertagnini, A., Del Carlo, P., and Di Roberto, A. (2017). Magma dynamics within a basaltic conduit revealed by textural and compositional features of erupted ash: the December 2015 Mt. Etna paroxysms. *Scientific reports* **7**, 1–14.

Poret, M., Corradini, S., Merucci, L., Costa, A., Andronico, D., Montopoli, M., Vulpiani, G., and Freret-Lorgeril, V. (2018a). Reconstructing volcanic plume evolution integrating satellite and ground-based data: Application to the 23 rd November 2013 Etna eruption. *Atmos. Chem. Phys. Discuss. Chem. Phys. Discussion*.

Poret, M., Costa, A., Andronico, D., Scollo, S., Gouhier, M., and Cristaldi, A. (2018b). Modeling Eruption Source Parameters by Integrating Field, Ground-Based, and Satellite-Based Measurements: The Case of the 23 February 2013 Etna Paroxysm. *Journal of Geophysical Research: Solid Earth* **123**, 5427–5450.

Pouget, S., Bursik, M., Singla, P., and Singh, T. (2016). Sensitivity analysis of a one-dimensional model of a volcanic plume with particle fallout and collapse behavior. *Journal of Volcanology and Geothermal Research* **326**, 43–53.

Prata, A. J. and Grant, I. F. (2001). Retrieval of microphysical and morphological properties of volcanic ash plumes from satellite data: Application to Mt Ruapehu, New Zealand. *Quarterly Journal of the Royal Meteorological Society* **127**, 2153–2179.

Prata, F. and Rose, B. (2015). Volcanic ash hazards to aviation. In: *The Encyclopedia of Volcanoes*. Ed. by H. Sigurdsson, B. Houghton, S. R. McNutt, H. Rymer, and J. Stix. Elsevier, 911–934.

Pyle, D. M. (1989). The thickness, volume and grainsize of tephra fall deposits. *Bulletin of Volcanology* **51**, 1–15.

Richter, D. H., Eaton, J. P., Murata, K. J., Ault, W. U., and Krivoy, H. L. (1970). *Chronological narrative of the 1959-60 eruption of Kilauea volcano, Hawaii*. Tech. rep.

Ricou, F. P. and Spalding, D. B. (1961). Measurements of entrainment by axisymmetrical turbulent jets. *Journal of Fluid Mechanics* **11**, 21–32.

Ripepe, M., Donne, D. D., Harris, A., Marchetti, E., and Ulivieri, G. (2008). Dynamics of Strombolian activity. *Washington DC American Geophysical Union Geophysical Monograph Series* **182**, 39–48.

Romero, J. E., Vera, F., Polacci, M., Morgavi, D., Arzilli, F., Alam, M. A., Bustillos, J. E., Guevara, A., Johnson, J. B., Palma, J. L., Burton, M., Cuenca, E., and Keller, W. (2018). Tephra From the 3 March 2015 Sustained Column Related to Explosive Lava Fountain Activity at Volcán Villarrica (Chile). *Frontiers in Earth Science* **6**, 98.

Rooney, G. G. and Linden, P. F. (1996). Similarity considerations for non-Boussinesq plumes in an unstratified environment. *Journal of Fluid Mechanics* **318**, 237–250.

Rosi, M., Bertagnini, A., Harris, A. J. L., Pioli, L., Pistolesi, M., and Ripepe, M. (2006). A case history of paroxysmal explosion at Stromboli: timing and dynamics of the April 5, 2003 event. *Earth and Planetary Science Letters* **243**, 594–606.

Rossi, E., Bonadonna, C., and Degruyter, W. (2019). A new strategy for the estimation of plume height from clast dispersal in various atmospheric and eruptive conditions. *Earth and Planetary Science Letters* **505**, 1–12.

Sahetapy-Engel, S. T. and Harris, A. J. L. (2009). Thermal-image-derived dynamics of vertical ash plumes at Santiaguito volcano, Guatemala. *Bulletin of volcanology* **71**, 827–830.

Sawyer, G. M. and Burton, M. R. (2006). Effects of a volcanic plume on thermal imaging data. *Geophysical Research Letters* **33**.

Schellart, W. P. (2010). Mount Etna–Iblean volcanism caused by rollback-induced upper mantle upwelling around the Ionian slab edge: an alternative to the plume model. *Geology* **38**, 691–694.

Schiano, P., Clocchiatti, R., Ottolini, L., and Busa, T. (2001). Transition of Mount Etna lavas from a mantle-plume to an island-arc magmatic source. *Nature* **412**, 900–904.

Schindelin, J., Arganda-Carreras, I., Frise, E., Kaynig, V., Longair, M., Pietzsch, T., Preibisch, S., Rueden, C., Saalfeld, S., Schmid, B., et al. (2012). Fiji: an open-source platform for biological-image analysis. *Nature methods* **9**, 676–682.

Scollo, S., Bonadonna, C., and Manzella, I. (2017). Settling-driven gravitational instabilities associated with volcanic clouds: new insights from experimental investigations. *Bulletin of Volcanology* **79**, 39.

Scollo, S., Boselli, A., Coltelli, M., Leto, G., Pisani, G., Prestifilippo, M., Spinelli, N., and Wang, X. (2015). Volcanic ash concentration during the 12 August 2011 Etna eruption. *Geophysical Research Letters* **42**, 2634–2641.

Scollo, S., Boselli, A., Coltelli, M., Leto, G., Pisani, G., Spinelli, N., and Wang, X. (2012). Monitoring Etna volcanic plumes using a scanning LiDAR. *Bulletin of volcanology* **74**, 2383–2395.

Scollo, S., Coltelli, M., Bonadonna, C., and Del Carlo, P. (2013). Tephra hazard assessment at Mt. Etna (Italy). *Natural Hazards and Earth System Sciences* **13**, 3221–3233.

Scollo, S., Del Carlo, P., and Coltelli, M. (2007). Tephra fallout of 2001 Etna flank eruption: Analysis of the deposit and plume dispersion. *Journal of Volcanology and Geothermal Research* **160**, 147–164.

Scollo, S., Prestifilippo, M., Bonadonna, C., Cioni, R., Corradini, S., Degruyter, W., Rossi, E., Silvestri, M., Biale, E., Carparelli, G., Cassisi, C., Merucci, L., Musacchio, M., and Pecora, E. (2019). Near-real-time tephra fallout assessment at Mt. Etna, Italy. *Remote Sensing* **11**, 1–18.

Scollo, S., Prestifilippo, M., Pecora, E., Corradini, S., Merucci, L., Spata, G., and Coltelli, M. (2014). Eruption column height estimation of the 2011-2013 Etna lava fountains. *Annals of Geophysics* **57**, 214.

Scollo, S., Prestifilippo, M., Spata, G., D'Agostino, M., and Coltelli, M. (2009). Monitoring and forecasting Etna volcanic plumes. *Natural Hazards and Earth System Sciences* **9**, 1573–1585.

Scollo, S., Tarantola, S., Bonadonna, C., Coltelli, M., and Saltelli, A. (2008). Sensitivity analysis and uncertainty estimation for tephra dispersal models. *Journal of Geophysical Research: Solid Earth* **113**.

Sellitto, P., di Sarra, A., Corradini, S., Boichu, M., Herbin, H., Dubuisson, P., Sèze, G., Meloni, D., Monteleone, F., Merucci, L., et al. (2016). Synergistic use of Lagrangian dispersion and radiative transfer modelling with satellite and surface remote sensing measurements for the investigation of volcanic plumes: the Mount Etna eruption of 25–27 October 2013. *Atmospheric Chemistry and Physics*.

Shampine, L. F. and Reichelt, M. W. (1997). The MATLAB ode suite. *SIAM Journal of Scientific Computing* **18**, 1–22.

Shampine, L. F., Reichelt, M. W., and Kierzenka, J. A. (1999). Solving index-I DAEs in MATLAB and Simulink. *SIAM Review* **41**, 538–552.

Snee, E., Degruyter, W., Bonadonna, C., Scollo, S., Rossi, E., and Freret-Lorgeril, V. (2021). A model for buoyant tephra plumes coupled to lava fountains with an application to the 29th of August 2011 paroxysmal eruption at Mount Etna, Italy. *Journal of Geophysical Research: Solid Earth*.

Spampinato, L., Calvari, S., Oppenheimer, C., and Boschi, E. (2011). Volcano surveillance using infrared cameras. *Earth-Science Reviews* **106**, 63–91.

Sparks, R. S. J., Bursik, M. I., Ablay, G. J., Thomas, R. M. E., and Carey, S. N. (1992). Sedimentation of tephra by volcanic plumes. Part 2: controls on thickness and grain-size variations of tephra fall deposits. *Bulletin of Volcanology* **54**, 685–695.

Sparks, R. S. J., Bursik, M. I., Carey, S. N., Gilbert, J., Glaze, L. S., Sigurdsson, H., and Woods, A. W. (1997). Volcanic plumes. Wiley.

Sparks, R. S. J. and Wilson, L. (1982). Explosive volcanic eruptions—V. Observations of plume dynamics during the 1979 Soufrière eruption, St Vincent. *Geophysical Journal International* **69**, 551–570.

Spilliaert, N., Allard, P., Métrich, N., and Sobolev, A. V. (2006). Melt inclusion record of the conditions of ascent, degassing, and extrusion of volatile-rich alkali basalt during the powerful 2002 flank eruption of Mount Etna (Italy). *Journal of Geophysical Research: Solid Earth* **111**.

Stothers, R. B., Wolff, J. A., Self, S., and Rampino, M. R. (1986). Basaltic fissure eruptions, plume heights, and atmospheric aerosols. *Geophysical Research Letters* **13**, 725–728.

Stovall, W. K., Houghton, B. F., Gonnermann, H., Fagents, S. A., and Swanson, D. A. (2011). Eruption dynamics of Hawaiian-style fountains: the case study of episode 1 of the Kīlauea Iki 1959 eruption. *Bulletin of Volcanology* **73**, 511–529.

Sumner, J. M. (1998). Formation of clastogenic lava flows during fissure eruption and scoria cone collapse: the 1986 eruption of Izu-Oshima Volcano, eastern Japan. *Bulletin of Volcanology* **60**, 195–212.

Suwa, H., Suzuki, Y. J., and Yokoo, A. (2014). Estimation of exit velocity of volcanic plume from analysis of vortex structures. *Earth and Planetary Science Letters* **385**, 154–161.

Suzuki, Y. J., Costa, A., Cerminara, M., Esposti Ongaro, T., Herzog, M., Van Eaton, A. R., and Denby, L. C. (2016a). Inter-comparison of three-dimensional models of volcanic plumes. *Journal of Volcanology and Geothermal Research* **326**, 26–42.

Suzuki, Y. J., Costa, A., and Koyaguchi, T. (2016b). On the relationship between eruption intensity and volcanic plume height: insights from three-dimensional numerical simulations. *Journal of Volcanology and Geothermal Research* **326**, 120–126.

Suzuki, Y. J. and Iguchi, M. (2019). Determination of the mass eruption rate for the 2014 Mount Kelud eruption using three-dimensional numerical simulations of volcanic plumes. *Journal of Volcanology and Geothermal Research* **382**, 42–49.

Suzuki, Y. J. and Koyaguchi, T. (2010). Numerical determination of the efficiency of entrainment in volcanic eruption columns. *Geophysical Research Letters* **37**.

Suzuki, Y. J. and Koyaguchi, T. (2015). Effects of wind on entrainment efficiency in volcanic plumes. *Journal of Geophysical Research: Solid Earth* **120**, 6122–6140.

Suzuki, Y. J. and Koyaguchi, T. (2013). 3D numerical simulation of volcanic eruption clouds during the 2011 Shinmoe-dake eruptions. *Earth, Planets and Space* **65**, 581–589.

Taddeucci, J., Alatorre Ibarguengoitia, M., Palladino, D. M., Scarlato, P., and Camaldo, C. (2015a). High-speed imaging of Strombolian eruptions: Gas-pyroclast dynamics in initial volcanic jet. *Geophysical Research Letters* **42**, 6253–6260.

Taddeucci, J., Alatorre-Ibargüengoitia, M. A., Cruz-Vázquez, O., Del Bello, E., Scarlato, P., and Ricci, T. (2017). In-flight dynamics of volcanic ballistic projectiles. *Reviews of Geophysics* **55**, 675–718.

Taddeucci, J., Edmonds, M., Houghton, b., James, M. R., and Vergniolle, S. (2015b). Hawaiian and Strombolian eruptions. In: *The Encyclopedia of*

Volcanoes. Ed. by H. Sigurdsson, B. Houghton, S. R. McNutt, H. Rymer, and J. Stix. Elsevier, 485–503.

Taddeucci, J., Palladino, D. M., Sottili, G., Bernini, D., Andronico, D., and Cristaldi, A. (2013). Linked frequency and intensity of persistent volcanic activity at Stromboli (Italy). *Geophysical Research Letters* **40**, 3384–3388.

Taddeucci, J., Scarlato, P., Capponi, A., Del Bello, E., Cimarelli, C., Palladino, D., and Kueppers, U. (2012). High-speed imaging of strombolian explosions: The ejection velocity of pyroclasts. *Geophysical research letters* **39**.

Terada, A. and Ida, Y. (2007). Kinematic features of isolated volcanic clouds revealed by video records. *Geophysical research letters* **34**.

Tournigand, P.-Y., Fernández, J. J. P., Taddeucci, J., Perugini, D., Sesterhenn, J., and Palladino, D. M. (2019). Time evolution of transient volcanic plumes: Insights from fractal analysis. *Journal of Volcanology and Geothermal Research* **371**, 59–71.

Tournigand, P.-Y., Taddeucci, J., Gaudin, D., Peña Fernández, J. J., Del Bello, E., Scarlato, P., Kueppers, U., Sesterhenn, J., and Yokoo, A. (2017). The initial development of transient volcanic plumes as a function of source conditions. *Journal of Geophysical Research: Solid Earth* **122**, 9784–9803.

Turner, J. S. (1969). Buoyant plumes and thermals. *Annual Review of Fluid Mechanics* **1**, 29–44.

Turner, J. S. (1979). Buoyancy effects in fluids. Cambridge university press.

Valade, S., Ripepe, M., Giuffrida, G., Karume, K., and Tedesco, D. (2018). Dynamics of Mount Nyiragongo lava lake inferred from thermal imaging and infrasound array. *Earth and Planetary Science Letters* **500**, 192–204.

Valade, S. A., Harris, A. J. L., and Cerminara, M. (2014). Plume Ascent Tracker: Interactive Matlab software for analysis of ascending plumes in image data. *Computers & Geosciences* **66**, 132–144.

Valentine, G. A. and Wohletz, K. H. (1989). Numerical models of Plinian eruption columns and pyroclastic flows. *Journal of Geophysical Research: Solid Earth* **94**, 1867–1887.

Vergniolle, S. and Ripepe, M. (2008). From Strombolian explosions to fire fountains at Etna Volcano (Italy): what do we learn from acoustic measurements? *Geological Society, London, Special Publications* **307**, 103–124.

Vicari, A., Ganci, G., Behncke, B., Cappello, A., Neri, M., and Del Negro, C. (2011). Near-real-time forecasting of lava flow hazards during the 12–13 January 2011 Etna eruption. *Geophysical Research Letters* **38**.

Vulpiani, G., Ripepe, M., and Valade, S. (2016). Mass discharge rate retrieval combining weather radar and thermal camera observations. *Journal of Geophysical Research: Solid Earth* **121**, 5679–5695.

Walker, G. P. L., Self, S., and Wilson, L. (1984). Tarawera 1886, New Zealand—a basaltic plinian fissure eruption. *Journal of volcanology and geothermal research* **21**, 61–78.

Wilson, L. (1980). Relationships between pressure, volatile content and ejecta velocity in three types of volcanic explosion. *Journal of Volcanology and Geothermal Research* **8**, 297–313.

Wilson, L. and Head III, J. W. (1981). Ascent and eruption of basaltic magma on the Earth and Moon. *Journal of Geophysical Research: Solid Earth* **86**, 2971–3001.

Wilson, L., Parfitt, E. A., and Head III, J. W. (1995). Explosive volcanic eruptions—VIII. The role of magma recycling in controlling the behaviour of Hawaiian-style lava fountains. *Geophysical Journal International* **121**, 215–225.

Wilson, L., Sparks, R. S. J., and Walker, G. P. (1980). Explosive volcanic eruptions—IV. The control of magma properties and conduit geometry on eruption column behaviour. *Geophysical Journal International* **63**, 117–148.

Wilson, L. and Walker, G. P. L. (1987). Explosive volcanic eruptions-VI. Ejecta dispersal in plinian eruptions: the control of eruption conditions and atmospheric properties. *Geophysical Journal International* **89**, 657–679.

Winker, D. M. and Osborn, M. T. (1992). Airborne lidar observations of the Pinatubo volcanic plume. *Geophysical research letters* **19**, 167–170.

Witsil, A. J. C. and Johnson, J. B. (2020). Volcano video data characterized and classified using computer vision and machine learning algorithms. *Geoscience Frontiers* **11**, 1789–1803.

Witt, T. and Walter, T. R. (2017). Video monitoring reveals pulsating vents and propagation path of fissure eruption during the March 2011 Pu'u'Ō'ō eruption, Kilauea volcano. *Journal of Volcanology and Geothermal Research* **330**, 43–55.

Witt, T., Walter, T. R., Müller, D., Guðmundsson, M. T., and Schöpa, A. (2018). The Relationship Between Lava Fountaining and Vent Morphology for the 2014–2015 Holuhraun Eruption, Iceland, Analyzed by Video Monitoring and Topographic Mapping. *Frontiers in Earth Science* **6**, 235.

Woitischek, J., Woods, A. W., Edmonds, M., Oppenheimer, C., Aiuppa, A., Pering, T. D., Ilanko, T., D'Aleo, R., and Garaebiti, E. (2020). Strombolian eruptions and dynamics of magma degassing at Yasur Volcano (Vanuatu). *Journal of Volcanology and Geothermal Research* **398**, 106869.

Wood, K., Thomas, H., Watson, M., Calway, A., Richardson, T., Stebel, K., Naismith, A., Berthoud, L., and Lucas, J. (2019). Measurement of three dimensional volcanic plume properties using multiple ground based infrared cameras. *ISPRS Journal of Photogrammetry and Remote Sensing* **154**, 163–175.

Woodhouse, M. J., Hogg, A. J., and Phillips, J. C. (2016). A global sensitivity analysis of the PlumeRise model of volcanic plumes. *Journal of Volcanology and Geothermal Research* **326**, 54–76.

Woodhouse, M. J., Hogg, A. J., Phillips, J. C., and Rougier, J. C. (2015). Uncertainty analysis of a model of wind-blown volcanic plumes. *Bulletin of volcanology* **77**, 1–28.

Woodhouse, M. J., Hogg, A. J., Phillips, J. C., and Sparks, R. S. J. (2013). Interaction between volcanic plumes and wind during the 2010 Eyjafjallajökull eruption, Iceland. *Journal of Geophysical Research: Solid Earth* **118**, 92–109.

Woods, A. W. (1988). The fluid-dynamics and thermodynamics of eruption columns. *Bulletin of Volcanology* **50**, 169–193.

Woods, A. W. (1993). A model of the plumes above basaltic fissure eruptions. *Geophysical Research Letters* **20**, 1115–1118.

Woods, A. W. (2010). Turbulent plumes in nature. *Annual Review of Fluid Mechanics* **42**, 391–412.

Woods, A. W. and Bower, S. M. (1995). The decompression of volcanic jets in a crater during explosive volcanic eruptions. *Earth and Planetary Science Letters* **131**, 189–205.

Woods, A. W. and Bursik, M. I. (1991). Particle fallout, thermal disequilibrium and volcanic plumes. *Bulletin of Volcanology* **53**, 559–470.

Yamamoto, H., Watson, I. M., Phillips, J. C., and Bluth, G. J. (2008). Rise dynamics and relative ash distribution in vulcanian eruption plumes at Santiaguito Volcano, Guatemala, revealed using an ultraviolet imaging camera. *Geophysical Research Letters* **35**.

APPENDIX A

DIMENSIONLESS ANALYSIS BETWEEN H, G AND F

The first step in the dimensional analysis is to determine the dimensions of each of the parameters of interest (G, the parameter defining the density stratification of the surrounding fluid, and F, the initial buoyancy flux) to H, which is the plume height in m. Each of the dimensions of each of the factors in G are written out and then simplified (equation set 1).

$$\begin{aligned} G &= \frac{-g}{\rho_1}\frac{-d\rho_0}{dx} \\ [G] &= [L][T]^{-2}[L]^{-1} \end{aligned} \tag{1}$$

Therefore, the dimensions of G can then be given as

$$[T]^{-2}. \tag{2}$$

Following the same procedure, the dimensions of F are given as

$$[F] = [L]^4[T]^{-3}. \tag{3}$$

The dimensions of H as given as $[L]$.

To then determine the dimensional relationship between H, G and F, it is proposed that $H \propto F^a G^b$. Therefore, in order to be dimensionally consistent

$$[L] = \left([L]^4[T]^{-3}\right)^a \left([T]^{-2}\right)^b, \tag{4}$$

which can be re-written as

$$[L] = [L]^{4a}[T]^{-2b-3a}. \tag{5}$$

Balancing the dimensions of length means that this can then be solved for a

$$1 = 4a, \tag{6}$$

so that

$$a = \frac{1}{4}. \tag{7}$$

Similarly, balancing the dimensions of time means this equation can also be solved for b

$$0 = 3a - 2b, \tag{8}$$

so that

$$b = -\frac{3}{8}. \tag{9}$$

Therefore H is related to F and G by

$$H \propto F^{\frac{1}{4}}G^{-\frac{3}{8}}. \tag{10}$$